Memoria de tesis para optar al grado de Doctor

UNIVERSIDAD AUTONOMA DE MADRID

Magnetoplasmonic Nanorings: Novel Architectures with Tunable Magneto-optical Activity in Wide Wavelength Ranges

Hua Yu Feng

Tesis codirigida por

Dr. Feng Luo y Prof. Alfonso Cebollada

Tutor

Prof. Rodolfo Miranda

Marzo 2017

for my parents

and

my love

Acknowledgements

Well, it is time for the end now…

Almost four years ago, I did imagine it would be a tough time for me to study abroad, and, to obtain my PhD degree. However, at that time I was also overwhelmed by the excitement that for the first time I could travel abroad and have a look at the different world outside my hometown and home country. What I couldn't think about then was that it could be really much longer than I ever expected, with a period of almost one sixth of my whole life until now, to overcome a series of obstacles, difficulties, and even contradictions and conflicts.

But still, it was fortunate for me that along all the way, I was not alone. Here, with my sincere gratitude from my most interior heart, I thank all of them who accompanied, helped, and lead me in the past years, and also, I believe, in the future. Without them, the life in the last four years could not have become so real, concrete, and colorful.

It was just a casual thing that Dr. Feng Luo, my Chinese supervisor, offered me a position in the institute IMDEA-nano via his former colleague in Feb. 2012. Just suddenly I was told about this when our old gangs played basketball in one afternoon-they needed a person who had some experience on thin film deposition and vacuum systems. Well, that should be me in our gang group. Then it was the interview with Dr. Feng Luo and Prof. Rodolfo Miranda, another old and friendly guy, who is the director of the institute and later tutor of my PhD thesis. They offered me an opportunity to apply for the CSC scholarship together and an extra bonus every month. Then it was the long preparation process, and then in Sept. 2012, I was here, in Madrid!

To begin the life here was really difficult. But Feng gave me the best help. The CSC scholarship offered us only one month's salary before I left China, with which I needed to handle all the expenses like the deposit for the rented room and a variety of other things. Feng lent me his own money, not a very large amount of money, but enough for me to pass the tough beginning days. In the rest of the years in Madrid, Feng continued to offer me more help like this, taking care of my life and work, and supporting me financially for the scientific conferences.

Although I was offered the position in IMDEA-nano, the life there was very short. As a new institute, actually at that time IMDEA-nano was not prepared to host all the researchers. After a short training process with Feng in the surface physics lab there, I was sent to another institute, IMM, where I began to cooperate with the magnetoplasmonic group there and met my Spanish supervisor, Prof. Alfonso Cebollada, and all the group members, Prof. Gaspar Armelles, Dr. Antonio García-Martín, Dr. David Meneses-Rodríguez, Dr. María Ujué González (MariaU), Dr. José Miguel García-Martín (Chemi), Dr. Fernando García Pérez, Dr. Renata Kekesi… Here my real scientific research began!!

It was interesting for me to see the people with a variety of expertise working and cooperating closely together. This is very different from what I saw in China before, where usually one person should learn and know almost everything and do them almost alone. Here everybody has their own favorite: Alfonso is an expert on MBE and vacuum systems, and Gaspar on optics and magneto-optics, MariaU on optics, Antonio on theoretical modeling, Jose Miguel on AFM and magnetics, David on lithography, Fernando on programming… All of these guys are cooperating and communicating very closely with each other, and at last, share the results. For me, more important was that they were so glad to share and help, even though I was a newcomer at that time and even could not speak English fluently!

I can still remember that for the first several months, our experiments were not going well. Failures continued one after another. Alfonso felt my depression and gave me the encouragement: "Don't feel too frustrated, this is the life, it will work someday".

Yeah, at last, it would work, just at that time we didn't know when. I was really nervous and frustrated. We just didn't abandon. Time just flew. The obstacle was just in my mind. Just until one day.

This is too clear in my mind and always repeats again and again, even today.
It was before my small surgery, I asked for the sickness leave and was walking on the way back home. Suddenly I felt I could almost locate where the problem was!! Oh, yes, that is it!
I draw it on the paper, wrote the email to the bosses and then waited in excitement. "We can discuss after you are back from your leave."
It was almost two months later that we could restart the experiment and verify my idea. Everything was within expectation and the idea turned out to work so well.
That was the first piece of my work. I was excited. Later there were the second, the third…

In that long run, with his great patience, Alfonso taught me how to be a serious scientist, and offered me the best help on almost everything, including this thesis. His strict training on my scientific activities, and his positive attitude and active role in life, are a real fortune to me.

During the period, David taught me the whole set of lithography method. Then it was Gaspar, Antonio, MariaU, Chemi, and Fernando…
Teaching, learning and discussing…
That was the happiest time I had ever experienced.
Sincere thanks to you all!

And special thanks to Gaspar, who taught me all the knowledge and techniques in the optics, and without whom the work in this thesis could be not done and the thesis could not be written. It was always a surprise and a pleasure to discuss with this guy-he knows so many things in such a clear and different way!!! The insightful advice and discussions from him are really a precious gift to me.

Of course, the work was not completed in the unique group. Help from the colleagues in IMM, Dr. Jorge M. Garc á, and in IMDEA-nano, Dr. Daniel Granados, Dr. Paolo Perna, and Universidad de Zaragoza, Dr. Raul Arenal, and University of Namur, Prof. Luc Henrard… Grateful thanks also to them! It was a great honor for me to have our names together in the author lists of the publications.

Also, every lab is running with the support from a lot of people and ours is not an exception. The friendly technicians in IMDEA-nano and IMM also offered me their kindest help: Dr. Manuel Rodr ́guez from IMDEA-nano, and Patricia, Lorena, Raquel, Carmen from IMM. The well-maintained instruments give us the most convenience during all the work. Thank you!

Science is not the only focus of the life here, although I spent a lot of time to learn this. A lot of administrative processes need to be done every year as a foreigner. I need to renew my ID in Spain and to apply travelling documents every year, which are both really complicated and tedious processes. But fortunately enough, I had the help from Patricia Lopez in IMDEA-nano, and later from Antonia, Maria in IMM, as well as from Alfonso, whose kind service and help saved me a lot of time in the paperwork preparation.

Sparetime life is another story. I met a lot of friends here. We talked, exchanged, laughed, played and travelled together. With them, the life became even more colorful. Lucas, Cesar, Terunori, Carolina, Alan, Jeselo, Jero, Andres, Blanca, Gopika, and all the others… my friends in IMM, with all of you, work is not a tedious process any more!! Guilin, Junqing, Longfei, Yansheng, Chen, my friends in IMDEA-nano, life with you guys is really more interesting. And my dear classmates when we studied Spanish in Shanghai, Jing, Youyou, Bo, Hongying, Siming, Guangchao, Yongjun, we relied on each other from the first day in Spain, and that friendship lasted for the last years and, will last forever. Well, still we have the basketball gangsters, Ping, Mu, Fei, Guixiang, Qinglong, Xiyan, Jie, Jian, Tiancun. You know how important you are to me!
Names are not only names. They were help and reliant. They are life. And all the time with you will be the most precious memory.

At last, I should thank my family and my dear girlfriend, Jiaojiao. Help from you was not only words, but the support from the heart. The greatest happiness is to be with all of you in the future life, whatever we have, love or quarrel.

Contents

Resumen

Gracias al reciente desarrollo de la nanotecnología, se ha hecho factible la fabricación de diferentes materiales y estructuras en la nanoescala, lo que ha permitido en las últimas décadas una intensa investigación de la interacción luz-materia en sistemas de reducida dimensionalidad. En este sentido la plasmónica, que estudia las resonancias electrónicas excitadas mediante campos electromagnéticos, atrae cada vez más atención debido a su capacidad de confinar eficientemente dichos campos en escalas nanométricas, lo que permite manipular la luz en la nanoescala y facilitar la miniaturización de numerosos dispositivos de interés.

Para realizar una manipulación completa de la luz, son necesarios elementos activos tales como moduladores y aisladores ópticos. Para ello, el efecto magneto-óptico (MO) es una de las mejores alternativas, con un campo magnético externo como elemento de excitación. Esto permite obtener velocidades de operación ultrarrápidas y modulaciones relativamente grandes. Además, el efecto MO es en sí mismo no recíproco, por lo que se ha aplicado ampliamente en aisladores ópticos.

Por lo tanto, al combinar plasmónica y magneto-óptica en una nanoestructura, los llamados sistemas magnetoplasmónicos dispondrán de las ventajas de ambos: miniaturización de los dispositivos y manipulación activa de la luz.

En esta tesis, siguiendo esta idea, se fabrica y estudia una nanoestructura típica con resonancias plasmónicas bimodales –el nanoanillo- con la funcionalidad MO adicional introducida en el seno del mismo. Tanto el protocolo de nanofabricación como las propiedades ópticas / MO de diferentes tipos de nanoanillos se estudian en detalle.

El protocolo de fabricación se implementa basándose en la técnica de litografía coloidal con máscara-agujero (HCL), que permite fabricar nanoestructuras con múltiples componentes y distribuidas aleatoriamente en un área grande (más de cm^2) en un solo proceso. Con este método, la ubicación espacial específica de cada elemento consituyente del nanoanillo (Au como componente plasmónico y Co como componente magnético en nuestro caso) se puede controlar en las tres dimensiones (3D) con precisión en la nanoescala. En este trabajo de tesis se optimizan dos parámetros importantes del proceso HCL, a saber, la densidad de las esferas de PS utilizadas para definir los nanoagujeros en la máscara y el grosor de la máscara en sí.

Controlando la morfología general de la nanoestructura y las localizaciones espaciales de los diferentes componentes dentro del nanoanillo, somos capaces de controlar finamente las características resonantes plasmónicas de las nanoestructuras y como consecuencia la respuesta MO, tanto en términos de posición espectral como de intensidad.

A partir de estructuras de nanodiscos de multicapas Au/Co/Au depositadas a incidencia normal, el ángulo de deposición se incrementa gradualmente hasta un cierto valor, con lo que el nanodisco evoluciona morfológicamente hacia la estructura nanoanillo. Como consecuencia, la resonancia plasmónica unimodal característica del nanodisco evoluciona a la bimodal del nanoanillo. El efecto de la resonancia de plasmón en la actividad MO de estas estructuras presenta una evolución similar a medida que evoluciona la estructura - de unimodal para nanodisco a bimodal para nanoanillo. Este comportamiento se explica con el modelo de hibridación plasmónica comparando con resultados teóricos.

Además, al aumentar el ángulo de deposición de la capa superior de Au, la sección transversal de la estructura de nanoanillo se puede sintonizar de manera detallada, con lo que las posiciones espectrales de las resonancias plasmónicas y los picos de actividad MO pueden ser controlados finamente. Por otra parte, la capa continua central de Co en el nanoanillo se puede substituir por sectores opuestos de Co o por discos opuestos de Co, lo que resulta en anisotropía óptica, con una actividad MO básicamente proporcional a la cantidad de Co.

Por último, con el propósito de mejorar aún más el efecto MO en tales estructuras, se genera una brecha en el anillo superior de Au, justo encima del disco de Co, lo que permite un mejor “enfoque” del campo electromagnético en el elemento MO activo

(disco de Co), con un aumento adicional de la actividad MO de un factor 3. La localización del campo EM en el área de separación de dicha estructura propuesta se confirma adicionalmente tanto teóricamente mediante cálculos de distribución de campos, como experimentalmente con cartografía de señales EEL (pérdida de energía de electrones).

Abstract

Light-matter interaction is an old but still active and fascinating field, with new phenomena and theories emerging consistently. Thanks to the development of the nanotechnology in the last decades, fabrication of different materials and structures in the nanoscale becomes feasible, therefore the light-matter interaction in nanoscale obtains a vast and intensive research. Among this field, plasmonics, which studies the resonantly oscillating electrons (plasmons) driven by the light field in the metallic nanostructures, draws more and more attention due to its ability to confine the light field efficiently in nanometric scale. This ability, which makes it possible to manipulate light in nanoscale and actually can miniaturize greatly the device volume, has already found potential application in the integrated optical circuits for optical computation. Furthermore, the confined light field in such a small space results in the greatly enhanced localized electromagnetic (EM) field which can be utilized to enhance the other light-matter interaction, e.g. the famous application in surface enhanced Raman scattering (SERS). On the other hand, this enhanced localized field is sensitive to the environmental refractive indices, which makes it useful for the concept of "lab-on-chip" for biological and chemical sensing.

For a full light circuit, light manipulators such as light modulator and optical isolator, are necessary, which allow modulating light wavevector and permit the light to pass through only along one direction but the opposite direction is forbidden (non-reciprocal effect), respectively. For this purpose, magneto-optical (MO) effect is a good option to manipulate the light actively (rotate the light polarization or control light reflection intensity) by the active magnetic field since it can realize an ultrafast operation speed (femtosecond level) and relatively large modulation depth. Moreover, the MO effect itself is non-reciprocal. Therefore, by combining the plasmonics and

magneto-optics in one nanostructure, the so-called magnetoplasmonics will give us both of their advantages: miniaturization of the devices and active light (or plasmon) manipulation. As a light-matter interaction process, the MO effect can also benefit from the localized field at the plasmonic resonance, which gives rise to the plasmon-enhanced MO effect. On the other hand, instead of measuring the light intensity and peak shift in the plasmonics-based sensing platform, MO signal contains the phase information of the light (e.g. Kerr ellipticity), which actually has been proved to give a much better signal-to-noise ratio as the sensing platform.

In this thesis, following these trends, a typical plasmonic nanostructure-nanoring- is studied with the further introduced MO functionality. Both the fabrication protocol and the optical/MO properties are studied.
The protocol is implemented based on the hole-mask colloidal lithography (HCL, Fig. 1) technique that allows fabricating multicomponent nanostructures randomly distributed on a large area (over cm^2).

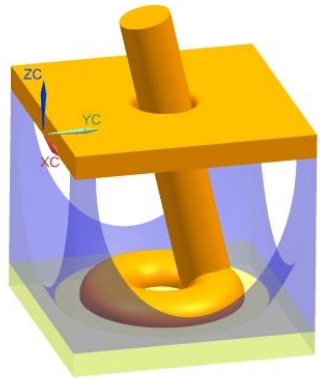

Fig. 1 Sketch for hole-mask colloidal lithography (HCL) method. The material (Au in the figure) deposits through the hole in the HCL template. With tilted angle deposition and rotation in the substrate, a nanoring structure can be formed.

With the HCL method, the specific position of plasmonic and magnetic components (Au and Co in this case, respectively) can be controlled in three dimensions with the precision in nanoscale. Two important parameters in the HCL template, the density of

the PS spheres used to define the holes in the template and the thickness of the Au mask, are optimized to adapt to the nanoring structure fabrication.

By controlling the overall morphology and the spatial location of the different components (Fig. 2), we are able to finely control the plasmonic resonant characteristics of the nanostructures and as a consequence the MO response, both in terms of spectral position and intensity. Starting from the Au/Co/Au trilayer nanodisk structures which are normally deposited, the unimodal plasmonic resonance evolves to the bimodal resonance of the nanoring as the deposition angle increases to a certain value. The enhanced MO effect of these structures exhibits similar evolution as the structures evolve. This behavior is explained with the plasmonic hybridization model.

Furthermore, by increasing the deposition angle during the deposition process, the cross-section of the nanoring structure can be tuned continuously, therefore the spectral positions of the plasmonic resonance and the enhanced MO peaks can be controlled in a fine way. The Co continuous layer in the nanoring can be further varied into opposite 2 Co sectors and 2 Co dots, which results in optical anisotropy, and the MO effect is found to be almost proportional to the Co amount.

At last, with the purpose to further improve the MO effect in such structures, a gap is generated in the top Au ring above the Co dot, which can further focus the EM field in the MO-active Co dot region and result in a further enhancement of the MO effect by a factor of 3 compared with the structures without such a gap.

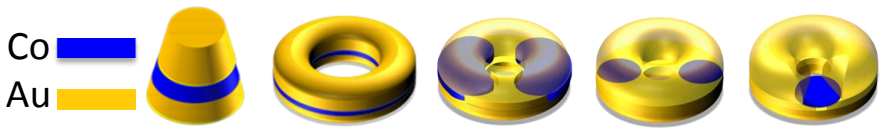

Fig. 2 Structures studied in this thesis. From left to right: Au/Co/Au nanodisk, Au/Co/Au nanoring, Co sectors nanoring, Co dots nanoring, and ring/split ring with a gap on top of Co dot.

Chapter 1

State of the Art and Motivation

1.1 Introduction

Optics is the topic studying light generation, control and detection [1]. Plenty of applications in different areas and daily life have been realized in this fascinating topic utilizing different properties of the light: communication, computing, medicine, sensing, and so on.

As an example, optical signal can be used instead of the electronic signal in a microprocessor used in computing, which is the heart of the current information technology and semiconductor industry, for the digital information exchange between transistors and integrated circuits [2,3]. This is proposed to solve the actual problem existing in the current technology: according to Moore's law, the number of the semiconductor transistors in the dense integrated circuit is doubled approximately every two years and now the characteristic dimensions are on the order of tens of nanometers or even smaller, therefore the metallic nanowire interconnects currently used are not sufficient to provide the necessary capacity required by this exponentially growing transistor number, due to the limited bandwidth of the electronic signal. The optical interconnects such as fiber optic cables, on the other hand, can provide a bandwidth much higher (>1000 times) than the electronic signal. However, due to the diffraction limit, the traditional optical or photonic components mainly based on the dielectrics, such as the optical fiber, lens, etc., are too bulky to be integrated with the electronic integrated circuits. Even the photonic crystal, which is a partial solution for this miniaturization and integration problem, is still too large in dimension compared with the electronic circuit component because its typical period is on the order of half of a wavelength (around hundreds of nanometers).

Plasmonics

In this sense, surface plasmon-based photonics, or "plasmonics", may offer a better solution to this problem [2-4]. Surface plasmons (SPs) are light waves propagating along, typically, a metal/dielectric interface, and coupled with the collective oscillation of electrons [5]. These waves are confined to the surface with exponentially decaying fields in both metal and dielectrics—on the metallic side, the decaying field relies on the skin depth which is on the order of 10nm. In this way, both of the advantageous large bandwidth of the optical signal and the compatibility with the current semiconductor technology can be kept, e.g. Cu, Al metals, etc. [6]. Therefore, the miniaturization and integration problems are both solved. Furthermore, the ultrafast dynamics of the surface plasmons, being relaxation times around 10 femtoseconds and coherent evolution times even shorter, makes them even more suited for the fast processing of the digital information [7].

The potential applications of surface plasmons have become realizable in the last two or three decades, mainly thanks to the advances in nanofabrication techniques, which make it possible the production and integration of nanoscale surface plasmonic devices. Besides this, plasmonic devices have also found applications in many other fields. For example, the spectral response of the plasmonic structures is very sensitive to the variation in the refractive index of the surrounding medium, allowing the detection of, for example, molecules in the vicinity of the plasmonic surface. This has been used extensively in biological and chemical sensing applications and has shown a high sensitivity [7, 8]. On the other hand, at plasmonic resonance, the electromagnetic (EM) field can be localized and enhanced greatly in the near field of the nanostructure, which can be applied to enhance the light-matter interaction process sensitive to the EM field intensity, such as the surface enhanced Raman scattering (SERS) [9], surface enhanced infrared absorption (SEIRA) [10], second and higher harmonics generation [11], and so on.

Active Plasmonics: Magnetoplasmonics

To realize purely plasmonic circuits, the surface plasmons carrying the digital signal should be manipulated and processed actively. Active plasmonic devices such as switches and modulators, are necessary in this sense. It is known that light can be manipulated with different mechanisms, for example, the thermo-, electro-, and

magneto-optical effects, etc. Correspondingly, all these effects can in principle be applied to manipulate surface plasmons and generate active plasmonic devices [3]. Among them, plasmonics mediated by a magnetic field [12] and termed as "magnetoplasmonics" [13], is a competitive candidate due to the intrinsically ultrafast property of the magnetic reversal [14] and the relatively large modulation depth [15].

Magneto-optical (MO) effect was first discovered by M. Faraday in 1845, as a rotation in the light polarization after light transmitted through a heavy glass (silicate borate of lead) in magnetic field (Faraday effect) [16] and later by J. Kerr for the reflected light from a pole of an electromagnet of iron (Kerr effect) [17]. In the last years, the MO effect has been applied to modulate the surface plasmons, and indeed, hybrid structures based on noble metal-ferromagnetic metal (e.g. Au/Co) have been explored for this purpose with a significant phase modulation by a magnetic field as small as a few millitesla, which is very promising for device applications such as magnetoplasmonic modulator and switch [15,18].

On the other hand, in magnetoplasmonic systems, the detection of the optical signal can be substituted with the MO signal, which has been applied as a different mechanism for sensing. Such MO surface plasmon resonance (MOSPR) sensors [19-23] improve significantly both of the detection limit [19,23] and figure of merit [22,23], even by orders of magnitude compared to that of the pure surface plasmon resonance (SPR) sensors. With proper functionalization of the surface of the MOSPR sensor, enhanced sensitivity for gas sensing can also be realized [24].

Furthermore, MO effect could also benefit from the plasmon excitation, giving rise to the enhanced MO activity mainly due to the EM field increase in the MO active material and/or the reduction in the reflectivity at plasmon resonance [13,18,25-28]. The enhanced MO activity can find its application in such as optical isolators [29,30]. Indeed, very recently, a large tuning range of the Faraday polarization rotation of up to 8.4° has been realized in a hybrid magnetoplasmonic system consisting of a MO EuSe slab of 220nm thickness and a one-dimensional plasmonic gold grating, with the further ability to be spectrally tailored to arbitrary wavelength within the transparency window of the MO slab [31].

Multimodal Magnetoplasmonic Nanostructures

Another aspect of relevance is that more complex nanostructures with multiple resonance modes and easy to be tuned in a large wavelength range are also necessary

for either passive or active devices. However, as an emerging field, magnetoplasmonic nanostructures made of purely metallic and supporting multiple resonance modes have been studied rarely. In this sense, nanoring structures, which support bimodal plasmonic resonance [32] and can be easily tuned in the visible and infrared wavelength range by modifying the dimensions, is a good model system to study the intertwined multimodal plasmonic resonance and MO properties. Additionally, by overlapping a split ring on top of a nanoring, a further enhancement in the EM field will appear in the gap area [33], generating a *hot spot*, which has the possibility to further boost the MO effect.

Due to the large and uniform EM field in the central hole part at plasmonic resonance, and the hole itself as a container with a significant volume for the analyte, the nanoring has already shown the competitive sensing ability as a plasmonic sensor [34]. Sensors based on magnetoplasmonic nanoring structures will certainly benefit from this study, with a possible interest in the increased figure of merit.

Nanofabrication

For this purpose, how to fabricate the nanostructures is another relevant issue. Although the current nanofabrication technology gives us a handful of options, techniques easy-to-use, low-cost and large-area-coverage are rare. In this sense, the hole-mask colloidal lithography (HCL) method [35] is chosen in this thesis for the nanostructure fabrication, which is based on the self-assembling pattern definition, and has been used to define various isolated nanostructures in an area up to several cm^2 or even larger. Therefore, the other purpose of this thesis is to adapt and optimize the HCL method in the Au/Co/Au multilayer nanoring fabrication by controlling its template parameters.

Before going to the discussion of the concrete experiments and results, in this chapter we will first introduce the fundamental knowledge and state of the art of the field of magnetoplasmonics, which are necessary to understand the following parts of this thesis. The emphasis will be put on the nanoparticle systems supporting localized surface plasmons, which is more related to this work. The existing nanofabrication techniques will be also introduced briefly. At last, the contents of the thesis will be listed.

1.2 Localized Surface Plasmons (LSP)

Generally, SPs can be classified into two main categories: localized surface plasmons (LSP) which are the localized modes supported by metallic nanoparticles of dimensions of the order or smaller than the wavelength of the incoming light; and surface plasmon polaritons (SPP), which can propagate along the planar metal surface.

Back to the ancient Roman times, metallic nanoparticles were already used for the staining of glass for decoration [5,7]. However, the clear mathematical foundation for this phenomenon was established and related with the LSP much later, around the beginning of 20^{th} century by Garnett [36] and Mie [37]. On the other hand, the SPP was investigated from around 1900 [38,39], and only in the 1950s, a complete understanding of the phenomenon was established [40].

In this section, the fundamental theory of LSPs and typical nanoparticles supporting LSPs will be introduced. The phenomenon such as the enhanced near field at plasmon resonance and the mechanism for applications such as sensing will be discussed.

1.2.1 Fundamentals of LSP (I): Single Nanoparticle

Localized surface plasmons (LSP) can be described as collectively and coherently oscillation of the conduction electrons in a small metallic nanoparticle driven by the oscillating electric field of the exciting light [41,42], as shown in Fig. 1.2.1(a). In such an oscillation, the restoring force due to the Coulomb attraction between the displaced electrons and the nuclei, as well as the collisions with the boundary of the electrons (especially for the particles smaller than the mean free path of the electron), confine the electron cloud in the nuclear framework and affect the coherent oscillation frequency. This coherent oscillation of the electrons with the light field in a nanoparticle is the so-called particle dipole plasmon resonance, namely, the LSP resonance.

At LSP resonance excitation, the near EM field will be strongly enhanced, being one of the most important characters of LSP resonance. A representative field enhancement picture of a nanosphere at LSP resonance excitation is shown in Fig.

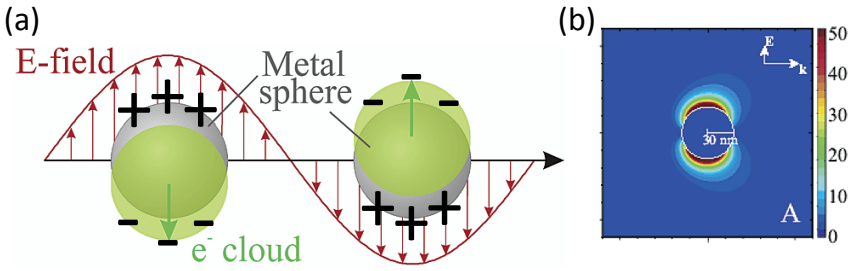

Fig. 1.2.1 (a) Schematic of plasmon oscillation for a sphere, showing the displacement of the conduction electron cloud with the driving light field. Green arrows show the displacement direction of the electron clouds and induced charge distributions are also schematically shown. (b) Calculated near field distribution for an Ag nanosphere with 30nm radius at plasmon resonance. (a)(b) are adapted from Ref. [41].

1.2.1(b).

The plasmonic resonance wavelength is determined by different factors, such as the density and effective mass of the electrons (material properties), shape and size of the nanoparticles. Here as a general example, we show the analytical expressions of LSP in small ellipsoid with its polarizability considering the dielectric tensor and shape effect [41,42], from which general conclusions and phenomena could be drawn.

The dielectric tensor contains all the optical information of the material. If the constituent material of a nanoparticle is nonmagnetic and optically isotropic metal, it has a diagonal dielectric tensor $\widetilde{\varepsilon_m}$, which can be expressed as

$$\widetilde{\varepsilon_m} = \begin{pmatrix} \varepsilon_m & 0 & 0 \\ 0 & \varepsilon_m & 0 \\ 0 & 0 & \varepsilon_m \end{pmatrix}, \qquad 1.2.1$$

It is worth to notice that all the non-zero elements in $\widetilde{\varepsilon_m}$ are complex numbers for a metal as an absorbing material. Meanwhile, the surrounding host dielectric medium is considered as nonmagnetic and isotropic with the dielectric tensor $\tilde{\varepsilon}_d = \varepsilon_d \tilde{I}$, where $\tilde{I}$ is the identity matrix.

When light with wavelength λ illuminates onto the nanoparticle, the applied light

field will induce a dipole with the dipole moment $\vec{p}$ proportional to the field, expressed as

$$\vec{p} = \varepsilon_d \alpha \overrightarrow{E_0}, \qquad 1.2.2$$

with α the polarizability of the nanoparticle, and $\overrightarrow{E_0}$ the electric field of the incident light.

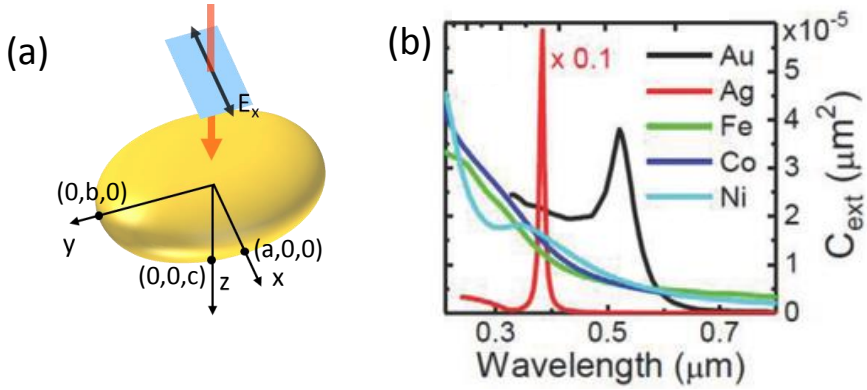

Fig. 1.2.2 (a) Ellipsoidal nanoparticle under consideration with semi-axis lengths of a, b, and c. As an example, light polarized along x direction is incident along z direction (red arrow). (b) Calculated extinction cross-sections of the 10nm-diameter spheres made from different materials and embedded in water. (b) is adapted from Ref. [13].

As a general case, the nanoellipsoid can be considered with the semi-axis lengths a, b, and c, respectively (Fig. 1.2.2(a)). Within the electrostatic approximation for an optically small ellipsoid, namely, the characteristic dimension lengths of the nanoparticle $(a, b, c) \ll \lambda$ and thus the light field can be considered as an uniform static electric field in the volume of the nanoparticle, the polarizability tensor $\tilde{\alpha}$ of the nanoellipsoid is diagonal and the diagonal tensor elements can be obtained by solving the Maxwell's equations analytically, expressed as [42]

$$\alpha_{ii} = 4\pi abc \frac{\varepsilon_m - \varepsilon_d}{3\varepsilon_d + 3L_i(\varepsilon_m - \varepsilon_d)}, \qquad 1.2.3$$

where $i = x, y, z$ and L_i the geometrical factors related to the shape and dimensions of the nanoparticle, ranging from 0 to 1.
The condition for the LSP resonance excitation is that the real part of the denominator in Eq. 1.2.3 vanishes, which is

$$\mathrm{Re}\big(3\varepsilon_d + 3L_i(\varepsilon_m - \varepsilon_d)\big) = 0, \quad 1.2.4$$

With the polarizability tensor $\tilde{\alpha}$, the absorption and scattering cross-sections of the nanoparticles can be calculated as

$$\sigma_{abs} = k\mathrm{Im}(\alpha_{ii}), \quad 1.2.5$$

$$\sigma_{sca} = \frac{k^4}{6\pi}|\alpha|^2, \quad 1.2.6$$

and the extinction cross-section as

$$\sigma_{ext} = \sigma_{abs} + \sigma_{sca}, \quad 1.2.7$$

where $k = 2\pi{\varepsilon_d}^{1/2}/\lambda$ is the wave vector of the incident light.

From the equations above, now it can be concluded that the spectral position of the plasmonic resonance is controlled by both the nanoparticle itself and the embedding dielectric medium (Eq. 1.2.4):

(1) For the nanoparticles, all the parameters such as the constituent material (ε), shape and dimensions (L_i), play their roles in the determination of the optical responses. (a) For a general ellipsoid with $a \neq b \neq c$ and thus three different L_i, three dipole plasmon resonances could be excited in different spectral positions. For spheroidal (two of the three semi axes are the same and thus two L_i) and spherical (all the semi axes are the same and only one L_i) nanoparticles, the numbers of the dipole plasmon resonances are two and one, respectively. (b) Due to the diversity of L_i ranging from 0 to 1, the wavelength positions of possible plasmon resonances can span in a very wide range for the small and ellipsoidal metallic nanoparticles.

(2) For a given shape and dimension, the resonance wavelength is a monotonically increasing function of ε_d, namely, the refractive index *n* of the surrounding medium.

In such a sense, the plasmonic resonance can be affected by the presence of a supporting substrate, a solvent layer on top of the particles, etc., which is the physical mechanism exploited in most of the sensing applications.

(3) At the plasmon excitation, we can also justify from Eqs. 1.2.5, 1.2.6 and 1.2.7 that the absorption, scattering as well as the extinction cross-sections obtain their maxima, corresponding to peaks in the optical spectra, which are characteristics of the plasmon excitation.

As examples, in Fig. 1.2.2(b) are shown the calculated extinction cross-sections of 10nm-diameter spheres made from different materials and embedded in water [13], where we can observe the different spectral positions and damping properties of the plasmons supported by the nanoparticles. For noble metals like Au and Ag with lower optical losses, the plasmonic resonances are well defined with sharp and intense peaks in the extinction cross section, while for the ferromagnetic metals with higher losses, the peaks are broader and lower in intensities.

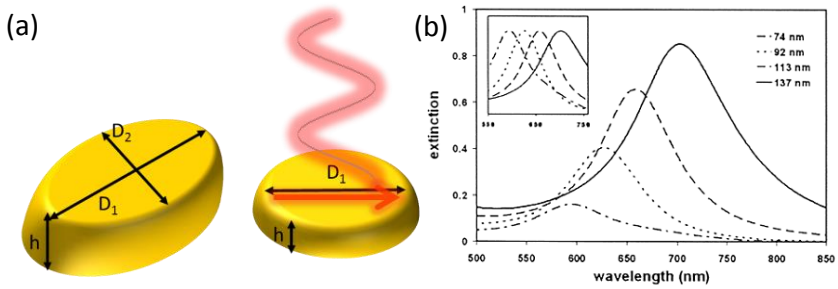

Fig. 1.2.3 (a) Sketches of the elliptical and round nanodisks with height *h*, long and short diameters D_1 and D_2. For the round nanodisk, D_1=D_2. Light is incident normally to the disk plane (right panel), and the nanodisk is polarized along the light polarization (red arrow). (b) Experimentally measured extinction spectra for the Au nanodisks with constant height 20nm and different diameters (74nm, 92nm, 113nm, and 137nm) for light incidence normal to the disk plane. Inset in (b) show the normalized extinction spectra. (b) is reproduced from Ref. [43].

Experimentally, the most studied structures supporting isolated LSPs are nanospheres, nanorods, nanodisks, etc. All of them can be approximately modeled with

nanoellipsoids with different dimensions and aspect ratios (which will affect L_i). In Fig. 1.2.3(a) the sketches of an elliptical nanodisk and a round one are shown, with the height h, long and short diameters D_1 and D_2, respectively. The approximate correspondence between the dimensions of such nanodisk and a nanoellipsoid is: $D_1 = 2a$, $D_2 = 2b$ and $h = 2c$. When light is incident normally to the nanodisk plane, a maximum extinction happens at the LSP resonance excitation, as shown in Fig. 1.2.3(b) for the experimentally measured extinction spectra for the Au nanodisks (D_1=D_2) with constant height 20nm and different diameters[43]. As it can be seen, the extinction peak shifts to red as the diameter and aspect ratio (aspect ratio=diameter/height) increases.

It should be noted here that for small nanoparticles within the electrostatic approximation, the spectral position of the LSP resonance can be predicted according to Eq. 1.2.4, but for large nanoparticles (e.g. Au disks in Fig. 1.2.3(b)) the width of the extinction peak calculated with this method is severely underestimated. Additional corrections should be made to obtain the correct polarizability tensor [41,43], which may result in the broader width and redshift of extinction peak. Furthermore, dispersions in size and shape, as well as edge roughness in experimental nanoparticles, that are not considered in the analytical model, can also contribute to the broader peak width. Retardation effect, on the other hand, due to the finite speed of the light, should be considered for large nanoparticles, which will result in higher order multipolar plasmon modes, e.g. the quadrupolar mode [41]. In such cases, the above results for single nanoparticles from the electrostatic approximation can still serve as guidance [44].

1.2.2 Fundamental of LSP (II): Plasmon Hybridization Model

The situation considered above is for isolated and morphologically simple nanoparticles. For nanoparticles with complex shapes, or nanoparticle oligomers, LSPs supported by different interfaces will couple with each other through *near field* interaction, in the range of several tens of nanometers (Fig. 1.2.1(b)). This can be considered with the plasmon hybridization model [45], which is an electromagnetic

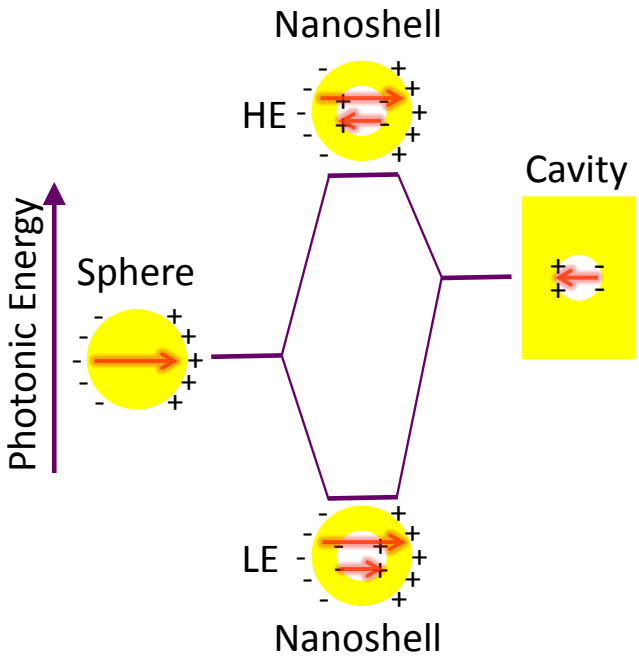

Fig. 1.2.4 An energy-level diagram of the plasmon hybridization in metal nanoshell structure from the sphere and cavity plasmons. Red arrows show the plasmonic dipoles. Adapted from Ref. [45].

analog of molecular orbital theory showing the complex electronic structures of the molecules result from the hybridization of electron wave-functions of simple atomic and molecular orbitals. This model treats a composite nanostructure as more elementary shapes and then calculates how the "free" primitive plasmon resonances of the elementary geometries *interact* with each other to split and shift the plasmon energies, namely, to generate hybridized plasmon modes. It has been applied to a series of nanostructures, such as nanoshell [45,46], nanoeggs [47], nanomatryushkas [45,48], nanorice [49], multiple nanoparticle assemblies [50,51], nanoparticle-film structure [52], nanorod dimers [53], nanoring [160] and disk-ring structures [162], etc. The simplest case is the hybridization of two primitive plasmons, resulting in two plasmon modes, a low-energy (LE) bonding mode and a high-energy (HE) anti-bonding mode. This is illustrated schematically in Fig. 1.2.4 with a nanoshell

structure, where plasmons (surface charges in the figure) supported by the inner surface (cavity) and outer surface (sphere) hybridize with each other due to the finite thickness of the shell layer.

Here we will show two more examples, vertical nanodisk dimers and nanorings. A vertical nanodisk dimer is composed of two stacked metallic (e.g. Au) nanodisks separated by a dielectric layer (e.g. SiO_2) (Fig. 1.2.5(a)), where upon normal light incidence, two LSP resonance dipoles can be excited in the top and bottom disks. When brought to proximity of each other, the two dipoles can interact and hybridize.

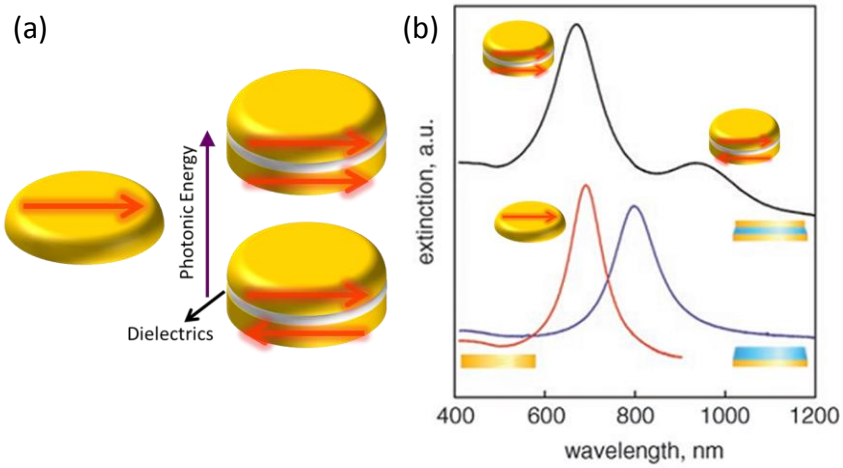

Fig. 1.2.5 (a) Plasmon hybridization in vertical disk dimers with the nanodisks separated by a dielectric layer. The LE antiparallel and HE parallel configurations result in the peak splitting. (b) Experimentally measured extinction spectra for the Au nanodisk dimer array (black curve). The disk has a diameter of 110nm. Thickness for all the three layers is 10nm. The red curve below corresponds to an Au nanodisk array of 20nm thickness with a similar diameter. The blue curve is for 10nm thick Au nanodisks capped with 20nm SiO_2. Adapted from Ref. [54].

As a result, two possible configurations can exist, as shown in Fig. 1.2.5(a), antiparallel and parallel, corresponding to the out-of-phase and in-phase oscillations of the two dipoles, respectively [54]. Therefore, two peaks appear in the extinction spectra, located in the LE and HE regions (Fig. 1.2.5(b)). In this case, the hybridization process is determined mainly by two factors: the degree of degeneracy

of the two primitive plasmons, namely, the "similarity" between them, and the interaction strength between them. Both factors were studied experimentally by varying either the disk aspect ratios or the SiO_2 spacer thickness [54].
Similar results were also obtained for planar nanodisk dimers [55], where besides the peak split and shift effects, the stronger near field coupling at light polarization parallel to the interparticle axis than along the transversal direction contributes to optical anisotropy. In such cases, the near field interaction and the corresponding spectra are strongly dependent on the spacing distance between the two nanodisks, exhibiting a distance-decaying character, therefore it can be applied as a plasmon ruler [55].

The plasmon hybridization model has been also applied to the analysis of the optical response of nanorings [140,160,162]. The nanoring structure can be considered as a concentric combination of a nanodisk (outer surface of nanoring) and a nanohole (inner surface) (Fig. 1.2.6(a)), which support the disk and hole LSP resonance dipoles at light incidence normal to the nanoring plane [160].

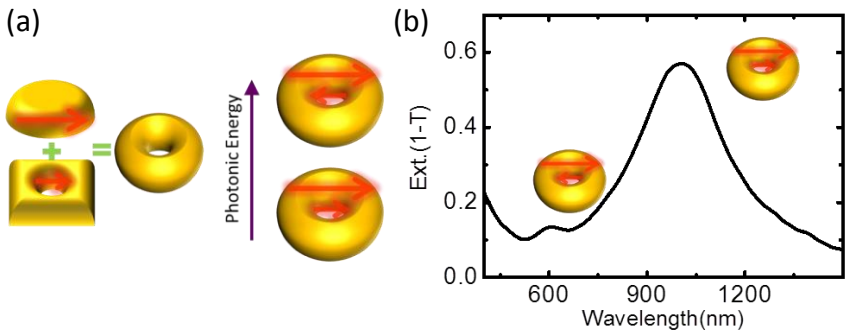

Fig. 1.2.6 (a) Plasmonic hybridization schemes of nanoring from interacting nanodisk and nanohole plasmons. The hybridization results in the two LE and HE modes. (b) Extinction spectrum of our Au nanoring measured with normal light incidence.

Similar to the nanodisk dimers, the hybridization of the disk and hole dipoles has two possible configurations: parallel LE mode and antiparallel HE mode (Fig. 1.2.6(a)). This results in the extinction peak splitting and shifting, as shown in Fig. 1.2.6(b), where a bimodal resonant behavior is observed, with a generally dominant peak in the

LE range and a weaker peak in HE range. The two constituent parallel dipoles in LE mode result in the larger dipole moment of this mode (sum of both) and thus a higher intensity in extinction, while the antiparallel dipoles of HE mode result in the small dipole moment (the difference between them) and a lower extinction intensity.
By affecting the primitive disk and hole LSPs, as well as their interaction strength in hybridization, the LE mode could be tuned in a wide wavelength range with control in outer and inner diameters of the nanoring, height [141,161], shape and area of the cross-section [148,152,158,160]. Although to a less extent, the HE mode can also be tuned similarly [148,160,161].
Additionally, high-order multipolar modes can also be excited in the large enough nanoring structures at the symmetry breaking situation, such as oblique light incidence onto the round nanoring[141,159], or elliptical nanoring with the in-plane shape anisotropy [142] (Appendix 4).

An interesting case similar to the nanoring structure is the split ring, for which the existence of the gap breaks the in-plane shape symmetry of the structure, resulting optical anisotropy and inducing the appearance of the high-order multipolar modes for even normal light incidence, which can be analyzed with the standing wave model (see Appendix 4). A great localization of electromagnetic (EM) field appears in the gap area for N=1 mode when the incident light is polarized parallel to the gap (Fig.1.2.7(a)) [56].
By overlapping a split ring directly on top of a nanoring, the general dipolar LE and HE modes of the nanoring (Fig. 1.2.6(b)) are still kept, while a similar additional EM field enhancement exists in the gap area of the newly created structure (Fig. 1.2.7(b)) [33], being a *hot spot* in this area.

From the discussion above, we can conclude that the plasmonic mode analysis is important for the consideration the nanoparticles supporting LSPs, which is mainly and intrinsically determined by the structure size, shape, constituent, system symmetry (light incidence angle, etc.) and so on. The near EM field distribution and the far field optical responses can then be analyzed with these modes.

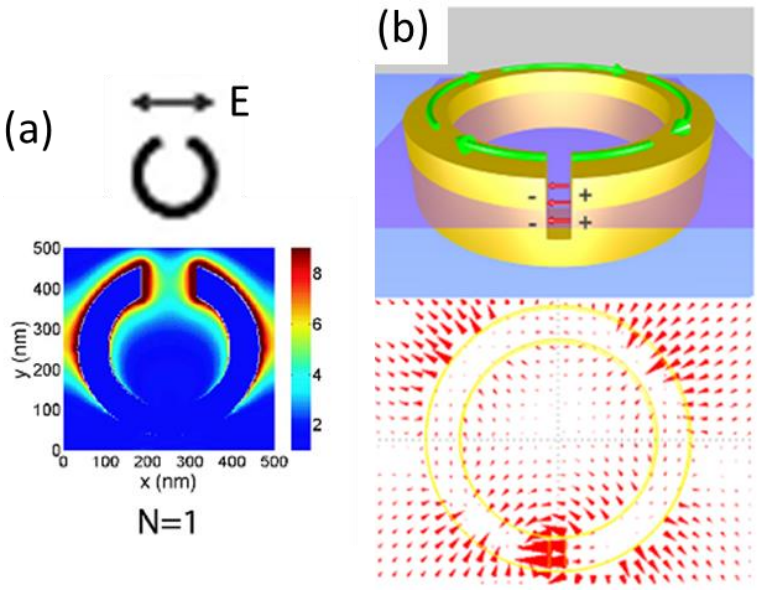

Fig. 1.2.7 (a) Electric field distribution of split ring structure at N=1 mode resonance, where the gap area has the largest field enhancement. Corresponding light polarization is shown above. (b) Top: sketch of the structure with a split ring directly on top of a nanoring. Charge accumulation on the wall of the gap is schematically shown for the LE resonance excited by azimuthally polarized light (green arrow). Bottom: electric field vector distribution in the purple plane in the top sketch. The electric field is enhanced in the gap region. (a) is adopted from Ref. [56] and (b) from [33].

1.3 Magneto-optical Effect

Here we introduce the fundamental concepts of the MO effect, mainly on the different configurations and their expressions with the dielectric tensors.

The effect of the magnetic field on the dielectric tensor $\tilde{\varepsilon}$ of a material is to introduce the off-diagonal elements (MO constants) therefore it becomes antisymmetric [12],

$$\tilde{\varepsilon} = \begin{pmatrix} \varepsilon & \varepsilon_{xy} & \varepsilon_{xz} \\ -\varepsilon_{xy} & \varepsilon & -\varepsilon_{yz} \\ -\varepsilon_{xz} & \varepsilon_{yz} & \varepsilon \end{pmatrix}, \qquad 1.3.1$$

with the off-diagonal elements proportional to the magnetic field for paramagnetic and diamagnetic materials, or to the magnetization for the ferromagnetic material. Consequently, either the polarization state, or the intensity of transmitted and reflected light, or even both, will be modified, depending on the configurations of the magnetization with respect to the light propagation. This is shown in Fig. 1.3.1, where the Faraday effect and polar, longitudinal, transverse MO Kerr effects (MOKE) are displayed sequentially.

1.3.1 Faraday Effect

More than 150 years ago, M. Faraday discovered that the polarization plane of a linear light is rotated when propagating through a flint glass in a magnetic field. The rotation angle $\theta_f(\omega)$ in such a case can be expressed as [57],

$$\theta_f(\omega) = V(\omega)Hl, \qquad 1.3.2$$

where H is the applied magnetic field, l the sample thickness and $V(\omega)$ the Verdet constant, which depends on both of the material and light frequency ω. This is the well-known Faraday Rotation or Faraday effect (Fig. 1.3.1(a)), observed in ferromagnets as well as non-magnets in a magnetic field. The rotation of light polarization plane depends on the relative direction of light propagation to the magnetization M of the material, therefore when the transmitted light is reflected back and propagates through the material again, the total rotation angle will be doubled to be $2\theta_f$, indicating that the Faraday effect is a non-reciprocal property. This actually applied to all the MO effects although they have different configurations.

Generally, the effect of the magnetic permeability tensor $\tilde{\mu}(\omega)$ of the material on the optical phenomena is small**,** which can be assumed that $\tilde{\mu}(\omega) = \mu_0\tilde{I}$ with $\tilde{I}$ the unit tensor and μ_0 the magnetic permeability of vacuum. Therefore light propagation in the material can be well described by the Maxwell equations with the dielectric tensor $\tilde{\varepsilon}$, as we see previously in the plasmonic effect. Considering the material with the cubic symmetry and the applied magnetic field H along the z-direction (Fig. 1.3.1(a)), the dielectric tensor takes the form of Eq. 1.3.3,

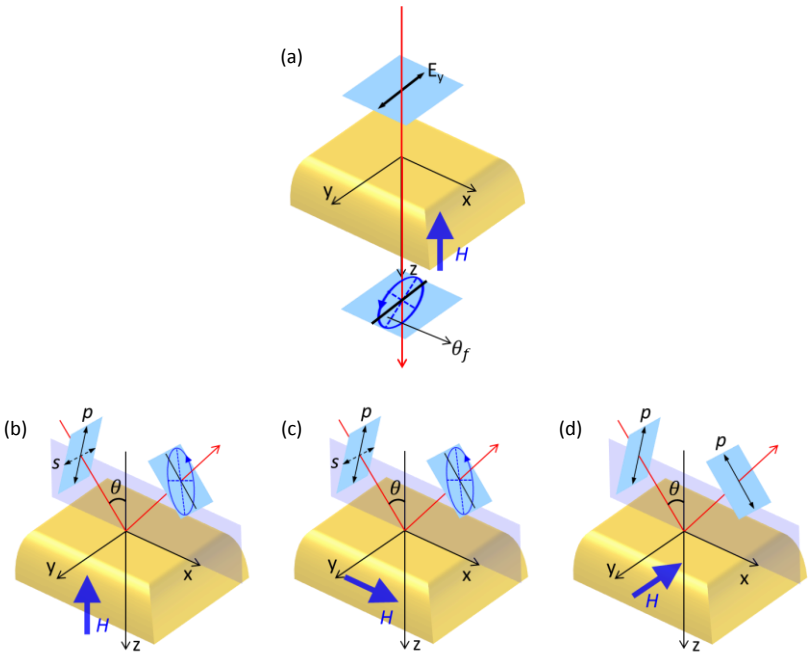

Fig. 1.3.1 Different configurations of the MO effects. (a) Faraday effect with light transmitted, magnetic field parallel to the light propagation. (b) Polar magneto-optical Kerr effect (p-MOKE) with light reflected, and magnetic field parallel to the light incidence plane and perpendicular to the sample plane. (c) Longitudinal MOKE (l-MOKE) with light reflected, magnetic field parallel to both of the light incidence plane and sample plane. (d) Transverse MOKE (t-MOKE) with light reflected, magnetic field perpendicular to the light incidence plane and parallel to the sample plane.

$$\tilde{\varepsilon} = \begin{pmatrix} \varepsilon & \varepsilon_{xy} & 0 \\ -\varepsilon_{xy} & \varepsilon & 0 \\ 0 & 0 & \varepsilon \end{pmatrix}, \qquad 1.3.3$$

with the element $\varepsilon_{ij} = \varepsilon'_{ij} + i\varepsilon''_{ij}$.

The linearly polarized light impinging to the material can be resolved into the two circularly polarized light waves (right$+$ and left$-$) with equal amplitudes and field vectors rotating toward opposite directions. By solving Maxwell equations, such

resolved waves experience different refractive indices [57],

$$N_{\pm}^2 = \varepsilon \pm i\varepsilon_{xy}, \quad 1.3.4$$

when propagating in the material. Therefore the two circularly polarized waves propagate with different velocities and attenuating rates.
After traveling through the material, the recombination of the two waves results in the elliptically polarized light (Fig. 1.3.1(a)). The phase difference in the transmitted right and left circularly polarized light caused by the difference of $Re(N_+)$ and $Re(N_-)$, gives the Faraday rotation angle per unit length $\theta_f(\omega)$,

$$\theta_f(\omega) = \frac{\omega}{2c} Re(N_+ - N_-), \quad 1.3.5a$$

with c the light speed in vacuum.
The amplitude difference caused by the difference between $Im(N_+)$ and $Im(N_-)$, gives the Faraday ellipticity per unit length $\varphi_f(\omega)$,

$$\varphi_f(\omega) = -\frac{\omega}{2c} Im(N_+ - N_-). \quad 1.3.5b$$

By further substitution of N_+ and N_- with the dielectric tensor elements (Eq. 1.3.4) and assuming the material as transparent ($\varepsilon'' = 0$, e.g. the ferromagnetic garnet), Eq. 1.3.5 can be rewritten as

$$\theta_f(\omega) = -\frac{\omega}{2c}\frac{\varepsilon_{xy}''}{n}, \quad 1.3.6a$$

$$\varphi_f(\omega) = -\frac{\omega}{2c}\frac{\varepsilon_{xy}'}{n}, \quad 1.3.6b$$

with $n = \frac{1}{2} Re(N_+ + N_-)$. Eq. 1.3.6 indicates that the Faraday rotation and ellipticity are proportional to the imaginary part and real part of the off-diagonal elements (MO elements) of the dielectric tensor, respectively [57].

1.3.2 Polar Kerr Effect

The MO effect in the light reflection configuration is called Kerr effect. According to the relative configuration of the light incidence plane and magnetization, MO Kerr effect (MOKE) can be classified into three types (Fig. 1.3.1 (b-d)): polar (p-MOKE), longitudinal (l-MOKE) and transverse (t-MOKE).

P-MOKE (Fig. 1.3.1(b)) corresponds to the case that the magnetization is normal to the sample plane, along z direction, and therefore parallel to the light incidence plane. The dielectric tensor takes the form of Eq. 1.3.3, the same as that in Faraday effect. When linearly p-polarized (s-polarized) light is incident onto the sample in such a situation, the reflected beam obtains a small s-polarized component (p-polarized). Therefore the reflected light becomes elliptically polarized with its major axis rotated from its initial incident polarization plane, as shown in Fig. 1.3.1(b). With the Fresnel reflection coefficients matrix $\begin{pmatrix} r_{xx} & r_{xy} \\ r_{yx} & r_{yy} \end{pmatrix}$, the complex Kerr rotation for the incident linearly x-polarized light, can be written as

$$\Phi_k = \theta_k + i\varphi_k = \frac{r_{yx}}{r_{xx}}, \tag{1.3.7}$$

Considering the system consisted of the semi-infinite non-magnetic medium with isotropic dielectric tensor $\tilde{\varepsilon}_d = \varepsilon_d \tilde{I}$, where $\tilde{I}$ is the identity matrix, and semi-infinite magnetic medium with the dielectric tensor in Eq. 1.3.3, the complex Kerr rotation in the p-MOKE can be expressed with the dielectric tensor as [12],

$$\Phi_k = \theta_k + i\varphi_k = -\frac{\varepsilon/\varepsilon_d\left(\sqrt{\varepsilon/\varepsilon_d - \sin^2\theta} + \sin\theta\tan\theta\right)}{\varepsilon(\varepsilon/\varepsilon_d - 1)(\varepsilon/\varepsilon_d - \tan^2\theta)}\varepsilon_{xy}, \tag{1.3.8}$$

with θ the incidence angle of the light (Fig. 1.3.1(b)). For Eq. 1.3.8 it is assumed that the MO constants in the material are much smaller than the optical constants, $|\varepsilon_{xy}| \ll |\varepsilon|$, and $n \gg k$, with $\varepsilon = (n + ik)^2$.
For the special case of light incidence normal to the sample ($\theta = 0$) from the vacuum

$\varepsilon_d = 1$, the expression Eq. 1.3.8 can be reduced to

$$\Phi_k = \theta_k + i\varphi_k = -\frac{\varepsilon_{xy}}{\sqrt{\varepsilon}(\varepsilon-1)}, \quad 1.3.9$$

which actually can also be derived with the similar method for the Eq. 1.3.6 by considering the reflection configuration and Fresnel relations [57].

Additionally, polar Kerr effect can also be considered with the modulus of the complex Kerr rotation, denoted as MO activity (MOA),

$$MOA = \sqrt{{\theta_k}^2 + {\varphi_k}^2}, \quad 1.3.10$$

1.3.3 Longitudinal Kerr Effect

This configuration corresponds to the magnetization parallel to both the sample and the light incidence plane (Fig. 1.3.1(c)). The corresponding dielectric tensor therefore takes the form

$$\tilde{\varepsilon} = \begin{pmatrix} \varepsilon & 0 & 0 \\ 0 & \varepsilon & -\varepsilon_{yz} \\ 0 & \varepsilon_{yz} & \varepsilon \end{pmatrix}, \quad 1.3.11$$

The effect of the magnetic field in this configuration is similar to the p-MOKE, that is, the reflected p(s)-polarized light obtains the small s(p)-polarized component thus becomes elliptically polarized. Given the same assumption that $|\varepsilon_{yz}| \ll |\varepsilon|$, and $n \gg k$, for a semi-infinite ferromagnetic material the Kerr rotation and ellipticity of the reflected light in the l-MOKE is given by [12]

$$\Phi_k = \theta_k + i\varphi_k = -\frac{\varepsilon/\varepsilon_d \sin^2\theta\left(\sin\theta\tan\theta - \sqrt{\varepsilon/\varepsilon_d - \sin^2\theta}\right)}{(\varepsilon/\varepsilon_d - 1)(\varepsilon/\varepsilon_d - \tan^2\theta)\sqrt{\varepsilon/\varepsilon_d - \sin^2\theta}}\,\varepsilon_{zy}. \quad 1.3.12$$

1.3.4 Transverse Kerr Effect

In this configuration, the magnetic field is applied parallel to the sample plane and perpendicular to the light incidence plane (Fig. 1.3.1(d)). The dielectric tensor now is

$$\tilde{\varepsilon} = \begin{pmatrix} \varepsilon & 0 & \varepsilon_{xz} \\ 0 & \varepsilon & 0 \\ -\varepsilon_{xz} & 0 & \varepsilon \end{pmatrix}, \quad 1.3.13$$

Different from the p-MOKE and l-MOKE, where the polarization state of the light is changed after reflection due to the conversion between the p- and s-polarized light, t-MOKE reveals in the change only in the intensity of reflected p-polarized light. For s-polarized light, its electric field is parallel to the magnetization, and thus suffers no MO effect.

The t-MOKE effect, namely, the intensity change in the reflected p-polarized light is described by [12]

$$t - MOKE = \frac{R_{pp}(+H) - R_{pp}(-H)}{R_{pp}(+H) + R_{pp}(-H)} \approx \frac{R_{pp}(+H) - R_{pp}(0)}{R_{pp}(0)}, \quad 1.3.14$$

which is the relative change in the reflectivity of p-polarized light upon reversal of the magnetic field direction, and $R_{pp} = |r_{pp}|^2$ with r_{pp} the Fresnel reflection coefficient for p-polarized light. $+H, -H$ and 0 in Eq. 1.3.13 are the applied magnetic field along positive, negative directions of y axis, and null magnetic field for the paramagnetic material. For ferromagnetic material, H should be substituted with the magnetization M of the sample. Within this definition of the t-MOKE, its quantity is limited between 1 and -1.

For a semi-infinite sample with a flat interface, and with the same assumption that $|\varepsilon_{xz}| \ll |\varepsilon|$, and $n \gg k$, the t-MOKE can be expressed analytically as [58]

$$t - MOKE = 2\varepsilon_d \sin(2\theta)\, Re\left(\frac{\varepsilon_{xz}}{(\varepsilon^2 - {\varepsilon_d}^2)\cos^2\theta - \varepsilon_d\varepsilon + {\varepsilon_d}^2}\right). \quad 1.3.15$$

From Eq. 1.3.12 and 1.3.15, we can see that *at normal incidence* of light, namely, $\theta = 0°$, *no MO effect* is observed for *longitudinal* and *transverse* configurations.

1.4 Intertwined Plasmonic and MO Effects: Magnetoplasmonics

As discussed in the last two sections, the LSP resonance of the nanoparticle results in enhancements in the scattering and extinction cross sections, EM near field, and so on. The MO effect, on the other hand, can modify the light polarization state or intensity after interaction with the material in the magnetic field. The combination of both effects, termed as *magnetoplasmonics*, in the LSP nanoparticle system, will result in the intertwined phenomena, e.g. for polar-Kerr configuration, enhanced MO effect (rotation and ellipticity of the reflected light) by plasmon resonance due to the near field enhancement in the MO active material, and rotated plasmonic dipole by the magnetic field, which will be introduced in this section.

1.4.1 Fundamental of LSP-Magnetoplasmonics: Single Nanoparticle

As shown in Eq. 1.3.1, the off-diagonal elements in the dielectric tensor should be considered for nanoparticles in a magnetic field, therefore when light is incident onto the small nanoparticles, the polarizability tensor Eq. 1.2.3 should take the new form [59,60,61],

$$\tilde{\alpha} = 4\pi abc \frac{\widetilde{\varepsilon_m} - \varepsilon_d \tilde{I}}{3\varepsilon_d \tilde{I} + 3\tilde{L}(\widetilde{\varepsilon_m} - \varepsilon_d \tilde{I})} \qquad 1.4.1$$

within the electrostatic approximation, where $\tilde{L}$ is the diagonal tensor containing the geometric factors L_i for $i = \mathrm{x}, \mathrm{y}, \mathrm{z}$, considering the shape effect of the nanoparticle.

For simplicity, in Fig. 1.4.1 we consider polar Kerr configuration with an elliptical nanodisk in the magnetic field normal to the nanodisk plane and light is incident normally. (It should be noted the light incident angle is over exaggerated in the figure) The dielectric tensor $\widetilde{\varepsilon_m}$ of the nanoparticle takes the form of Eq. 1.3.3. Due to the existence of the off-diagonal elements in the tensor, conversion between the x and y (or p and s at off-normal light incidence) components of the light field after the reflection will result in the elliptically polarized reflected light.

After some mathematical derivation and by assuming $\varepsilon_{xy} \ll \varepsilon_m$ thus the quadratic elements of ε_{xy} can be neglected in the results, Eq. 1.4.1 becomes

$$\tilde{\alpha} = \frac{4\pi abc}{3} * \frac{1}{\overline{L_x} * \overline{L_y} * \overline{L_z}} * \begin{pmatrix} (\varepsilon_m - \varepsilon_d)\overline{L_y} * \overline{L_z} & \varepsilon_{xy}\varepsilon_d\overline{L_z} & 0 \\ -\varepsilon_{xy}\varepsilon_d\overline{L_z} & (\varepsilon_m - \varepsilon_d)\overline{L_x} * \overline{L_z} & 0 \\ 0 & 0 & (\varepsilon_m - \varepsilon_d)\overline{L_x} * \overline{L_y} \end{pmatrix} \quad 1.4.2$$

with $\overline{L_\iota} = L_i(\varepsilon_m - \varepsilon_d) + \varepsilon_d$ for $i = \mathrm{x, y, z}$.

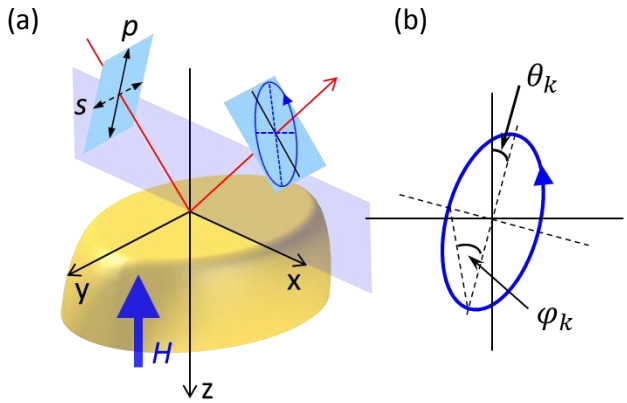

Fig. 1.4.1 (a) Nanoparticle in a magnetic field with polar Kerr configuration. Linearly polarized light becomes elliptically polarized after reflection from the nanodisk. (b) The Kerr rotation θ_k and ellipticity φ_k angles after reflection are shown.

For p-MOKE effect, the magnitude to be experimentally characterized in the far field is the complex Kerr rotation Φ_k (Eq. 1.3.8) with θ_k the rotation and φ_k the ellipticity, respectively (Fig. 1.4.1). For an x-polarized light incident normally to the

nanodisk, the polar Kerr effect can be expressed with the polarizability tensor $\tilde{\alpha}$ Eq. 1.4.2 as,

$$\Phi_k = \theta_k + i\varphi_k \approx \frac{\alpha_{yx}E_x}{\alpha_{xx}E_x} = \frac{\varepsilon_{xy}\varepsilon_d}{(\varepsilon_m-\varepsilon_d)\overline{L_y}} = \frac{3}{4\pi abc} * \frac{\varepsilon_{xy}\varepsilon_d}{(\varepsilon_m-\varepsilon_d)^2} * \alpha_{yy}. \quad 1.4.3$$

Generally, from Eq. 1.4.2 to 1.4.3 the following *rules of thumb* can be concluded in intertwined MO and localized surface plasmonic effects:

(1). At the LSP resonance excitation (α_{yy} reaches its maximum, Eq. 1.4.3), the polar Kerr effect will be maximized.

(2). For a nanodisk at dipolar resonance induced by x-polarized light, the effect of the magnetic field in the polar Kerr configuration is to generate *a rotation* in the plasmonic dipole along x direction ($\alpha_{xx}E_x$) and thus obtain a perpendicular dipole component along y direction (MO dipole, $\alpha_{yx}E_x$).

(3). From Eq. 1.4.3, the amplitude of this rotation, or, the polar Kerr effect, is proportional to both the MO constant ε_{xy} of the nanoparticle and interestingly, to the polarizability component α_{yy} along y direction, which is orthogonal to the incident x-polarization of the light.

(4). In Eq. 1.4.3, MO effect is also affected by the surrounding dielectric medium ε_d, which is the physical mechanism for the sensing applications with LSP enhanced MO effect [22,23].

(5). It is worth to note that, for the nanodisk structure considered above, $\alpha_{xx} = \alpha_{yy}$, therefore the maximum in MO spectrum and extinction peak appear in the similar spectral range. For nanostructures with in-plane optical anisotropy, such as the elliptical nanodisk, $\alpha_{xx} \neq \alpha_{yy}$, the enhancement in the MO effect may be located differently from the extinction peaks in spectral position, as expected from Eq. 1.4.3 [61,62].

Eqs. 1.4.1 to 1.4.3 for the polar Kerr configuration can be easily generalized to the other configurations, namely, the longitudinal [22,63,64] and transverse [64] Kerr configurations, by considering the remaining off-diagonal elements in the dielectric tensor of the nanoparticle. Moreover, the condition that light is incident off-normally can also be included, where the different components of the light field and the induced plasmonic dipole components supported by the nanoparticle along each

direction should be considered [64].

Similar to the LSP resonance, for large nanoparticles where the electrostatic approximation is not satisfied, additional corrections such as the radiative correction [65] and dynamic depolarization correction [62] should be included in the polarizability tensor $\tilde{\alpha}$ from Eqs. 1.4.1 to 1.4.3.

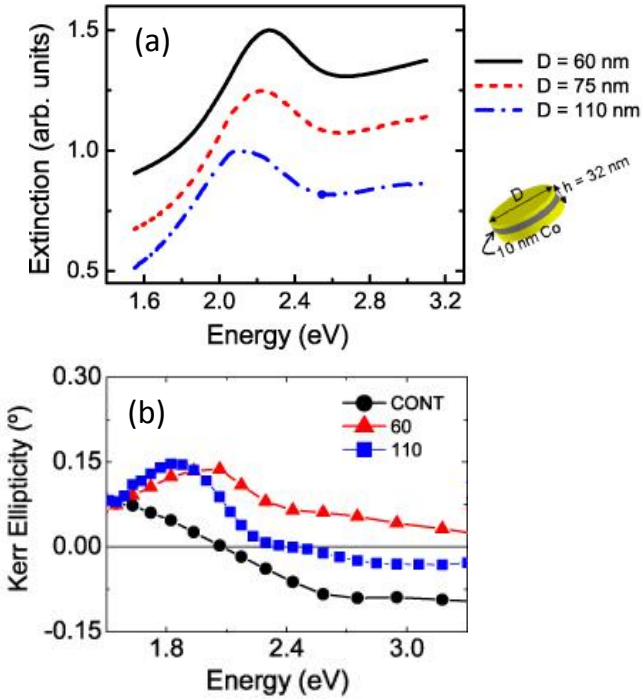

Fig. 1.4.2 Optical extinction (a) and Kerr ellipticity spectra (b) for Au/Co/Au nanodisks in polar Kerr configuration and normal light incidence. Au/Co/Au nanodisks have 60, 75 and 110nm diameters. Black dots and line in (b) correspond to the continuous film with the same amount of material. Adapted from Ref. [66].

As a general case, in Fig. 1.4.2 are shown the experimental extinction and MO spectra for Au/Co/Au nanodisk structures [66] in polar Kerr configuration and normal light incidence. The constituent materials for this nanostructure will be discussed in next subsection. As it can be seen, Kerr ellipticity spectra (Fig. 1.4.2(b)) of the nanodisks obtain maxima in the similar spectral range of the extinction peaks (Fig. 1.4.2(a)), corresponding to the LSP resonance excitation, whereas the continuous film with the

same amounts of Au and Co materials exhibit much less Kerr ellipticity in the same spectral range. Furthermore, a similar red-shifting behavior as the diameter increases is observed in both Kerr ellipticity and extinction spectra. All of these behaviors manifest the enhancement in MO effect by the LSP resonance excitation.

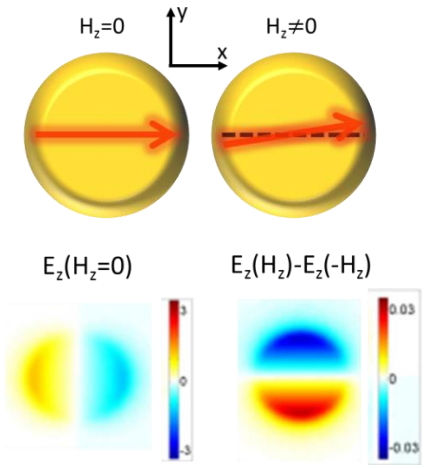

Fig. 1.4.3 Top: schematic sketch of the plasmonic dipole (red arrow) excited in a nanodisk by x-polarized light at zero magnetic field (H_z=0, left) and magnetic field induced rotation in the plasmonic dipole when $H_z \neq 0$ (right). Dashed black line is parallel to the x-axis for clarity. Bottom: calculated near field intensity of the E_z component of an Au/Co/Au nanodisk for x-polarized light incidence at zero magnetic field (left) and the difference of the E_z components for magnetic saturation along opposite directions (z and –z directions, right). The bottom figure is adapted from Ref. [67].

Rotation in the plasmonic dipole of the nanodisk by the magnetic field is schematically shown in the top panel of Fig. 1.4.3. As an evidence for this rotation, the bottom panel in Fig. 1.4.3 shows the calculated E_z field distribution for a nanodisk at plasmonic resonance excited by x-polarized light incident normally to the disk plane, where a typical dipolar field distribution along x direction is clearly observed. After the application of the magnetic field H_z, the plasmonic dipole along x direction obtains a small component along y direction. By subtracting the E_z field distributions for magnetic fields H_z along z and –z direction, the x-components in the near field distribution can be removed, as shown on the right, where the pure MO dipole

component along y direction is observed [67]. Note the different color scale for the two distributions, for MO dipole it is two orders of magnitude smaller than the plasmonic dipole.

1.4.2 Constituent Materials for Magnetoplasmonic Systems

As shown in Fig. 1.4.2, a nanodisk made of Au/Co/Au multilayer exhibits an enhanced MO effect at LSP resonance excitation. The combination of Au and Co is a common choice in current studies of magnetoplasmonic systems. Besides them, magnetoplasmonic systems can, of course, consist of other optional materials.

Almost all materials exhibit MO activity, but the performance strongly depends on different aspects. As shown in Fig. 1.4.4, MO constants of ferromagnetic Co are three orders of magnitude larger than that of diamagnetic Au [68], therefore a 3 orders of magnitude larger magnetic field would be needed to obtain similar MO activity in Au than in Co (in similar structures). This difference is due to the different physical origins of the MO effects in these materials: for Au, the MO effect is from the conduction electrons, while for the ferromagnetic metals the spin-orbit interaction of *d* electrons plays a more important role.

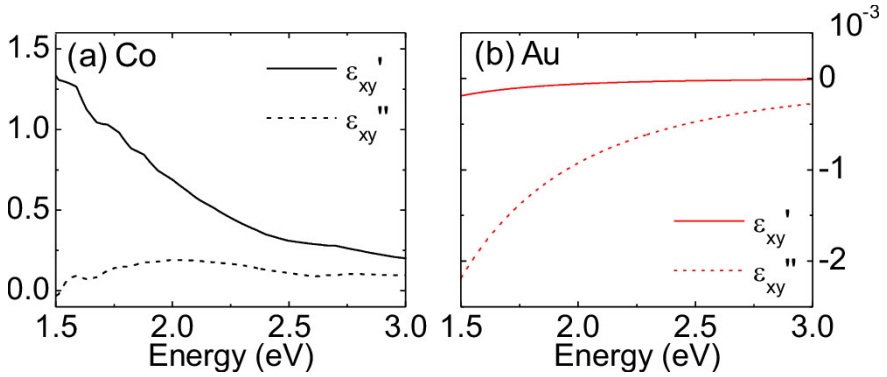

Fig. 1.4.4 Real (continuous line) and imaginary (dashed line) parts of the MO dielectric constants of Co at magnetic saturation (left) and Au (right). For Co, the data were experimentally obtained, and for Au through a Drude model calculation at 1T. Data are adopted from Ref. [68].

On the other hand, plasmonic performances of the metals are also different as we can see in Fig. 1.2.2(b). Noble metals such as Au and Ag exhibit much better plasmonic properties with well-defined LSP resonances, than the ferromagnetic metals Fe, Co and Ni which have much larger optical losses.

In this way, although many efforts have been devoted to study magnetoplasmonic systems made of pure ferromagnetic metals, e.g. Co [69-71], Ni [22,23,62-64,72], Fe [73], and permalloy [74], a better approach to realize the optimum magnetoplasmonic systems is to combine both noble and ferromagnetic metals, where ferromagnetic metal endorses MO effect and noble metal is responsible for plasmonic property. Example nanoparticles supporting LSP resonances in this approach are Au/Co/Au nanodisk [27,60,67,68, 75], Au/$[Co/Pt]_n$/Au round and elliptical nanodisks [76,77,78,79], Ag shell/Co core [80] and Au shell/Fe core nanospheres [81], etc.
Additionally, dielectric MO materials can also offer a large MO effect but much less optical loss due to the transparency in the optical range. Systems with combined noble metals and MO dielectrics thus offer another possibility, e.g., Au shell/Fe_2O_3 core nanospheres [82 , 83], $Co_xFe_{3-x}O_4$ shell/Au Core nanowires [84], Ag/$CoFe_2O_4$ dumbbell-like nanoparticle pairs [85]. It should be noted that for these nanoparticles, the dielectric parts not only contribute to the MO activity, but also modify greatly the dielectric environment ε_d, which should be considered in the plasmonic resonance [82].

In this thesis, the combined Au/Co/Au system is chosen for all the nanostructures. Obviously, for this system the nanostructure configurations, e.g. amount ratio of materials, or layer position in the nanostructure, play an important role in the determination of the device performances. To apply Eqs. 1.4.1 to 1.4.3 for this kind of nanostructures, an effective dielectric tensor of the nanoentity can be used by considering both $\tilde{\varepsilon}_{Au}$ and $\tilde{\varepsilon}_{Co}$ and their relative volume ratio,

$$\varepsilon_m = (1-\nu)\varepsilon_{Au} + \nu\varepsilon_{Co}, \qquad 1.4.4$$

$$\varepsilon_{xy} = \nu\varepsilon_{xy,Co}, \qquad 1.4.5$$

where $\nu = \frac{V_{Co}}{V_{Co}+V_{Au}}$ is the volume ratio of Co in the total nanodisk [60]. Since $\varepsilon_{xy,Au}$

is orders of magnitude smaller than $\varepsilon_{xy,Co}$ (Fig. 1.4.4), in Eq. 1.4.5 the contribution from the Au part can be neglected. Generally, Eqs. 1.4.4 and 1.4.5 represent optical and MO properties of the intermixed metal, by considering the whole nanostructure with a homogeneous material distribution, and especially a uniform EM field distribution inside the nanostructure.

However, such prerequisites are not always satisfied. For example, in Fig. 1.4.5(a) the electric field distribution of an Au nanodisk at resonance is shown, where larger fields can be observed near to the top and bottom interfaces. Therefore, Co layer position inside the Au nanodisk actually also affects the MO activity.

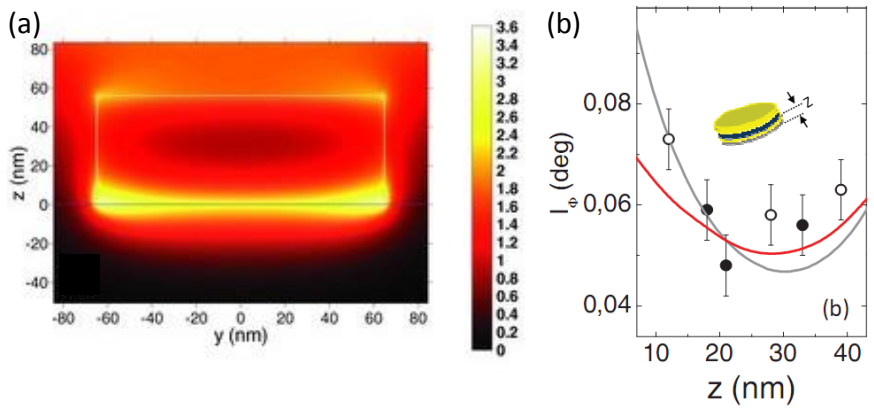

Fig. 1.4.5 (a) Electric field distribution for an Au nanodisk (h=54nm, D_1=D_2=130nm) at LSP resonance, normalized to the incident light field. (b) MO activities of Au/Co/Au nanodisks with Co layers located at different z positions. Grey line corresponds to the calculated field at the z position inside a *pure* Au disk in (a). Red line corresponds to the calculated field at the Co layer position (z) in the Au/Co/Au disk. Open and solid symbols are experimental MO activity data. Adapted from Ref. [86].

As it can be seen from Eq. 1.3.7, both increase in r_{xy} and reduction in r_{xx} of the nanostructure surface can contribute to the enhanced MO effect. For the nanoparticles supporting LSP, on the one hand, r_{xx} usually reaches its minimum at LSP resonance excitation. On the other hand, provided a very thin Co layer of thickness d inserted in the Au nanodisk, r_{xy} can be expressed as [26,86],

$$|r_{xy}| \propto \langle E_x E_y \rangle d |\varepsilon_{xy}|, \qquad 1.4.6$$

where $\langle E_x E_y \rangle$ is the average value of the product of the electric field components in the MO active Co layer normalized to the incident light intensity, representing the field intensity inside. As it can be seen, r_{xy} is proportional to the field intensity inside the MO layer. Being field enhancement one of the main characteristics of LSP resonance excitation, an enhancement in r_{xy} and thus an enhanced MO effect will be induced at LSP resonance. However, for Co layer located in different vertical positions of the nanodisk, $\langle E_x E_y \rangle$ will have different values (Fig. 1.4.5(a)), therefore the MO effect will be enhanced differently. This is shown in Fig. 1.4.5(b) where the MO activity (I_Φ) exhibits maxima when Co layer is located near to the two interfaces.

Conclusively, Eqs. 1.3.7 and 1.4.6 provide us the criterion of the magnetoplasmonic system design to obtain the best MO performance: concentrating EM field in MO active part, reducing the reflection of the system, or a combination of both.

1.4.3 Progress in LSP-Magnetoplasmonics

During the last years, the emerging LSP-magnetoplasmonics have experienced an expansive evolution, as summarized in Table 1.4.1, from basic nanodisk [22,23,27,60, 62,63,67,68,75-77]/nanosphere [80,81] to more complex elliptical nanodisk [61,78,79], nanowire [28], and then near-field coupled disk dimers [60,67,70,75], and then far-field coupled periodical disk arrays [87,88].

Generally, the previous discussion about the enhanced MO effect at LSP resonance, rotation of the plasmonic dipole by the magnetic field (e.g. at polar Kerr configuration), etc., can be applied directly to the isolated and morphologically simple nanoparticles, including the ellipsoidal nanoentities (e.g. core/shell nanosphere, round and elliptical nanodisk, etc.) consisting of either the noble/ferromagnetic metal combination or pure ferromagnets, or even the pure noble metal [59]. The main concerns in such structures which may be different from Fig. 1.4.2 and Fig. 1.4.3 are:

(1) due to the large optical loss of the pure ferromagnet, the LSP is greatly damped, therefore the extinction peak and the MO enhancement can be much broader in, for example, Ni nanodisks [61];

(2) for structures with in-plane anisotropy $\alpha_{xx} \neq \alpha_{yy}$, according to Eqs. 1.4.2 and 1.4.3, the MO enhancement may be located in a shifted spectral range than the

extinction peak, as for Ni elliptical nanodisks [61].

When it comes to complex nanostructures, for example, disk dimers (Table 1.4.1), the situation could be much more complicated: on the one hand, either or both of the disks could be MO active and plasmon hybridization should be considered not only for the pure optical dipoles, but also for the MO dipoles; on the other hand, due to the introduction of the magnetic field, different configurations of the light incidence and magnetic field should be considered, especially for the horizontal nanodisk dimers [70] where plasmon hybridizations are different for different incident light polarizations.

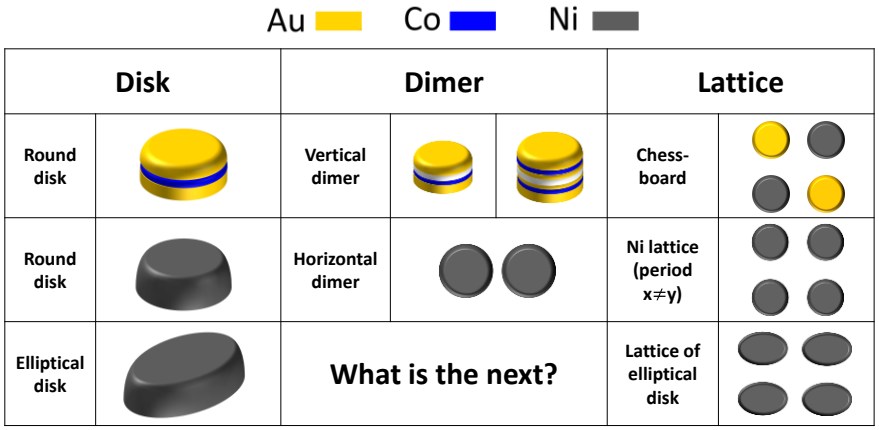

Table 1.4.1 Summary of the main LSP related magnetoplasmonic nanostructures.

Here we discuss several reported examples of magnetoplasmonic disk dimers, mainly the Au/Co/Au system.

The first one is an Au disk dimer spaced with 20nm SiO_2, where only one Co layer is inserted either above or below the SiO_2 spacer (Fig. 1.4.6) [75]. As discussed in subsection 1.2.2, the plasmon hybridization between the top and bottom disk dipoles causes the split and shift of the plasmon resonance. Here this behavior is also affected by the Co layer, since field distributions at LSP resonances are modified by Co dispositions (Fig. 1.4.6(a-d)). In extinction spectra, it manifests as different relative intensities of the HE and LE peaks when Co is placed above or below SiO_2 spacer: a larger field intensity in the overall structure implies a larger extinction intensity. On the other hand, the MO activity shows similarity between the two, being LE

enhancement always more intense since field inside the Co layer is always higher for LE resonance. This offers us an advantage for applications such as optical isolators, being a simultaneous high MO activity but low optical loss (black marked dimer) in the specific LE range.

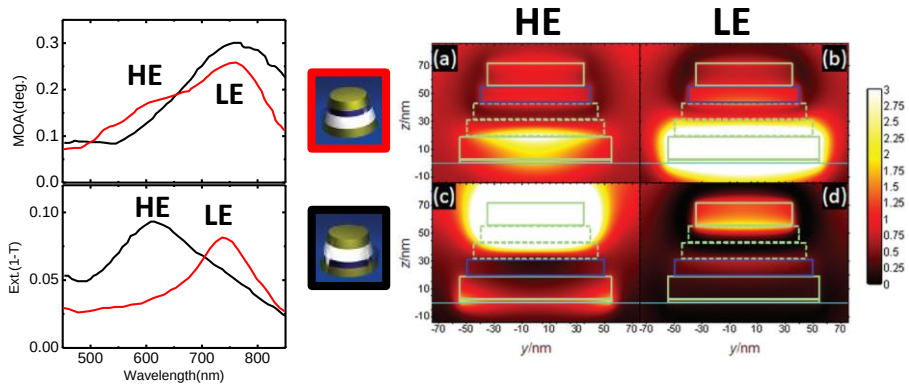

Fig. 1.4.6 Left: optical and MO responses of the Au disk dimers spaced with SiO_2 with a Co layer inserted above (red) and below (black) the SiO_2 spacer. Layer thicknesses are 15nm Au, 10nm Co, 20nm SiO_2 and 15nm Au. Approximate values of the upper and lower nanodisk diameters are 70 nm and 110 nm respectively. Right: (a-d) Electric field distributions for the two structures and for both LE and HE peaks. Adapted from Ref. [75].

The distance between the disks in the magnetoplasmonic disk dimer should also play an important role in the determination of the MO performance via the plasmon hybridization strength. This has been studied in the Au/SiO_2/Au disk dimer system with inserted Co layer inside the bottom Au disk, by varying SiO_2 thickness (Fig. 1.4.7) [67]. When SiO_2 spacer is very thick (50nm), no hybridization happens. Two peaks can be observed in the extinction spectrum, corresponding to the individual LSP resonance of the top and bottom disks. Due to the conic shape of the whole structure, aspect ratios of the top and bottom disks are different, therefore the corresponding LSP resonances are located at different spectral positions. On the other hand, only one peak can be observed in the corresponding MO activity, which is attributed to the MO effect of the bottom Au/Co/Au disk. As the SiO_2 thickness decreases from 50nm to 5nm, plasmon hybridization happens, resulting in the resonance shift. Meanwhile, a sizable MO behavior in the top Au plasmonic disk is

induced by the MO dipole of the bottom disk via near field interaction (Fig. 1.4.7(b)). Subsequently, the two MO dipoles interact and hybridize with each other, resulting in the splitting and shifting of MO activity peaks, even disappearance of the MO effect in some specific wavelength ranges (Fano-resonance marked with a green diamond in Fig. 1.4.7(a)).

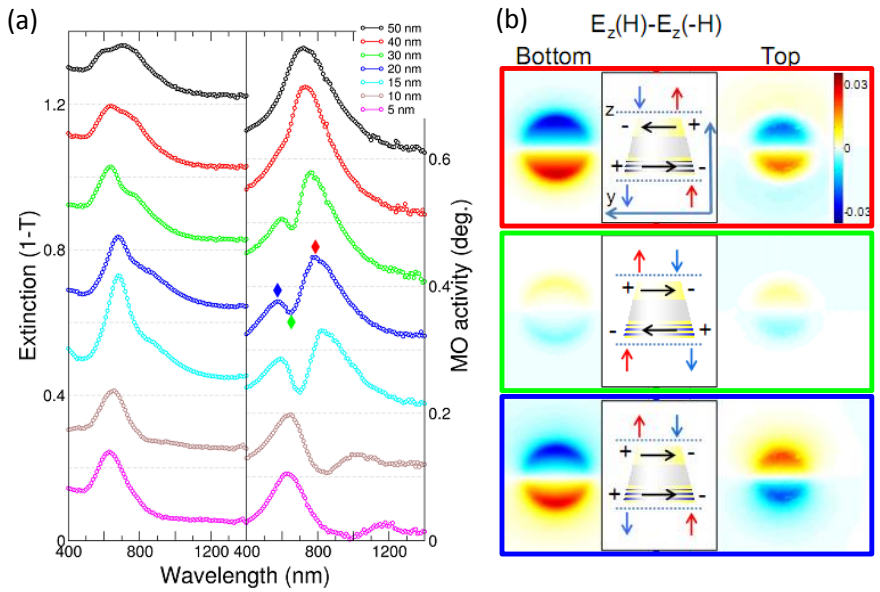

Fig. 1.4.7 Effect of hybridization strength on MO performance in a nanodisk dimer. (a) optical extinction and MO activity (polar configuration) of the dimers. (b) MO dipole field distributions for the wavelength positions marked in (a) with diamonds, obtained from the differences between optical distributions of opposite (H and –H) magnetizations. Adapted from Ref. [67].

The above case is with the intrinsic MO dipole supported by the bottom disk. Further situations with intrinsic MO dipole(s) supported by either top or bottom disk, or both disks, have also been considered with intermediated spacing distance (20nm) and hybridization strength [60]. Similar effects, namely, the induced MO dipole in the non-intrinsic MO active disk and hybridization between the two MO dipoles, have been obtained. Moreover, the effect of Co amount in such a combined noble/ferromagnetic metal system on the plasmonic and MO performances has also

been studied since Co can endorse MO activity but damp the LSP resonance. The results manifest that the largest MO activity appears in the dimer with Co only in the top disk for an intermediate Co ratio (25%).

All the effects discussed above are based on the polar Kerr configuration. A similar effect of the hybridization strength on MO performance has also been studied in horizontal Ni-Ni disk dimers in longitudinal Kerr configuration (Table 1.4.1) [70], where both disks are intrinsically MO active.

Additionally, magnetoplasmonic disk arrays (right column in Table 1.4.1) supporting the so-called MO surface lattice resonances (MO SLR) has also been studied [87,88], where sharp features can be observed in the MO spectra, in contrast to that of the randomly distributed nanoparticle system.

1.4.4 Application of LSP-related Magnetoplasmonic System

The most direct application of magnetoplasmonic systems can be conceived for their use in non-reciprocal devices, e.g. optical isolators, in the integrated telecommunication systems, since they provide enhanced MO effect. On the other hand, the MO signal can act as a probe of the EM field distribution inside the nanostructures which is difficult to reach with conventional methods, since it can be detected in the far field and the MO performance in the magnetoplasmonic system is related directly to the EM field intensity inside the MO active component [86]. The enhanced MO signal in such magnetoplasmonic system also offers a method in the far field for the magnetic field and domain detection.

Moreover, the plasmon enhanced MO effect is sensitive to the local refractive index, therefore the magnetoplasmonic system can serve as a platform for the bio- and chemical sensing. Compared to the traditional plasmonic sensors, MO signals are detected in the magnetoplasmonic sensors, but not the absolute light intensity, which can, on the one hand, improve the detection limit, and on the other hand, enhance the signal-to-noise ratio and figure of merit [19,23].

Since the hybridization of MO dipoles in the nanodisk dimer strongly depends on the spacing distance between the two disks, nanometric characterization, namely, nanoruler, can be realized with such a nanodisk dimer, either vertical or horizontal

[70]. Such a system benefits with a highly improved figure-of-merit compared to the pure plasmonic ruler and a possible manipulation with an external magnetic field.

1.5 Nanofabrication Method

Development in plasmonic and magnetoplasmonic fields in the last decades is highly motivated by the progress in nanofabrication technology. Different methods and techniques, especially a variety of lithography methods [89,90] have been used for the nanostructure and device fabrication, such as optical lithography, electron-beam (E-beam) lithography, focused ion beam (FIB) lithography, nano-imprint lithography, X-ray interference lithography, nanosphere lithography, colloidal lithography, hole-mask colloidal lithography, etc.

Each method has its own advantages and disadvantages. For example, E-beam lithography [91], that uses an electron beam directly to expose the resist, shows a great resolution to sub-10 nm. Currently, it is extensively used in the definition of plasmonic structures with arbitrary shapes and/or periodic arrays. However, it requires special instruments to realize the exposure process, which is costly in both economics and time for a large-area production. Similar problems also exist in FIB lithography [92] for mass production. The other promising techniques for fast and parallel processing, such as X-ray interference lithography [93], can produce structures with a high resolution in a massive way. However, complex equipment is also required and the feasible nanostructure shapes are limited. Furthermore, structures defined by such lithography methods are usually 2-dimensional (2D), therefore generation of 3-dimensional (3D) structures needs repeated exposure and development processes, which suffer the problems of alignment and long production time.

Meanwhile, soft lithography methods based on nanospheres offer another possibility with the advantages of low cost and large area for the massive production. With the so-called nanosphere lithography where close-packed nanospheres are used as evaporation or etching mask, nanostructures arranged hexagonally can be produced in an area over cm^2, but with a limited number of possible shapes **[**94**]** and a drawback of clogging during evaporation [90]. The colloidal lithography method, which uses as well nanospheres as the mask but in a fashion of random and sparse distribution, can help to define nanostructures randomly distributed in a large area, even over dm^2 [43,117]. By modifying colloidal lithography method, the so-called hole-mask

colloidal lithography (HCL, Fig. 1.5.1) utilizes holes generated with colloidal lithography in a metal film as the mask [35], and offers more freedom on controlling shape and dimension of the nanostructures, especially for structures in 3D and with multiple components [35,90]. With a repetitive HCL process [98], structure collections (or metasurface) with a variety of shapes can be fabricated on the same substrate.

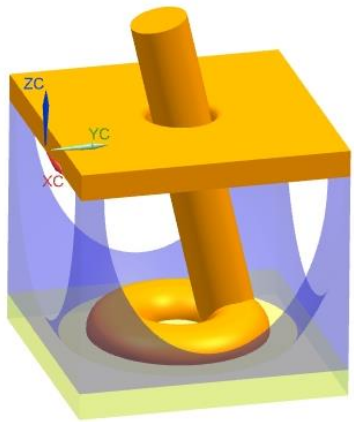

Fig. 1.5.1 Sketch for the hole-mask colloidal lithography (HCL) template and the deposition of nanoring structure.

For the fabrication of the specific nanoring structure, different methods have been applied, e.g., colloidal lithography combined with second deposition by sputtering for Au nanoring [158], chemical synthesis for Ag nanoring with a good crystalline quality [95], as well as E-beam lithography [142,159] and so on.

Considering that the study in this thesis is about the fabrication and optical and MO properties of nanoring structure, HCL method combined with multiaxial deposition is chosen as the fabrication method due to its advantages in economy and versatility on controlling the structure shapes and components. Indeed, a variety of ring-related nanostructures have already been presented by other groups with HCL method, e.g. split ring [96,97], chiral split ring [98,99], as well as disk-related structures [90], e.g. disk and disk oligomers.

1.6 Contents of the Thesis

For the study of LSP-magnetoplasmonic systems, clearly two sub-fields have been formed: one is to study nanostructures with more complex morphologies and components, and to explore the multiresonant plasmonic and MO modes, as well as the correlated phenomena and mechanisms; the other one is to study nanostructure arrays with periodical coupling and the phenomena, mechanisms therein.
Following the first direction, in this thesis, I am going to study the intertwined plasmonic and MO properties of Au/Co nanoring structures. For this purpose, the first technical goal is to explore and optimize HCL method for the fabrication of nanoring and related structures. After that, the intertwined MO and plasmonic properties of these structures, as well as the mechanisms behind, will be studied.

This thesis is organized as follows:
In Chapter 2, methodology and experimental techniques used in this study are introduced. Experimental instruments such as deposition chambers with molecular beam epitaxy (MBE) and sputtering, characterization equipment like atomic force microscope (AFM), spectroscopic ellipsometry (SE), magneto-optical Kerr effect spectroscopy, etc., will be introduced.

In Chapter 3, HCL method and its optimization for nanoring fabrication will be discussed. Related template parameters, such as nanosphere density, mask film thickness, etc., and parameters for deposition control such as the deposition angle, will be optimized and discussed in detail.

In Chapter 4, the nanoring will be explored as a novel magnetoplasmonic system. A series of Au/Co/Au trilayer nanostructures from nanodisk to ring will be fabricated and characterized. Evolution in plasmonic modes from unimodal for nanodisk to bimodal for nanoring, and the resulted evolution in MO enhancements will be discussed. With theoretical simulation, the hybridization between the disk and hole MO dipoles at resonance will be used for the explanation of bimodal resonance in MO activity of nanoring.

In Chapter 5, we explore methods to modify the plasmonic and MO responses of nanoring structures. Modifications in the nanoring morphology and distribution of central Co layer inside the nanoring will be applied and the corresponding optical and MO properties of the nanostructures will be characterized. The former one offers a method to realize fine control of mode shift by modification in subtle structure morphology. In the latter case, Co layer is controlled to form opposite Co-dots, Co-sectors, and Co-continuous ring. This results in the in-plane optical anisotropy of the system. The MO effect, on the other hand, is proportional to the Co amount in the nanostructure.

In Chapter 6, a method to improve the MO performance of the nanoring structure is explored. A split ring is put on top of the Au/Co/Au nanoring structure with the gap above the embedded Co dot. Due to EM field localization in the gap region of the split ring, a further enhancement in the MO effect is obtained compared to the structure without this gap, and this enhancement in MO effect can be optimized via tuning the gap angle to reach a factor of 3.

Chapter 2

Methodology

and Experimental Techniques

In this thesis, as we show in Chapter 1, the optical and magneto-optical properties of magnetoplasmonic nanorings in the visible and near infrared range will be studied. For this purpose, both the fabrication and characterization of these nanoring structures will be considered. This is a complex and systematic process, where multiple technical approaches using a number of instruments will be applied.

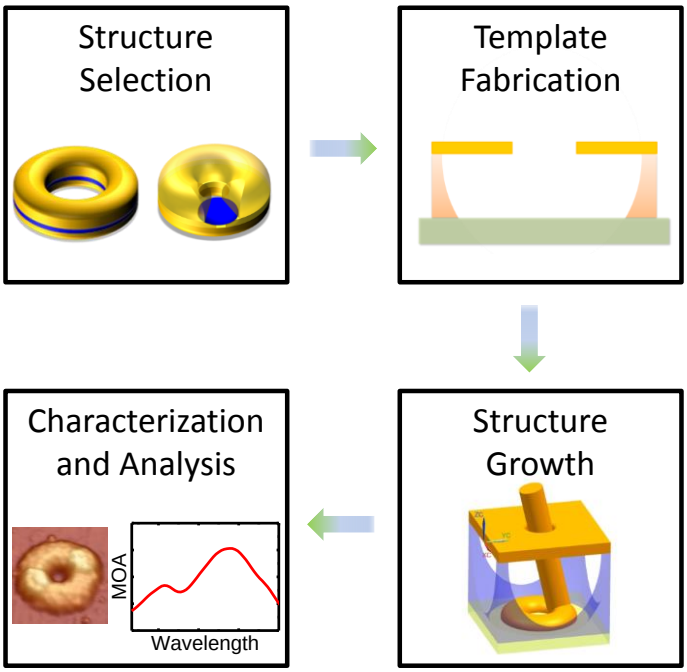

Flow Chart 2.1 The general experimental process in this thesis.

To make it clear, in Flow Chart 2.1 the sequence of the whole experimental process is shown, which can be divided into four steps: structure selection (disk, disk-ring, ring with insertions, ring-split ring), template fabrication (hole-mask colloidal lithography method), structure deposition (multiaxial thermal and electron-beam evaporation, magnetron sputtering), characterization and analysis (morphological, optical and magneto-optical properties). During each step and procedure, a combination of different techniques are applied and, whenever needed, optimized, for which one can refer to Table 2.1 and 2.2 where the techniques are listed. All the steps and the use of the corresponding techniques were individually and independently carried out by the Ph.D. candidate. For further analysis, theoretical simulation is carried out in parts of the work by Dr. Antonio García-Martín from IMM, Madrid, Spain, and Prof. Luc Henrard from the University of Namur, Namur, Belgium.

In what follows, the most relevant experimental techniques listed in the tables will be introduced. Due to its critical aspect with fabrication part, and the specific innovations introduced to optimize the structures, the hole-mask colloidal lithography (HCL) template preparation and its use in the multiaxial deposition process will be presented separately in Chapter 3. First, the ultrahigh vacuum molecular beam epitaxy (UHV-MBE) and sputtering systems used for the deposition and growth of the nanostructures, as well as for the HCL template preparation will be generally described. During this deposition process, metals and dielectrics are deposited with magnetron sputtering, thermal evaporation, and electron beam (E-beam) evaporation techniques, for which the working principle will be introduced. All of these will be included in Section 2.1. Second, the characterization techniques, such as the atomic force microscopy (AFM) for morphological characterization (Section 2.2), optical microscope combined with the spectrometer, and spectroscopic ellipsometry for optical properties (Section 2.3), and magneto-optical Kerr effect (MOKE) spectroscopy for magnetic and magneto-optical properties (Section 2.4), will be discussed in detail. Some of the techniques used in the preparation of the hole-mask colloidal lithography (HCL) template, for example, oxygen plasma stripper and reactive ion etching (RIE), will be briefly introduced in Appendix 1.

Hole-mask Colloidal Lithography Template Preparation

Step		Technique	Sections
Step (I)	Substrate Cleaning	Ultrasonic Bath	
	PMMA Coating	Spinner and Hot Plate	
Step (II)	O_2 Plasma	O_2 Plasma Stripper	Appendix 1
	PDDA/PS Spheres Deposition	Spinner	
Check-point		AFM	
Step (III)	Au Deposition	UHV Deposition System	2.1
	O_2 Plasma (optional)	O_2 Plasma Stripper	Appendix 1
	PS Sphere Removal	Tape-stripping	
Check-point		AFM	
Step (IV)	PMMA Removal	RIE Etching	Appendix 1
Check-point		AFM	
To be Continued: Sample Growth….			

Table 2.1 Hole-mask colloidal lithography template preparation process and techniques used therein, and the corresponding sections in this chapter. At each check-point, the template is examined with AFM routinely. The techniques are listed according to the actual sequence used in the experiment.

Nanostructure Growth and Characterization

Step		Technique	Sections
Growth (UHV-MBE system)	Ti, Co, SiO_2	E-beam evaporation	2.1
	Au	K-cell (thermal evaporation)	2.1
Lift-off		Ultrasonic Bath	
Characte-rization	Morphology	AFM	2.2
		SEM	
	Magnetics	t-MOKE	2.4
		p-MOKE	2.4
	Optics (Extinction)	Optical Microscope + Spectrometer (unpolarized)	2.3
		Spectroscopic Ellipsometer (polarized)	2.3
	Magneto-optics	t-MOKE	2.4
		p-MOKE	2.4
	EM Field Distribution	EELS	

Table 2.2 Techniques used in the sample growth and characterization, and the corresponding sections in this chapter. The techniques are listed according to the actual sequence used in the experiment. The scanning electron microscopy (SEM) and electron energy loss spectroscopy (EELS) marked with red are done with the help of Dr. Daniel Granados from institute IMDEA-nano, Madrid, Spain, and Dr. Raul Arenal from Universidad de Zaragoza, Zaragoza, Spain, respectively.

2.1 Deposition

Different deposition techniques are used in two ultra-high vacuum (UHV) deposition systems. The Au layer in the HCL template is deposited with magnetron sputtering,

while for the Au/Co/Au layered nanostructures, both electron-beam (E-beam) evaporation (for Co) and thermal evaporation (for Au) are used. With these systems, the morphologies and constituents of the nanostructures can be precisely controlled in the nanometric scale, which are important for the study of the plasmonic and magneto-optical properties. In this section, we will first briefly introduce the two deposition chamber systems used in the experiments (subsection 2.1.1), and later the deposition techniques installed in these chambers will be discussed (subsections 2.1.2-2.1.4).

2.1.1 Deposition Systems

Two UHV systems are used in our experiments, one focuses on the magnetron sputtering of metals (system (I), Fig. 2.1.1) and the other one is equipped with E-beam evaporation and thermal evaporation components, as well as several magnetron sputtering components (system (II), Fig. 2.1.2), which actually allows molecular beam epitaxy (MBE) on the single crystal substrate. In Fig. 2.1.1 and Fig. 2.1.2 are shown the view of the two systems, as well as their respective componential sketches. Generally, similar vacuum systems are working to provide the UHV environment to the two systems, with the turbo pump to provide the working vacuum and the ion pump for the stand-by vacuum. The turbo pump is further backed up with a mechanical rotary pump.

The sputtering system (I) (Fig. 2.1.1(a)) works with up to 4 magnetron sputtering components, which contain different metallic targets inside, such as Au, Co, Ag, etc. In this system (Fig. 2.1.1(b)), the main deposition chamber and the load-lock are isolated from each other with a gate valve. Two magnetically manipulated rods in the load-lock and the deposition chambers are used for the transference of the sample between them, and allow for linear movement and polar rotation. Before the deposition process, the sample is first introduced into the load-lock and mounted onto the transfer rod, where it will be pre-pumped to a base pressure below 5×10^{-7} mbar with the turbo pump and back-up mechanical rotary pump. After the base pressure in the load-lock is reached, the sample will be transferred to the holder rod in the deposition chamber. With the sample, the holder rod is moved to the sputtering position and rotated to face normally or obliquely to the sputtering target as required. The shutter on the magnetron sputtering component controls the On/Off of the

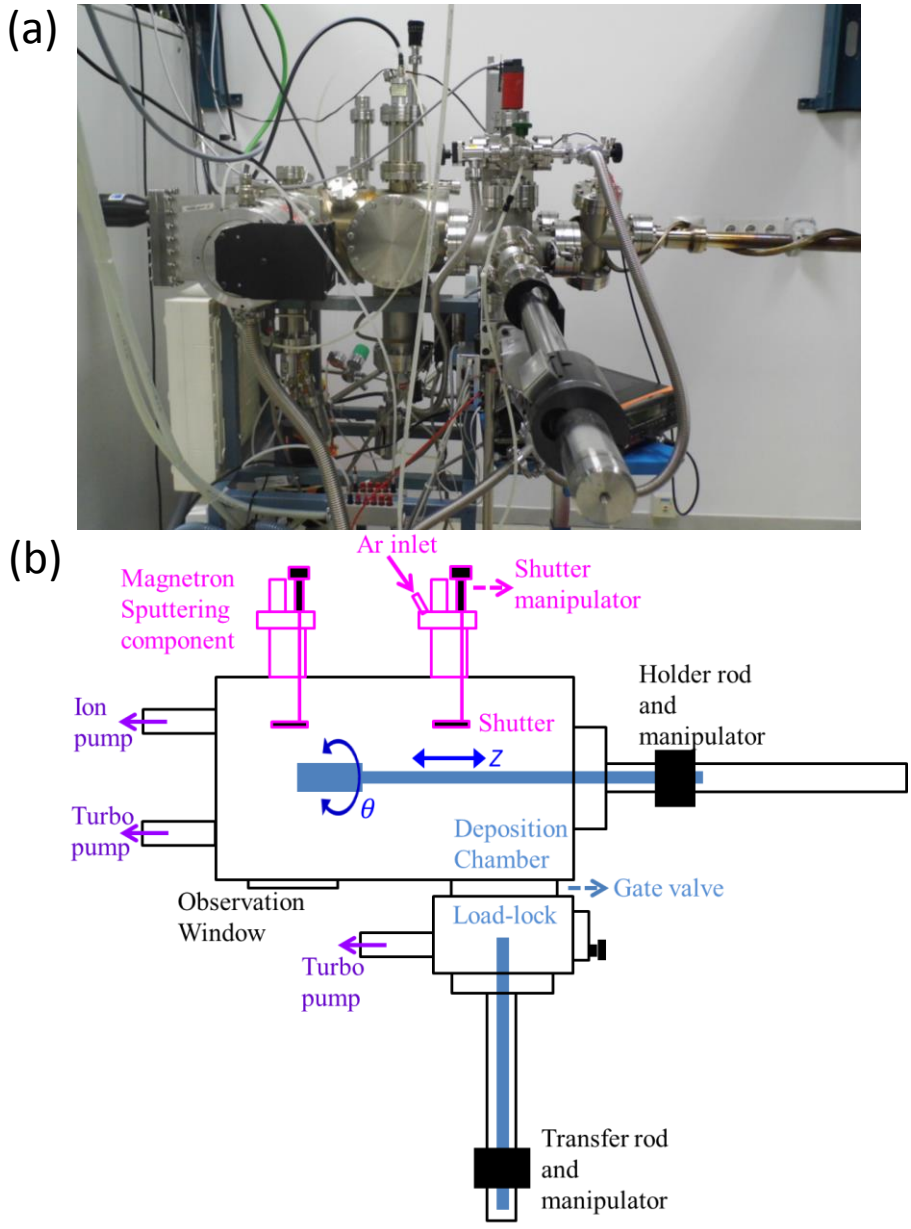

Fig. 2.1.1 (a) View of the small deposition system (I) used in the experiments. (b) Sketch of the system (I). Different parts of the system are displayed with different colors. Several sputtering components (pink) are mounted with different targets.

deposition process and allows the pre-sputtering of the target before the deposition in case of any contamination on the target surface. The inlet of working gas Ar is controlled with a needle valve. Pressures in the load-lock and the deposition chamber are monitored with a dual gauge sensor: a Pirani gauge for the pressure range of 10^{3}-10^{-2} mbar, and a hot cathode Bayard-Alpert gauge for the range of 10^{-2}-10^{-10} mbar. A mass spectrometer (Pfeiffer Prism QMS 200), which allows the leakage test and residual gas analysis via the detection of the charge-mass ratio of the ionized atoms and molecules accelerated by the electric field, is connected to the main deposition chamber.

The MBE system (II) works similar to the sputtering system, but apart from 6 magnetron sputtering components, it is also equipped with a Knudsen cell for Au thermal evaporation and a 3-source E-beam evaporator for the Ti, Co and SiO_2 evaporation (Fig. 2.1.2). The pre-pump and transference processes are the same as those in system (I): the to-be-deposited template or sample is fixed with tungsten wires on a molybdenum holder platform (Fig. 2.1.3(a)), which will be mounted in the load-lock and pre-pumped, and then introduced into the main deposition chamber, being fixed with clips on the sample carrier (Fig. 2.1.3(b)). The sample carrier is manipulated by the MultiCentre 3944 module (UHV Design, Fig. 2.1.2(b)), which allows 400mm horizontal linear movement of the sample between different evaporators (Z axis), 360° polar rotation (θ), as well as continuous in-plane azimuthal rotation (φ), driven by motors outside and isolated from UHV chamber. Besides, the sample carrier (Fig. 2.1.3(b)) has a heater module designed to heat the sample to a maximum of 700℃ and the temperature is monitored with a K type thermocouple. For the nanodisk or continuous film structures deposited normally to the substrate, the azimuthal rotation of the sample carrier can improve the homogeneity of the deposit. For nanoring structure, the polar and azimuthal rotations of the substrate allow the required simultaneous tilted-angle deposition and the in-plane rotation. For E-beam evaporation, a quartz balance is used to monitor the deposition rate *in situ*. The typical working pressure for the thermal and E-beam evaporation is around 10^{-9}~10^{-10} mbar, which is monitored with several dual gauges distributed separately in different monitoring points of the system.

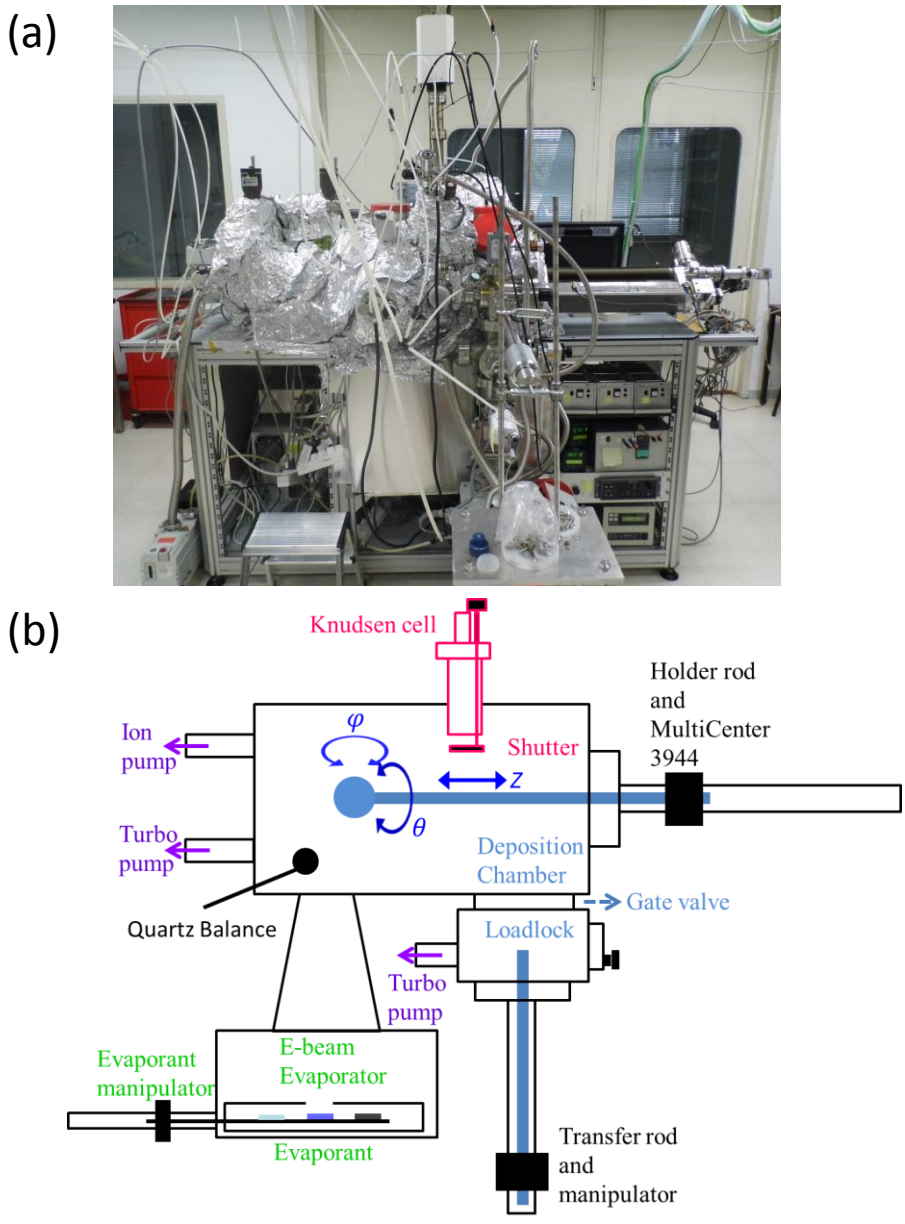

Fig. 2.1.2 (a) Molecular beam epitaxy (MBE) system (II). (b) Sketch of the MBE system (II). Besides several magnetron sputtering components (not shown), a Knudsen cell is used for the Au thermal evaporation (pink), and e-beam evaporator is used for Ti, Co, SiO_2 evaporation (green).

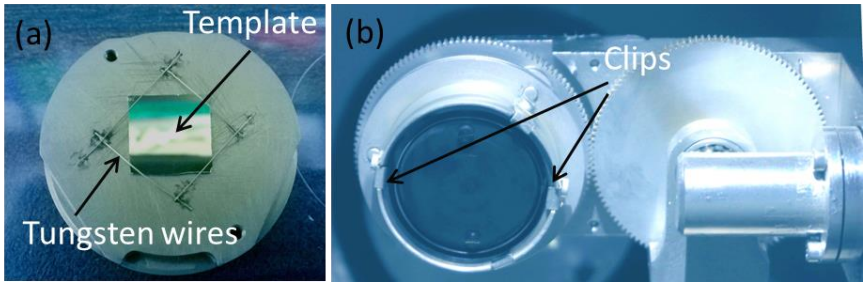

Fig. 2.1.3 (a) Holder platform with a template on top fixed with tungsten wires after the deposition process. (b) Sample carrier with the clips to fix the sample holder. The heater module is on the backside and monitored with a K type thermocouple. The gear sets to drive the in-plane rotation of the sample carrier is also shown.

2.1.2 Magnetron Sputtering

In both fundamental research and industrial application, sputter deposition is one of the most widely used methods for thin film deposition, due to its feasibility, reproducibility, precise control of the deposition rate, thickness, and composition [100]. Since the mechanism of the sputtering process is purely mechanic, it is very suited for the deposition of metals with high melting point. By mixing with a reactive gas into the inert gas (e.g. O_2), reactive sputtering can be used for the deposition of dielectric thin films which are non-conductive. During the deposition process, the chamber is first evacuated to a low pressure, where the inert Ar gas is injected. Similar to the generation of O_2 plasma, the electrons in the low pressure have a long mean free path and can be accelerated to a high speed by the DC electric field applied between the substrate and the target (cathode). The collisions between the electrons and the Ar atoms thus ionize the latter, generating the Ar^+ plasma (Fig. 2.1.4). The positive Ar^+ ions are accelerated and drift to the cathode (top blue plate in Fig. 2.1.4), where the target is located and the accelerated Ar^+ ions with a large mass and kinetic energy strike and transfer their momenta to the target atoms and atom clusters to cause them to sputter. Due to the dispersion in the sputtering directions, only a part of the sputtered atoms and clusters can arrive at the substrate to form the deposit and the deposition rate has an inverse square relationship to the working distance. It is easy to imagine that the deposition rate in this process is also determined by the gas species

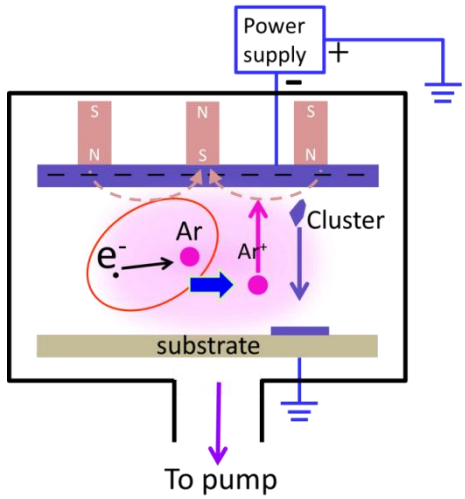

Fig. 2.1.4 A sketch for the principle of magnetron sputtering with Ar as the working gas.

(determine the mass of the atom), gas pressure and the voltage or power fed to the system. On the other hand, the addition of the permanent magnets on the rear side of the cathode and target can provide a magnetic field that causes the accelerated electrons to move helicoidally, thus the electrons are confined around the target and furthermore, the helicoidal movement of the electron improves the probability of collisions with the Ar atoms and thus the efficiency of the Ar ionization. As a result, in such a way the stable Ar^+ plasma could be generated at a relatively lower Ar gas pressure. The low plasma pressure increases further the mean free path of the sputtered atoms and clusters, resulting in a higher deposition rate. RF sputtering can also be applied in the magnetron sputtering, which can avoid the accumulation of the charge on the target and make it feasible to deposit the non-conductive materials.

In our experiments, a commercial magnetron sputtering component (A300 series A3CV & CTM, AJA International) is used (Fig. 2.1.5(a)), for which the water cooling, Ar gas inlet needle (Ar line), and electric power connections are integrated compactly in the same configuration. A chimney is used to collimate the drift direction of sputtered materials. Both the DC and RF modes can be applied with this component and the deposition rate is approximately proportional to the feeding power, with DC mode gives higher rates than the RF one on conductive targets for a given power level. Because of the specific magnet configuration and the magnetic field distribution (right

of Fig. 2.1.5(b)), the target (e.g. Ti, left of Fig. 2.1.5(b)) is etched unevenly as shown, where an erosion track is formed around the center into a ring and eventually the target will be penetrated. The deposition rate is controlled by the input power and the Ar pressure. The standard sputtering parameters for the Au layer deposition in the HCL template preparation are 1.0×10^{-3} mbar for Ar gas pressure, and 20W for power, with the deposition rate around 1.73 Å/s.

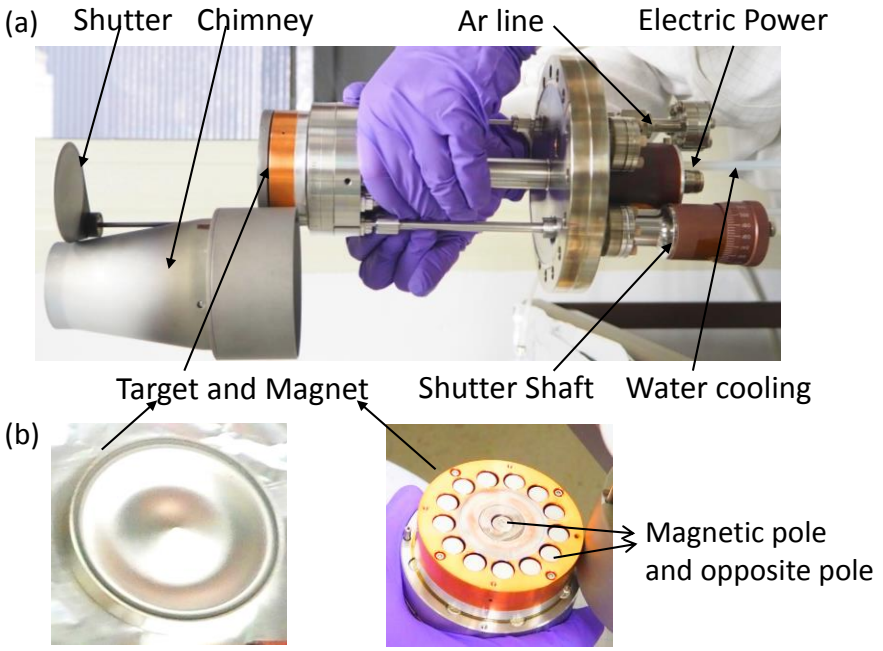

Fig. 2.1.5 (a) Magnetron sputtering component (A300 series A3CV & CTM, AJA International) used in our experiment. (b) Left: Ti target after intensive usage. Right: magnet configuration (the central one has an opposite pole with respect to the surrounding magnets.)

2.1.3 Thermal Evaporation

Thermal evaporation is one of the simplest physical vapor deposition techniques and is commonly used for the metal deposition. The basic process is that the material is heated in vacuum until its surface atoms have sufficient energy to leave the surface, namely, being evaporated. When the evaporated atoms or molecules (with a thermal

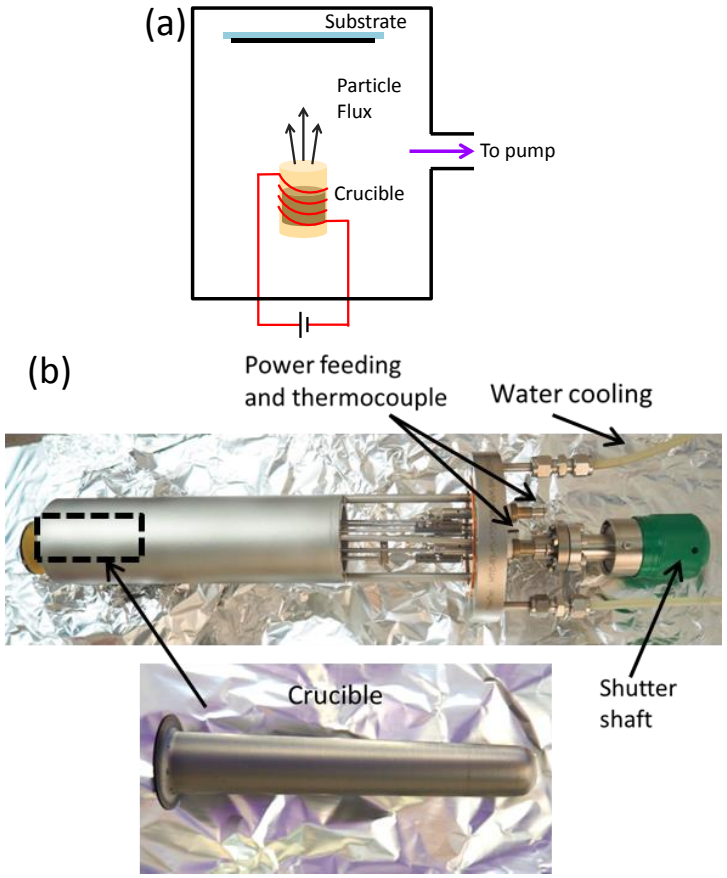

Fig. 2.1.6 (a) Sketch for the principle of the thermal evaporation. (b) The commercial Knudsen-cell (HTC-63-10-1700-284-WK-SHM) used in the experiments. Bottom: the graphite crucible used in the cell (image amplified).

energy less than 1eV) reach the substrate, they will become condensate and cover the substrate. As shown in Fig. 2.1.6(a), the ceramic crucible in a UHV chamber is filled with the evaporant materials and surrounded by a tungsten or tantalum resistance wire. With radiative heating by the wires, the crucible is heated in a controlled fashion. A thermocouple sensor and a PID heater controller are used to monitor and control accurately the temperature. The evaporant in the crucible is thus heated, melted, and vaporizes to form a gaseous flux from the open end of the crucible. Thanks to the high vacuum environment, the evaporated particles in the flux have a mean free path that is

longer than the distance between the evaporation source and the substrate, which facilitates the deposition process by reducing the collisions between the evaporated particles and the other particles. Parameters controlling the deposition rate are thereby the heating power, base pressure, substrate temperature and so on.

In our experiments, a commercial Knudsen-cell (HTC-63-10-1700-284-WK-SHM, CreaTec Fischer & Co. GmbH, Fig. 2.1.6(b)) is used as the Au evaporation component, with the ability to provide a temperature up to 1700℃. The crucible, shutter, water cooling section, and electric power source are integrated together compactly, with the thermocouple (type C) and PID controller (CU-3504-S1-DC, CreaTec Fischer & Co. GmbH) to monitor and control the temperature. The standard temperature ramps for heating up and cooling down are 3 sec/deg. For Au evaporation in our experiments, the temperature is accurately controlled at 1400^{o}C to provide a stable evaporation and deposition rate around 0.25Å/s.

2.1.4 Electron-beam Evaporation

E-beam evaporation is another form of physical vapor deposition technique, for which an ingot in a pocket is bombarded and heated by an intense electron beam under high vacuum, generating a gaseous flux of material atoms and coating the substrate in sight of the flux. Due to the accurate control and wide range of deposition rates (1 nm/min~100 um/min), efficient utilization of the material, and good control in the film morphology, E-beam evaporation has been widely used in industry and fundamental research [101]. In Fig. 2.1.7(a), a sketch is shown to explain the working principle of the E-beam evaporation setup. The deposition chamber is evacuated to a high vacuum to allow a large mean free path of the electrons, which are thermionically emitted from the tungsten filament, and pass through the chamber to reach the target ingot. High voltage (several kilovolts) between the target ingot and the tungsten filament accelerates the electrons to a high kinetic energy. Upon colliding the ingot, the electron beam transfers energy to the target atoms and thus heats the target ingot, causing it to melt, evaporate or sublimate. The atom flux generated in this way (with thermal energy, less than 1eV) then precipitates on the substrate in sight of the flux and forms the thin film. To avoid the chemical interactions between the filament and the atom flux, the filament is kept out of sight of the flux. A magnetic field is applied to steer the electron beam passing from the filament to the center of

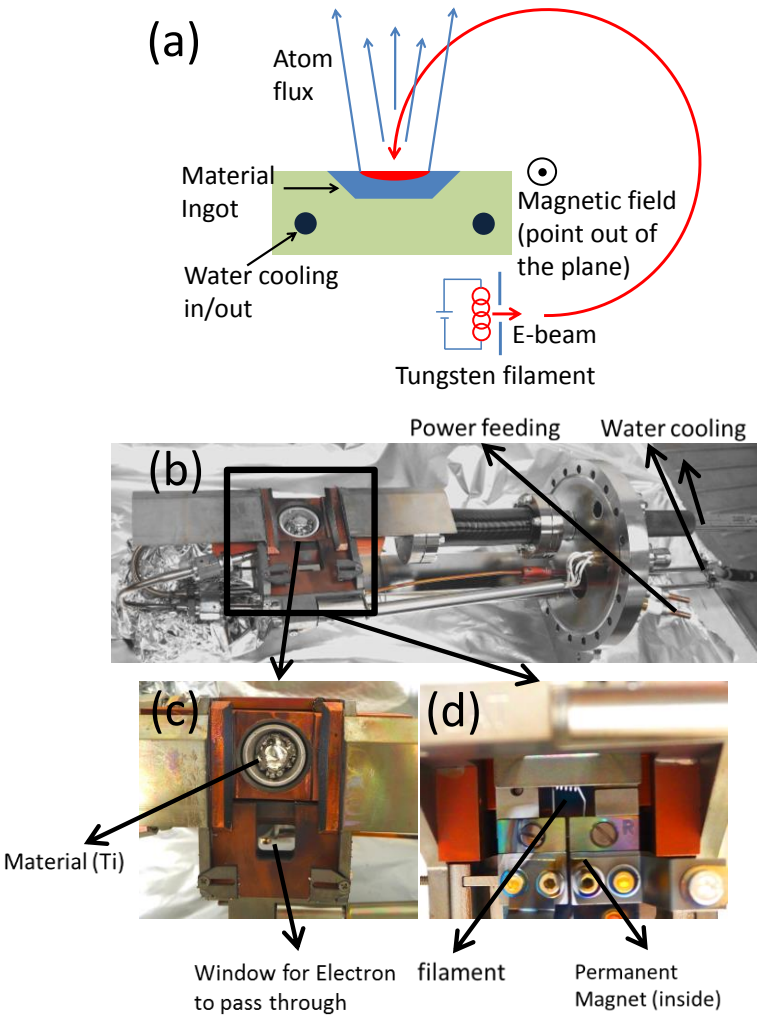

Fig. 2.1.7 (a) Sketch for the principle of E-beam evaporation. (b) E-beam evaporation component used in our MBE system. (c) Top view of material container part (amplified). A Ti ingot is inside the crucible and the deflected electrons bombard the ingot through the window. (d) Side view of (c). The electron-emitting filament is shown and the permanent magnet for deflecting the electron beams is below the filament (inside and not shown).

the ingot in a 270° arc. Usually, an additional electromagnetic coil known as the "sweep coil" is employed to focus and steer the electron beam in a defined pattern in order to heat the ingot surface more evenly, which is typically referred to "XY

sweeping". This is more important for material with a poor heat conductivity, such as SiO_2. The other advantage of the sweeping is that a larger pocket can be used to allow more material to be evaporated in a single evaporation run without filling again the pocket and breaking the vacuum. The pocket (graphite crucible) containing the ingot as well as the magnet is cooled with water flow. Parameters controlling the deposition rate are the vacuum pressure, E-beam current, and accelerating voltage.

For our work, we use the Telemark Model 568 UHV multi-pocket E-beam source as shown in Fig. 2.1.7(b), where three pockets and crucibles containing the Co, Ti (Fig. 2.1.7(c)), and SiO_2 are available. The power is supplied with the Telemark TT-6 Cheetah E-beam source power supply, which provides the direct current (up to 750mA) and regulated high voltage power (-8~6KV), and can be operated from the controller or a remote station. The power supply is accompanied with a filament transformer to provide the power source to the electron-emitting filament with an output (max.) of 8V at 50A. The XY sweep is controlled with the Telemark electron-beam source XY Sweeper, which allows a four mode of operation (position only, triangular, circular, or spiraling) at various frequencies. For the deposition process, an accelerating voltage -7KV and different E-beam currents, ~42mA, ~45mA, and ~25mA are used for the Ti, Co, SiO_2 evaporation, respectively. The deposition rates are around 0.2 Å/s for all. For the SiO_2 deposition, the additional XY sweeping is also applied to heat the source material more evenly. To monitor the in situ deposition rate, a quartz balance is equipped within the chamber over the E-beam evaporator (Fig. 2.1.2), which is based on the sensitivity of the resonant frequency of an exposed quartz crystal to the accumulated mass of the deposited film onto its surface.

2.2 Morphological Characterization Technique

Given the morphology of the structures in nanoscale, atomic force microscopy (AFM) is a very useful tool to characterize the nanostructure in 3-dimensions, therefore for most of the work in this thesis, AFM is used for the morphological characterization.

In 1986, the AFM was developed by Binning et al, as a successor of the scanning tunneling microscope (STM, Nobel prize in Physics in 1986 for the inventors) [102]. Both of them are different versions of the scanning probe microscopy (SPM), for which typically a sharp probe (tip) is applied to scan across a sample surface and the

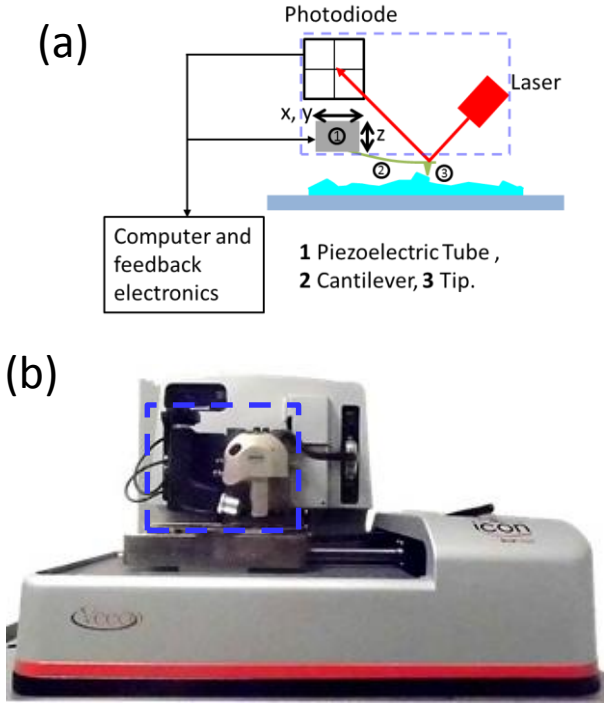

Fig. 2.2.1 (a) Sketch for the operation principle of AFM. (b) AFM system used in our experiment (Veeco^{TM} DIMENSION icon). The scanner head, squared in (b), corresponds to the squared parts in (a), namely, the laser, cantilever, piezoelectric tube, photodiode detector.

tip-surface interaction is monitored to give the morphological and the other related information of the surface, with a vertical resolution on the order of fractions of a nanometer and horizontal resolution on the order of nanometers, depending mainly on the tip radius. According to the kind of interaction monitored, a variety of SPM forms have been realized: STM and AFM as mentioned above, lateral force microscopy (LFM), magnetic force microscopy (MFM), electric force microscopy (EFM), and so on.

The working principle of the AFM is schematically shown in Fig. 2.2.1(a), as well as the Veeco^{TM} DIMENSION icon AFM microscope (Fig. 2.2.1(b)) used in our experiments. The essential part of the AFM is the cantilever (2 in the figure) with a sharp tip (3 in the figure) on its end, which scans along the surface of the sample

during the measurement.

When the tip is brought into the proximity of the sample surface, interaction forces (mechanical contact force or atomic force) between the tip and the sample lead to a deflection of the cantilever. To measure the deflection of the cantilever and thus the interaction force, a laser light is incident on to the cantilever end and reflected back to a 4-quadrant photodetector. As the cantilever is deflected vertically or laterally, the reflected laser spot on the photodetector will depart from the original position by a certain distance proportional to the cantilever deflection. The corresponding light intensities in different halves or quadrants collected by the photodetector thus give the information of the cantilever deflection in the form of a voltage. The cantilever is held by a holder (not shown) which is connected to the piezoelectric tube (1 in Figure 2.2.1(a)) in the scanner head (blue squared in Figure 2.2.1(b)). The vertical (z-direction) and horizontal (x, y-directions) movements of the cantilever are driven and controlled by the piezoelectric tube with the electric signal from the computer. A feedback system (computer and the piezoelectric tube) is used to control the vertical (z-direction) position of the cantilever in order to keep its setpoint state. In the current case (Fig. 2.2.1), only the cantilever moves during the measurement, and the sample (also the supporting platform) keeps stationary. For some other systems the situation is reversed: the piezoelectric tube is connected to the supporting platform, and the sample (platform) moves during the measurement instead of the cantilever.

Different modes can be operated in AFM systems according to the character of the tip motion: contact, tapping, and non-contact mode. Here only the most used tapping mode in our experiments will be introduced.

In tapping mode, the tip scans across the sample surface driven by the piezoelectric tube. The cantilever is driven by an additional piezoelectric piece on the holder to oscillate vertically at or near to (usually slightly below) its resonance frequency with an amplitude typically around 20-100nm. Therefore the tip taps on the surface during the measurement and contacts the surface only at the bottom of the whole swing. Since the cantilever vibrates, the light signal collected and the voltage generated by the photodetector now is AC and sinusoidal. This voltage is rectified and low-pass filtered into a DC voltage with the lock-in amplifier, which is proportional to the cantilever oscillation amplitude. While the tip is approaching the sample surface or encounters a higher region in the surface, the interaction force between the tip and sample surface causes the oscillation amplitude (at the free state) to decrease although

the piezo piece excites the cantilever with the same energy. While the tip ascends or encounters a lower region, the amplitude increases. By setting a "setpoint" amplitude (actually the setpoint DC voltage), the feedback system will compare the actual amplitude to the setpoint, and subsequently, the vertical position of the cantilever at each (x, y) point is controlled by the piezoelectric tube to recover its "setpoint" oscillation amplitude. This vertical position is recorded by the computer to form the morphological image of the sample surface. This way, the tip-sample interaction is maintained constant during the imaging process. Changing the setpoint amplitude thus modifies the amount of force applied to the sample surface. This tapping mode has a high lateral resolution (1nm to 5nm). The typical oscillation amplitude (20-100nm) allows the tip to contact the surface through the adsorbed fluid layer on the sample surface without getting stuck. Since the contact between the tip and the sample is not continuous, one advantage of the tapping mode is the reduction of the frictional forces which can damage both the tip and sample.

Besides the oscillation amplitude, the phase of the cantilever oscillation can also be recorded and compared with the driving signal, which is sensitive to the material properties and can provide additional information of the sample. Silicon cantilevers with a tip radius around 10 nm from NanoSensors^{TM} are used.

2.3 Optical Characterization Techniques

For optical characterization, an optical microscope combined with a spectrometer is used for the unpolarized transmission measurements and spectroscopic ellipsometry (SE) is used for the polarized optical extinction measurements. Besides, with SE data and appropriate construction of the optical model, the optical constants of the nanostructures can be extracted.

2.3.1 Optical Microspectroscopy

For unpolarized optical extinction measurement of nanostructures, we use an optical setup consisting of an optical microscope (OLYMPUS BX51, Fig. 2.3.1(a)) and a spectrograph (Andor Shamrock SR-303i-B, Fig. 2.3.1(b)) which are connected with an optical fiber.

As a multifunctional optical microscope, the OLYMPUS BX51 model provides the optical imaging of bright/dark field, fluorescence, polarized light etc., by integrating all the optical components together compactly [103]. Bi-directional light incidence is allowed with two individual light sources: for reflection measurement, the light from a halogen lamp is incident from the top of the sample; for transmission measurement, another halogen lamp illuminates from the bottom. For our unpolarized extinction measurement, the transmission mode is chosen and light incident from the bottom passes through a series of optical components such as lens, filters, mirrors, field diaphragm and condenser, and at last is focused onto the sample. The light transmitted through the sample is then collected by the objective and sent to the oculars for observation or to the spectrometer through the optical fiber for the wavelength-resolved intensity measurement.

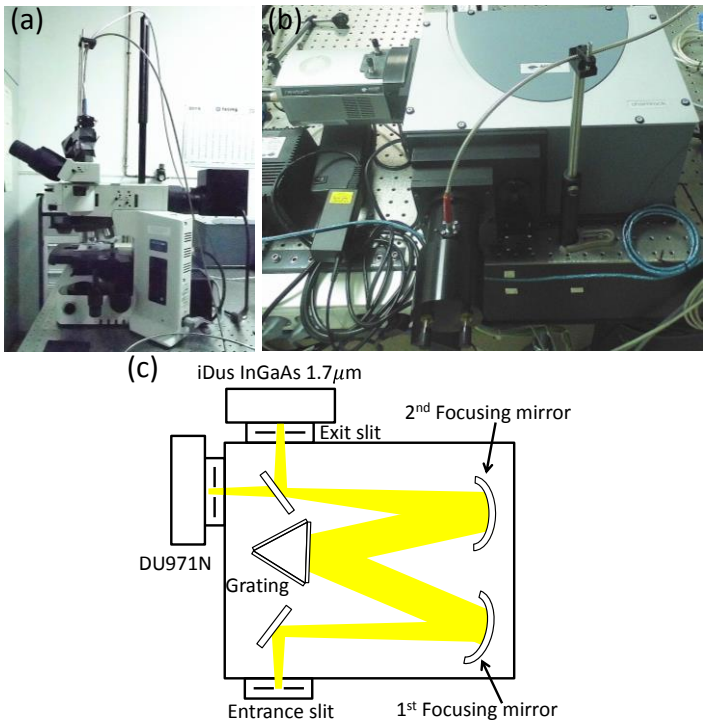

Fig. 2.3.1 Photographs of (a) OLYMPUS BX51 optical microscope and (b) Andor Shamrock SR-303i-B spectrograph. (c) The unfolded Czerny-Turner configuration for the spectrograph.

The Andor Shamrock SR-303i-B model spectrograph is an unfolded Czerny-Turner configuration optical bench with a focal length of 303mm and dual exit slit (Fig. 2.3.1(c)) [104]. The 1st focusing mirror has a focal length such that it can collimate the light emitted from the entrance slit, that is, the light beam reflected from the 1st focusing mirror becomes parallel. The collimated light beam is then directed onto the diffracting grating (300 line/mm ruled, 500nm blaze for visible and 1200nm blaze for near infrared range), where the light is dispersed and the chromatic components are directed to different directions. The dispersed light is then focused by the 2nd focusing mirror onto the detector plane, where an Andor Newton DU971N electron multiplying CCD is used for the visible wavelength range and an Andor iDus InGaAs 1.7μm array detector is used for the near-infrared (NIR) range.

For extinction measurements, the transmission mode is usually used with a bare glass substrate as the reference. Transmitted light intensities are recorded for both the nanostructure sample on the glass (I_s) and the reference glass (I_{ref}), as well as the background signal (I_{back}) of the system. The optical extinction is expressed as

$$Ext. = 1 - \frac{I_S - I_{back}}{I_{ref} - I_{back}} \qquad 2.3.1$$

2.3.2 Spectroscopic Ellipsometry

Spectroscopic ellipsometry (SE) is a fast, non-destructive, extremely sensitive and versatile characterization technique for the determination of the optical properties of the sample, and has been widely applied in the *in situ* and *ex situ* measurements in material deposition, etching, oxidation, thermal annealing situations [105]. Optical and material properties of the sample such as the refractive index, dielectric constants, absorption coefficient, optical anisotropy, film thickness (single or multiple layers), doping concentration, surface and interfacial roughness, etc., can be in principle determined in a single measurement and analysis loop.

SE measures the relative phase change in a reflected polarized light, therefore the sensitivity exceeds that of an intensity measurement. As a convenience, no special reference samples are needed because the absolute intensity of the reflected light is

not necessary to be measured, which actually improves further the accuracy of the SE. Combined with variable angle of light incidence, SE can be even more powerful, allowing to acquire large amounts of data from a given sample, and subsequently to determine the parameters such as layer thickness and optical constants more precisely, compared with single angle measurements.

However, similar to other optical characterization techniques, SE never measures the sample parameters of interest directly, rather measures some quantity that is a function of the parameters of interest. Therefore, the realization of the extraordinary sensitivity of the SE requires that the experimental data must be fit to an optimized model with the fitting parameters providing the desired information of the sample. The whole procedure can be divided into four steps, as shown in Fig. 2.3.2 below. In the following, we will discuss how the optical measurement and analysis of the data are carried out.

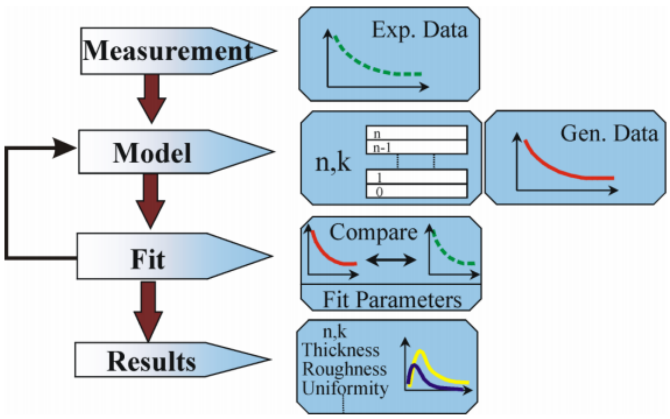

Fig. 2.3.2 SE data analysis flowchart. After the measurement, an optical model describing the sample is established, then the generated data from the model are compared and optimized (both automatically and manually) to fit the experimental data. When the optical model fits the experimental data best and the mean square error (MSE) reaches its minimum, optical parameters and material parameters of the sample are derived from the model. Adopted from Ref. [107].

SE Measurement and Analysis

Light field incident to the sample can be separated into two orthogonal components,

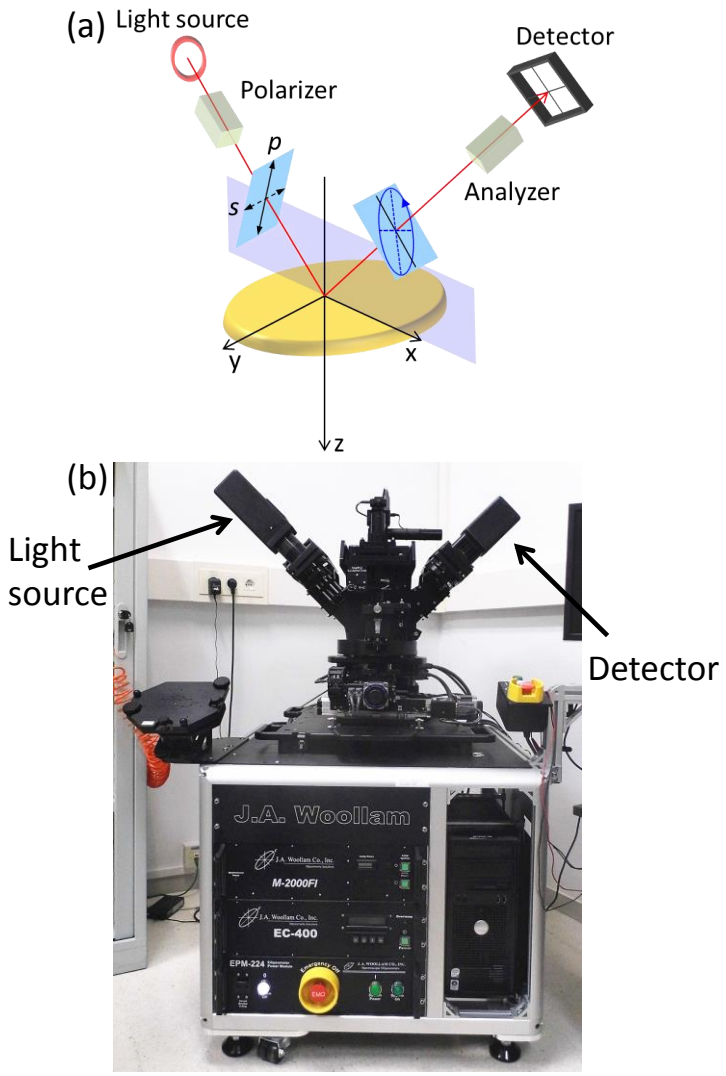

Fig. 2.3.3 (a) General configuration of an ellipsometer. (b) Spectroscopic ellipsometer (M2000Fi J. A. Woollam Co.™) used in the experiments.

as shown in Fig. 2.3.3(a): the p-polarized light parallel and s-polarized light perpendicular to the incidence plane, respectively. For p- and s-light, the sample has different reflection coefficients r_p and r_s. After reflection, the ratio between these two reflection coefficients can be expressed as,

$$\rho = \tan(\psi)\, e^{i\Delta} = \frac{r_p}{r_s}, \qquad 2.3.2$$

with ψ and Δ the angles representing the amplitude ratio and phase difference between the reflected p- and s-light. For transmission measurement, the reflection coefficients are substituted by the transmission coefficients. The spectroscopic ellipsometry is designed to measure the (ψ, Δ) angles for each wavelength in an accurate and reproducible way.

Generally, all the ellipsometers have in common a light source, a polarizer to generate the linearly polarized light before the sample, a polarizer working as an analyzer after the sample, and a detector to measure the intensity of the light (Fig. 2.3.3(a)). The M2000Fi J. A. Woollam Co.™ system (Fig. 2.3.3(b)) used has a Xenon (Xe) lamp as the light source and CCD array as the detector, covering the spectral range from visible to the near infrared (400nm~1700nm). The light is dispersed onto the CCD detector array to allow the spectroscopic measurements simultaneously. Typical measurement time is a few seconds.

Different methods have been applied to modulate the incident or reflected light in order to generate a sinusoidal signal to be detected by the detector and extract the (ψ, Δ) angles, such as the polarization modulation ellipsometers (PME), rotating polarizer/analyzer ellipsometers (RPE/RAE), etc. For our M2000Fi J. A. Woollam Co.™ system, a compensator rotating during the measurement (not shown in Fig. 2.3.3(a)) is inserted into the light beam path, which is denoted as rotating compensator ellipsometer (RCE) configuration. This configuration has many advantages: accurate measurement of (ψ, Δ) over the complete range ($\psi = 0 - 90°, \Delta = 0 - 360°$), no residual input/output polarization sensitivity, and the ability of direct measurement of depolarization effects. The signal analysis process is similar to the polar MOKE system which will be discussed in the next section [106].

The (ψ, Δ) data measured in different wavelength ranges can be used to determine different optical and material properties of the sample. For example, the film thickness can be inferred with the optical interference in the less absorptive wavelength range, usually the lower energy part. In the high energy region of the spectra, the light absorption generally increases and the penetration depth of light becomes smaller, thus the optical interference is negligible. However, band structure and surface roughness can be studied within this region.

For an ideal bulk sample with a flat surface, the optical constants can be extracted with the equation [107],

$$\varepsilon = \varepsilon' + i\varepsilon'' = (n + ik)^2 = \sin(\varphi)^2 \left[1 + \tan(\varphi)^2 \left(\frac{1-\rho}{1+\rho}\right)^2\right], \quad 2.3.3$$

where φ is the incidence angle of the light and ρ is defined in Eq. 2.3.2. However, the ideal bulk case is rarely met in the real sample due to the oxidization, surface roughness or overlayer, thus the optical constants ε', ε''or n, k can not be directly extracted from the ellipsometric data and an optical model describing the sample should be constructed for further analysis. For example, a layered optical model can be established with each layer parameterized by its thickness and optical constants, considering the main characteristics of the sample, such as the surface roughness, graded optical constants, substrate, etc. As the simplest case, in Fig. 2.3.4 we show a thin film on top of an optically thick substrate, where the incident polarized light experiences multiple reflections and refractions in the thin film.

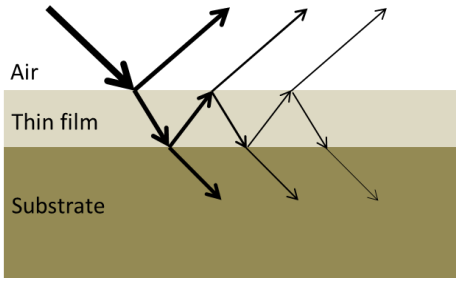

Fig. 2.3.4 The simplest optical model of the sample with one thin film on the optically thick substrate.

A most instructive way to solve this problem (to obtain the (ψ, Δ) angles of the reflected light) is based on the summation of all reflected beam components [105,106]. In principle, there are infinite number of reflected and transmitted beams, however the splitting of the beam into reflection and transmission, as well as the absorption (if there is any) will reduce and attenuate the light beams quickly as they propagate in the thin film. The Fresnel reflection and transmission coefficients for each of the split light beam components, which are function of the refraction indices of the media and

the incidence angle, can be calculated for either p- or s-polarized light with the help of Snell's law. After this, each of the reflected light components from the surface of the thin film back to the ambient air can be calculated and summed together to obtain the total reflected beam, with which the total (pseudo) Fresnel reflection coefficients r_p and r_s can be calculated by normalizing to the incident light beam. Therefore the (ψ, Δ) angles can be extracted from this model according to Eq. 2.3.2. Similar process can also be applied to the transmitted light.

For multilayers, or graded films, the above method is still applicable, but with greatly increased difficulty in the calculation. Therefore transfer matrix method [108] may be more suited to this case. For composite materials and roughness, the effective medium approximations (EMA) can also be applied [36,109].

The generated data of (ψ, Δ) are then compared with the measured SE data. If the model is a good representation of the sample so that all the necessary parameters are considered properly, the generated data will be in good agreement with the SE data. To estimate the quality of the match between the generated data and the measured data, as well as to improve the accuracy of the optical model, error evaluation and optimization of the model are important. Different methods have been proposed for this [105]. In the CompleteEASE™ software which accompanies our M2000Fi J. A. Woollam Co.™ ellipsometer system, the error is estimated with the MSE (mean square error) and expressed as,

$$\mathrm{MSE} = \sqrt{\frac{1}{3j-m}\sum_{i=1}^{j}[(N_{Ei}-N_{Gi})^2 + (C_{Ei}-C_{Gi})^2 + (S_{Ei}-S_{Gi})^2]} \times 1000, \qquad 2.3.4$$

where j is the number of the measured wavelength, m the number of the fit parameters, $\mathrm{N} = \cos(2\psi)$, $\mathrm{C} = \sin(2\psi)\cos\Delta$, $\mathrm{S} = \sin(2\psi)\sin\Delta$, and the subscriptions Ei and Gi represent the experimental and generated data, respectively. The lower the MSE value, the better the fit between the measured and model generated SE data.

Besides the smallest MSE value, a good optical model should also be unique, and the model fit parameters must be physical. It is always possible to reduce the MSE by adding more layers and/or fit parameters to the model, but unless the MSE is significantly reduced, the simplest model should be chosen, and the additional model

complexity is not justified.

2.4 Magneto-optical Characterization

2.4.1 Polar Magneto-optical Kerr Effect

To measure the complex polar Kerr rotation (Kerr rotation and ellipticity) in the fabricated nanostructures, we use a home-made setup for polar magneto-optical Kerr effect spectroscopy (p-MOKE) with the polarization modulation technique, which allows the simultaneous measurement of the Kerr rotation and ellipticity with a high sensitivity. The scheme of the setup is shown in Fig. 2.4.1(a), for which the light is incident at a nearly normal angle (<3°) to the sample surface. With varied magnetic field, the setup allows measuring the MO hysteresis loops at a particular wavelength, and with the magnetically saturated sample, it allows the measurement of MO spectra from visible to near infrared range. The setup used in our experiments is shown in Fig. 2.4.1(b).

As schematically shown in Fig. 2.4.1(a), the light is coming from a Xenon lamp. After reflected by a series of concave mirrors (not shown), the light is focused onto the entrance slit of the monochromator (SpectraPro-2150i, Acton Research Corporation), which has the 150mm focal length, dual indexable gratings of 600 grooves/mm (1000nm blaze) and 1200 grooves/mm (500nm blaze), and a spectral resolution of 0.4nm or better for the 10μm wide by 4mm high slits and the standard 1200 grooves/mm grating. The light with selected wavelength by the monochromator is polarized by the first polarizer P_1 with the principal axis oriented 45^o with respect to the setup in-plane (p-direction). Subsequently, the linearly polarized light is modulated periodically by the photoelastic modulator M (PEM-90 model) between the linear and circular polarization states. The modulation frequency is ω_m with the phase-shift amplitude φ_0, therefore the instant phase shift is $\varphi = \varphi_0 \sin(\omega_m t)$. The modulated light is then focused onto the sample (S) which is located between the two poles of an electromagnet, with the magnetic field perpendicular to the sample plane (polar configuration). The maximum magnetic field H applied in our experiments is 1.2 T. The light reflected by the sample surface is focused onto the second polarizer P_2, which is used as the analyzer and also for the calibration of the system with its

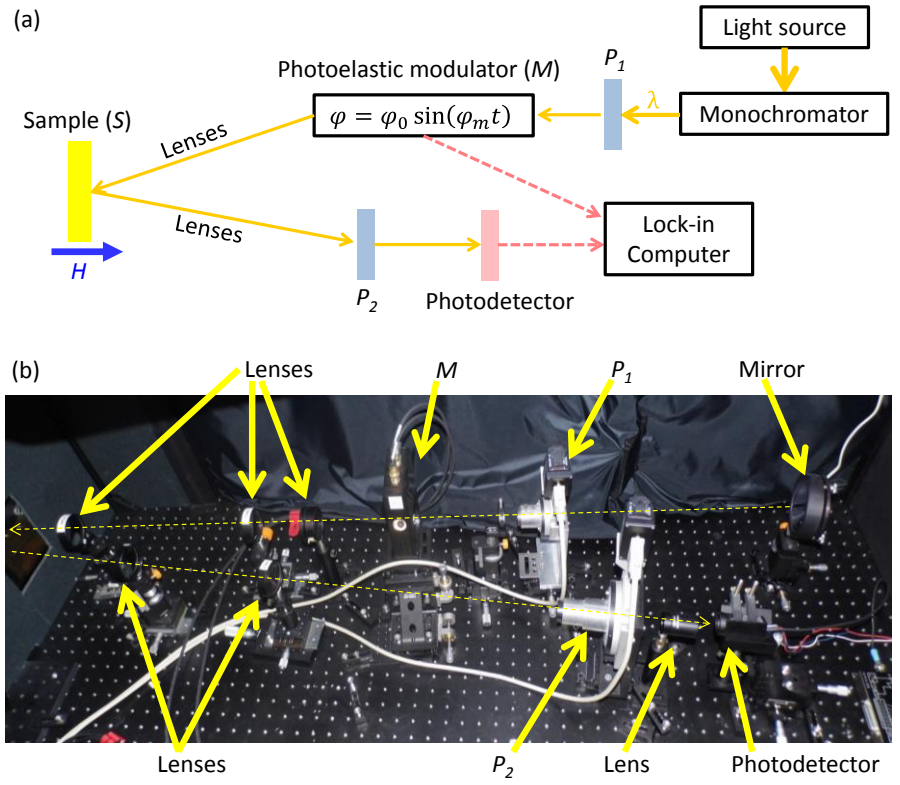

Fig. 2.4.1 (a) Schematic sketch for the home-made p-MOKE. P_1 and P_2 are the polarizers working as the initial polarizer and analyzer, respectively. (b) Photograph of the setup used in our experiments. Dashed yellow lines show the light path.

principal axis adjustable by an angle β from the p-direction. At last, the polarized beam impinges in the photodetector (photomultiplier for the 400-800nm, and InGaAs photodiode for 800-1500nm) connected to a current multiplier, which converts the current into voltage and amplifies the signal. The amplified signal and the reference frequency signal from the photoelastic modulator are sent to and filtered in the two lock-in amplifiers, and then compared and analyzed with a computer program in order to obtain the Kerr rotation and ellipticity data.

To describe the system mathematically, Jones matrix is applied to represent each

optical component. The electric field $\overrightarrow{E_r} = \begin{pmatrix} E_{r,p} \\ E_{r,s} \end{pmatrix}$ of the detected light can be expressed with the incident light field $\overrightarrow{E_i} = \begin{pmatrix} E_{i,p} \\ E_{i,s} \end{pmatrix}$,

$$\overrightarrow{E_r} = P_2 \cdot S \cdot M \cdot P_1 \cdot \overrightarrow{E_i}, \qquad 2.4.1$$

The Jones matrices for each optical component and the sample are

$$P_1 = \frac{1}{2}\begin{pmatrix} 1 & 1 \\ 1 & 1 \end{pmatrix},$$
$$M = \begin{pmatrix} e^{i\varphi/2} & 0 \\ 0 & e^{i\varphi/2} \end{pmatrix},$$
$$S = \begin{pmatrix} r_{pp} & r_{ps} \\ r_{sp} & r_{ss} \end{pmatrix},$$
$$P_2 = \begin{pmatrix} \cos^2\beta & \sin\beta\cos\beta \\ \sin\beta\cos\beta & \sin^2\beta \end{pmatrix}, \qquad 2.4.2$$

where the Fresnel coefficients in the reflectivity tensor of the sample *S* are,

$$r_{pp} = |r_{pp}|e^{i\delta_{pp}},$$
$$r_{ss} = |r_{ss}|e^{i\delta_{ss}},$$
$$r_{ps} = -r_{sp} = |r_{ps}|e^{i\delta_{ps}} = -|r_{sp}|e^{i\delta_{sp}}.$$

Assuming the light incidence from the monochromator is unpolarized with the intensity I_i, the detected light intensity by the photodetector can be obtained now from Eq. 2.4.1,

$$I_r = |E_{r,p}|^2 + |E_{r,s}|^2 = \frac{1}{2} I_i(A + B\cos\varphi + C\sin\varphi), \qquad 2.4.3$$

with the coefficients A, B and C are given by (when $\beta = 0$),

$$A = |r_{pp}|^2 + |r_{sp}|^2,$$

$$B = -2|r_{sp}||r_{pp}|\cos(\delta_{pp} - \delta_{sp}),$$
$$C = 2|r_{sp}||r_{pp}|\sin(\delta_{pp} - \delta_{sp}), \quad 2.4.4$$

Therefore from Eq. 2.4.3 and Eq. 2.4.4 the detected light intensity is a function of the phase shift φ introduced by the photoelastic modulator. This phase shift presents a sinusoidal function of its modulating frequency ω_m as mentioned earlier, thus its sine and cosine functions can be extended as the Fourier series,

$$\sin\varphi = \sin(\varphi_0 \sin(\omega_m t)) = 2J_1(\varphi_0)\sin(\omega_m t) + 2J_3(\varphi_0)\sin(3\omega_m t) ...,$$
$$\cos\varphi = \cos(\varphi_0 \sin(\omega_m t)) = J_0(\varphi_0) + 2J_2(\varphi_0)\cos(2\omega_m t) + \cdots, \quad 2.4.5$$

where $J_i(\varphi_0)$ with $i = 0, 1, 2$ ... are the Bessel functions of the *i*th order at φ_0. With Eq. 2.4.5, the detected light intensity normalized to the incident light intensity finally reads,

$$\frac{2I_r}{I_i} = I_0 + I_1\sin(\omega_m t) + I_2\cos(2\omega_m t) + I_3\sin(3\omega_m t) ..., \quad 2.4.6$$

where I_0, I_1, and I_2 are the intensities for the DC, first and second harmonic signals detected by the computer and lock-in amplifiers,

$$I_0 = A + BJ_0(\varphi_0),$$
$$I_1 = 2CJ_1(\varphi_0),$$
$$I_2 = 2BJ_2(\varphi_0), \quad 2.4.7$$

and *A*, *B* and *C* are the coefficients defined in Eq. 2.4.4.

The Kerr rotation and ellipticity defined as Eq. 1.2.7 for p-polarized light is

$$\Phi_{k,p} = \theta_{k,p} + i\varphi_{k,p} = \frac{r_{sp}}{r_{pp}} = \frac{|r_{sp}|}{|r_{pp}|}e^{i(\delta_{sp} - \delta_{pp})}, \quad 2.4.8$$

where the Fresnel coefficients in Eq. 2.4.2 have been inserted. Therefore by normalizing the first and second harmonic signals detected by the lock-in amplifiers

to the DC one in Eq. 2.4.7,

$$\frac{I_2}{I_0} = -4J_2(\varphi_0)\frac{|r_{sp}|}{|r_{pp}|}\cos(\delta_{sp} - \delta_{pp}) = -4J_2(\varphi_0)\theta_{k,p},$$

$$\frac{I_1}{I_0} = 4J_1(\varphi_0)\frac{|r_{sp}|}{|r_{pp}|}\sin(\delta_{sp} - \delta_{pp}) = 4J_1(\varphi_0)\varphi_{k,p}, \qquad 2.4.9$$

for which it is assumed that $|r_{sp}| \ll |r_{pp}|$, and $J_0(\varphi_0)\sim 0$ at a specific φ_0 angle. By now we notice that the normalized signals detected by the lock-in at ω_m and $2\omega_m$ directly yield the Kerr ellipticity and rotation, respectively. In addition, by taking ratios of two signals measured simultaneously, fluctuations due to the instabilities of the light source and of the optical setups are then efficiently eliminated. However, the values of $J_2(\varphi_0)$ and $J_1(\varphi_0)$ can not be calculated since the phase-shift φ_0 introduced by the photoelastic modulator varies upon the wavelength. Therefore calibration of the $J_2(\varphi_0)$ and $J_1(\varphi_0)$ values at each wavelength is necessary. For this, the adjustments in the β angle of the second polarizer P_2 [110] and the amplitude of the phase shift φ_0 introduced by the photoelastic modulator, as well as the insertion of a compensator into the optical path [110], or calibration with a bulk sample whose ellipticity is known (e.g. Ni bulk sample) [111], can be applied.

By setting $\beta = \frac{\pi}{2}$, the complex Kerr rotation of the sample for s-polarized light can be also derived similarly and measured with the same setup, which is useful for the samples with the in-plane anisotropy.

2.4.2 Transverse Magneto-optical Kerr Effect

Additionally, a transverse-MOKE (t-MOKE) system has been used in selected structures to measure the in-plane hysteresis loops.

In Fig. 2.4.2(a) the schematic sketch of the system is shown, where the sample is placed between the two poles of the electromagnet, with the magnetic field applied in the sample plane. The magnetic field is controlled by the power source (voltage and current) for the electromagnet, which is further controlled by a frequency generator providing the sinusoidal functions. Therefore the magnetic field in the t-MOKE setup

is oscillating in a sinusoidal way and is probed by a magnetic field probe. The probed signal of the magnetic field is sent to the digitizing oscilloscope and the computer program where it will be used as the abscissa axis of the hysteresis loop. The setup used in our experiments is shown in Fig. 2.4.2(b).

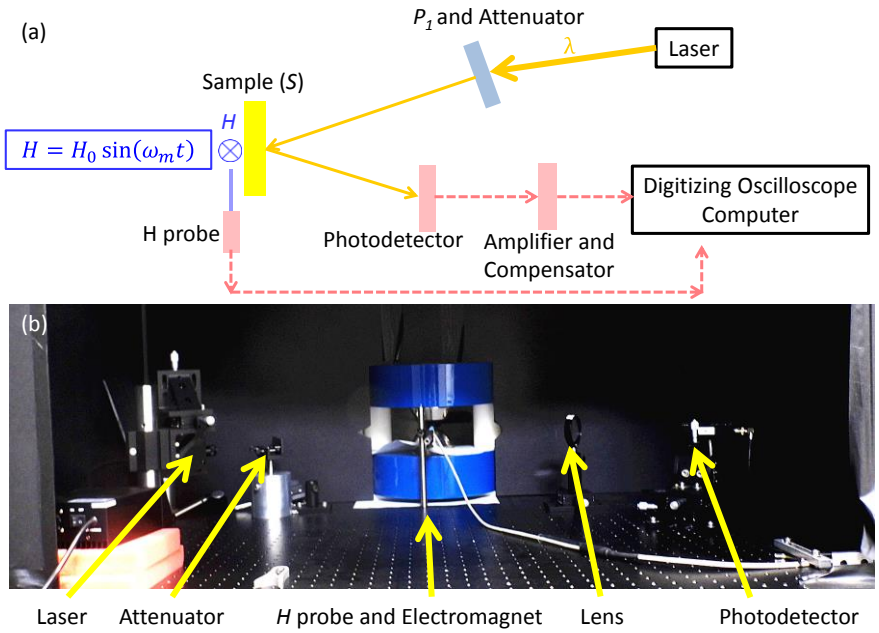

Fig. 2.4.2 (a) Scheme of the t-MOKE system. P_1 is a polarizer for p-light generation. (b) Photograph of experimental setup used in our measurements.

The light from a laser source passes through firstly an optical attenuator and then the polarizer P_1 with its principal axis oriented along p-direction. The p-polarized light is reflected by the sample, and reaches the photodetector. As the magnetic field varies, the reflected light intensity will vary simultaneously. The detected light signal will be amplified by a preamplifier and later sent to a compensator to compensate the DC signal inside, therefore only the AC signal oscillating with the magnetic field is left. This AC signal is sent to the digitizing oscilloscope and computer as the vertical axis which is the transverse MO signal and represents the magnetization variation in the hysteresis loop for ferromagnetic material. The trigger signal from the frequency generator is used for the synchronization of the system, namely, the magnetic field,

digitizing oscilloscope and the computer program. Usually, the measured t-MOKE signal (namely, the hysteresis loops) will be averaged over 100 times to minimize the error and noise.

Chapter 3

Hole-mask Colloidal Lithography: Method and Optimization

Hole-mask colloidal lithography (HCL) is a truly versatile and simple bottom-up nanofabrication method, which is based on the colloidal lithography concept proposed in 2007 [35]. Similar to the nanosphere lithography, for which evaporation through the empty spaces between organized hexagonal close-packed 2D colloidal crystals defines the resulting pattern, the HCL method uses an Au thin film with nanoholes inside and supported by the sacrificial layer as a mask (thus is termed as hole-mask) to define the pattern during the evaporation and/or etching processes (Fig. 1.5.1). The nanoholes are made with colloidal lithography and the sacrificial layer is used to make room for the nanostructure formation and to remove the Au hole-mask after the whole process. The HCL method provides effective means of patterning large surface areas (over cm^2 or even dm^2) with diverse functional nanoarchitectures in a simple, low-cost and high-speed way. Examples of the nanostructures fabricated with HCL include arrays of nanodisks and oriented elliptical nanostructures, nanodisk pairs (dimers), nanocones, embedded nanodisks, and the other ring related nanostructures listed in Chapter 1. These nanostructures have been applied in a series of different fields, such as the surface enhanced Raman scattering (SERS) [35], sensing [112], magnetics [113], cell adhesion studies [114] and so on. Besides low-cost and large-area fabrication, additional advantages of this method are: first, the mask formulation and thus the subsequent nanostructure are substrate-independent and all the nanostructure can be formed with the same initial mask; second, the method is material-independent, and a wide range of materials have been applied to form the nanostructures (Au, Ag, Pd, Pt, SiO_2, Co etc.); third, complex layered nanoarchitectures can be developed easily by sequential deposition.

In this thesis, combined control of azimuthal (φ) and polar (θ) orientation of the template during deposition will allow the fabrication of multicomponent structures with increasing complexity, from standard multilayer nanodisks, to rings, rings with inserted dots or sectors, and split rings on rings with inserted dots. In this chapter, the template fabrication process, the nanostructure deposition process, and the related parameter optimization will be introduced in detail.

3.1 Template Fabrication

In general, the process can be divided into four main steps (Fig. 3.1.1 and Table 2.1 in Chapter 2): (I) preparation and resist-coating of the substrate ((1-2) in Fig. 3.1.1); (II) Incubation of polystyrene (PS) spheres on PMMA ((3-5)); (III) Au mask generation ((6-7)); (IV) RIE etch ((8)). Here each step will be introduced in detail.

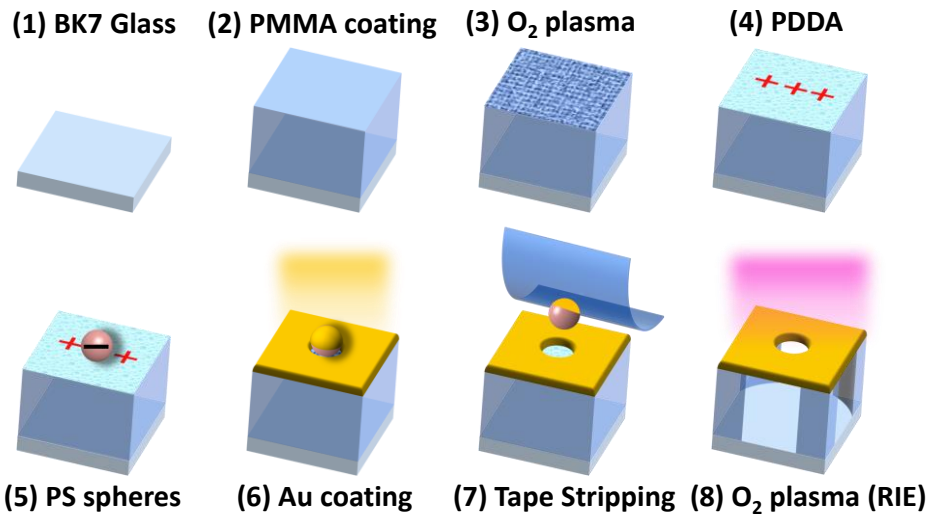

Fig. 3.1.1 Template fabrication process. The steps marked with colored squares correspond to the different images in Fig. 3.1.3. Step (1) Clean BK7 glass substrate. (2) Spin-coating of PMMA on BK7 glass. (3) PMMA surface textured by O_2 plasma. (4) Positively charged by poly-diallyldimethyl-ammonium (PDDA). (5) Polystyrene (PS) spheres incubation. (6) Au coating. (7) Tape stripping of the PS spheres. (8) RIE etching to generate cavities in the PMMA layer. Center: Nanostructure deposition with the template. At last the template is removed by lift-off in acetone and ultrasonic bath.

Step (I). Preparation and resist-coating of the substrate

In this step, the substrate (BK7 glass or silicon wafer) is cut into small squares, cleaned in an ultrasonic bath and spin-coated with poly(methyl methacrylate) (PMMA) resist.

The choice of the substrate depends on the spectral response of the nanostructure. In this thesis, most of our structures exhibit plasmonic resonance in the range from visible to near infrared, therefore the BK7 glass substrate is chosen for all the samples due to its high transparency in this range.

The glass substrate is usually cut into $1\times1cm^2$, after which a standard cleaning process is always applied to remove the possible contamination. For example, the so-called TAA process is used in our experiments: the substrate is firstly immersed into the trichloroethylene (T) and supersonically bathed for 5min at around 60℃, then followed by the similar bath process but with the acetone (A) and isopropanol (A) instead of trichloroethylene. The substrate is at last rinsed with distilled water and dried with an N_2 gas blow.

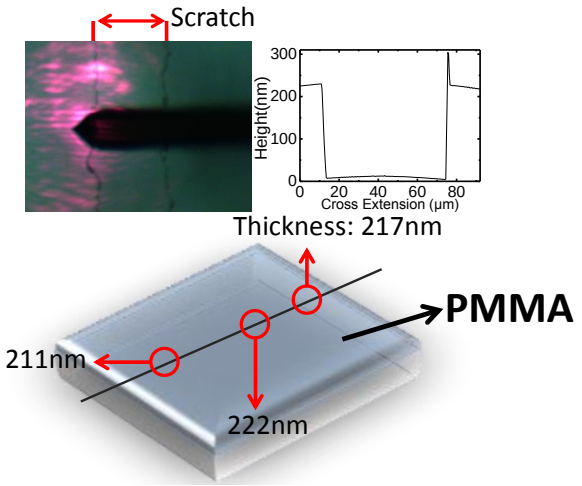

Figure 3.1.2 Thickness distribution of the PMMA layer on a BK7 glass substrate ($1\times1cm^2$) measured with AFM. The thicknesses were measured along a scratch, as schematically shown with the black line. The photographs on top show the positions of the AFM tip over the scratch during the measurements.

The cleaned substrate ((1) in Fig. 3.1.1) is spin-coated with PMMA resist ((2) in Fig. 3.1.1) of a thickness around 200nm. Typical parameters for the PMMA spin-coating process in our lab are: 40μL PMMA A4 solution, spin-speed 6000rpm for 60s, followed by a soft baking on a hotplate (180℃, 5min in air). In Figure 3.1.2 is shown the thickness distribution of the PMMA resist on a BK7 glass, being around 220 nm in the central part, and 210~215nm in the marginal part. The variation in the thickness is due to the centrifugal force during the spinning process. As will be shown in the next section, PMMA thickness is critical in the determination of the nanostructure morphology for the tilted-angle deposition process.

Step (II). Incubation of PS spheres on PMMA

In this step, the PMMA surface is textured and incubated with PS spheres ((3)-(5) in Fig. 3.1.1). In order to avoid spontaneous dewetting of the PMMA surface during the subsequent polyelectrolyte covering and particle incubation steps, the PMMA is subjected to the O_2 plasma treatment (50W, 15s, 450mtorr O_2) to reduce its hydrophobicity ((3) in Fig. 3.1.1). In Fig. 3.1.3(a) an AFM image of the PMMA surface after the O_2 plasma etching is shown.

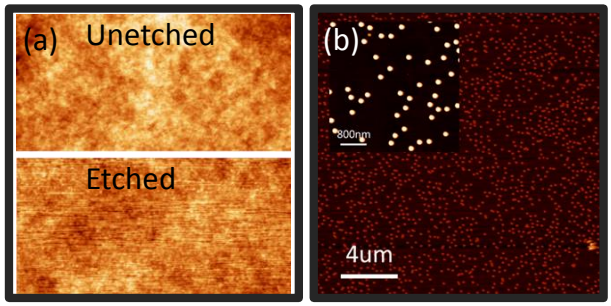

Fig. 3.1.3 (a) AFM image of the PMMA surface after O_2 plasma treatment. (b) AFM image of the typical PS sphere distribution (124nm in diameter). Inset: amplified AFM image of the same sample.

By pipetting a solution containing the poly-diallyldimethyl-ammonium (PDDA) onto the surface, the PMMA resist is functionalized with positive net charge ((4) in Fig. 3.1.1). Typical parameters for this process are: 70μL PDDA solution with the concentration of 0.02 wt.% in distilled water, 100rpm spinning for 60sec. The excess

PDDA solution is removed by carefully rinsing (1min) with de-ionized water and the substrate is blown-dried with N_2. The resulted PDDA layer has a thickness around tens of angstroms and homogeneous charge distribution on the surface according to the literature [115].

Incubation of the PS nanospheres is done by the deposition of a water suspension containing the negatively charged polystyrene (PS) nanospheres ((5) in Fig. 3.1.1). Typical parameters for this process are: 70μL PS sphere suspension in distilled water with 0.02 w/v% concentration (124nm, Microparticles GmbH), 100rpm spinning for 60sec. The electrostatic attraction between the negatively charged PS spheres and the positively charged PDDA layer causes the spheres to be incubated on the surface. Meanwhile, the electrostatic repulsion between the PS colloids defines a uniformly distributed and short-range-ordered array. Similar water rinsing (1min) and N_2 blow-drying processes are applied to remove the excess PS sphere suspension. The N_2 flow should be intense enough in order to achieve a rapid removal of the extra water and to avoid rearrangement of the PS colloids due to capillary forces during the drying process. Typical distribution of PS spheres (124nm diameter) prepared in this way is shown in Fig. 3.1.3(b).

It is easy to imagine that the solution concentrations and the deposition time determine the charge distribution and subsequently the PS sphere distribution and density on the PMMA surface, therefore the PS sphere density can be tuned and optimized accordingly. This will be discussed in detail in section 3.3.

Step (III). Au mask generation

In this step, the template is covered with Au ((6) in Fig.3.1.1), after which the PS spheres are removed by a tape-stripping process, leaving holes in the Au thin film in the area previously occupied by the PS spheres ((7) in Fig. 3.1.1)).

The Au membrane works on one hand as the resistant etch-mask to the subsequent O_2 reactive ion etching (RIE) process ((8) in Fig. 3.1.1); on the other hand, it works as the deposition or etching mask during the nanostructure formation process (central image in Fig. 3.1.1). Actually, different materials such as Au, Ag, Cr, etc. [35] have been used for this metallic mask. All the deposition methods, such as thermal evaporation, E-beam evaporation, and magnetron sputtering, can be used for the coating process but with different mechanical properties of the thin films, which will be discussed in the following sections. The Au film has a typical thickness of 30nm in

our experiments. The hole in the Au film is the projection of the PS sphere, thus the holes are patterned in the short-range order defined by the PS spheres and the hole diameter is determined by the diameter of PS sphere. The shape of the hole is determined by the deposition angle of Au. In section 3.3 control of the hole diameter and shape will be discussed in detail. The thickness of Au film is a relevant parameter for the determination of the nanostructure morphology, which will be discussed in section 3.2.

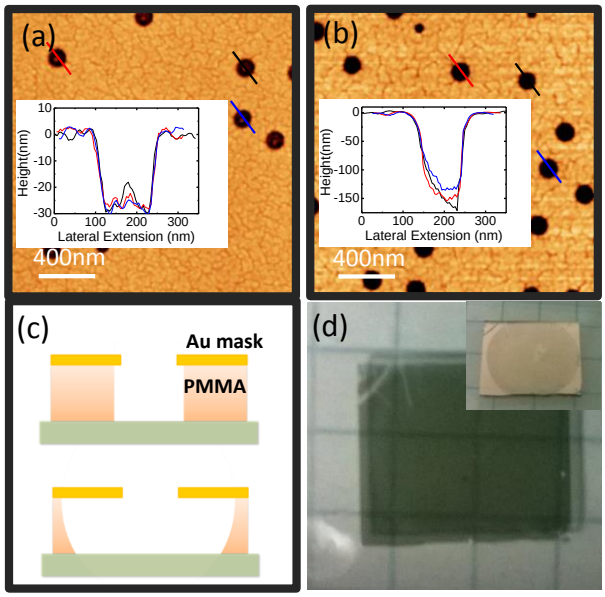

Fig. 3.1.4 (a) AFM image of the template with holes in the Au membrane after the tape stripping step. Straight lines mark the sample holes and directions of the profiles. Inset: profiles of the holes showing the thicknesses of the Au. (b) AFM image of the template after a typical 450s RIE etching. Inset: profiles of the holes. (c) Cross-sectional sketches of the templates etched normally (top) and over-etched (bottom). (d) Photo of the fabricated template (~120nm hole diameter, 30nm Au membrane, 1×1cm^2 BK7 glass). Inset: the same template but photographed with an oblique angle that the bright yellow color of the Au membrane can be appreciated.

On the other hand, Au films deposited with different methods have very different mechanical properties, therefore a minimum Au thickness is necessary to keep the

shape of the hole after the RIE etching process, especially when the PMMA layer is overetched and a part of the Au film around the hole is free-standing (Fig. 3.1.4 (c)). This factor and its effect on the nanoring formation will be discussed in detail in subsection 3.3.2.

A typical template after the tape-stripping is shown in Fig. 3.1.4(a), where the holes in the sputtered Au film with diameters around 120nm can be clearly seen. The thickness of the Au film is around 30nm, as shown in the hole profiles in the inset of Fig. 3.1.4(a).

Step (IV). RIE etch

The reactive ion etching (RIE) with O_2 is used to transfer the Au hole-mask pattern into the sacrificial PMMA layer ((8) in Fig. 3.1.1). Typical parameters for the RIE process are: base pressure 1×10^{-6} mtorr, forward power 50W, O_2 flux 50sscm/min. Within 150s of etching, the 200nm PMMA layer exposed to the plasma can be selectively and effectively removed to form cavities, leaving the template covered with a thin film mask supported by a perforated polymer film. For nanoring structure more cavity room in the PMMA layer is needed, therefore etching with longer time such as 450s is used to extend the cavities horizontally. The similar etching process is also applied in the HCL template used for the nanodisk dimers [35]. Sketches for these two kinds of templates etched with different time are schematically shown in Fig. 3.1.4(c). A representative AFM image of the template after etching is shown in Fig. 3.1.4(b), with hole profiles in the inset.

After the RIE etch, the HCL template is obtained. A photograph of the fabricated template is shown in Fig. 3.1.4(d). With an oblique angle in the inset of Fig. 3.1.4(d), the central area with nanoholes (hole-mask part) shows a darker color different from the rest part (the marginal part without holes).

The etching selectivity between the hole-mask and polymer layer leads to a partial undercut in the PMMA layer, which is perfectly suitable for the lift-off processing. After deposition process, the template will be removed by a lift-off process in acetone and supersonic bath for 2h, leaving only the nanostructures on the substrate for further characterization.

3.2 Nanostructure Fabrication with HCL Template - A Geometrical Consideration

The morphological parameters of the plasmonic nanostructure determine its optical and magneto-optical responses, therefore precise control of the deposition process and thus the nanostructure morphology are important. During the deposition process, the hole pattern in the template is transferred to the nanostructures on the substrate. In this section, the deposition process will be discussed in detail with a geometrical model (Fig. 3.2.1).

All of the nanostructures realized with the HCL template, such as the single layered or multilayered disk, disk dimer, split ring, etc., are deposited in the similar way by controlling the deposition angle θ and the rotation φ, as shown in Fig. 3.2.1 (a), where all the template parameters are listed: diameter of the hole *D*, thickness of the Au membrane *t*, thickness of the PMMA layer *T*. The resulted morphological parameters of the nanostructure can be derived via the simple trigonometry. It is worth to note that, besides the method depicted in Fig. 3.2.1, where the Au hole-mask is used as the deposition mask, the perforated PMMA layer can also be used as the deposition mask, by selective removal of the Au hole-mask with Au etchant. Precise control of the nanodisk diameter can be realized in this way, as discussed in Ref. [35**]**. Nanodisk and ring structures are deposited with different deposition angle θ, therefore we can classify the deposition process into two categories accordingly. Given the fixed parameters *T*~200nm, *t*~30nm, *D*~124nm and continuous rotation φ, for angle θ from 0^o to 16^o, the diameter of the resulted structure increases but the disk-like shape is still kept (Fig. 3.2.2(a) and Fig. 4.1.1 in Chapter 4). The diameter Φ_{disk} and height H_{disk} (Fig. 3.2.1(b)) are,

$$\Phi_{disk} = 2\mathrm{T}\tan\theta + \mathrm{D}, \qquad 3.2.1$$

$$H_{disk} = H_{disk0} * \frac{D^2}{{\Phi_{disk}}^2}, \qquad 3.2.2$$

where H_{disk0} is the height of the disk deposited normally ($\theta = 0°$), determined only

by the deposition time. In Eq. 3.2.1 and 3.2.2 we assume that the total volume of the deposit keeps the same as θ evolves and the deposit is distributed homogeneously in a cylindrical volume with the diameter of Φ_{disk}. Actually, these assumptions are very rough and the deposit is not a perfect cylinder but with a dip in the center of the disk for large enough θ and Φ_{disk} (examples for this can be found in Fig. 4.1.1 in Chapter 4, samples deposited at θ=0~16°).

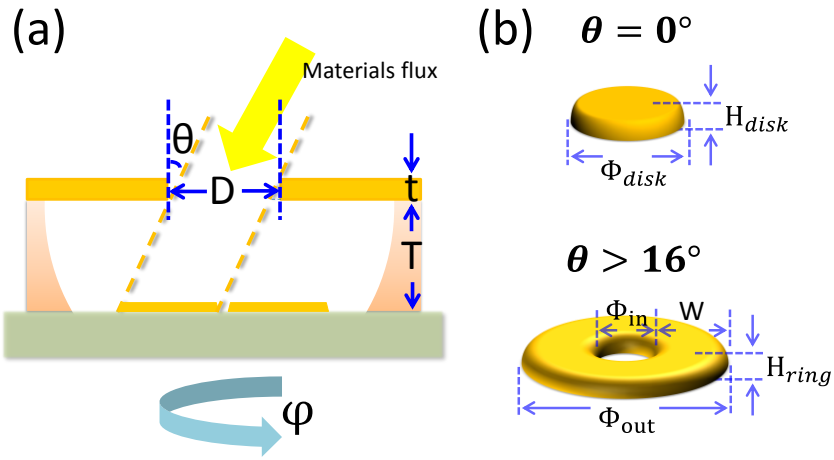

Fig. 3.2.1 (a) Sketch of the deposition process with HCL template. (b) Sketches of disk and ring nanostructures with the morphological parameters.

For $\theta > 16°$, the central dip turns out to be a hole in the center, thus a nanoring structure is formed with the outer and inner diameters Φ_{out}, Φ_{in}, arm width W, and height H_{ring} (Fig. 3.2.1(b) and Fig. 3.2.2(b)(c)),

$$\Phi_{out} = 2T\tan\theta + D, \quad 3.2.3$$

$$\Phi_{in} = \Phi_{out} - 2W = 2(T+t)\tan\theta - D, \quad 3.2.4$$

$$W = D - t\tan\theta, \quad 3.2.5$$

$$H_{ring} = H_{disk0} * \frac{D^2}{\Phi_{out}^2 - \Phi_{in}^2}, \quad 3.2.6$$

with the same assumption as in Eqs. 3.2.1 and 3.2.2. Similar calculations can be found in Ref. [116] and [97].

From the above equations, we can conclude that each parameter of the template and deposition process has their own effect on the ultimate morphology of the nanostructure and allows controlling it. For a given template, the deposition angle θ and rotation φ determine the shape of the nanostructure. In Fig. 3.2.2 we show two representative nanostructures: nanodisk (a) and nanoring (b) deposited at $\theta = 0°$ and $22°$, where the characteristic single peak and dual peaks in the cross-sectional profiles can be observed (insets). The profiles in the insets are averaged from ten different structures in each sample. The whole evolution from disk to ring will be studied in detail in chapter 4.

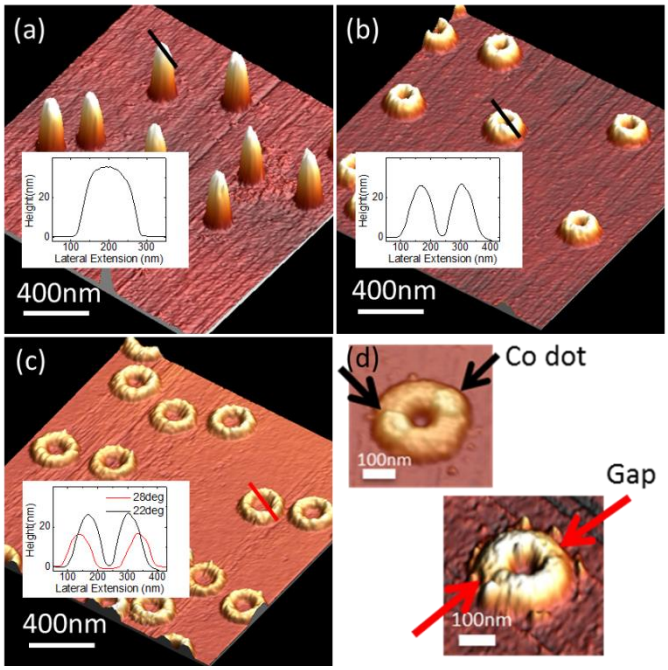

Fig. 3.2.2 AFM images of nanodisk (a) and nanoring (b)(c) structures deposited with $\theta = 0°$(a), $22°$(b) and $28°$(c), respectively. (d) AFM images of nanostructures with opposite Co-dots and Co-sectors on top of Au ring. Black arrows show the Co-dots and red arrows for the gaps between Co-sectors. Insets in (a-c): profiles along the directions shown in the AFM images, averaged from 10 different structures for each sample.

It is easy to imagine that the increase of θ and thus the diameter Φ_{out} are not

unlimited: the cavity in the perforated PMMA layer has the vertical walls (Fig. 3.1.3(e)). The largest θ realized in our experiments is $28°$ for a template with the typical parameters of T~200nm, t~30nm, D~124nm and RIE etching for 540s. The resulted nanoring is shown in Fig. 3.2.2(c), where it can be observed the outer diameter of the ring is increased (red profile in inset). Further increase in θ will deposit material onto the PMMA wall which will be lost in the lift-off process.
Moreover, with the HCL template, different materials can be deposited to form multilayered structures by changing evaporation sources (Au, Co, etc.) and each layer can be controlled independently in position and shape. For example, in Fig. 3.2.2(d) opposite Co-dots and Co-sectors are deposited onto the Au rings. The Au ring is obtained with continuous rotation φ, while the Co-dot and Co-sectors are from fixed φ and oscillating rotation of φ, respectively. Some other structures like the disk dimers, trimers, split ring can be obtained in the similar way.

In Eqs. 3.2.1-3.2.6, it is also assumed that the thickness of Au hole-mask t keeps constant during the deposition process. However, this is not fulfilled in the reality and the thickness t increases during the deposition process due to the deposit itself. On the other hand, during the deposition process, the hole diameter D is successively decreasing as a result of material deposition onto the rims of the nanoholes. This is the shrinking effect of the HCL method, which has been actually utilized to control the hole diameter in order to generate ultra tiny nanoparticles and control accurately their relative positions [116]. Both of these effects have important impacts on the nanostructure morphology, therefore we discuss them here:

1. Thickness of Au membrane *t*

For a typical nanoring structure deposited at $\theta = 24°$ with 25nm height, the increase in t after the deposition process is around 120nm (Fig. 3.2.3). From Eq. 3.2.4-3.2.6, t affects the width W of the nanoring structure and thus the inner diameter, as well as the height. For such a large increase in t, the reduction in the width of W is also large. In the case of Fig. 3.2.3, the calculated width W is reduced from 110nm to 57nm at the end of the deposition process, according to Eq. 3.2.5. This means, on the one hand, a conic shape in the ring profile when it grows higher (Fig. 3.2.2); on the other hand, a lower deposition efficiency for a larger t. In the most extreme case with a large enough t, it would be impossible (W=0) to deposit any material through the hole at a

tilted-angle θ even if the hole is not clogged. All the material would deposit onto the rim of the hole-mask but not reach the substrate.

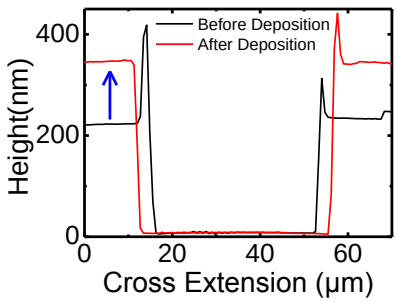

Fig. 3.2.3 Template thicknesses before (black) and after (red) the deposition process of a nanoring structure at $\theta = 24°$ with 25nm height. Measured from scratches on the template before and after the deposition. Blue arrow shows the increase in thickness.

2. Shrinking of the hole diameter *D*

During the deposition process, a part of the material will deposit onto the rims of the nanoholes, which will shrink the diameter of the hole *D*. This also contributes to the conic shape of the profiles of the nanostructures and the reduction in the deposition rate, even prevents further deposition by clogging the hole [35,116]. The shrinking rate of the hole depends strongly on the evaporation technique as well as on materials of the deposition and of the hole-mask. In our experiments with the sputtered Au hole-mask, the observed shrinking effect is not as obvious as that in the Ref. [35] and [116], as shown in Fig. 3.2.4, where only small differences in the hole diameters can be seen after such long deposition processes.

In the equations above, we also assumed that the total volume of the material deposited keeps the same during the evolution of θ. However, as discussed in both 1 and 2, this is not real. Both of the increase in *t* and shrinkage in *D* result in a smaller volume for deposition angle $\theta > 0°$, and the resulted height of the nanostructure is thus always less than the one calculated with the equations. On the other hand, the other assumption that the deposited material is distributed homogeneously in a cylindrical volume for the nanodisk structure, is not fulfilled either. As can be observed in Fig. 3.2.2(a), the nanodisks show a conic shape. This assumption would

underestimate the height of the nanostructure. Both of these two assumptions and the corresponding errors in the height estimation of the nanostructure should be considered in the fabrication and characterization of nanostructures.

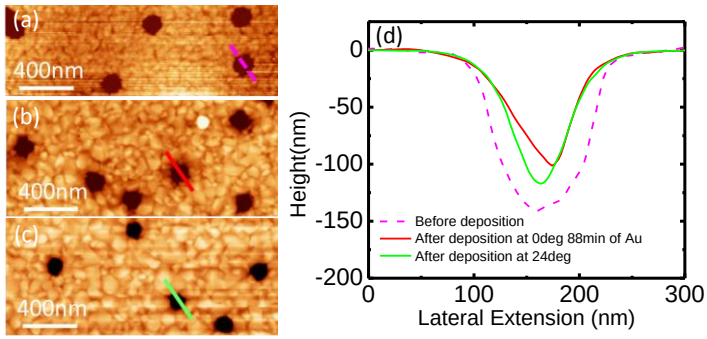

Fig. 3.2.4 AFM images of templates before (a) and after the deposition processes of nanodisk ((b), 88min of Au at $\theta = 0°$) and nanoring ((c), ~120min of Au and Co at $\theta = 24°$). (d) Profiles of the holes before and after the deposition processes. Each profile is averaged from 10 different holes of each template. Dashed and solid lines in (a-c) show the measured directions of the profiles.

3.3 Template Optimization

As seen in sections 3.1 and 3.2, all the template parameters have their effects on the deposited nanostructures. For example, the density of the nanostructure is determined by the hole and PS sphere density in the template, the shape of the nanostructure has the impact from the shape of the hole, etc. In this sense, it is necessary to find appropriate approaches to control and optimize these template parameters. In this section, we will discuss how to control and optimize the PS spheres density, the effect of Au membrane thickness on the nanostructure formation, and its optimization. The effect of the hole diameter and shape, as well as their optimization, will be discussed in Appendix 2.

3.3.1 PS Sphere Density

In the HCL template fabrication, the PS spheres are self-organized on the PMMA surface, and work as the lithographic mask for the generation of the nanoholes in the Au film. The HCL method thus benefits from the self-assembly process with the advantages of large entity number and large area. This makes the HCL method especially suited for the applications like the biosensors, biomaterials, and catalysis, where a very large number of nanometric features are required to produce measurable signals or create useful devices.

In this thesis, the HCL is used to generate the nanoring structure, which extends horizontally and thus has a larger outer diameter than the hole in the template. This means that there is an upper limitation of the hole density, and a further increase in it would cause the touching between the neighboring rings. On the other hand, the nanorings should also have a minimum density so that a measurable signal can be detected in the optical and magneto-optical characterizations. Therefore an appropriate density of the PS nanospheres and thus nanoholes in the template should be found.

The self-assembly process is conducted under the influence of electrostatic sphere-sphere (repulsive) and sphere-film (attractive) interactions, which results in the short-range-ordered structures described by the random sequential adsorption model (RSA) [117]. The inherent randomness of the initial adsorption step of particles causes the uniformity over large surface areas.

Given enough time the adsorbed PS spheres will ultimately reach a saturation density and coverage. Therefore the adsorption process and thus the saturation density are affected by a variety of interactions like particle-particle, particle-surface interactions, hydrodynamic interactions and diffusion. By affecting these interactions, important factors controlling the saturation density and coverage of the PS spheres are the concentration of the PDDA solution, pH of the PS sphere suspensions, sphere surface charges, sphere size and polydispersity.

Although it has been found in the literature that the PS sphere concentration in the suspension has no effect on the saturation density, in our results we found it did affect the density, possibly due to the short incubation time (1min) in our process. As a comparison, in Ref. [117], the saturation time is typically 5min and longer. The

interruption of the adsorption process before the saturation coverage is reached thus can be used to reduce the density, but with a sacrifice of the distribution homogeneity. For our experiments, the optical and MO responses are averaged effects of a collection of millions of the nanostructures over a large area of the sample (>1mm^2), therefore the local homogeneity is not so critical.

In total, we choose 3 parameters to control the PS sphere density: the concentrations of the PS suspension and PDDA solution, and the incubation time of the PS spheres.

To study the concentration effect, the deposition time for 70μL PDDA solution and incubation time of the 70μL PS spheres suspension is both 60s, as well as with 100rpm spinning. The concentration of PS sphere suspension is varied from 0.0001% to 0.2 w/v % and the concentration of PDDA solution is varied from 0.02% to 2 v/v %.

In Fig. 3.3.1 are shown the AFM images of PS sphere distributions with the varying solution concentrations and they are summarized in Table 3.3.1. As PS sphere concentration increases (along the rows) or the PDDA concentration increases (along the columns), the density is increasing and the distribution is getting homogeneous. The better homogeneity for the higher concentrations of PS sphere and PDDA solutions means that a shorter time is needed to reach the saturation coverage in such cases. For a low concentration of PS sphere suspension within the range of 0.0001~0.02 w/v %, the PS sphere concentration has a larger influence on the ultimate distributions than the PDDA concentration. PS sphere concentrations of 0.0001~0.001 w/v % result in a very low PS sphere density. Further increase in the PS sphere concentration (>0.02 w/v %) results in a larger density and more homogeneous distribution, but more dimers or multimers will appear, which is unwanted for the experiment. For a higher PDDA concentration ($\geq$0.2 v/v %), the problem of multimers becomes even more serious. In Table 3.3.1, the number of the nanoparticles in the AFM image, the first neighbor distance (FND), and the area coverage are shown, where the FND is important for nanoring generation as nanoring has a horizontal extension than the nanodisk.

For the PS sphere concentration 0.02 w/v % and PDDA concentration 0.02 v/v %, the FND is 330nm (from the 20×20μm^2 AFM image), which is enough for the deposition of nanoring with diameter around 300nm. It should be noted that due to the limited radius of the AFM tip, the FND is underestimated, namely, the real FND is larger than

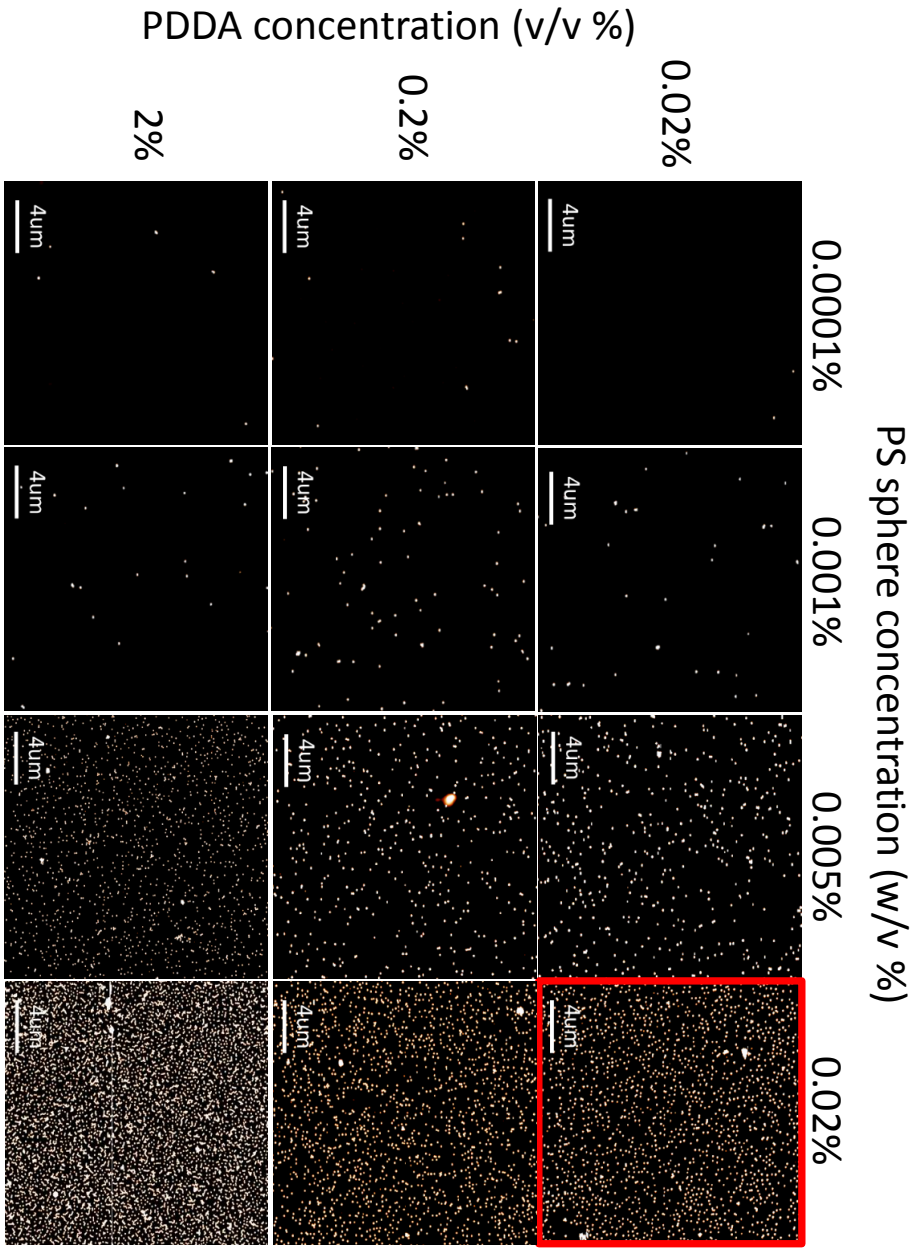

Fig. 3.3.1 (to be continued) AFM images of PS spheres distribution controlled by the concentrations of PDDA solution and PS sphere suspension.

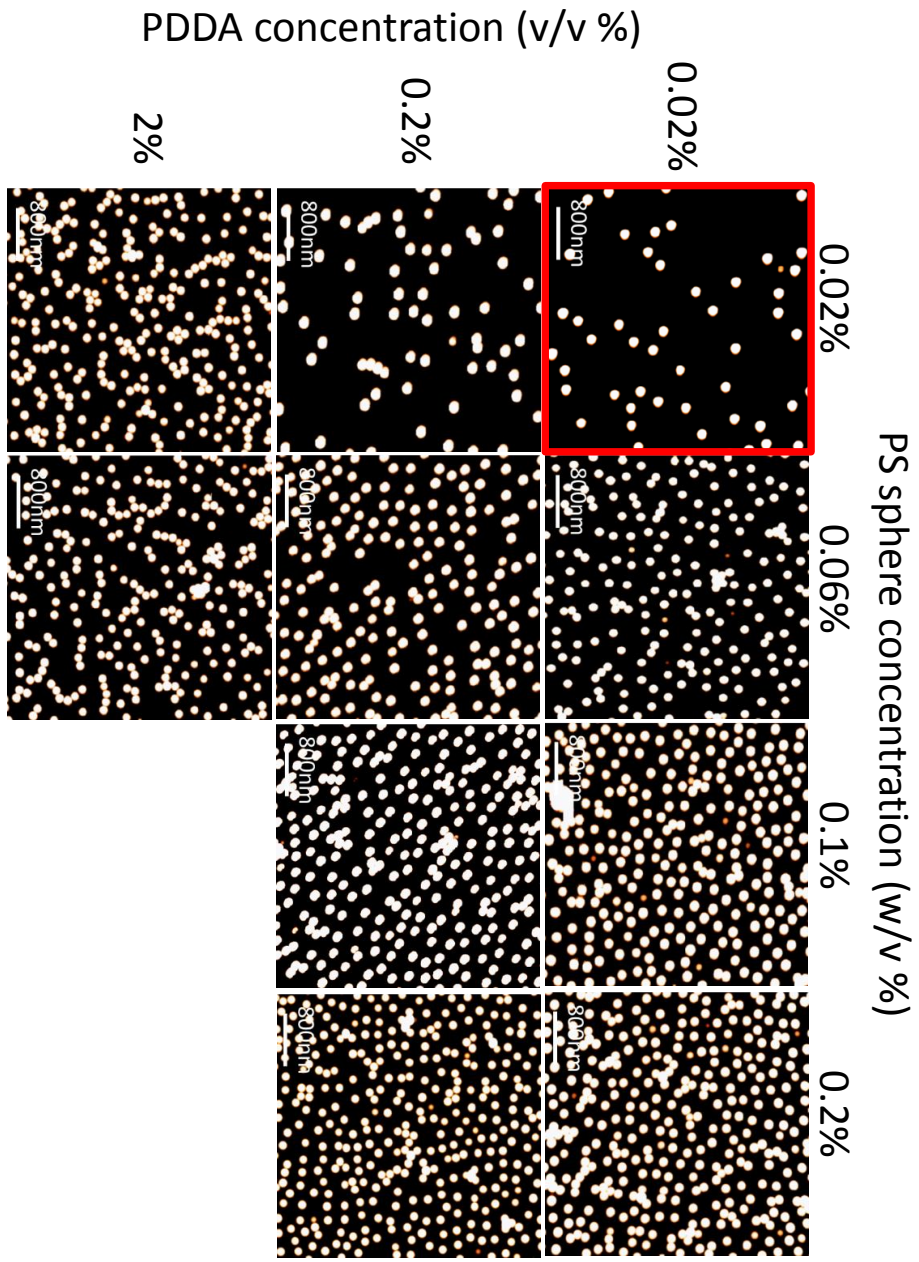

Fig. 3.3.1 (continued)

PDDA \ PS		0.0001%	0.001%	0.005%	0.02%
0.02% FND: First Neighbor Distance	Sphere No.	2	31	468	1682
	FND(μm)	3.83	1.79	0.50	0.33
	Area Coverage	0.00%	0.08%	1.19%	5.07%
0.2%	Sphere No.	13	81	451	1652
	FND(μm)	2.46	1.07	0.54	0.30
	Area Coverage	0.03%	0.16%	1.19%	3.92%
2%	Sphere No.	5	23	1529	4358
	FND(μm)	5.54	2.00	0.29	0.21
	Area Coverage	0.01%	0.04%	2.50%	14.55%

PDDA \ PS		0.02%	0.06%	0.1%	0.2%
0.02% FND: First Neighbor Distance	Sphere No.	49	193	244	266
	FND(nm)	370	217	218	201
	Area Coverage	3.78%	9.8%	25.51%	27.87%
0.2%	Sphere No.	71	179	223	289
	FND(nm)	313	240	216	195
	Area Coverage	3.89%	14.23%	23.20%	29.18%
2%	Sphere No.	276	263		
	FND(nm)	157	162		
	Area Coverage	14.97%	12.29%		

Table 3.3.1 Statistics of the PS sphere distribution. Red squares mark the chosen parameters for templates used in this thesis. Data in the top table are from the first half AFM images in Fig. 3.3.1 with the scale bar of 4μm and data in the bottom table are from the other half AFM images in Fig. 3.3.1 with the scale bar of 800nm.

330nm.

On the other hand, the incubation time of the PS sphere is varied from 20s to 60s. The concentration of PS sphere suspension is fixed at 0.2 w/v % and the PDDA concentration is 0.2 v/v %. All the other parameters are kept as the same. The results

are shown in Fig. 3.3.2.

As it can be seen, the PS sphere density is greatly reduced for incubation time ≤40s (~1500 particles for 60s incubation time in an area of 20×20μm^2 and ~1000 for 40s and less). However, the sacrifice is that the distribution homogeneity is worse for less incubation time, namely, more and larger patches containing no PS spheres can be observed especially in the 20×20μm^2 AFM images.

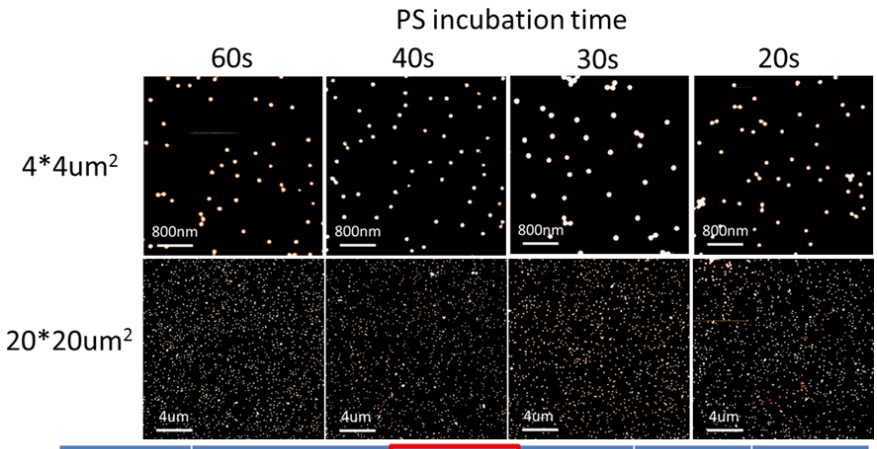

		60s	40s	30s	20s
4*4um^2 FND: First Neighbor Distance	Sphere No.	48	67	44	57
	FND(nm)	388	281	345	303
	Area Coverage	1.42%	1.98%	1.30%	1.68%
20*20um^2	Sphere No.	1517	1067	1069	999
	FND(nm)	295	362	361	346
	Area Coverage	2.27%	1.60%	1.60%	1.50%

Fig. 3.3.2 Incubation time of PS spheres for controlling the PS sphere distribution. PDDA deposition time is 60s for all the samples.

With all of the considerations, the best protocol to reach an appropriate distribution of PS spheres is concentrations of 0.02 % w/v for PS sphere suspension and 0.02 % v/v for PDDA solution, 60s for PS sphere incubation, which are the parameters marked with red squares in Fig. 3.3.1 and Fig. 3.3.2. This process is highly reproducible, which has been verified both in the template and nanostructure characterization.

3.3.2 Au Film Thickness

During the deposition process, the nanostructure deposited on the substrate is the projection of the hole in the template (Fig. 3.2.1), thus the shape and diameter of the hole are critical for controlling the nanostructure's morphology. In this subsection and the following, the effect of the template hole shape and diameter on the nanostructure will be discussed.

First, the mechanical rigidity of the Au film strongly influence the shape of the hole and the reproducibility of the template which is found to be related with the Au film thickness, therefore optimization of the Au thickness is important and critical.

The Au mask works, on one hand, as the resistant mask to the RIE etching in order to protect the PMMA layer underneath; on the other hand, as the deposition mask to allow deposition of the material through the holes onto the substrate. As discussed in the last section, its thickness t is important for the determination of the nanoring morphology. Furthermore, this thickness is also critical for the maintenance of the hole shape, especially for the sputtered Au film. As shown in Fig. 3.3.3(a), after overetching with RIE, Au films with different thicknesses manifest different curvatures around the holes: thinner Au films bend at their ends, while thicker ones keep straight. This is due to the larger stiffness of the thicker Au film.

This difference actually results in the different widths of the material fluxes: for the same PS sphere thus the same nominal hole diameter, the thinner and bent Au films define a larger hole diameter and a thicker material flux (bright yellow flux), while the thicker and rigid ones define a smaller hole and a thinner material flux (blue flux). This is confirmed by the AFM images of the templates with varying Au film thicknesses (Fig. 3.3.3(b)-(e)): for thin Au film, such as 10nm, the areas around the holes have a darker color in the AFM image, implying a lower height there (white square in (b)), which is not observed in the other templates (c-e) with larger Au film thickness. This is the direct proof for the bent Au film around the hole. Furthermore, the areas marked with white squares in (b) and (c) show that the too thin Au films around the holes are easily dragged up by the AFM tip. For the 10nm Au film there are even small cracks (red squares in (b)), which will lead to cavities below PMMA after RIE etching process and small Au deposits onto the substrate after deposition process (red square in Fig. 3.3.4(b)). The hole shapes for 10nm and 15nm Au films

are not round but partially elliptical. As the sputtered Au thickness increases to 30nm and 35nm (Fig. 3.3.3(d) and (e)), the Au films are flat over the whole template, with well-defined round holes. However, a further increase in thickness will cause peeling off of the Au film in the tape-stripping process. Therefore 30nm sputtered Au film is favorable in our experiments.

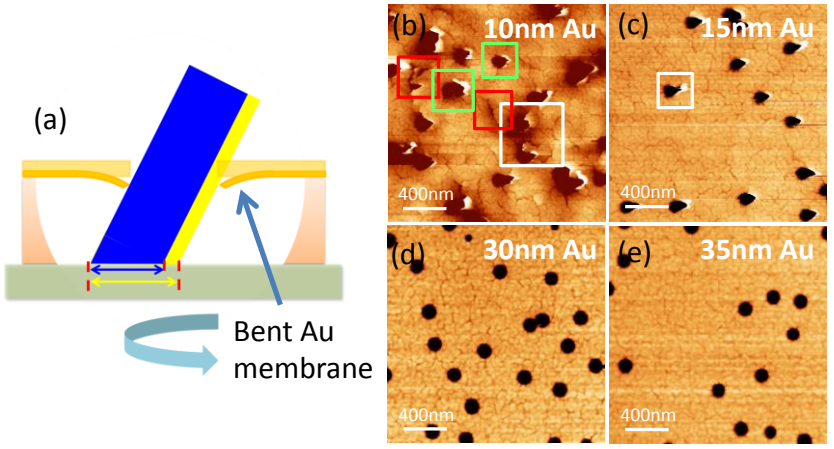

Fig. 3.3.3 (a) Sketch: Au film behavior of different thicknesses, after overetching with RIE. (b-e) AFM images of the template topographies after overetching, with sputtered Au film thicknesses 10nm (b), 15nm (c), 30nm (d), and 35nm (e), respectively. Green squares in (b) show the inhomogeneous hole sizes which result in the different nanostructure sizes in Fig. 3.3.4 (b) and (c).

The bent Au films around the holes have unfavorable effects on the formation of the nanostructures, especially for the nanorings, which are twofold (Fig. 3.3.4): first, the bent Au film leads to the larger hole diameter, as shown in Fig. 3.3.3(a), resulting in a larger width of the nanoring, which will induce even disappearance of the central hole (Fig. 3.3.4(b)); second, the hole diameters are different over the whole template (Fig. 3.3.3(b)), consequently the deposited nanostructures will have a bad homogeneity (green squares in Fig. 3.3.4(b) and (c)). Furthermore, the reproducibility of these templates is even worse, as shown in Fig. 3.3.4, where all the nanostructures are deposited with templates of the same parameters (10nm sputtered Au film and the other parameters are the same) and similar deposition parameters ($\theta = 35°$, deposition time 66min (a), 88min (b), 132min (c), respectively). The obtained

nanostructures range from disk to ring with varying sizes and irregular shapes. As will be seen in the later chapters, nanostructures deposited with 30nm Au hole-mask template exhibit very good morphology and reproducibility.

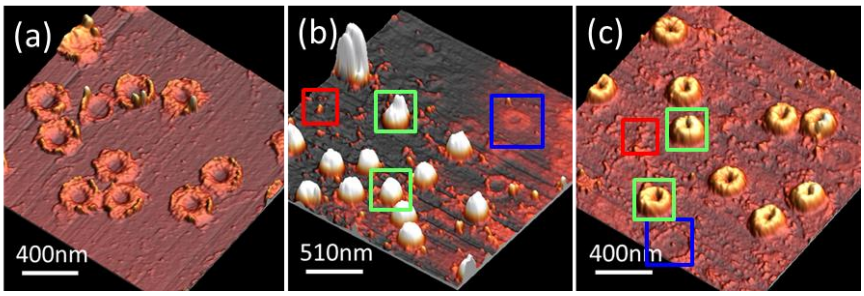

Fig. 3.3.4 AFM images of the nanostructures deposited for 66min (a), 88min (b), and 132min (c) of Au at $\theta = 35°$. The templates are the same with 10nm sputtered Au film. Red squares in (b) and (c) show the Au deposit through the cracks in the Au film in Fig. 3.3.3(b). Blue squares in (b) and (c) show the remaining nanoring traces of the adhesive Ti layer deposited previous to Au (Au deposits are removed in the lift-off process). Although there is Ti nanoring traces in (b), the other remaining nanostructures are disks but not rings. Green squares of the same size in (b) and (c) show the inhomogeneous nanostructure sizes.

It seems that this bent Au film around the hole was not observed in the other authors' work [35,90,96,98,116], where most of the Au, Ag, Cr hole-masks were deposited with thermal or e-beam evaporation method and had the thickness of 10nm or 15nm. This means that the evaporated metallic mask has a different mechanical property than the sputtered one. However, for the work in this thesis, this is an important finding that only with the sputtered Au mask thick enough, homogeneous and reproducible fabrication of nanostructures becomes feasible.

3.4 Conclusion

In this chapter, we discuss the hole-mask colloidal lithography (HCL) method in detail. First, we introduce the general fabrication process of the HCL template. With a geometrical consideration, the deposition of nanostructures with the HCL template is discussed. The feasible nanostructures are mainly disk- and ring-related ones, for

which the dimensions and morphologies can be easily controlled by the template and deposition parameters.

Further modification and optimization of the template parameters are also discussed. The control of the PS sphere density on the template is explored by tuning the PDDA solution and PS sphere suspension concentrations. The optimization of Au hole-mask depends on the deposition methods: for sputtered one which is mostly used in our experiments, a thickness of 30nm is required. The shape and diameter of the hole can be controlled by the deposition angle of Au mask and simultaneous rotation in the substrate. Furthermore, the hole diameter can be modified by the deposition of an additional Au layer with rotation in the substrate.

Chapter 4

Enhanced MO Activity in Magnetoplasmonic Nanorings

As discussed in Chapter 1, the magnetoplasmonic nanodisk structure is unimodal with the LSP resonance and the enhanced MO peak appearing in the same spectral range, usually visible. For the applications such as sensing and communications, optical and MO responses in specific spectral ranges are usually desired, therefore extension of the response spectra of the nanostructures is necessary. The nanoring structure supports usually the bimodal resonance spanning from visible to near infrared (NIR). In this chapter, the results of our Au/Co/Au nanoring structures with plasmon enhanced MO properties will be presented and discussed.

4.1 Plasmon Enhanced MO effect: from Nanodisk to Nanoring

In this section, we will study the optical and magneto-optical (MO) responses of the nanoring structures. For this, a series of Au/Co/Au trilayered nanostructures from disk to ring are fabricated and characterized, where the evolution in the morphology and the induced modifications in magnetic, optical and MO properties of the nanostructures can be observed.

4.1.1 Fabrication

The structures are fabricated with the HCL method by modifying gradually the polar

(θ) deposition angle, as shown in Fig. 4.1.1. The HCL templates are prepared with the standard process, with 124nm PS spheres, 200nm PMMA and 30nm sputtered Au mask. The deposition process is then performed in the ultra-high vacuum MBE system with electron-beam evaporation for Ti and Co, and Knudsen cell for Au. For all the structures, a 1-2nm Ti layer is deposited first to improve the adhesion of the subsequent Au and Co layers to the BK7 glass substrate. The deposition rates are 0.02nm/s for both Ti and Co, and 0.03nm/s for Au. The rotation speed of the substrate about its surface normal is 3rpm for all the samples. Additionally, off-normal deposition angle θ is controlled independently to allow tuning in the nanodisks and nanorings fabrication. Sample morphology is characterized by AFM and representative AFM images are listed in Fig. 4.1.1.

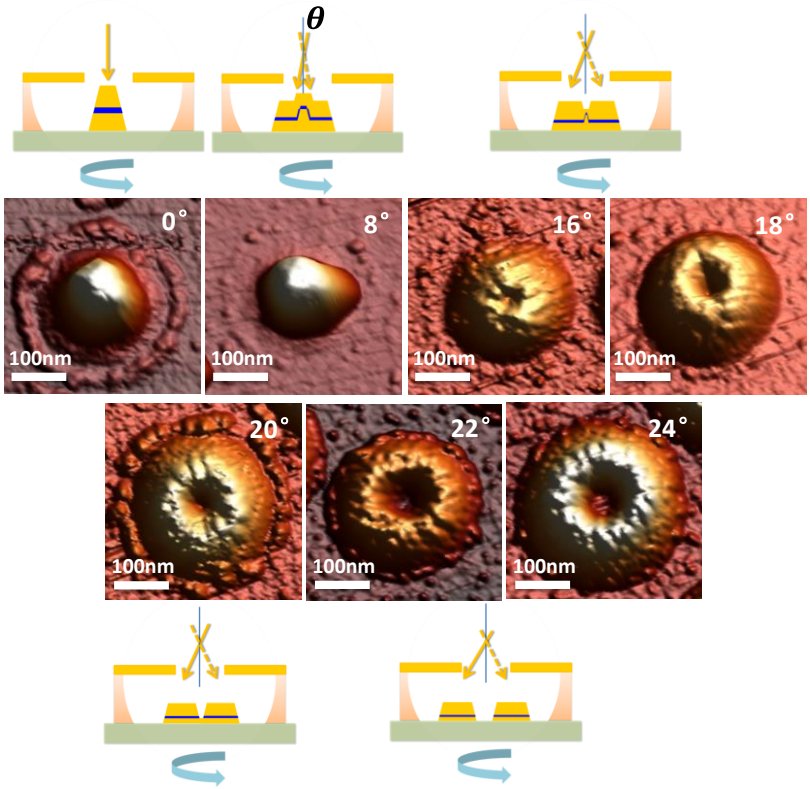

Fig. 4.1.1 Deposition of nanostructures from disk to ring by controlling the deposition angle θ from 0° to 24°. Representative AFM images of the corresponding samples are shown.

At normal deposition (θ=0°) the material is deposited in the region below the hole, forming disks. By slightly changing the deposition angle off-normal (θ=8°), opposite deposition angles will produce deposits that overlap in the central region, resulting in over-accumulation of material and larger height in this region with respect to the edge of the nanodisk. Further increase of deposition angle will lead to a situation where a dip in the central part of the disk starts opening up (θ=16° and 18°), until deposits produced by opposite angles are just in the limit of physical contact (θ=20°). This case can be considered as the transition between disk and ring formation, from which the central dip becomes a fully hollow region. For larger deposition angles (θ=22° and 24°), the deposits from opposite angles are away from each other and the substrate rotation about its surface normal leads to ring formation.

Following this procedure, 32nm Au, 22nm Co and 64nm Au are sequentially deposited at θ=0° to obtain the Au/Co/Au trilayer nanodisks. With the purpose of maintaining the amount of plasmonic and ferromagnetic material identical for all the samples, the deposition time of each Au and Co layer for all the other structures is kept the same as that in the θ=0° situation, resulting in a gradual reduction of the structure height and increase in the outer diameter due to spatial redistribution of the deposited material as the deposition angle increases. The representative AFM images in Fig. 4.1.1 confirm the described morphological evolution, with a disk shape for θ=0° and 8°, disks presenting a dip in the central part for 16°, 18° and 20°, and clear ring shape for 22° and 24°.

This morphological evolution becomes even more evident if one compares the AFM profiles of all the structures, as shown in Fig. 4.1.2. These AFM profiles are obtained by averaging profiles from 10 different nanostructures in each sample. As it can be seen, the overall evolution of the structural shape is clear, being a well-defined disk for θ=0°, a nanodisk with a taller central part and a shorter edge for 8°, nanodisks with a central dip for 16° and 18° and nanoring structures with actually hollow central parts for 20°, 22° and 24°. The morphological parameters, i.e. outer diameter (Φ_{out}), height (H) extracted from these profiles, are also listed in Fig. 4.1.2，together with the resulting aspect ratio (AR=Φ_{out}/H) [43], which exhibits the gradual increase with deposition angle θ. Additionally, the corresponding parameters calculated using simple geometrical considerations in section 3.2 and the resulting aspect ratios are also shown in the parenthesis, showing excellent agreement with the results extracted

from the AFM profiles, except for the θ =8° sample due to the overlapping effect of the deposits which is not considered in the geometrical calculation.

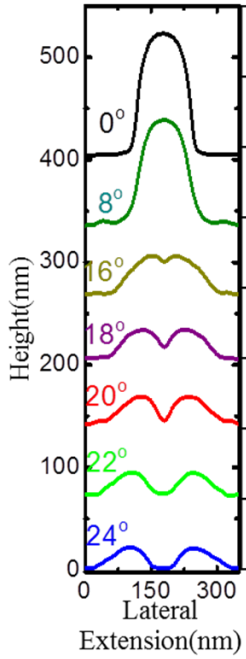

θ (deg.)	Φ_{out} (nm)	H (nm)	AR
0	130 (124)	118 (118)	1.1 (1.1)
8	170 (180)	103 (55)	1.7 (3.2)
16	240 (238)	37 (31)	6.5 (7.5)
18	245 (253)	27 (28)	9.1 (8.9)
20	260 (269)	26 (25)	10 (10.5)
22	270 (285)	22 (23)	12.3 (12.2)
24	300 (302)	20 (21)	15 (14.1)

Fig. 4.1.2 Left: AFM profiles of the nanostructures. The profiles are shifted vertically for better comparison. Right: morphological parameters of these nanostructures (outer diameter Φ_{out} and height H, and aspect ratio (AR) Φ_{out}/H. In the brackets are the geometrically calculated parameters according to the geometrical considerations in section 3.2.

For a better observation of the good control of the structure morphology with the HCL method, in Fig. 4.1.3 the experimental and geometrically calculated Φ_{out}, H, and AR are plotted versus the deposition angle. As it can be seen, outer diameter Φ_{out} and aspect ratio AR increase, and the height H decreases monotonically as the deposition angle increases. The only deviation between experiment and calculation appears at 8°. The shadow-marked regions in the figure correspond to the transition from nanodisk to nanoring around the angle range θ=16° to 18°.

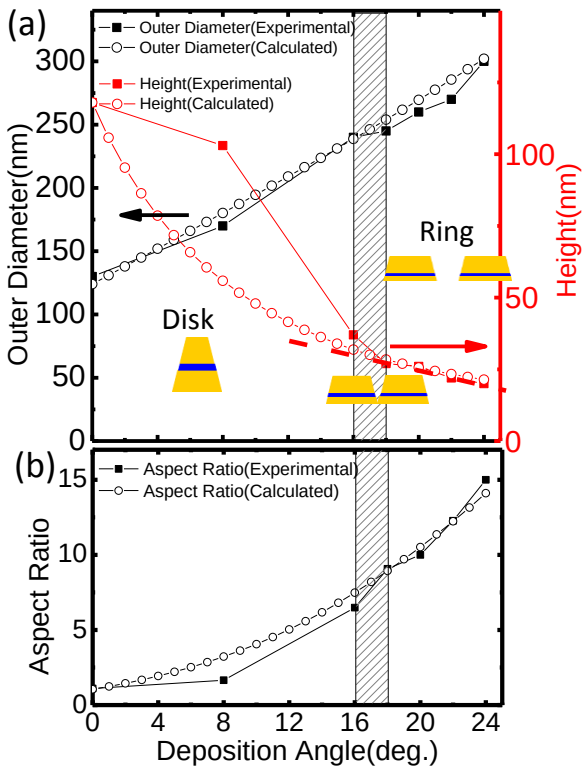

Fig. 4.1.3 Evolution of the morphological parameters of the nanostructures versus the deposition angle: outer diameters Φ_{out}, heights H in (a) and aspect ratios AR in (b).

4.1.2 Magnetic Characterization

The magnetic properties of the nanostructures are characterized with the transverse MOKE (t-MOKE) and polar MOKE (p-MOKE) systems. The obtained hysteresis loops are shown in Fig. 4.1.4, with the out-of-plane and in-plane hysteresis loops measured from p-MOKE (Fig. 4.1.4(a)(c)) and t-MOKE ((b)(d)).

At a first glance, a magnetic anisotropy with in-plane easy axis can be concluded for all the samples from the low saturation field and the high remanent magnetization in the in-plane loops, compared with the high saturation field and low remanent magnetization for the out-of-plane ones. Magnetic anisotropy can have numerous, non-excluding origins, such as crystallinity, shape, surface, interface, etc. [118]. For

the current case, due to the polycrystalline nature [119] and specific thickness of the Co layer which is around or larger than 4nm, it is the shape anisotropy that determines the in-plane easy axis since the Co layers in all the samples have aspect ratio≫5.0 (outer diameter/thickness).

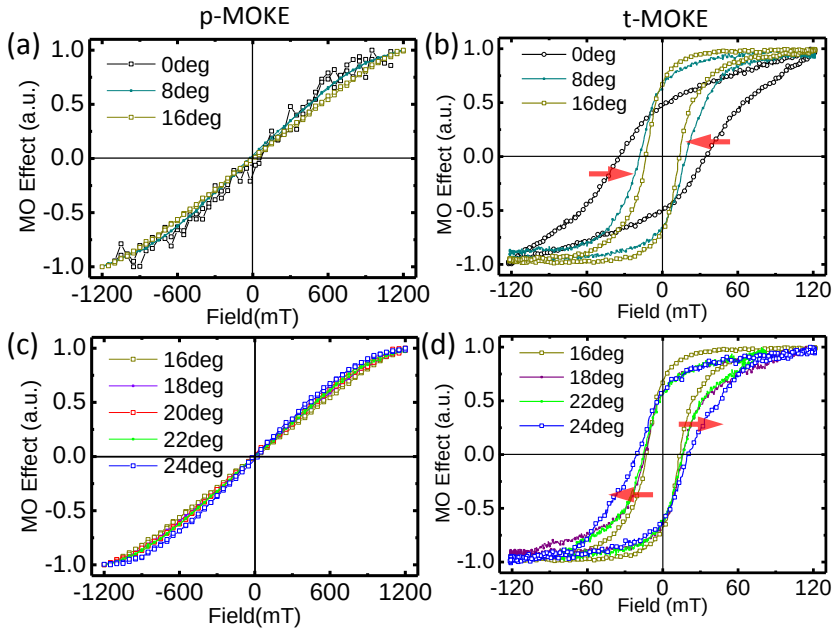

Fig. 4.1.4 Out-of-plane (left) and in-plane (right) magnetic hysteresis loops of the nanostructures measured from the p-MOKE and t-MOKE, respectively. Red arrows show the evolution trends of the T-MOKE loops as θ increases.

Generally, the obtained T-MOKE loops in Fig. 4.1.4 can be classified into two categories with the θ =16° sample as the transition point: on the one hand, the structures deposited from θ =0° to 16° exhibit increasing in-plane remanence and decreasing coercive field (Fig. 4.1.4(b)); on the other hand, the structures deposited from θ=16° to 24° exhibit an opposite behavior in the in-plane remanence and coercive field (Fig. 4.1.4(d)), as shown with the red arrows in the figures.

As known from the last section with the discussion on the structural morphology, from θ=0° to 24° the fabricated nanostructures experience an evolution from disk to ring with the transition point around 16°-18°. Therefore we can imagine the change in

the magnetic behavior should also be attributed to this transition from disk to ring and the corresponding transition in the magnetic domain state, since magnetic properties such as coercivity and remnant magnetization in such nanoelements stem from the domain structures as discussed below.

Although we are in lack of a more detailed study of the domain state in such nanostructures, the hysteresis loop shape and its evolution behavior give us the information about the magnetic domain state and mechanism of magnetization reversal. We can draw our conclusions about the domain states in the nanostructures by comparing with the results in the literature.

It should be first noted that the nanoparticles here are loosely distributed in lack of long-range coherence, with very weak interactions between the nearest neighbors. Therefore the hysteresis loops in Fig. 4.1.4 are characteristic of individual non-interacting nanoentities. Of course, the loops show a spread in switching fields due to the possible differences in the grain structures and random defects [118,120] among the nanostructures.

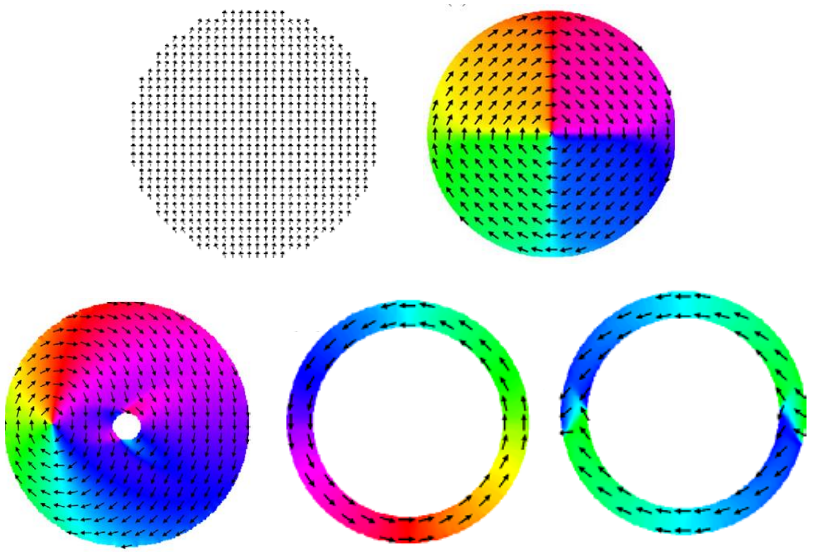

Fig. 4.1.5 Possible domain states for nanodisk and nanoring structures. Top: single domain (left) and vortex (right) states for nanodisks. Bottom: vortex core (left) states in thick nanorings, vortex (central) and onion (right) states for thinner nanorings. Figure for single domain of nanodisk is adopted from Ref. [123] and the rest from Ref. [128].

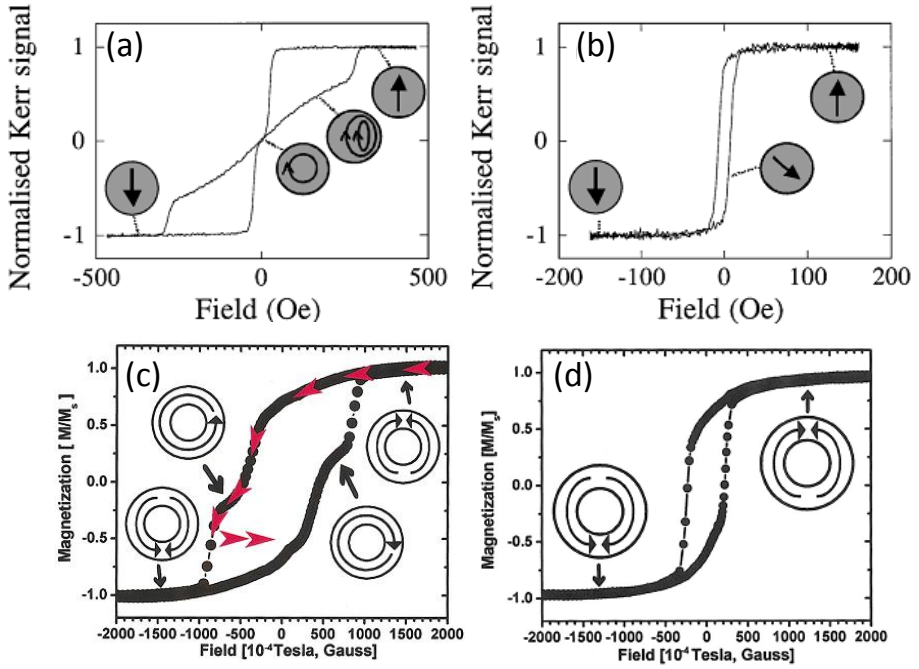

Fig. 4.1.6 (a-b) Hysteresis loops measured from polycrystalline supermalloy ($Ni_{80}Fe_{14}Mo_5$) nanodisk magnets of diameter d and height h. The magnetization states are schematically shown. (a) Multiple switching process for nanodisk with d=300nm, h=10nm: single domain to vortex, and at last back to single domain. (b) Single switching process between single domain states for nanodisk with d=100nm, h=10nm. (c-d) Hysteresis loops measured for polycrystalline Co ring arrays with outer diameter D, inner diameter d, and height h for a ring. (c) Multiple switching process for ring with D=1200nm, d=900nm, and h=15nm): onion and vortex states. (d) Single switching process for ring with D=1700nm, d=1250nm, h=4nm: only onion states. (a) and (b) are adopted from Ref. [123] and (c)(d) from Ref. [127].

For the nanodisk and nanoring structures, several domain states are possible to exist (Fig. 4.1.5), such as single domain, vortex, vortex core, and onion, etc. The vortex and vortex core states correspond to the very low remnant magnetization (for example, Fig. 4.1.6(a)(c)) [121-127], which is not observed in Fig. 4.1.4(b) and (d). Moreover, the transition between different domain states will generate a step shape in the loops (for example, Fig. 4.1.6(a)(c)) [121,123,124], which is not observed, either. Therefore

no vortex or vortex core state are expected and only one possible domain state could exist in the current nanoparticles (for example, Fig. 4.1.6(b)(d)).

For small nanodisks one possible and stable state is the single domain [121,123] with critical dimensions of the nanoentity. For example, the critical volume of the nanodisk for the single domain state is about 5×10^5 nm^3 or even smaller [122-124]; the specific thickness and diameter of the nanodisk [118,122,123], as well as the quality of the film [124], also play very important roles. The largest Co volume in these nanoparticles (θ=0°) fabricated here can be estimated with the morphological parameters from the AFM images, which is around 3×10^5 nm^3. For the nanodisk deposited at θ >0°, the volumes should be even smaller as we explained in section 3.2. In this sense, all the nanodisk volumes are smaller than the critical transition volume (5×10^5 nm^3) between single domain and multi-domain states. Moreover, the coercive field in Fig. 4.1.4(b) is becoming smaller as the thickness decreases and diameter increases for θ from 0° to 16° (red arrows), and the magnetic reversal process is driven by a relatively weak field below 100mT. All of these behaviors are similar to the magnetic nanodisk with single domain in the previous studies, such as the polycrystalline supermalloy ($Ni_{80}Fe_{14}Mo_5$) nanodisk in Ref. [123] (an example is shown in Fig. 4.1.6(b)). In this way, for θ =0° to 16° nanodisks the magnetization state should be dominated by the single domain, and due to the large thickness of θ=0° nanodisk, possible multi-domain state could exist [121,124].

On the other hand, for the nanoring structure, the onion state has a higher remanence than the others (e.g. vortex state, etc.) (Fig. 4.1.6(d)) [127]. Furthermore, by studying the phase diagram of the switching behavior of the nanoring with different geometric parameters [125], it is found that the main geometrical factor that determines the single onion-onion switching is the film thickness, being around 4nm and weakly depending on the particular values of ring width and outer diameter. With thickness below this value, only single onion-onion transition can happen since exchange energy favors this onion state. Combined with the single step switching process and by comparing the in-plane loops with the single onion-onion transition loops in the literature (Fig. 4.1.6(c)(d)) [127,128], it can be concluded that only the onion state exists in the magnetic reversal process of nanoring structures for θ from 18° to 24°.

In all, the transition in the in-plane hysteresis loops at θ = 16° corresponds to the morphological transition from Co nanodisk to nanoring at this angle and the magnetic domain state transition from single domain of nanodisk to onion state of nanoring. No

obvious trend can be observed in the out-of-plane loops, due to the dominant in-plane anisotropy.

4.1.3 Optical and MO Characterizations

The optical response of the fabricated nanostructures is characterized with an optical microscope combined with a spectrometer with normally incident light and the Kerr rotation and ellipticity are obtained using a p-MOKE system with light incidence nearly normal to the sample, as described in subsection 2.4.1 in Chapter 2.

The morphological evolution (Fig. 4.1.3) as a function of the deposition angle has its direct consequence in the optical and MO spectral responses of the studied structures. This is illustrated in Fig. 4.1.7, where we show the spectral dependence of the extinction (left) and MO activity (MOA) in polar configuration (right) defined as the modulus of the complex Kerr rotation (Eq. 1.3.10 in subsection 1.3.2 in Chapter 1). Kerr rotation and ellipticity spectra of these structures are shown in Appendix 5. First of all, as it can be seen for each nanostructure, the spectral dependences of optical extinction and MOA spectra are very similar, confirming the cross correlation between plasmon resonance excitation and its enhancement in the MOA due to the field localization in the nanostructure at resonance [27]. Additionally, a clear parallel evolution of both extinction and MOA as a function of deposition angle is also observed: for $\theta = 0°$ and 8°, both extinction and MOA spectra exhibit a single resonance. With increasing θ a new spectral feature begins to appear as a shoulder in the high energy side of the main peak. This additional feature becomes more intense and clearly observable for θ=20°, 22° and 24°**.** In this way, the enhanced MOA is successfully extended from visible range to near infrared.

Obviously, the single mode feature observed for nanodisk structures ($\theta = 0°$ and 8°) in the optical extinction spectra corresponds to the excitation of the nanodisk dipolar resonance mode as discussed in subsection 1.2.1 in Chapter 1. The low extinction and MOA values observed in these two structures relative to the rest structures are simply due to the low aspect ratios and therefore small polarizabilities and dipole moments [27,43**]**. On the other extreme of the series of structures, the bimodal behavior for nanoring (θ=20°, 22° and 24°) can be interpreted in terms of the dipolar disk-hole plasmon hybridization model as discussed in subsection 1.2.2 in Chapter 1, inducing a bonding dipolar mode in the low-energy (LE) range and an antibonding dipolar mode

in the high-energy (HE) range (Fig. 1.2.6). Similarly to the nanodisk structure [27], the insertion of Co into the Au nanoring structure causes the damping in the plasmons thus broader peak widths compared to the pure Au nanoring with similar dimensions (Fig. 1.2.6 in Chapter 1), due to the larger optical loss of Co material.

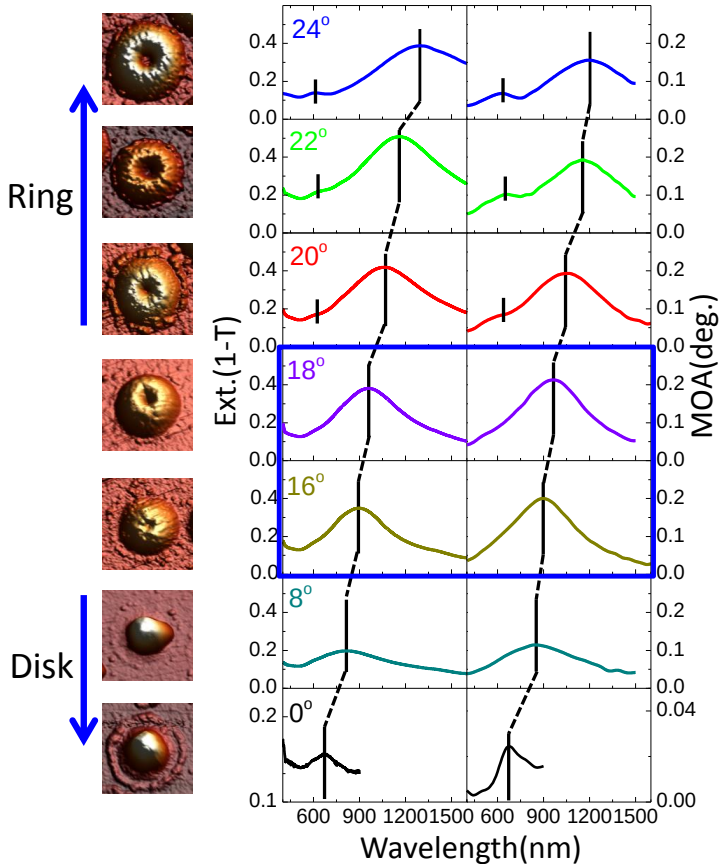

Fig. 4.1.7 Left: AFM images of the nanoentities. Right: Spectra of optical extinction (left) and MO activity (right) for the corresponding nanostructures, showing unimodal to bimodal evolution from disk to ring. The black lines are guides to the eye of the evolution of the disk mode and LE mode of nanoring, and the black bars mark the HE mode in the nanoring. Note the different scales for spectra of nanodisk deposited at $\theta = 0°$. Blue square shows the transition region from disk to ring.

On the other hand, the intermediate structures grown at θ =16° and 18°

corresponding to disks with a central dip, show an intermediate behavior, with a main resonance in low energy range and a very small shoulder in high energy range. This means the emergence of the hole dipole in the nanostructure with the dip and the subsequently induced, though very weak, interaction (hybridization) with the disk dipole, which results in the spectral shift and split of the plasmon resonance and emergence of the bimodal feature.

As discussed in section 1.4 in Chapter 1, for such Au/Co/Au trilayer nanostructure, the MO effect is mainly contributed by the Co content which has much larger MO constants than Au. Therefore the enhancement of the electromagnetic (EM) field at plasmon excitation in the MO-active Co layer results in the enhanced MOA for both of the LE and HE modes. This effect and the corresponding effect of the magnetic field on the plamonic dipoles, will be explained in section 4.2 with the theoretical simulation results.

The spectral position of the plasmonic resonance and therefore of the MO peak of a nanodisk is strongly correlated with its aspect ratio (AR). Though the nanoring structure can not be simply described with a disk dipole, it seems from the parallel evolution of the LE extinction peaks and MOA peaks (Fig. 4.1.7) that this LE mode in the nanoring is still controlled mainly by the disk dipole via the aspect ratio AR. For this, in Fig. 4.1.8 we plot the wavelength position for both optical and MO modes versus the corresponding aspect ratios of the structures.

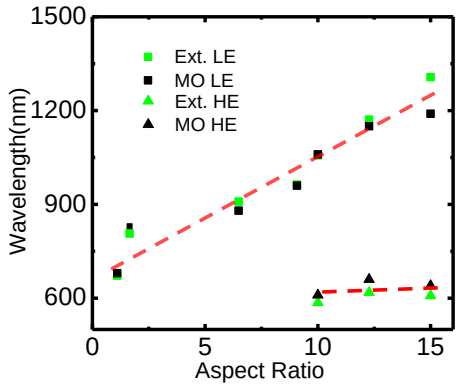

Fig. 4.1.8 LE and HE optical and MO resonance wavelength position as a function of the aspect ratio (dashed lines are guides to the eye).

As it can be seen, the low energy (LE) optical and MO modes for both nanodisks and nanorings gradually red shift in an identical linear fashion with increasing aspect ratio, from 650 nm for pure nanodisk structures up to 1200 nm for pure nanorings. This confirms our assumption that the AR is the controlling factor of these modes and highlights the "disk-like" nature of the low energy mode in the nanoring resonance, with few effects from the hole. Meanwhile, in Fig. 4.1.8 the spectral position of high energy (HE) mode is also shown for the nanoring structures, which are the only ones where this mode is observed. In this case its position hardly depends on the aspect ratio, as expected since it basically depends on the cross-section of the nanoring [142,160].

4.2 Theoretical Model

To better understand the observed behavior of the nanoring structure, rigorous theoretical calculations using Finite Element Methods (FEM) have been performed with COMSOL software by Dr. Antonio Garc á-Mart ń at IMM. The actual fabricated nanorings exhibit a very complex structure, both for the rough surface and irregular cross-section shape. Carrying out a calculation that takes into account all the experimental structural details exceeds the computing capability, therefore a simpler system is used instead, formed by rotating the hemi-ellipsoids whose dimensions are the best approximation of the actual cross-section of nanorings, being inner and outer diameters the two variable parameters. A sketch comparing the actual average cross-section shape of the fabricated reference rings and the used hemi-ellipsoids is shown in Fig. 4.2.1(a) with blue bars showing the Co layers. As it can be seen, the actual irregular shape of the fabricated nanorings is theoretically substituted by a simpler geometrical form, while the relevant structural parameters are maintained. The different layer thicknesses used in the calculations are 7nm, 5nm, and 14nm for the bottom Au, Co and top Au layers, respectively, which are typical for the fabricated nanorings. The spectral dependence of extinction and MO activity calculated for two of the nanoring structures with variable inner and outer diameters are shown in Fig. 4.2.1(b), being 30-230nm (inner-outer diameter) and 30-265nm.

As it can be observed the calculated extinction spectra show a dominant low energy peak, whose position red shifts with increased outer diameter, while its intensity remains similar. A shoulder appears on the high energy side of the dominant peak,

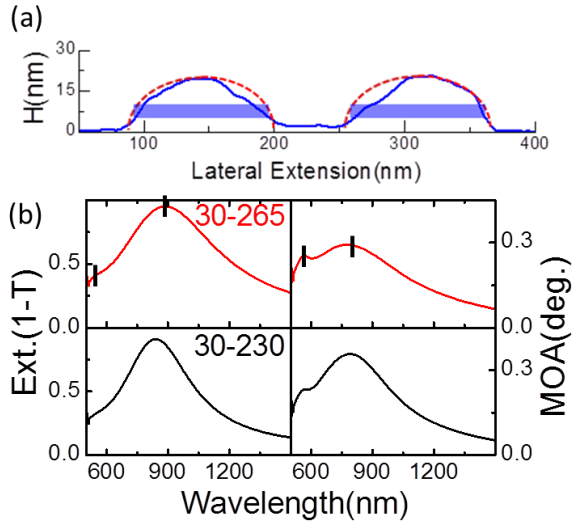

Fig.4.2.1 (a) Averaged AFM profile of a nanoring structure (blue) and illustration of hemi-ellipsoids used in theoretical calculations (dashed pink curves). The blue bars mark the positions of Co layers. (b) Calculated optical extinction (left) and MO activity (right) spectra of two nanoring structures with 30-230nm and 30-265nm inner-outer diameters. Black bars in the spectra of 30-265nm nanoring indicate the spectral positions of the optical and MO modes whose field distribution will be discussed in Fig. 4.2.2.

which is also similar to the experimental spectra of the nanoring structure. On the other hand, the MO spectra present two peaks that red-shift with increased outer diameter, and the low energy peak decreases while the high energy peak increases in the intensities as the outer diameter increases. There is a clear overall blue shift of the theoretical peak positions with respect to the experimental ones, which is simply due to the specific geometrical values used in the calculations, mainly smaller aspect ratios (outer diameter vs. height, for LE modes) and thicker walls (Fig. 4.2.1(a), for HE modes) than in the experiments, but that do not affect the interpretation of the observed effects.

To clarify the nature of the different modes excited in the structures and their contributions to the MO response of the system, in Fig. 4.2.2 are presented the calculated z-component of the electric field (E_z) for the 30-265nm nanoring at a plane 1.5 nm below the glass substrate-nanoring interface upon x-polarized light at normal incidence, both in absence of an external magnetic field (upper panels) and as the

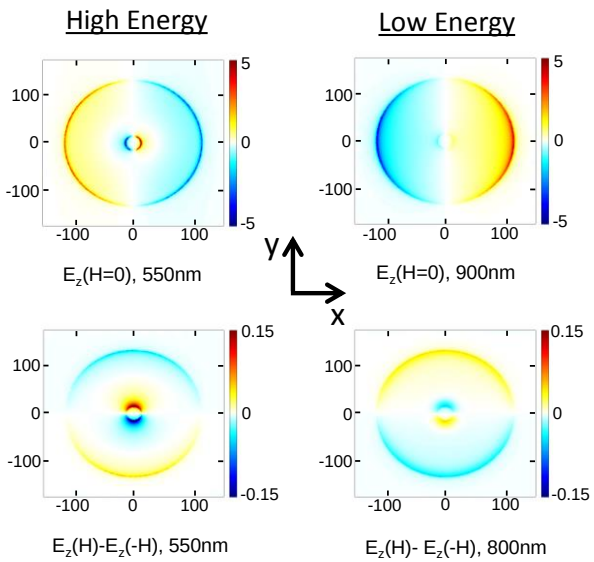

Fig. 4.2.2 Upper panels: calculated near field intensity of the E_z electric field component for the 30-265nm nanoring sample upon x-polarized light in the absence of magnetic field at the spectral positions marked below. Lower panels: calculated differences of the E_z components for magnetic saturation along opposite directions at the spectral positions marked below. The near field intensities are calculated in a plane 1.5nm below the glass substrate-ring interface.

difference for magnetic saturations along opposite directions (lower panels).

As it can be observed, in absence of an external magnetic field the E_z distributions (E_z(H=0)) can be fairly well described as those produced by two dipoles oriented along the x-axis, one related to the outer diameter of the nanoring (disk-like dipole, $P_{x,disk}$) and the other one related to the inner diameter of the ring (hole-like dipole, $P_{x,hole}$). The effect that the magnetic field has on these two dipoles is to generate y-components for both of them, which can be obtained from the difference of the distribution of E_z for magnetic saturations along opposite directions (E_z(H)-E_z(-H)). These distributions clearly show that for both peaks the magnetic field induces a rotation in x-dipoles $P_{x,disk}$ and $P_{x,hole}$, giving rise to a field profile that can be associated to magnetic field induced y-dipoles $P_{y,disk}$ and $P_{y,hole}$. This disk-hole dipole hybridization model with their associated charge distributions is also illustrated

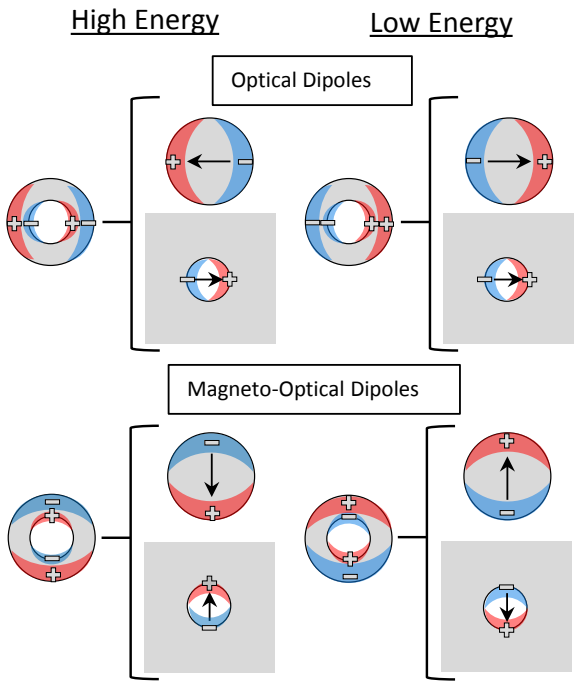

Fig. 4.2.3 Schemes illustrating the symmetry of the obtained modes according to a simple plasmon hybridization model both for optical (upper panels) and MO parts (lower panels).

in Fig. 4.2.3 for both x- (optical) and y- (MO) components where the hybridization process can be clearly appreciated.

The intensity of the optical extinction is determined by the total dipole moment along x direction, which can be considered by the individual dipole moments and taking into account their relative phases [60]. Clearly the LE mode corresponds to the in-phase oscillation of $P_{x,disk}$ and $P_{x,hole}$ and the total dipole moment is the sum of these two, while the HE mode corresponds to the out-of-phase oscillation of $P_{x,disk}$ and $P_{x,hole}$ and the resulted total dipole moment is their difference. Therefore, apart from the specific values of the $P_{x,disk}$ and $P_{x,hole}$ dipole moments which are determined by the optical constants of the material at the corresponding wavelengths and aspect ratio of the nanostructure, their relative phases in the LE and HE wavelength positions further increase the difference in the extinction intensities.

Regarding the MO activity, the relevant parameter determining its magnitude is the

balance between the net y- and x-dipoles as discussed in subsection 1.4.1 in Chapter 1. The total dipole moment along the y direction is determined by $P_{y,disk}$ and $P_{y,hole}$, for which, very interestingly, are both out-of-phase for LE and HE modes as shown in Fig. 4.2.2. To evaluate the MOA, a rough but qualitative estimation of the total dipole moment along y direction ($|P_y|$) can be obtained by multiplying the values of the E_z component of the difference (lower panels in Fig. 4.2.2) by the distance to the center of the nanoring, and integrating these products over the positive region of the y-axis. With this method, we consider all the contributions of $P_{y,disk}$ and $P_{y,hole}$, as well as the contribution from their relative phase. The analogous process is applied to obtain the total dipole moment along x direction ($|P_x|$), with the E_z component without magnetic field (upper panels in Fig. 4.2.2) multiplied by the distance to the center of the nanoring and integrating the products over the positive region of the x-axis. The ratio $|P_y|/|P_x|$ is directly related to the MO activity.

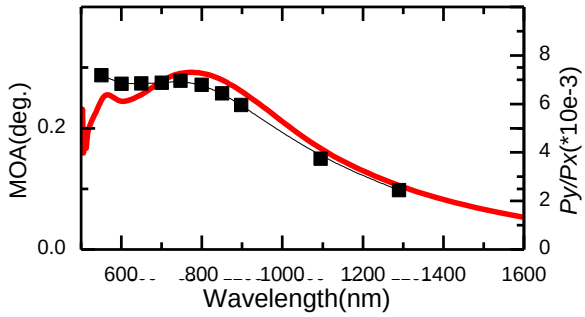

Fig. 4.2.4 Calculated $|P_y|/|P_x|$ (black square dots) for sample 30-265nm using simple dipole distribution arguments. Its spectral dependence and relative intensity qualitatively reproduce the calculated MO spectrum (red). The black continuous curve connecting the points is a guide to the eye.

The obtained results from Fig. 4.2.2 for a series of spectral positions of 30-265nm nanoring are shown as black square dots in Fig. 4.2.4, compared with the calculated MOA of the same structure. As it can be seen, in spite of the crudeness of this approach, the agreement with the rigorously calculated MO activity is actually rather good, indicating that it is indeed the balance of the net dipole along y-direction, normalized to that along x-direction, that responsible for the observed MO activity of the system. This agreement, on the other hand, confirms the validity of our disk and

hole dipole hybridization model for the plasmonic and the MO response of the nanoring structure.

4.3 Conclusion

In this chapter, we discuss the plasmonic and MO responses of the nanoring structures.

A series of Au/Co/Au multilayered nanostructures from disk to ring are fabricated with the HCL method. The nanodisk presents unimodal plasmonic resonance and MO activity, while the nanoring structure presents bimodal resonance and MO activity in the LE and HE range. We find out that for our nanostructures the spectral positions of the LE plasmonic and MO modes are controlled by the aspect ratio (outer diameter/height) of the nanostructure.

The application of magnetic field induces the rotation in the optical disk and hole dipoles of the nanoring polarized by the incident light, yielding the MO disk and hole dipoles perpendicular to the original optical dipoles. With the plasmon hybridization model, the bimodal MO activity is explained as the hybridization of the MO disk and hole dipoles.

Magnetic properties of the nanodisk and nanoring structures are also studied with the MOKE systems and the transition between the magnetization behaviors of the nanodisk and nanoring structures is attributed to the transition in the magnetic domain states, namely, from the single domain state of nanodisk to onion domain state of nanoring.

Chapter 5

Modification in Nanoring: Au and Co Layer Redistribution

Since the plasmon resonance in the nanostructure is also related to its morphology, in this chapter first we will develop the method to further finely control the optical and MO responses of the nanoring by tuning morphology of the nanoring. On the other hand, the MO effect of the system is determined by the EM field intensity inside the MO active layer. For Au/Co/Au multilayered nanodisks, the distribution of the EM field inside resonant nanostructure is not homogeneous. Up to now, the studies about field distribution in such multilayered structures have been only focused on the vertical EM field distribution caused by the position variation of MO layer within the structure [21,86,129-131] (for example, Fig. 1.4.5 in Chapter 1). However, the effect of the horizontal, or, in-plane distribution (position) of the MO active material on the MO response of the nanostructures has not been explored yet. Actually we have observed in Fig. 4.2.2 in Chapter 4 that the horizontal distribution of the EM field is not homogenous all over the nanoring at resonance. In particular, EM field tends to be more intense at the two poles of nanoring along the light polarization. Therefore it is interesting to imagine whether the MO effect would be more effectively enhanced or not if Co is located only at these pole positions.

These two aspects mentioned above, the morphology tuning and internal Co redistribution, can be explored with the Au/Co/Au nanoring generated by the HCL technique. The HCL method provides us the convenience to control each layer independently. Therefore, the subtle morphology of the nanoring by controlling the distribution of top Au layer and the in-plane distribution of Co layer, could be engineered by the deposition parameters such as deposition angle, time, and rotation of the substrate. Simultaneously, the amount ratio of Au/Co materials is tuned in this way.

In this chapter, we study two series of structures. For the first series we finely tune the structure morphology by separating the top Au layer into several sub-deposits and increasing the deposition angle for each and the induced subtle change in the optical and MO responses, being mainly the spectral shift, will be studied; for the second one, the Co layer in the nanoring will be varied from continuous Co ring, to opposite Co sectors and opposite Co dots, for which the induced modification in the EM field distribution, and thus the optical and MO responses will be discussed.

5.1 Top Au Ring Redistribution Effects

For the application requiring optical and MO response in a specific spectral range, a detailed design of the magnetoplasmonic structures may be desired. For the nanoring structure, the plasmonic response can be tuned in a fine way by the cross-section area and shape, as discussed in subsection 1.2.2 in Chapter 1. In this section, we apply the similar method by tuning only the top Au layer in our Au/Co/Au nanoring, to realize a fine control of both optical and MO responses.

5.1.1 Fabrication

The nanoring structures are prepared with the HCL technique combined with off-normal deposition and rotation in the template. In Fig. 5.1.1 a sketched description of this fabrication process is presented. In this specific case, using a fixed deposition angle of $\theta = 22°$, a 1-2 nm thick Ti nanoring is deposited to enhance adhesion, followed by 7 nm thick Au and 5 nm thick Co nanorings. Next, the deposition angle for the last Au layer is used as a variable parameter to finely tune the nanoring cross section. This is schematically described in the deposition sketches on the left of Fig. 5.1.1. The resulted nanorings are also schematically sketched in Fig. 5.1.1 where the effects of the redistribution of this upper Au layer are shown. Representative AFM images of these three nanoring structures are shown on the right of Fig. 5.1.1. The corresponding AFM profiles obtained by averaging 10 different nanorings in each sample are also shown in Fig. 5.1.2.

The specific deposition conditions for each sample are: for sample (I), the same deposition angle (θ=22°) is used for the whole structure, obtaining a vertical piling of

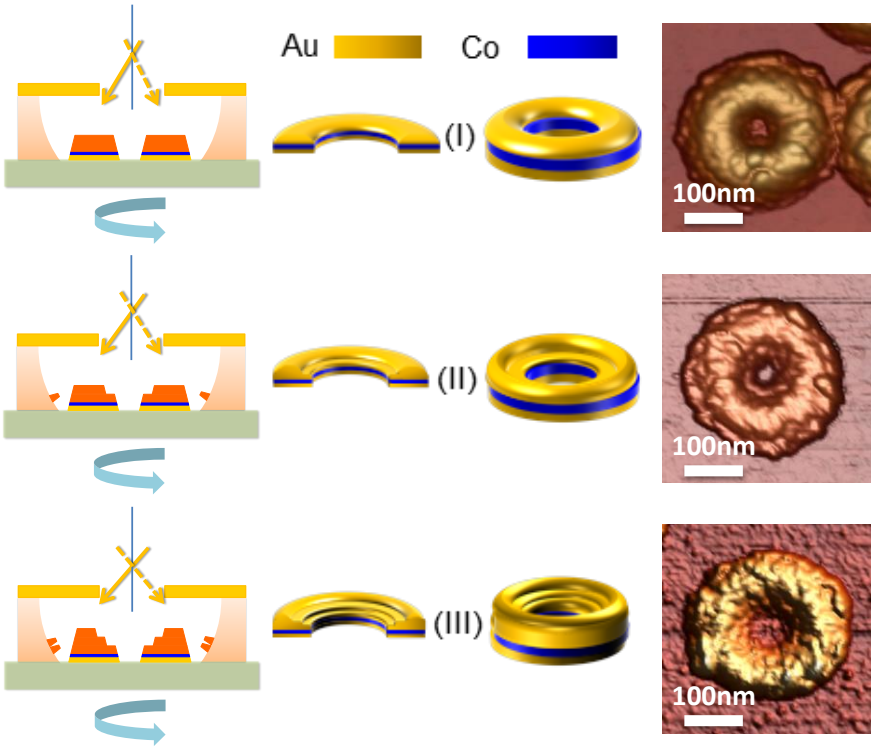

Fig. 5.1.1 Left: schematic description of the ring fabrication process. Top Au layer are shown with darker color. Central: 3D sketch of the nanorings. Right: AFM images of the nanoring structures.

the different layers; for samples (II) and (III) the distribution of the upper Au layer is controlled by depositing it in 2 or 3 sub-deposits and increasing by 2° the deposition angle between each sub-deposit. This increasing deposition angle of the top Au layer implies that a part of the Au is actually deposited out of the nanoring structure but on the vertical walls of the PMMA resist, as shown in Fig. 5.1.1 and at last they are removed during the PMMA lift off process. As a consequence the final thickness of the top Au layers are 13 nm, 9 nm, and 6 nm for samples (I), (II), and (III), respectively, as characterized from the AFM profiles in Fig. 5.1.2. Additionally, the AFM profiles clearly show the gradual shift of the apex-to-apex distance as a function of the Au top layer deposition conditions, with typical distances that vary roughly

from 130nm for the top Au layer deposited at 22^{o} (sample (I)), 150nm for the top Au layer deposited separately at 22^{o} and 24^{o} (sample (II)), to 170nm for the top Au layer deposited separately at 22^{o}, 24^{o}, and 26^{o} (sample (III)). It can be clearly seen how the gradual variation of the deposition angle for the topmost Au layer leads to nanoring structures with cross-sections having different apex positions with little effect on the outer diameter. On the other hand, the smaller internal diameter obtained for the two smaller Au deposition angles in samples (I) and (II) is due to the finite AFM tip size effects (typical radius of curvature of 5-10 nm), which influence more the image for the steeper internal ring walls.

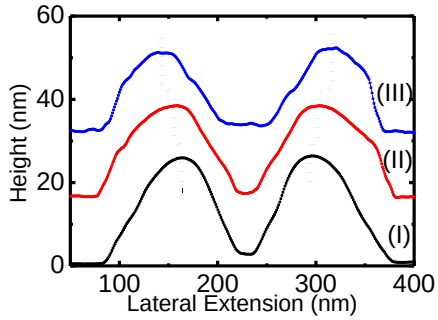

Fig. 5.1.2 Averaged AFM profiles of the three nanoring samples in Fig. 5.1.1. Data have been vertically shifted for clarity.

5.1.2 Optical and MO Characterizations

The optical extinction of the nanorings is measured with the optical microscope combined with the spectrometer. The out-of-plane magnetic properties and MO activity spectra of the nanoring structures are characterized with the p-MOKE system.
In Fig. 5.1.3 the out-of-plane hysteresis loops are shown. As discussed in subsection 4.1.2, the magnetic properties of these nanorings are mainly from the Co layers which are the same for all of the structures, therefore the hysteresis loops do not change. The structures are basically saturated at magnetic field of 1000mT, where the MO activity spectra of the nanostructures are characterized.
In Fig. 5.1.4 we show the spectral dependence of the extinction (left) and MO activity (MOA) in polar configuration (right) of these nanoring structures. As it can be seen, a strong peak in the extinction spectra is observed in the 1200-1300 nm range,

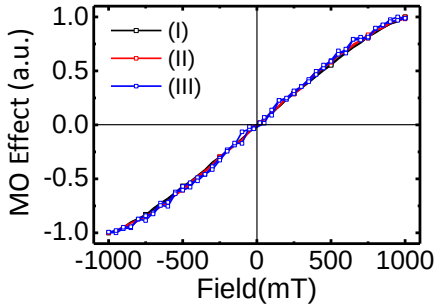

Fig. 5.1.3 Out-of-plane magnetic hysteresis loops of the three nanoring samples (I)-(III) measured from the p-MOKE system.

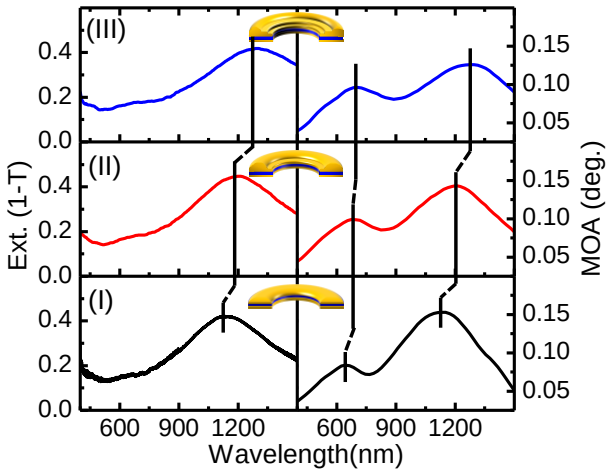

Fig. 5.1.4 Extinction (left) and MO activity (MOA) (right) spectra for the fabricated nanoring structures with different redistributions of the topmost Au layers.

corresponding to the LE bonding mode. The position of this peak experiences a gradual red shift as the nanorings' section apex to apex distance increases from sample (I) to sample (III), while its intensity remains almost unaltered. Additionally, a very weak shoulder is also observed between 600-700 nm, which can be attributed to the HE antibonding mode. On the other hand, in the MO spectra two well defined features are observed, in the same spectral regions where the optical LE and HE modes are observed, with a similar red-shift behavior as the increased apex to apex

distance for both features. Regarding the intensity of the MO activity, the low energy (LE) peak decreases its intensity as the apex to apex distance increases, while the intensity of the high energy (HE) one slightly increases, yielding a global increase of the HE vs. LE MOA ratio.

As discussed in subsection 4.1.3, the spectral position of the LE mode is controlled by the aspect ratio (AR) of the structure. From sample (I) to (III), the thickness of the top Au layer decreases, therefore the height (H) of the nanoring is getting smaller. Meanwhile the section apex to apex distance increases, illustrating a trend that the material is being distributed more outward, which implies a larger effective outer diameter (Φ_{out}) (Fig. 5.1.2). Both of these yield a gradually increasing aspect ratio (AR=Φ_{out}/H) from sample (I) to (III), which governs the gradual red-shifting of the LE mode in the extinction and MO spectra.

In conclusion, by separating deposition of the top Au layer into several sub-deposits at increasing deposition angles, we are able to control the cross-section of the nanoring and thus the plasmonic and MO responses in a fine way, which provides us an option to design the device with any desired wavelength response.

5.2 In-plane Co Redistribution Effects

In this section, we redistribute the Co layer into opposite Co dots, sectors, as well as Co continuous ring, and study the effect on optical and MO responses.

5.2.1 Fabrication

The nanorings are fabricated with the HCL technique, as shown schematically in Fig. 5.2.1. The whole deposition process can be divided into four steps. Step (I): Deposition of bottom Au ring. Prior to the Au, a thin Ti ring layer of 1∼2nm is deposited to improve the adhesion of the nanostructure to the glass substrate. Both of Ti and Au are deposited with $\theta = 24°$ and continuous rotation in the substrate about its surface normal (φ continuous) to form the ring structure. All the following steps are done at $\theta = 24°$. Step (II): Co layer. Opposite Co dots or sectors are placed on top of the bottom Au rings by selecting specific azimuthal φ angles or angle spans. For dots, $\varphi = 0°$ and $180°$ are selected. For sectors, oscillating rotations of the

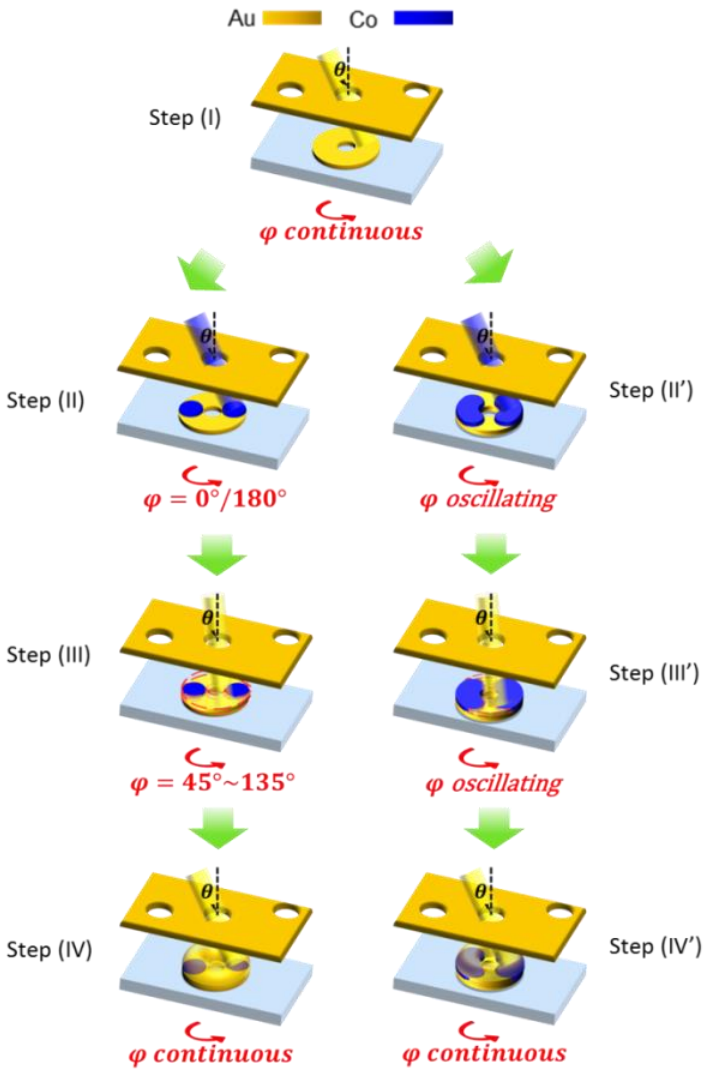

Fig. 5.2.1 Deposition sketches of the nanorings with opposite Co dots (left) and sectors (right). The whole process is divided into four steps: deposition of bottom Au ring (step (I)), Co dots or sectors (step (II)), gap filling Au (step (III)), and top Au ring (step (IV)).

substrate by $\varphi = 0{\sim}120°$ and $180{\sim}300°$ are selected. For Co continuous ring sample, continuous rotation in the substrate, namely, $\varphi = 0{\sim}360°$ is used (not shown in the figure). Step (III): Gap filling. The remaining gap space between the

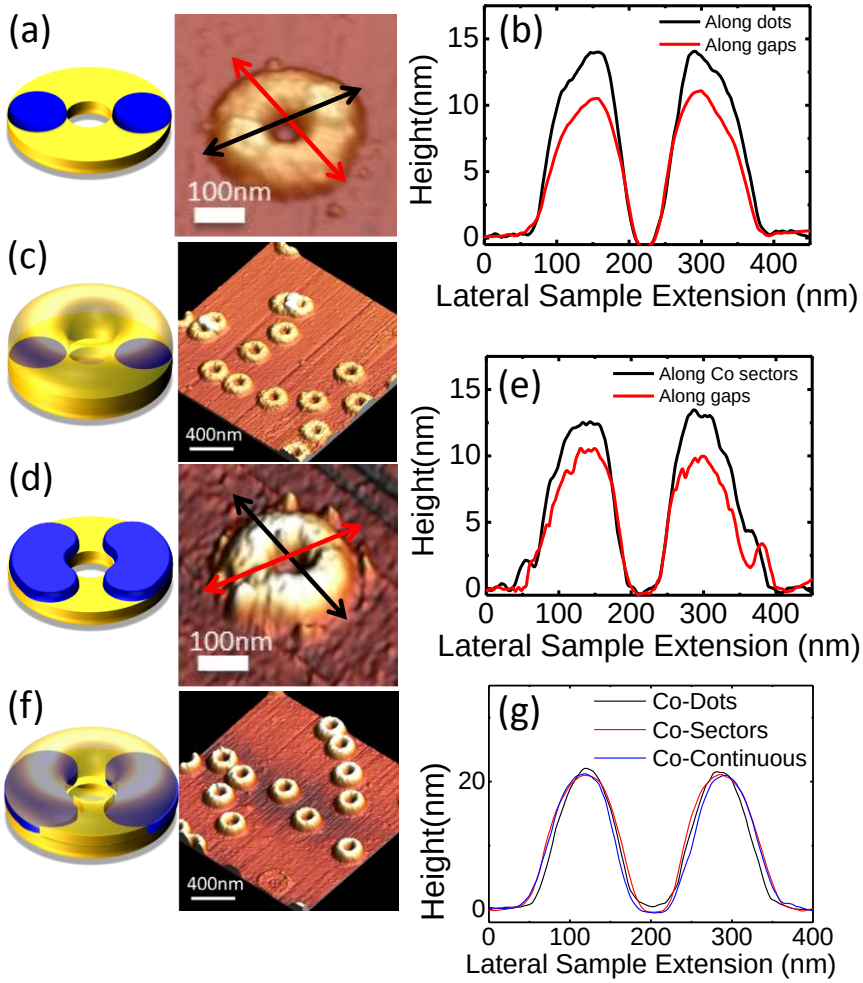

Fig. 5.2.2 Sketches and AFM images of the structures. (a) Sketch and AFM image of the Co dots sample after the deposition of Co dots. (b) Profiles along the dots (black arrow in (a)) and gaps (red arrow in (a)). (c) Sketch and AFM image of the completed Co dots sample. (d-f) are the same as (a-c) but for the Co sectors sample. (g) AFM profiles of the three structures after completely finished. All the AFM profiles are averaged from at least 10 different structures in each sample.

opposite Co dots or sectors are filled with Au by azimuthal oscillation φ of the substrate. For Co dots sample, $\varphi = 45\sim135°$ and $225\sim315°$ of Au deposition are selected for gap filling. For Co sectors sample, $\varphi = 120\sim180°$ and $300\sim360°$ are

applied. For Co continuous ring sample, no such a step is necessary. Step (IV): Top Au ring. A final Au ring is deposited on top to protect the Co constituents from oxidization and finish the structure. Thickness of each layer is: bottom Au 7 nm; Co dots/sectors/ring 5 nm; top Au 13 nm. Adequate time is used for the deposition of each layer to arrive at the desired thickness.

In Fig. 5.2.2 the AFM images of the nanostructures fabricated in this way are shown, with (a-c) for the Co dots structure and (d-f) for the Co sectors structure. The intermediate stages during the deposition process of two Co dots (Fig. 5.2.2(a)) and sectors (Fig. 5.2.2(d)) on top of the bottom Au rings are obtained by lift-off of the HCL template after step (II), where the opposite Co dots and sectors can be appreciated with gaps in between. The AFM profiles (Fig. 5.2.2(b)(e)) measured along the black and red arrows clearly confirm the height differences between the disk (sector) and the gap. After filling the gaps and deposition of the top Au layer, all the nanorings exhibit similar morphologies, as observed in Fig. 5.2.2 (c)(f) the AFM images for Co dots and sectors structures, and in Fig. 5.2.2(g) the profiles for the three structures.

5.2.2 Optical and MO Characterizations

After fabrication, the optical properties of the nanoring samples are characterized in transmission mode with the spectroscopic ellipsometry which provides the ability to measure the polarized optical extinction. The magnetic properties (out of plane) and magneto-optical properties are also characterized with the polar configuration of the MOKE system.

Magnetic Properties

By varying the magnetic field applied normally to the sample plane, the out-of-plane hysteresis are measured with the p-MOKE system, as shown in Fig. 5.2.3 where the signal is normalized for each of the sample. As it can be observed, the loops are similar to the nanodisk and nanoring structures in subsection 4.1.2 in Chapter 4. All the samples are saturated around 1100mT, where the MO spectra of the nanostructures are characterized.

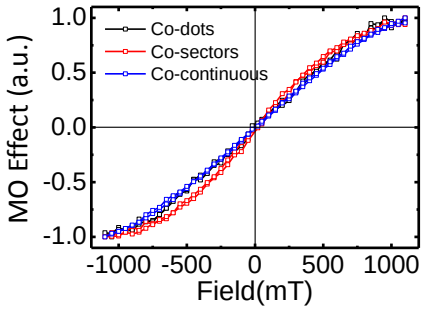

Fig. 5.2.3 Normalized polar Kerr MO signal vs. magnetic field for the Co dots, Co sectors, Co continuous ring nanoring samples.

Optical Properties: Optical Anisotropy

The polarized optical extinction spectra are shown in the left column of Fig. 5.2.4, being the light polarizations parallel (continuous line, x-polarization) and perpendicular (circles, y-polarization) to the direction along Co dots/sectors (insets in Fig. 5.2.4(a-b)). Overall, the two high energy (HE) and low energy (LE) resonant modes typically observed for nanorings are also visible here. In particular and despite the fact that the rings are morphologically isotropic, a clear optical anisotropy in the LE peak is found for the Co dots and sectors structures, due to their intrinsic compositional distribution of Co. Interestingly, the optical anisotropy is enhanced by the plasmonic resonance [132].

For the Co dots and sectors structures, the spectral position of the LE peaks for x-polarized light is located at higher energy than that for y-polarized light (Fig. 5.2.4(a-b)). All of these behaviors are reproduced qualitatively by the numerical simulation (Fig. 5.2.4(d-f), done with discrete dipoles approximation, DDA, by Prof. Luc Henrard from University of Namur). In the simulation, the LE peaks are blue-shifted compared to the experimental ones due to the different environment considered in the simulation (vacuum), and the HE peaks appear as shoulders on the left of the LE peaks instead of well-defined peaks.

These behaviors, namely, the optical anisotropy and peak locations, can be understood with the EM field redistribution induced by the inhomogeneous Co inside the nanostructures as shown in Fig. 5.2.5(a), where the electric field distributions at LE plasmonic resonances along the central plane of the Co constituents are displayed.

The electric fields outside the structures show characteristic dipolar patterns and the

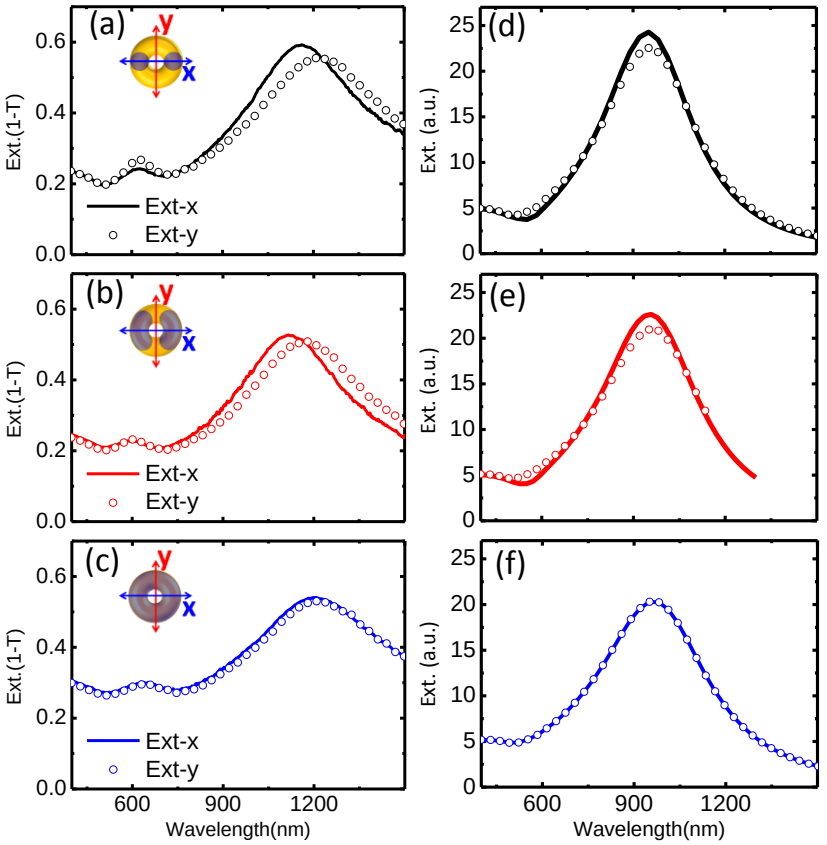

Fig. 5.2.4 Optical responses of the Co dots, sectors, continuous ring samples. (a-c) Measured polarization dependent extinction spectra. Light polarizations are along the directions shown in the insets. (d-f) Simulated extinction spectra (DDA method) with structures embedded in vacuum.

fields inside the structures have more intense parts in the poles perpendicular to the light polarization. For the structure with Co continuous ring inside, certainly no difference is there in the field distributions for x- and y-polarized light.

However, for the structures with inhomogeneous Co distributions (Co dots, sectors), the field patterns *inside* the nanostructures are affected by the Co distribution since Co has a higher optical loss than Au. For example, the inside field of Co dots structure for x-polarized light is stronger in the pole parts along y direction. For y-polarized light,

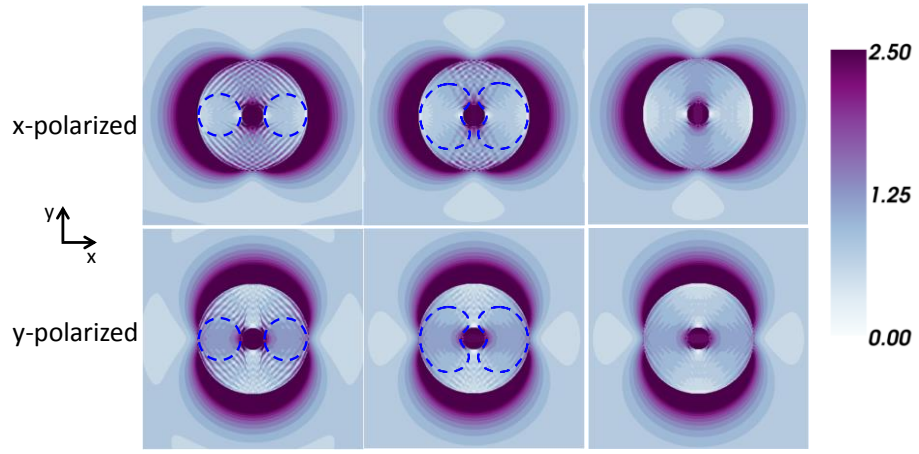

Fig. 5.2.5 Electric field magnitude distribution in the central plane of Co inclusion layer for the Co dots (left), sectors (central) and continuous ring (right) structures, obtained from the DDA simulation for the LE extinction peaks in Fig. 5.2.4(d-f) and for x-polarized light (E_x, top) and y-polarized light (E_y, bottom). The standing-wave-like distribution of the field intensity is due to the discretization of the dipoles in the simulation. The dashed blue lines correspond to the positions of the Co dots and sectors. (For the structure containing a Co continuous ring, the field maps are the same one, but rotated for easy comparison with the other structures.)

it should be more intense in the pole parts along x direction. However, due to the existence of Co dots, the fields tend to be stronger in the areas around the Co dots. This difference in the field distributions for x- and y-polarized light induced by inhomogeneous Co constituents, should be responsible for the optical anisotropy at plasmonic resonance.

Magneto-optical Properties

The spectral dependences of the magneto-optical activity (MOA) which is the modulus of the measured complex Kerr rotation, are plotted in Fig. 5.2.6(a) for all the samples and for both x- and y-polarized light. Here the MOA is expressed as

$$MOA_{x,y} = \sqrt{{\theta_{x,y}}^2 + {\varphi_{x,y}}^2}, \qquad 5.2.1$$

with $\theta_{x,y}$ the Kerr rotation and $\varphi_{x,y}$ the ellipticity, and subscripts *x*, *y* for x- and y-polarized light. As discussed in Chapter 1 (Eq. 1.3.7), $\theta_{x,y}$ and $\varphi_{x,y}$ are related to the coefficients of the reflectivity matrix as following,

$$\theta_x + i\varphi_x = \frac{r_{yx}}{r_{xx}}, \quad 5.2.2a$$

$$\theta_y + i\varphi_y = \frac{r_{xy}}{r_{yy}}. \quad 5.2.2b$$

As previously observed in Au/Co/Au nanoring samples, two peaks correlated with the enhancement by plasmon resonances are observed in the MOA spectra, but now with a gradual evolution of both their spectral position and intensity as a function of the Co configuration. Not only the corresponding LE MOA mode, but also the HE one is observed to be increasing in magnitude for structures evolving from Co dots to a complete Co ring. There is no appreciable difference observed between MOA_x and MOA_yspectra for the two perpendicular light polarizations within the experimental error. From Eqs. 5.2.1 and 5.2.2, both optical (r_{xx}, r_{yy}) and magneto-optical (r_{xy}, r_{yx}) contributions are involved in the MOA spectra presented in Fig. 5.2.6(a). Since $r_{xx} \neq r_{yy}$ for the Co dots and sectors structures (if we considered the optical responses in Fig. 5.2.4(a-b)), there should be difference between MOA_x and MOA_y ($r_{xy} = -r_{yx}$). This is not observed in Fig. 5.2.6(a), possibly due to the experimental error and small value of the difference between r_{xx} and r_{yy}. In this sense, it is more appropriate to present and compare the pure MO contribution (polarization conversion) as R_{xy} or R_{yx}, which is the squared modulus of off-diagonal elements of the reflectivity matrix

$$R_{xy} = r_{xy}^* r_{xy}, \quad 5.2.3a$$
$$R_{yx} = r_{yx}^* r_{yx}, \quad 5.2.3b$$

Eq. 5.2.3 can be further expressed with Eqs. 5.2.1 and 5.2.2 as

$$R_{xy} = {MOA_y}^2 R_{yy}, \quad 5.2.4a$$
$$R_{yx} = {MOA_x}^2 R_{xx}, \quad 5.2.4b$$

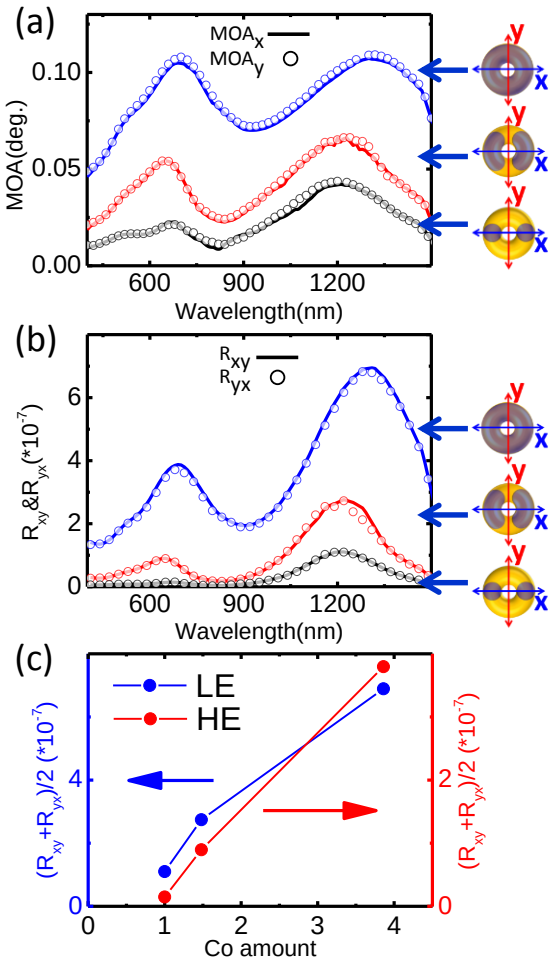

Fig. 5.2.6 (a) Magneto-optical activity (MOA) for the Co dots (black), Co sectors (red), Co continuous ring (blue) structures, and for both light polarizations. (b) Pure polarization conversion (R_{xy} and R_{yx}) for the same structures and light polarizations. (c) The dependence of the averaged pure MO component intensity ($(R_{xy} + R_{yx})/2$) for the HE and LE peaks in (b) on the amount of Co (normalized to the Co dots sample, 1 stands for the amount of Co in the Co dots sample).

with $R_{xx} = r_{xx}^* r_{xx}$ and $R_{yy} = r_{yy}^* r_{yy}$ the reflectivity for the x- and y-light, which can be modeled and calculated from the transmission data of the samples with the CompleteEASE^{TM} software for the spectroscopic ellipsometry. The model process

and results are in the Appendix 3**.** The spectral dependence of these pure MO contributions R_{xy} and R_{yx} is presented in Fig. 5.2.6(b). Two peaks are located in each spectrum at the spectral regions of the extinction peaks, indicating the enhancement of the MO effect by the plasmonic resonance. The intensities of these two peaks increase as the structure evolves from Co dots towards Co continuous ring. In Fig. 5.2.6(c), the evolution of the averaged peak magnitudes of R_{xy} and R_{yx}, as a function of the Co amount is presented for both HE and LE modes. As it can be seen, a nearly linear increase of the pure MO response with the amount of Co is observed, irrespective of the Co disposition within the structures. This implies that in the studied structures, the general MO effect is determined by the Co amount, not by the Au/Co amount ratio.

5.3 Conclusion

In this chapter, thanks to the accurate control of position, shape and dimension of the deposit with the hole-mask colloidal lithography method, we study the effect of the redistribution of the material on the optical and MO responses in the nanoring structure.

On the one hand, we modify the cross-section and subtle morphology of the nanoring structure by separating the deposit of top Au ring into several parts with increasing angles. Since the enhancement in MO activity originates from the plasmonic resonance, which is further related to the fine detail of the structure morphology (cross-section in this case) of the nanoring, this provides us a way to finely control both of the optical and MO response of the nanoring.

On the other hand, we tune the in-plane distribution of Co in the Au/Co/Au nanoring structure from Co continuous ring to opposite Co sectors and opposite Co dots. Since the Co has different optical constants from Au, the in-plane electric field distribution of the nanostructures at light illumination is modified, inducing polarization dependent optical responses in the Co dots and sectors structures, namely, the in-plane optical anisotropy. The MO responses of these structures exhibit the monotonous increase as the Co amount increases from the Co dots to Co continuous ring, being still Co the determinant for the MO response in these structures.

Chapter 6

Boosted MO Activity in Ring/Split-ring Structure

As discussed in Chapter 1, in the Au/Co noble/ferromagnetic metallic layered system, the polarization conversion r_{xy} of the system is proportional to the electromagnetic (EM) field inside the MO active Co layer according to Eq. 1.4.3 provided the Co layer is thin enough, therefore one alternative method to maximize the MO effect could be localizing as much as possible EM field in the Co region. However, since the optical loss of Co is higher than Au, the field will be "expelled" from the Co region as we discussed in Chapter 5, and it is not straightforward to spatially localize the plasmon resonance induced EM field enhancement in the MO component. To overcome this limitation, strategic design of the plasmonic structure with a "hot spot" and to locate the MO active Co component in this hot spot may be necessary.

With all of these in mind, in this chapter, we are going to study the magnetoplasmonic response of the broken nanoring structure with the Co dot located under the gap. This structure consists of a bottom complete Au nanoring with a Co dot embedded inside and a top Au split ring with the gap on top of the Co dot. The optical property and the enhancement in the MO effect of the structure will be studied. Furthermore, the electric field distribution of the nanostructure at plasmonic resonance will be studied experimentally with spatially-resolved electron energy loss spectroscopy (SR-EELS) and theoretically with discrete dipoles approximation (DDA), which provide us an intuitive image of the field distribution and confirms the increase in the EM field in the gap region which is the origin of the further MO enhancement.

6.1 Fabrication

The nanostructures used in this study are fabricated with the hole-mask colloidal lithography (HCL) technique as shown schematically in Fig. 6.1.1. The 7nm Au bottom ring (with a thin 1~2nm Ti ring layer underneath to improve adhesion to the substrate), 7nm Co dot, 7nm Au filling layer (a split ring), and 13nm top split ring with varying gap angles β (0°, 30°, 60°, 90°, 120°) are sequentially deposited with a tilted deposition angle $\theta = 24°$. The Co dot has a diameter around 120 nm, which is the width of nanoring and the diameter of the hole in the HCL template. The gap of the split ring is chosen to be right above the Co dot embedded in the bottom Au ring, as shown in the sketch at the bottom of Fig. 6.1.1, where the gap angle β is indicated. To avoid the possible Co oxidation, the gap is filled with SiO_2. To further confirm the MO effect enhancement by the gap, a control sample with gap angle $\beta = 60°$ and the Co dot embedded opposite to the gap is also fabricated.

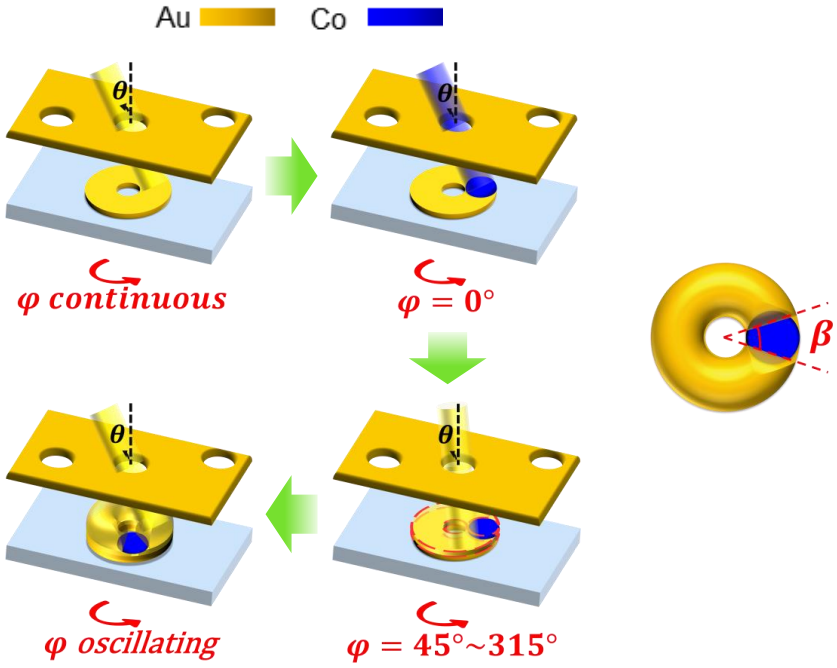

Fig. 6.1.1 Left: sketch for the deposition process. Right: top view of the sketch of the nanostructure with gap angle β.

In Fig. 6.1.2 we show the AFM images of a representative nanostructure fabricated in this way with the gap angle $\beta = 120°$, unfilled (Fig. 6.1.2(a)) or filled (Fig. 6.1.2(b)) with SiO_2 in the gap. The gaps can be appreciated in both of the cases. The profiles of such nanostructures are shown in Fig. 6.1.2(c), with red and blue lines for the structure unfilled with SiO_2 along the directions illustrated in the inset, and grey line for the structure filled with SiO_2 along the direction crossing the gap as shown in Fig. 6.1.2(b). All the profiles are averaged from at least 10 different structures of the same sample. As it can be observed, the gap area before filling SiO_2 has a height around 13nm lower than the rest of the nanostructure, which is the height of the top Au split ring layer. After filling SiO_2 (~ 7nm), the height of the gap area increases (gray line).

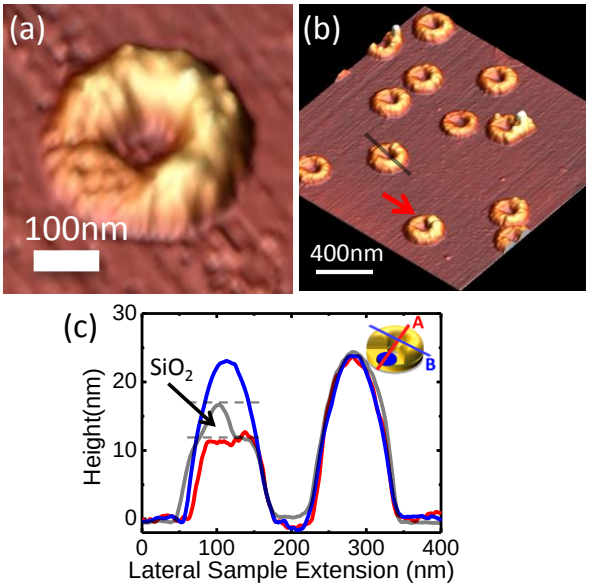

Fig. 6.1.2 AFM images of the ring-split ring nanostructure with gap angle $\beta = 120°$ without (a) and with (b) SiO_2 filling in the gap. Red arrow in (b) indicates the position of the 120° gap. (c) Profiles of the ring-split ring structures with $\beta = 120°$ gap angle unfilled with SiO_2 along the directions depicted in the inset (red and blue lines), and filled with SiO_2 (grey lines) along the direction illustrated by gray line in (b). After filling SiO_2 the gap area obtains a height 7nm higher than before.

6.2 Optical and MO Characterizations

After fabrication, the optical properties of the nanoring samples are characterized in transmission mode with spectroscopic ellipsometry (SE). The magneto-optical properties are also characterized with the polar configuration of the MOKE system.

Magnetic Properties

By varying the magnetic field applied normally to the sample plane, the out-of-plane hysteresis are measured with the p-MOKE system, as shown in Fig. 6.2.1 where the MO signal is normalized for each sample. As it can be observed, all the nanostructures exhibit similar magnetization reversal behavior as expected since the same Co dot is embedded and surrounded by similar Au materials in each structure. All the samples are saturated around 1100mT, where the MO spectra are characterized. In the inset of Fig. 6.2.1, the hysteresis curve of the sample with 120° gap in this series of nanostructures is compared with the Co dots sample in Chapter 5 which has no gap on top, and shows very similar behaviors due to the similar Co dot or dots inside the structures.

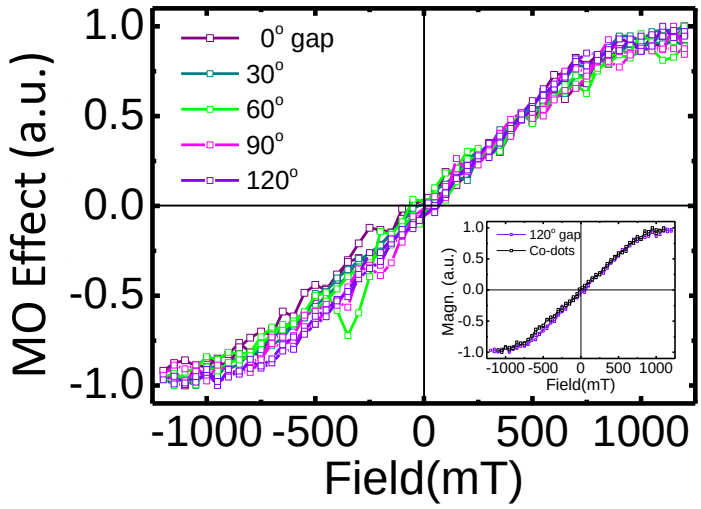

Fig. 6.2.1 Normalized out-of-plane MO signal vs. magnetic field for the structures with Co dot embedded inside and below the gaps.

Optical Properties

In Fig. 6.2.2, we show the experimental and simulated optical extinction spectra of the nanostructures for both x- and y-polarized light as defined in the insets: x-polarization along the Co dot and gap direction, and y-polarization perpendicular to this direction. The experimental results are measured with spectroscopic ellipsometry (SE), and the simulation is done with discrete dipoles approximation (DDA), by Prof. Luc Henrard from University of Namur.

As can be seen, the two characteristic high energy (HE) and low energy (LE) modes of nanoring are still observed for all the structures, being the LE one more intense. This LE mode exhibits a redshift and an increasing peak width as the gap opens up, especially when the light is polarized along the y-direction. Furthermore, optical anisotropy exists for each structure. Specifically, optical anisotropy is already present in the structure without gap ($\beta = 0°$) due to the in-plane compositional symmetry breaking induced by the Co dot, similar to the 2-Co-dots structure in Chapter 5. As the gap is introduced ($\beta = 30°$) and opening up, this optical anisotropy increases largely. All of these behaviours are qualitatively reproduced by the simulation. Due to the different environment (vacuum) considered in the theory, the extinction peaks in the simulation appear blue-shifted with respect to the experimental ones.

Obviously, the shift of LE modes and the increasing optical anisotropy (Fig. 6.2.2) as the gap opens up can be easily understood with the morphological modification of the gap and the subsequently induced redistribution of EM field at the LSP resonance excitation, as shown in Fig. 6.2.3, where the electric field distributions in the central plane of the Co dot for all the structures and both light polarizations are shown.

For the structure without gap ($\beta = 0°$), the larger optical loss of Co dot induces the "expelling" of the electric field from the Co region to the Au region, especially for y-polarized light where electric field inside is more intense on the pole parts along x direction, as can be observed in Fig. 6.2.3. This has been discussed with the Co 2 dots sample in Chapter 5 and is responsible for the optical anisotropy at resonance of this structure.

The introduction of the gap (from $\beta = 30°$ to $\beta = 120°$) clearly further modifies electric field distribution around, exhibiting a great enhancement, especially for y-polarized light. This modification is due to the new surface created by the gap, which supports new charge distribution at LSP resonance [33]. The current difference

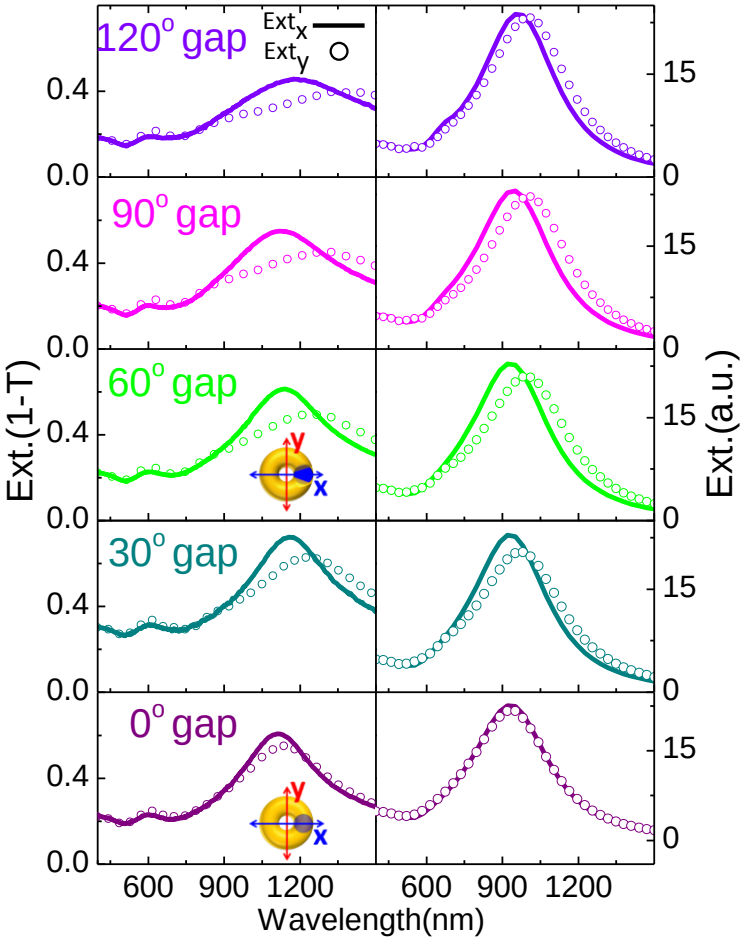

Fig. 6.2.2 Experimental (left) and simulated (right) optical extinction spectra of the nanostructures for both x- and y-polarized light as defined in the insets: x-polarization along the Co dot and gap direction, and y-polarization perpendicular to this direction. The experimental results are measured with spectroscopic ellipsometry (SE), and the simulation is done with discrete dipoles approximation (DDA), by Prof. Luc Henrard from University of Namur.

in the field distributions between x- and y-polarized light induced by the gap introduction is mainly responsible for the increased optical anisotropy and spectral shift of LE modes as the gap angle increases. Additionally, as gap opens up, the amount of the filling SiO_2 in the gap is increasing, which also contributes to the

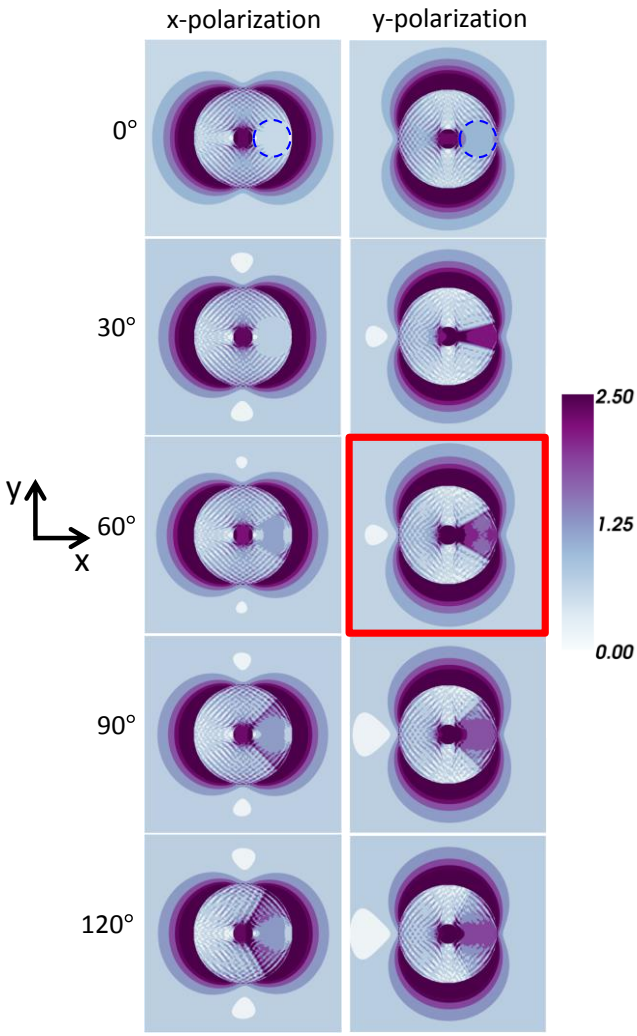

Fig. 6.2.3 Electric field magnitude distribution in the central plane of Co dot, corresponding to the LE extinction peaks in Fig. 6.2.2 obtained from the DDA simulations. For x- and y-polarized light, E_x (left) and E_y (right) components are shown, respectively. The standing-wave-like distribution of the field is due to the discretization of the dipoles in the simulation method. The dashed blue circles in the first row correspond to the position of the Co dot. Red square marks the 60° structure with maximum MO effect.

optical anisotropy and mode spectral shift.

This field further enhancement in the gap area is further confirmed experimentally

with spatially-resolved (SR) high-resolution electron energy loss spectroscopy (EELS), which is a very powerful technique to experimentally obtain the in-plane EM field distribution at plasmon resonances [133,134]. The SR-EELS analyses are performed on the β=60° gap structure, which exhibits the maximum MO effect (see below). Fig. 6.2.4(a) displays the high-angle annular dark field (HAADF)-STEM micrograph of this nanostructure, in which the gap area is clearly visible. In Fig. 6.2.4(b), the sum of the EELS spectra (black solid line) obtained from the area marked with the blue square (i) in Fig. 6.2.4(a) is shown, along with the unpolarized optical extinction spectrum (black circles) measured for the same sample, using wavelengths as the horizontal axis for easier comparison between each other.

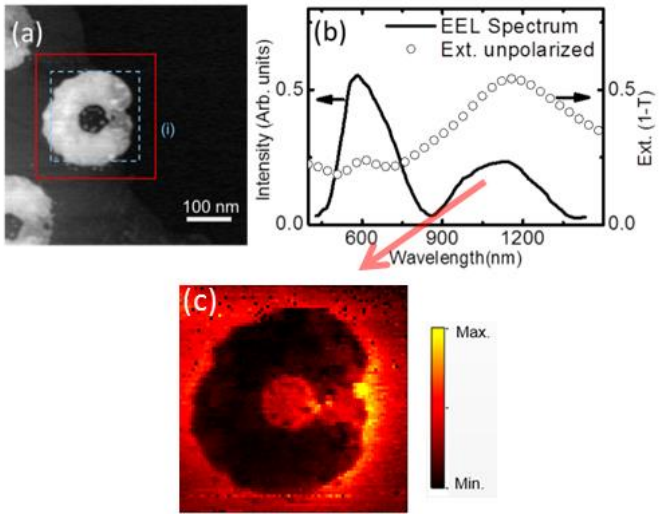

Fig. 6.2.4 (a) HAADF-STEM image of the nanostructure with gap angle $\beta = 60°$, where an EELS SPIM has been recorded in the area marked with red square. (b) EEL spectrum, after background subtraction, corresponding to the sum of 400 spectra collected from the blue marked area (i) in (a), together with the extinction spectrum of the same sample for unpolarized light. (c) EEL signal intensity map for the LE mode (red arrow) of this nanostructure. EELS experiment is done by Dr. Raul Arenal from Universidad de Zaragoza, Spain.

As it can be seen, there is a remarkable similarity between these two spectra, with both HE and LE modes clearly observed in the EELS spectra, but with different

relative intensities due to the different excitation mechanisms involved in the two measurements [133,135]. Finally, the EEL signal map corresponding to the EM field intensity distribution of the LE mode is displayed in Fig. 6.2.4(c). A clear increase in the EM field in the region surrounding the split ring gap is observed, with a magnitude much larger than the other area surrounding the structure. We should clarify here that the map in Fig. 6.2.4(c) corresponds to the EM field distribution induced by the unpolarized light, therefore this field map can be considered as a combined E_x and E_y field distribution in Fig. 6.2.3 for the 60° gap structure. In this way, both of the EELS experiment and simulation confirm that a "hot spot" with further enhanced EM field is generated in the gap area of the nanostructure.

Magneto-optical Properties

The magneto-optical activity (MOA) spectra for both light polarizations of the nanostructures are shown in Fig. 6.2.5(a). Similar to the process in Chapter 5, here we also extract the pure MO components (modulus of the polarization conversion) R_{xy} and R_{yx} with the optical extinction (Fig. 6.2.2(a)) and MOA data. The derived reflectivities with the CompleteEASE™ software for all the structures are shown in Appendix 3. The R_{xy} and R_{yx} spectra are shown in Fig. 6.2.5(b). Due to the simple plasmon enhanced mechanism of the MO effect, two HE and LE peaks are observed in all the corresponding MOA spectra as well as in the pure MO effect, R_{xy} and R_{yx} for all the structures. The redshift behavior of the LE plasmonic modes as the gap opens up results in the redshift of the LE MO peaks, and the optical anisotropy results in the anisotropy of MO activity. After removing the optical contribution in MO effect, the pure MO components, R_{xy} and R_{yx}, display the same magnitudes within the experimental error.

More importantly, the intensity of the LE MO peak shows a very strong dependence on the gap angle, exhibiting a maximum for intermediate angle around 60°. This is clearly shown as an evolution in Fig. 6.2.5(c), where we present the averaged intensities of R_{xy} and R_{yx} at LE peak positions as a function of the gap angle (black squares). The maximum value at intermediate gap angle (60°) exhibits an enhancement by a factor of 3 with respect to the 0° gap (no gap). A qualitatively similar behavior is also observed for the weaker HE mode (blue squares) but with the maximum MO effect at 30° gap angle.

The MO effect in such Au/Co/Au nanostructure is related to the MO constant $\varepsilon_{MO,Co}$

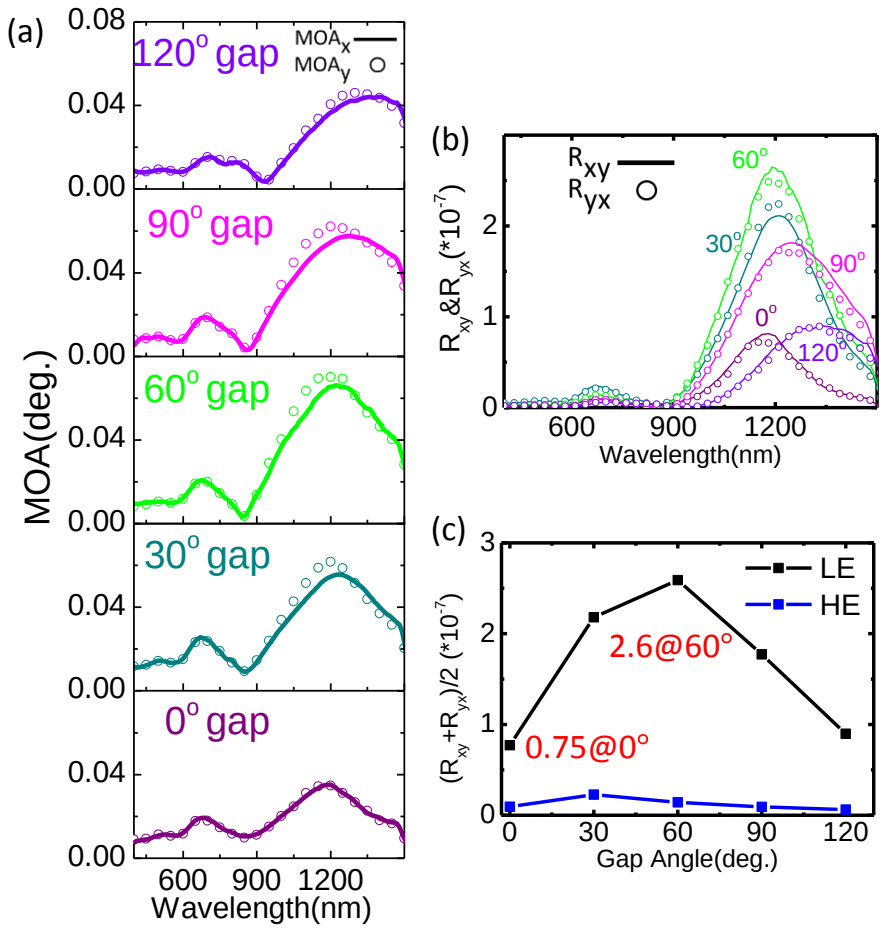

Fig. 6.2.5 (a) Magneto-optical activity (MOA) spectra of the nanostructures for both light polarizations. (b) Pure MO components R_{xy} and R_{yx} extracted from experimental optical extinction (Fig. 6.2.2) and MOA data. (c) Dependence of the LE (black squares) and HE (blue squares) MO peak intensities (averaged R_{xy} and R_{yx}) on the gap angle. Connection lines are guides for eye.

(off-diagonal elements in the dielectric tensor) of the Co material, as well as the field intensities E_x and E_y inside the Co regions. Therefore, it is reasonable to assume that the observed behavior in the gapped structures, with a strong dependence of the MO effect on the gap angle is due to the efficient localization of the EM field in the Co dot. This assumption can be actually confirmed by the electric field distribution in

Fig. 6.2.3. As it can be seen, for x-polarized light we observe a gradual increase of the intensity of the electric field inside the Co dot with increasing gap angle. On the other hand, for y-polarization, the electric field in the Co exhibits maximum values for gap openings of 30° and 60°, and being less intense for larger gap angles. This dependence on the gap angle for y-polarization is identical to that observed for the LE MO activity, therefore confirming the gap antenna effect as the responsible for the observed enhancement in the MOA. Similarly, the EEL signal further enhancement in the gap area in Fig. 6.2.4(c) confirms this explanation experimentally.

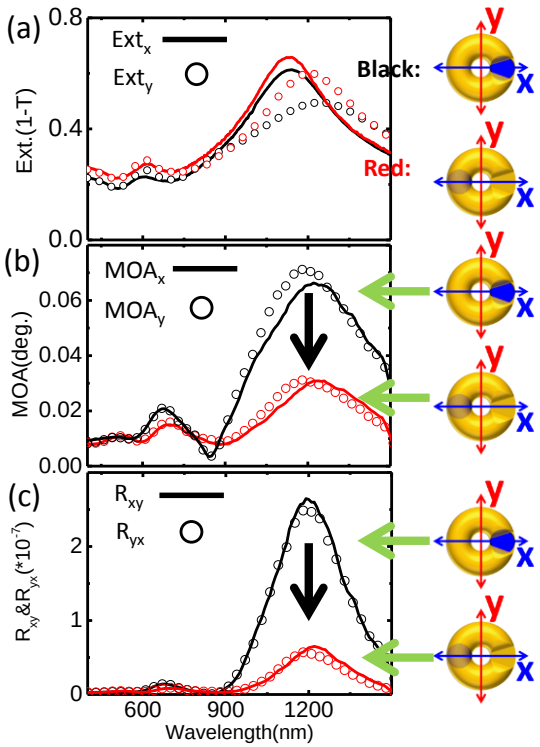

Fig. 6.2.6 Comparison between samples with Co dot embedded under (black) and opposite to (red) the gap of $\beta = 60°$. Incident light polarizations with respect to the nanostructures are shown as insets. Extinction (a), MO activities (b) and pure MO components (c) spectra of the two structures are shown.

To further confirm this gap-enhanced MO effect, another structure with the Co dot in the opposite position to the gap region is also prepared (Fig. 6.2.6). As it can be

observed, although the extinction spectra are similar (Fig. 6.2.6(a)), the MO activity obtains a reduction by a factor of two (Fig. 6.2.6(b)), and the pure MO components reduce even much more (around a factor of 5, Fig. 6.2.6(c)). This is a sound proof that the further EM field localization by the gap results in the enhancement in the MO effect.

6.3 Conclusion

In this chapter we present a proof-of-concept structure fabricated by HCL technique, which demonstrates the route to maximize EM field in desired regions where MO-active elements are placed and yields outstanding results in terms of further enhanced MO activity. A new structure which consists of a split ring placed directly on top of a magnetoplasmonic ring element is presented. An extra EM field localization is generated in the gap area, which is on top of the Co nanodot inserted in the bottom Au ring. In addition to the intrinsic plasmon enhanced MO activity of the magnetoplasmonic ring, the MO activity is further enhanced by the extra EM field localization in the gap. Furthermore, by considering different gap openings, a fine tuning and optimization of the extra EM field localization is obtained, resulting in a further increase of MO effect by a factor of 3 with respect to the equivalent magnetoplasmonic ring without additional gap. The enhancement in the EM field in the gap area is further confirmed both theoretically with electric filed distributions for each structure and light polarization, and experimentally with EEL signal mapping image at the low energy resonance range corresponding to the field distribution excited by unpolarized light.

Chapter 7

Conclusion and Overlook

Throughout this thesis, the fundamental optical and magneto-optical (MO) responses of randomly distributed nanoring structures are systematically studied in the visible and near infrared range and the mechanisms of localized surface plasmon (LSP) resonance enhancement on the optical extinction and MO activity are discussed. Furthermore, a series of methods have been proposed in order to control and even improve the optical and MO performances of the nanoring structures.

First, a complete protocol based on the hole-mask colloidal lithography (HCL) method is optimized to adapt to the fabrication of nanoring structures. The fabrication of the HCL template is systematically studied: the PS sphere density on the template can be controlled by varying concentrations of the PDDA solution and PS sphere suspension, which will in turn determine the nanostructure density; the thickness of the Au mask in the template is critical for the nanoring formation and for sputtered Au mask a minimum thickness of 30nm is required in our process. Moreover, although not used in this thesis, further control of the hole shape and diameter have been explored by varying the deposition angle for the Au mask and rotating the substrate, even by an additional deposition of Au after the template is completed.

The deposition process of the nanostructures with the HCL template is considered geometrically. Basically, the morphology of the nanostructure is controlled by the deposition angle and rotation in the template. With an adequate tilted angle and continuous rotation, a nanoring can be formed. By alternating the material source, the nanoring structures with multiple components (such as Au/Co/Au) are feasible. Nanodisk (dot) and nanosector (slit ring) structures can also be fabricated with non-rotation or oscillating rotation in the template.

With this fabrication protocol, a series of Au/Co/Au trilayer structures starting from the nanodisk to nanoring have been completed and studied. As the deposition angle increases, the fabricated nanostructures evolve from the nanodisk to nanoring.

Meanwhile, the unimodal plasmonic resonance behavior of the nanodisk evolves to the bimodal resonance behavior of the nanoring. This also results in the transition from single enhancement peak to double peaks in the MO effects of the nanostructures. It is found that the aspect ratio (outer diameter/height) of the nanostructure is the main factor that determines the spectral position of plasmonic resonance in the low energy (LE) range as well as the corresponding MO peak. For nanoring structure, the spectral position of the other high energy (HE) peak is mainly controlled by the cross-section of the nanoring arm.

The behavior of bimodal optical and MO responses of the nanoring is well explained with the plasmon hybridization model. The incident x-polarized light induces the dipolar disk and hole plasmons supported by the outer (disk-like dipole) and inner (hole-like dipole) surfaces of the nanoring, respectively. Without the magnetic field, the disk-like dipole couples (hybridizes) with the hole-like dipole in a parallel or antiparallel fashion to give the LE or HE resonance modes. In presence of polar magnetic field which points perpendicularly to the structure plane, both of the disk-like and hole-like dipoles rotate in-plane, namely, obtain dipolar y-components, and the sum of the y-components (MO dipoles) normalized to the sum of the x-components (optical dipoles) is proved to give the ultimate MO effect.

By increasing the deposition angle during the deposition process, the cross-section of the nanoring structure can be controlled continuously, which means a fine control of the aspect ratio of the nanostructure, therefore the spectral positions of the plasmonic resonance and the enhanced MO peaks can be controlled in a fine way.

Furthermore, with non-rotation or oscillating rotation in the template, the Co components embedded in the nanoring are controlled to form opposite Co dots and opposite Co sectors, respectively. The different optical constants of Co from Au modify the in-plane electric field distribution of the nanostructures at plasmonic resonance, inducing the in-plane optical anisotropy. The MO responses of these structures, on the other hand, are still proportional to the Co amount.

At last, a proof-of-concept method is proposed to further enhance the MO effect in such magnetoplasmonic rings (which has already exhibited the enhanced MO effect by plasmonic effect) via maximizing the electromagnetic (EM) field in desired regions where MO-active Co elements are placed. This is done by generating a gap on top of the Co nanodot embedded in the Au nanoring. An extra EM field localization is realized in the gap area at the LE plasmonic resonance, resulting in the further

enhanced MO effect. By considering different gap openings, a fine tuning and optimization of the extra EM field localization is obtained, and consequently the optimized MO effect has an enhancement factor of 3 with respect to the equivalent magnetoplasmonic ring without an additional gap. This localization of the EM field in the gap area is further confirmed both theoretically with simulated electric field maps, and experimentally with EEL signal mapping image.

Following the work in this thesis, future studies can be done in different fields.

First, as already shown in the earlier work by the other authors, nanoring structure can be used as a good plasmonic bio-sensing platform. With the magneto-optical functionality, the MO signal contains the phase information of the light, which could lead to a much better signal-to-noise ratio in the sensing performance. Therefore, it is worth to explore the potential of the magnetoplasmonic nanoring as the sensing platform.

Second, new nanostructures with MO functionalities, such as split rings, rods, stacked structures, can be realized with the HCL method. Since different effects are involved in these structures, for example, optical anisotropy for the split rings and rods, optical magnetic dipole observed in the split rings and stacked disks, their interaction with the MO effect and control by the magnetic field would be very interesting.

Third, as a versatile method, the HCL method has already shown its ability in the fabrication of chiral structures. Since both of the chiral and MO effects can rotate the light polarization (optical activity and MO activity) which is greatly enhanced at the plasmonic resonance, structures with both chiral and MO functionalities are interesting, with which the interaction between the chiral and magneto-optical effects, as well as the possible manipulation of chiral effect by magnetic field, could be studied and realized.

At last, due to the limitation in the HCL method, e.g. only randomly distributed structures can be obtained, horizontal cross-coupling between the isolated nanorings and its corresponding impact on the plasmonic and MO effects in the nanoring dimers or nanoring arrays, are not possible to study in the current work. Therefore, on the one hand, to further develop the current HCL method, for example, to combine it with the optical lithography, in order to obtain periodic arrays, will be interesting and necessary. On the other hand, the other lithography methods, such as the nanosphere lithography, electron beam lithography, etc., can also be improved and used to

fabricate nanoring arrays in a large area (over mm^2). Due to the resonant radiation coupling between the isolated nanostructures, sharp features can appear in the spectra and possible greatly enhanced MO effect could be observed. Both of them will lead to a better performance as a sensing platform, as well as the optical elements such as the optical isolator.

Appendix

A1 Some Other Techniques Used in the Template Fabrication

A1.1 Oxygen Plasma Stripper

Oxygen (O_2) plasma has been widely applied in the surface cleaning and modification process, especially for the organic and polymer surfaces [136]. To generate the O_2 plasma, O_2 gas is fed into a vacuumed chamber and subjected to a strong radio frequency (RF) electromagnetic field which is usually provided by a frequency generator. During the switching process of the electric field, the remnant free electrons in the chamber will be accelerated to a high speed, in order to strike, ionize and excite the O_2 molecules, as well as break their molecular bonds (red circles in Fig. A1.1(a)).

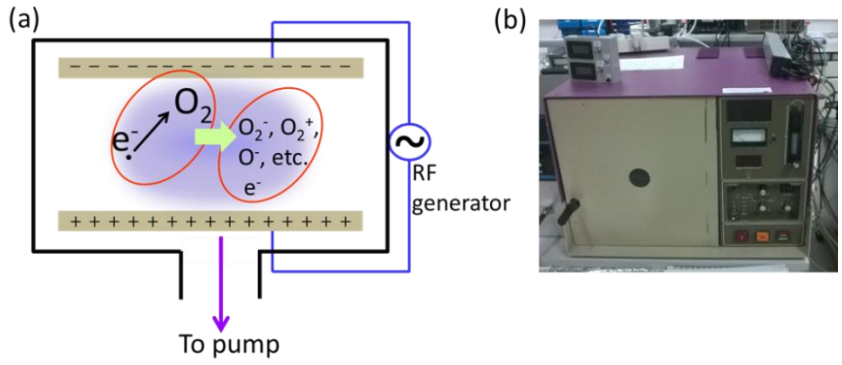

Fig. A1.1 (a) Sketch of the O_2 plasma generation. (b) O_2 plasma stripper used in the experiment.

The created ionized oxygen species such as O_2^+, O_2^-, O_3, O^+, O^-, etc., as well as the second free electrons are accelerated also by the electric field and bombard each other and the remaining O_2 molecules. Thus a chain reaction is formed and the plasma is created. When the excited states relax to the lower energy states, photons with vacuum ultraviolet (VUV) energy are released. This is why the light blue color is always observed in the O_2 plasma. The VUV energy photons is very efficient to break the organic bonds, meanwhile the ionized oxygen species can effectively react with the organic material to produce H_2O, CO_2 and hydrocarbons, etc.

In our template fabrication process (Table 2.1 in Chapter 2), after coating PMMA layer onto the substrate (glass or silicon) with the spinner, the short-time etching with O_2 plasma can create textures on the PMMA surface and modify the surface chemistry [136], resulting the reduced hydrophobicity, which will facilitate the deposition of nanospheres in the following procedures. Fig. A1.1(b) shows the O_2 plasma stripper used in the experiments. Typical O_2 pressure, feeding power, and time for the PMMA etching process are 450mtorr, 50W, and 15s, respectively.

A1.2 Reactive Ion Etching (RIE)

Similar to the O_2 plasma, reactive ion etching (RIE) also uses the high frequency electromagnetic field to generate plasma in low-pressure gases [137]. As shown in Fig. A1.2(a), the wafer or substrate to be etched is situated on the bottom of the chamber, and being electrically isolated from the rest part of the chamber. During the oscillation cycle of the applied electric field, the electrons could be electrically accelerated much faster than the massive ions, with a portion of them striking both the wall of the chamber and the wafer. The electrons absorbed into the walls are simply fed out to ground and will not cause any change to the electric state of the system. On the other hand, the portion of electrons reaching to the electrically isolated wafer will be accumulated and generate a total negative charge (solid black arrow in Fig. A1.2(a)). Due to the higher velocity and thus faster loss of free electrons in the gaseous part, the plasma which is originally neutral gets now positive charges, therefore a positive voltage between the plasma and the wafer will be established. Driven by this voltage, the positive ions in the plasma drift to the wafer (dashed arrow in Fig. A1.2(a)), where these ions can both chemically react with the wafer surface and physically sputter the

material off due to their large kinetic energies. The etched profiles in the sample with RIE are usually anisotropic due to the almost vertical delivery of the reactive ions, meanwhile the etching results also depend strongly on the process parameters, such as the pressure, gas species, as well as the RF power fed into the system. Typical gases for etching process are O_2, CF_4, as well as the gas mixture such as O_2 and Ar, etc., according to the materials to be etched.

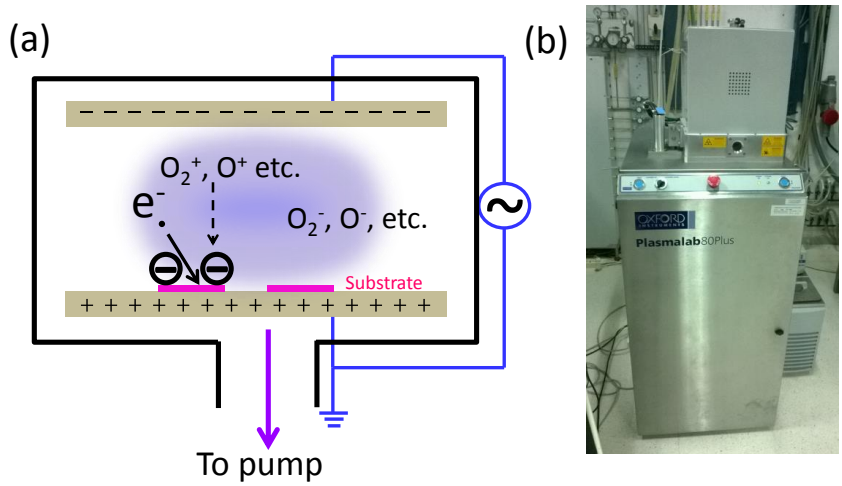

Fig. A1.2 (a) Sketch of the operation principle of the RIE system. Electrons accumulate on the isolated substrate and a total negative charge is formed. The voltage difference between the plasma (positive charge due to the loss of electrons) and substrate accelerates the oxygen (or some other positive radicals) radicals to the substrate, where both reaction and sputtering effects happen to etch the substrate. (b) RIE system used in our experiments.

In Fig. A1.3 we schematically show a cross-section sketch of the HCL template to be etched by the RIE. During the etching process, O_2 gas is fed into the chamber and O_2 plasma is induced by the RF field. The accumulated electrons on both of the Au mask layer and PMMA surfaces and the positive charges in the plasma cause the positive oxygen ions to drift and strike the PMMA layer as well as the Au layer. Due to the different material properties, PMMA is etched efficiently by the simultaneous physical sputtering and chemical reaction. Therefore vertical pores are formed in the PMMA layer (dashed vertical lines) uncovered by the Au layer, and extra etching time

will cause the vertical pores to extend horizontally (dashed black curves). Due to the anisotropic etching property of RIE, the etching efficiency along the vertical direction is much higher than that along the horizontal direction, therefore a longer time period will be needed to obtain the enough room horizontally. In our experiments, a RIE system (Oxford Instruments Plasmalab 80Plus) is used (Fig. A1.2(b)). Typical etching power and time are 50W, 150s for HCL templates of nanodisk structures, and 50W, 450s for templates of nanoring structures.

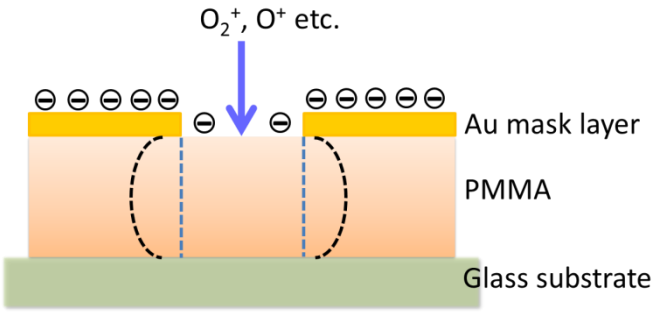

Fig. A1.3 Schematic etching process of a HCL template with RIE system. Only PMMA uncovered by Au will be etched efficiently.

A2 Further Optimization of the HCL Template

A2.1 Hole Shape Control

Different hole shapes can be used to generate nanostructures with various morphologies, such as the round/elliptical nanodisks, round/elliptical nanorings, etc. The hole is the direct projection of the PS sphere, therefore with normal or oblique deposition of Au and non-rotation in the substrate, round or elliptical hole can be generated (Fig. A2.1), which can be used for the deposition of the round nanodisk, split ring, or elliptical nanodisk, etc.

In Fig. A2.1 we show the sketch for the generation of the elliptical holes with oblique deposition of Au mask. The hole diameter can be calculated with

$$D_1 = R \tan\frac{\pi/2-\theta}{2}, \quad \text{A2.1a}$$

$$D_2 = R \cot\frac{\pi/2-\theta}{2}, \quad \text{A2.1b}$$

$$D_{hole} = D_1 + D_2, \quad \text{A2.1c}$$

where R is the radius of the PS sphere and D_{hole} is the long axis of the elliptical hole. It is obvious that the short axis of the elliptical hole is always $2R$.

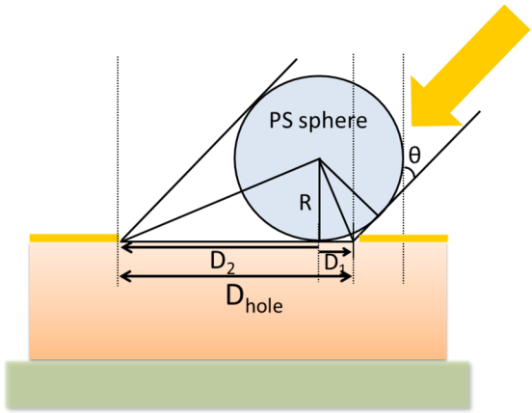

Fig. A2.1 Sketch of the elliptical nanohole generation by oblique deposition of Au.

A representative template deposited by sputtering at $\theta = 45°$ is shown in Fig. A2.2(a) and below is the corresponding averaged profiles along the long and short axes of the holes. The corresponding elliptical nanodisks are shown in Fig. A2.2(b), which are deposited normally with this template. The disk profiles along the long and short axes shown below manifest different diameters. As a statistic, the diameters of the elliptical hole and nanodisk in (a) and (b) along both the long and short axes are shown in the table (Fig. A2.2(c)). The smaller diameters of the hole than the disk are due to the finite radius of the AFM tip, which usually results in larger diameter for disk but smaller one for hole. The experimental aspect ratios (long/short axes) for the nanohole and nanodisk are smaller than the geometrically calculated one according to Eq. A2.1, and the relatively large difference between them is possibly due to the experimental errors in the parameters.

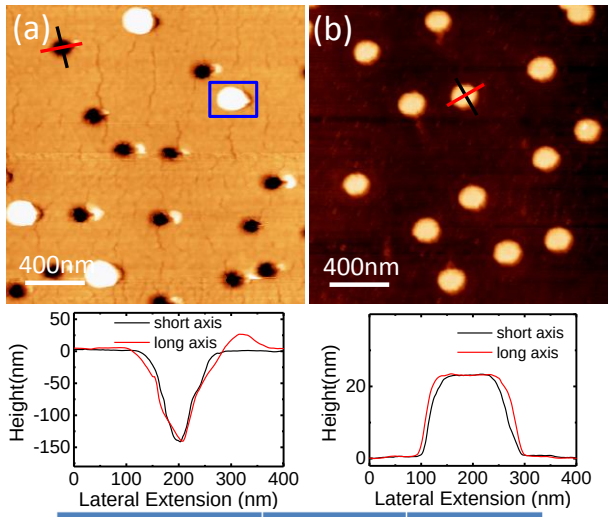

(c)	hole	Disk
Long (L, nm)	171.3	189.2
Short (S, nm)	138.6	174.3
Aspect Ratio (L/S)	1.24	1.08
Calculated L/S	1.41	1.41

Fig. A2.2 (a) AFM image of the template after RIE etching (Au deposition angle $\theta = 45°$). Blue square shows the PS sphere remaining on the template. Black and red lines show the directions for the profile measurement. Below: averaged profiles of the hole along short (black) and long (red) axes. (b) AFM image of the elliptical nanodisk deposited normally with the template in (a). Below: averaged profiles of the disk along short (black) and long (red) axes. (c) Statistics of the diameters of the elliptical nanohole and nanodisk, and the experimental and calculated aspect ratios.

A2.2 Hole Diameter Control

For normal deposition of the Au mask for the template fabrication, the hole diameter *D* in Fig. 3.2.1 is the same as the diameter of the PS sphere, therefore the control of the hole diameter *D* can be realized by varying the size of the PS sphere. On the other

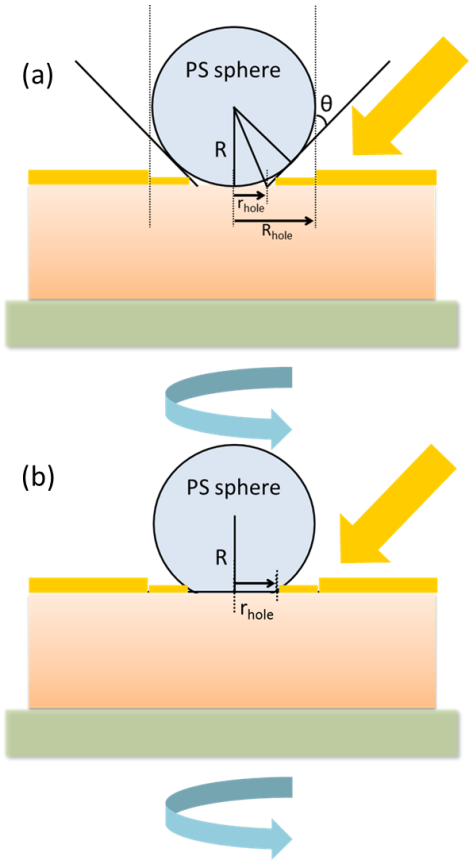

Fig. A2.3 Control of the hole diameter by tilted-angle deposition of Au mask and rotation in the substrate. (a) Sketch of the ideal deposition geometry. (b) Actual deposition geometry where the interface between the PS sphere and the PMMA layer is flat. The flat interface determines the limited hole diameter that can be realized with this method.

hand, during the nanostructure deposition process, the shrinking effect of the hole can also be utilized to modify the hole diameter precisely [116]. However, in our experiments, this effect is not obvious (Fig. 3.2.4). Here we show a method to control the hole diameter systematically and precisely, by the combination of tilted-angle deposition of the Au mask and simultaneous rotation in the substrate (Fig. A2.3).

40nm Au film is deposited with thermal evaporation at a tilted angle θ and rotation in the substrate, as shown in Fig. A2.3(a), where the radius of the hole is

$$r_{hole} = R \tan\frac{\pi/2-\theta}{2}, \qquad \text{A2.2}$$

with $R = R_{hole}$, and R the radius of the PS sphere. The PS sphere works as the deposition mask, and thus the Au film around the hole has a smaller thickness which is a half of the deposited thickness as schematically shown in the figure. The thermally evaporated Au film has a better stiffness than the sputtered one as mentioned previously, therefore this 20nm thick Au film around the hole will not be bent.

In Fig. A2.4(a) the AFM images of the obtained templates after RIE etching are shown for a series of θ from $20°$ to $50°$. The deeper color around the holes in the templates manifests the thinner Au film of the thickness around 20nm. After 1320s Au deposition at a normal angle with these templates to obtain the nanodisk structure, the template surfaces obtain a larger roughness (Fig. A2.4(b)), where larger Au grains can be seen. Generally the obtained nanodisks have round shapes (Fig. A2.4(c)(d)), except that for the $50°$ template, where the nanodisk has a half-round shape. The profiles (Fig. A2.4(e)) show gradually smaller diameters for both holes and disks as θ increases.

In Fig. A2.5 these diameters are statistically summarized and plotted versus θ, as well as the hole diameters geometrically calculated according to Eq. A2.2. The calculated and experimental hole diameters agree well, while the nanodisk diameters show larger values due to the finite radius of the AFM tip. The hole diameter is reduced to 53nm for $\theta = 50°$, being almost a half of 110nm for $\theta = 0°$, and the nanodisk diameter also obtains a reduction of 1/4 (158nm for $\theta = 0°$ and 119nm for $\theta = 40°$). Apart from the AFM tip effect which overestimates the disk diameter but underestimates the hole diameter, the larger nanodisk diameter also has the other contribution of the tilted-angle deposition: the normal deposition of Au to form the nanodisk is only "nominal", that is, a small misalignment always exists between the K-cell and the substrate holder, which induces a slight tilted-angle deposition and contributes to the larger nanodisk diameter than the hole diameter.

The reduction in the hole diameter with this method is obvious and by varying the angle θ, precise control of the hole diameter can be realized. However, the smallest diameter can be reached with this method is limited. As it can be seen in Fig. A2.4, the disk diameter deposited with $\theta = 50°$ template is even larger than that deposited

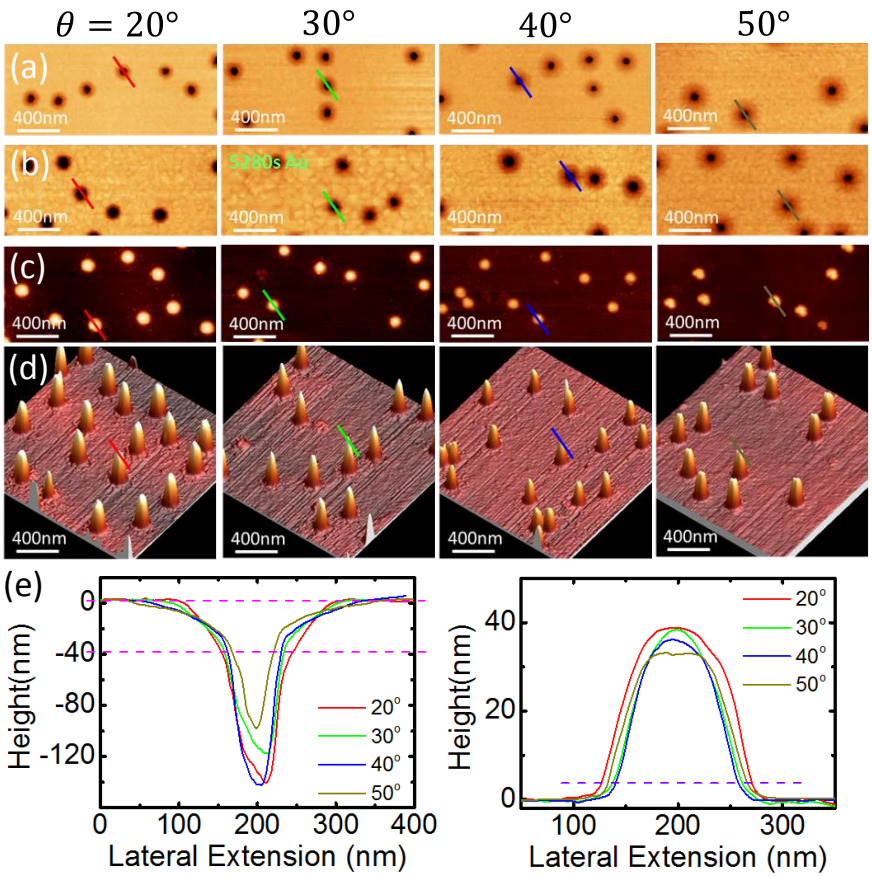

Fig. A2.4 AFM images of templates obtained with different θ from 20° to 50° and nanodisks normally deposited with these templates. Templates after RIE etching (a), after normal deposition of 1320s Au (b). 2D (c) and 3D (d) AFM images of the corresponding Au nanodisks nominally deposited for 1320s. Colored lines show the profile directions of holes and nanodisks. (e) Left: profiles of the holes in the templates after RIE etching corresponding to (a). Dashed pink lines show the thickness of the Au membrane around 40nm. Hole diameters in Fig. A2.5 are measured along the lower pink line. Right: profiles of the nanodisks measured along the directions shown in (c) and (d). Nanodisk diameters in Fig. A2.5 are measured along the dashed purple line.

with $\theta = 40°$ template. This is due to the fact that the PS sphere and the PMMA material are not completely rigid and their touching surfaces are not smooth, thus the

touching interface between them is not tangent to each other but flat, as shown in Fig. A2.3(b) [117]. In this sense, the deposited Au mask is limited by the flat interface, resulting in the irregular shape and larger diameter of the hole and nanodisk for a larger θ (Fig. A2.4(c-d)).

Tilted angle for template (°)	Calculated hole diameter (nm)	Experimental hole after RIE (nm)	Disk diameter (nm)
0	124	110	158
20	86	92	145
30	71	76	126
40	58	68	119
50	45	53	134

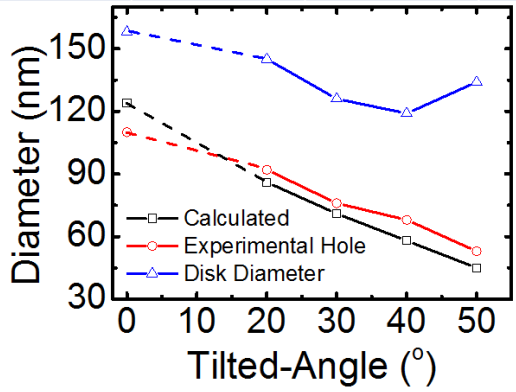

Fig. A2.5 Top: statistical table of the calculated and experimental hole diameters, and the corresponding diameters of the nanodisks deposited at "nominally" normal angle. Data for $\theta = 0°$ template are from a standard template with sputtered 30nm Au film at normal angle (0°). Bottom: diameters plotted versus θ. The solid and dashed lines are guides for eye.

The rim of the hole formed with tilted-angle deposition of Au mask and simultaneous rotation in the substrate shows a small slope (Fig. A2.4(a) and (e)) compared with that in the Au mask deposited normally (Fig. 3.1.4(b) and Fig. 3.2.4(b)(d)). Deposition of Au onto this slope is possible to further reduce the hole diameter. Because the nanodisk structure deposited with the $\theta = 50°$ template has an irregular shape (Fig.

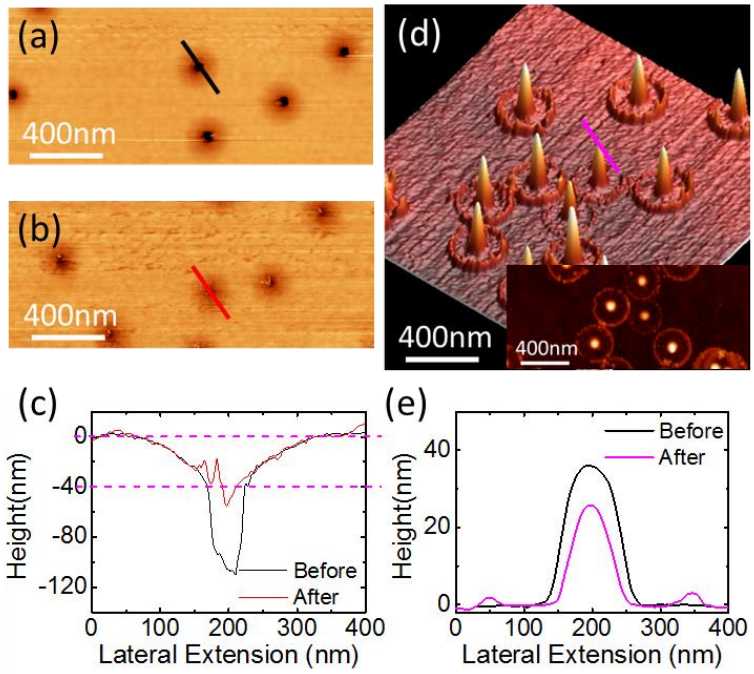

Fig. A2.6 Further reduction of the hole diameter with repetitive deposition of Au at a tilted-angle 40°. AFM images of the templates after RIE etching for $\theta = 40°$ before (a) and after (b) another deposition of 50nm Au at 40° tilted angle. (c) Profiles of the holes measured along the directions marked in (a) and (b). Each profile is averaged from 10 different holes in the template. Dashed pink lines show the 40nm Au mask before the further deposition. (d) 3D AFM image of the nanodisks deposited normally with the further shrinked template. Inset: 2D AFM image of the same sample. (e) Profile (pink line) of nanodisk in (d), compared with the nanodisk deposited without the further shrinking process (black line is from θ =40° sample in Fig. A2.4).

A2.4(c)), the θ =40° template is chosen for this purpose. After RIE etching of the template, another deposition of Au is done at 40° tilted angle until a thickness of 50nm, combined with the simultaneous rotation in the substrate. Since there is no PS sphere as the deposition mask, Au will be deposited on the rim (slope) of the hole. The AFM images of the template before and after this further deposition are shown in Fig. A2.6(a) and (b), respectively. The hole profiles show similar diameters (Fig. A2.6(c)) which is beyond our expectation, however, the nanodisk structure deposited

with this further shrinked template at a normal angle manifests a smaller diameter as shown in Fig. A2.6(d)(e), confirming the effectiveness of this method. The circles surrounding the nanodisks (Fig. A2.6(d)) are formed during the further deposition process of Au mask at 40°, which could be avoided by a larger angle than 40°.

A3 Optical Modelling with SE Data and CompleteEASE™

A3.1 Oscillator Model

Here we briefly discuss some of the theoretical oscillator models for the optical constants of the materials, which have been used in this work. In general, according to the material properties and the wavelength range being considered, different models can be applied [105]. For example, Drude model is usually considered for free-carrier absorption of metals in the visible and infrared range, Lorentz model and Tauc-Lorentz model are used for the electric polarization in the visible/UV range, and Sellmeier or Cauchy model for the spectral range with transparent characteristics. Here the Lorentz, Sellmeier and Cauchy models will be introduced.

Lorentz model is a classical model describing the oscillation of an electron bound to a fixed atomic nucleus and driven by the light field $E = E_0 exp(i\omega t)$. By assuming that the electron oscillates in a viscous fluid with a damping coefficient T and a restoring force between the electron and nucleus, the movement of the electron can be expressed according to the Newton's second law,

$$m_e \frac{d^2x}{dt^2} = -m_e T \frac{dx}{dt} - m_e \omega_0^2 x - eE_0 \exp(i\omega t), \qquad \text{A3.1}$$

where e and m_e are the electron's charge and mass, respectively. The first term on the right of Eq. A3.1 gives the viscous force, which is proportional to the speed to the electron, the second term is the restoring force with ω_0 the resonant frequency, and the last term is the driving force from light field. Eq. A3.1 represents the forced

oscillation of the electron by the external light field. The solution of Eq. A3.1 takes the form

$$x(t) = aexp(i\omega t), \quad \text{A3.2}$$

with $a = -\frac{eE_0}{m_e}\frac{1}{(\omega_0^2-\omega^2)+iT\omega}$.

With N_e the number density of the electrons, the dielectric polarization in the material can then be expressed as $P = -eN_e x(t)$, therefore the dielectric constant of the material is given by

$$\varepsilon = 1 + \frac{P}{\varepsilon_0 E} = 1 + \frac{e^2 N_e}{\varepsilon_0 m_e}\frac{1}{(\omega_0^2-\omega^2)+iT\omega}, \quad \text{A3.3}$$

with ε_0 the vacuum dielectric constant.
In the actual data analysis, Eq. A3.3 is commonly expressed in photon energy En, instead of frequency,

$$\varepsilon = 1 + \sum_j \frac{A_j}{En_{0j}^2 - En^2 + iT_j En}, \quad \text{A3.4}$$

where the dielectric function is described as the sum of the different oscillators, and the subscript j denotes the *j*th oscillator, En_{0j} the resonant energy, T_j the damping factor, and A_j the oscillator strength.

The Sellmeier model and Cauchy model correspond to the wavelength range where the imaginary part of ε is close to zero in the Lorentz model, and they can be derived by assuming $T \to 0$ at $\omega \ll \omega_0$. Note that when $T = 0$ in Eq. A3.3, the imaginary part $\varepsilon'' = 0$. Therefore by setting $T = 0$ and rewriting the photon energy En with $\omega/c = 2\pi/\lambda$ in Eq. A3.4, the Sellmeier model is

$$\varepsilon' = n^2 = A + \sum_j \frac{B_j \lambda^2}{\lambda^2 - \lambda_{0j}^2}, \quad \text{A3.5a}$$

$$\varepsilon_2 = 0, \quad \text{A3.5b}$$

where A and B_j represent analytical parameters for data analysis, and $\lambda_0 = \frac{2\pi c}{\omega_0}$ corresponds to ω_0.

The Cauchy model can be obtained from the series expansion of Eq. A3.5,

$$\mathrm{n} = \mathrm{A} + \frac{B}{\lambda^2} + \frac{C}{\lambda^4} + \cdots, \quad \text{A3.6a}$$

$$k = 0. \quad \text{A3.6b}$$

In the following as examples, we give an optical model of our nanoring structure on glass substrate with a combination of Lorentz oscillators describing the nanoring layer and a Cauchy model for the substrate, which is accomplished with the M2000Fi spectroscopic ellipsometer (SE, Fig. 2.3.3(b)) and the CompleteEASE^{TM} software.

A3.2 Optical Model for Nanorings on Glass

To extract the optical constants and reflectivities of nanoring samples with Co inhomogeneous distribution and ring-split ring structures, a biaxial optical model is used to describe the optical responses of the nanostructures, where the Lorentz oscillator model is applied to simulate the resonant behavior of the nanostructure and the Cauchy model is applied for the transparent BK7 glass substrate.

In Fig. A3.1 the interface of the CompleteEASE^{TM} software is shown. In the analysis option, we can establish an optical model to describe the sample (black rectangle), then the parameters used in the optical model can be fit to the experimental data and optimized automatically to obtain the best agreement in between (red rectangle), namely, the smallest MSE. In the panel at the bottom (green rectangle), the generated data from the fitted optical model (black dashed line) is compared with the experimental data (red solid line).

As an example, the sample of a ring-split ring structure with a 90° gap is modeled in Fig. A3.1. Due to the in-plane optical anisotropy, the layer of the 25nm nanostructure is modelled with a layer of biaxial symmetry and each axis (x, y, z) is modelled with several Lorentz oscillators corresponding to the resonant modes for light polarization

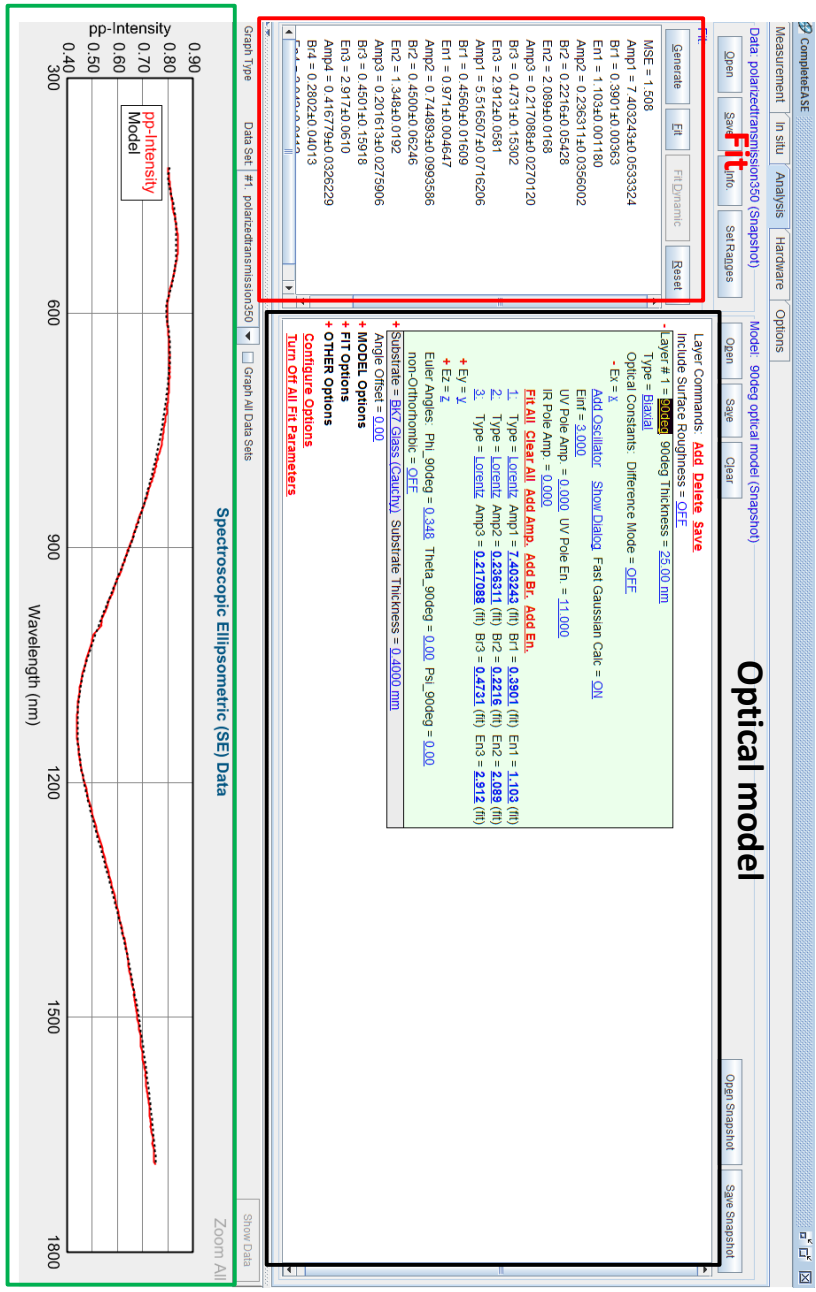

Fig. A3.1 CompleteEASE™ software interface for the analysis of the SE data. The optical model is established and optimized to simulate the nanoring-split ring structure with a 90° gap as an example.

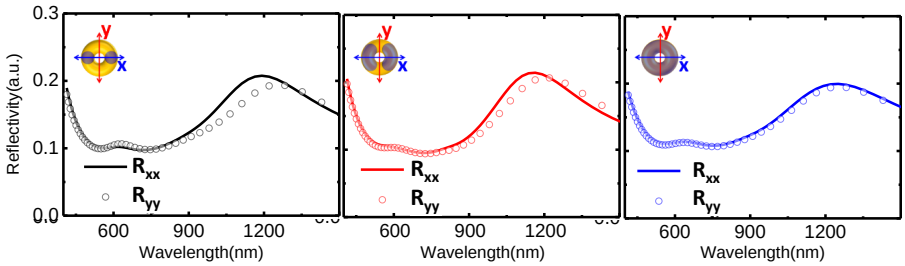

Fig. A3.2 Calculated reflectivities for Co dots, Co sectors, Co continuous ring samples, with the optical models established in CompleteEASE^{TM} software.

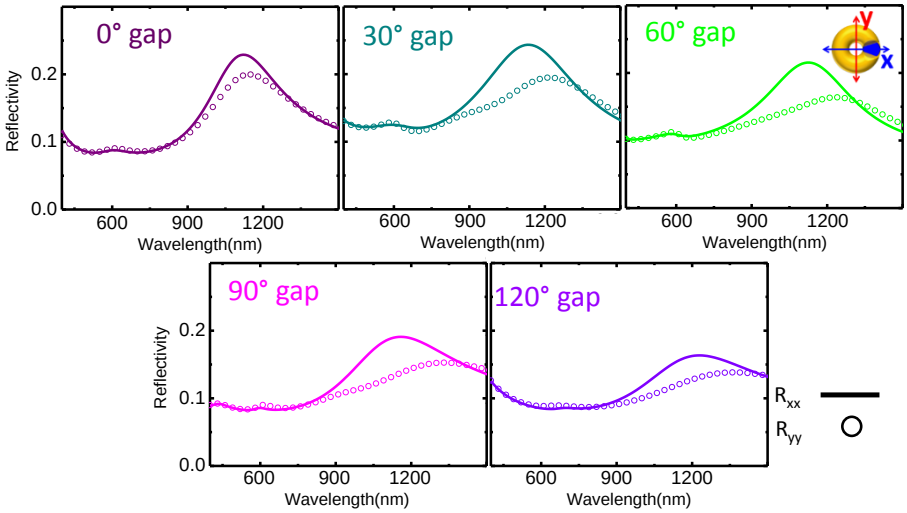

Fig. A3.3 Calculated reflectivities for ring-split ring nanostructures, with the optical models established in CompleteEASE^{TM} software.

along this axis. The amplitude (Amp), full width of the half maximum (Br=breadth), and resonant energy (En) can be used as the fitting parameters (Eq. A3.4), which are shown in bold. The transparent 0.4mm thick BK7 glass substrate is modelled with a Cauchy model (Eq. A3.6), with A, B, C as the fitting parameters.

The fitted and optimized model gives a very good agreement with the measured data (bottom panel in Fig. A3.1) and the MSE is 1.315 which is very low. With this optical model, the polarized reflectivity of the sample can be calculated with the "Simulate Data" function (not shown in the figure) in "OTHER Options".

As a summarization, in Fig. A3.2, the calculated polarized reflectivities of the Co dots, Co sectors, Co continuous nanoring samples are shown (Chapter 5), where the optical anisotropy can be observed in the Co dots and Co sectors samples. In Fig. A3.3, the calculated reflectivities of the ring-split ring nanostructures are shown (Chapter 6).

A4 Further Information about Ring LSPs

In Chapter 1 we introduce the basic theory about the plasmon hybridization for nanoring structures with the coupling of disk and hole plasmons. However, the plasmon hybridization theory there can only help us understand the bimodal resonance of the nanoring at normal light incidence. For light incident obliquely [159] and structures with anisotropic shapes (e.g. elliptical nanoring) [142], the previously dark modes such as the quadrupolar mode will appear (Fig. A4.1), which can not be easily understood with the hybridization of disk and hole plasmons. The other models, such as the standing wave model [142], can give us a more intuitive picture of such modes. For this reason and for the completeness of the thesis, we will give a short introduction of current studies about the nanoring plasmonics, and then the standing wave model is introduced. Additionally, at last the fabrication methods and applications of LSP nanorings will also be summarized.

Actually a series of analytical theory and simulation methods have been applied [32,138-143,150,158-160,162] to understand the plasmonic behavior of the nanorings. The first one was proposed by Aizpurua, et al. [158], by considering the strong electromagnetic (EM) coupling between the inner and outer walls for the nanoring with a width much smaller than the radius, and gave the symmetric and antisymmetric charge distributions for the bimodal resonance, which is actually very similar to the plasmon hybridization consideration. Analytical results in non-retarded approximation have also been given for nanotorus structures [139,140,150], which is a special case of the nanoring structure.

A4.1 Standing Wave Model

Originally, the standing-wave model was introduced to analyze a linear wire antenna of finite length l, which is argued as the incident wave with wavelength λ polarizes

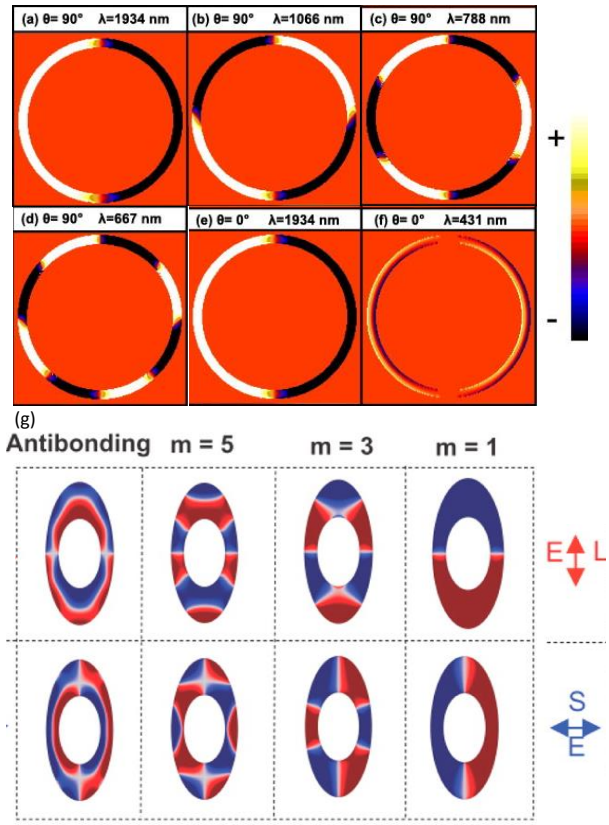

Fig. A4.1 (a–f) Calculated surface charge distribution on the top surface of a gold nanoring of outer diameter=528 nm, width=24 nm, and height=168 nm. Each panel (LSP resonance mode) corresponds a peak in extinction spectra. (a-d) are the modes excited by the laterally (obliquely) incident light (incident angle θ=90°), and (b-d) are higher ordered multipolar modes. (e, f) are modes excited by normal light incidence. (a,e) are the bonding dipolar mode, and (f) the antibonding mode. (g) Charge distributions for LSP modes excited by normal light incidence but for an elliptical nanoring. m=1 is the bonding dipolar mode. m=3 and m=5 are the higher ordered mode. (a-f) are adapted from Ref. [159] and (g) from [142].

the ends of the wire thereby giving rise to a surface charge wave propagating along the wire (Fig. A.4.2) [144]. The model can be expressed as [145,146],

$$l = m\lambda_m/2n, \qquad \text{A4.1}$$

where λ_m is the wavelength of the resonance of mode index m and n the effective refractive index of the surrounding medium (usually determined by both of the supporting substrate and cladding material, a typical expression of this can be seen in Ref. [143,146]). The fundamental resonance is represented by $m = 1$. Depending on the geometrical symmetry of the structure, specific light polarizations may be needed for excitation of the high ordered resonance mode (m>1), which can be seen in Ref. [147] for wire and in [159] for ring.

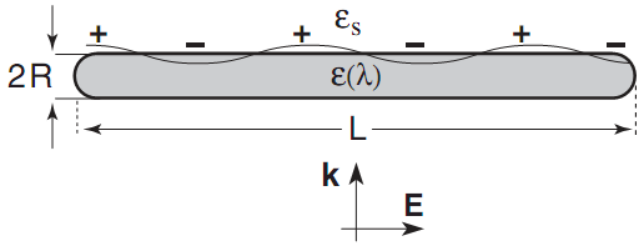

Fig. A4.2 A single nanoantenna element represented by a metal nanorod. Incident light with wavelength λ polarizes the ends and gives rise to a standing surface charge wave. Figure is adopted from Ref. [144].

As it can be expected from Eq. A4.1, the standing wave model can be used as a simple and quantitative description of the resonance peaks of the nanoantenna structures by relating the resonance wavelengths with the dimensions of the nanostructures (e.g. length of the nanowire, perimeter of the ring). Therefore, the resonances of such structures can be simply predicted from the corresponding dimensions. At the resonant wavelength λ_m, the wire behaves approximately as a simple electric dipole (m=1) or higher ordered multipole (m>1) with nodes between the dipoles, which specifies the nature of standing waves oscillating along the wire.
This simple model then is generalized to the other metallic nanostructures, such as the non-closed structures like split-ring (U or C shaped wire) [143,146], L-shaped wire [143], and closed structures like square ring (Fig. A4.3(a)) [143], round ring [142], and elliptical ring (Fig. A4.3(b)) [142]. The multiple plasmon resonances supported by the mentioned structures can be obtained from the modified standing wave model for nanowire [142,145],

$$l_{eff} = \frac{m(\lambda_m + \lambda_0)}{2n}, \qquad \text{A4.2}$$

with l_{eff} the effective length of the structure along the light polarization direction, and λ_0 a constant number depending on the geometry of the structure, such as the cross-section symmetry and radius.

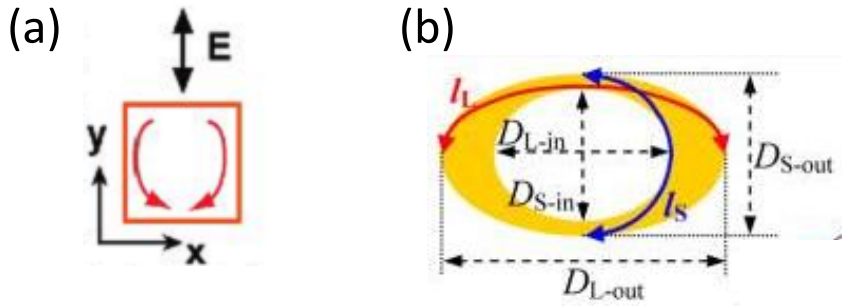

Fig. A4.3 (a) Sketch of the mirror dipoles (curved arrows) of the dipolar bonding resonance mode induced by the incident light in a square ring. **E** is the direction of light polarization relative to the ring. (b) Sketch of the effective lengths l_{eff} ($l_L \neq l_S$) of elliptical ring with a nonuniform cross section, for light polarizations along long (L) and short (S) axes. (a) is adopted from Ref. [143], (b) from Ref. [142].

For non-closed structures, the effective length l_{eff} is the total length of the structure. For closed structure without in-plane anisotropy, such as ring and square ring, the effective length l_{eff} is a half of the total perimeter and Eq. A4.2 can be used to explain the fundamental dipolar mode ($m = 1$, LE bonding mode in Fig. 1.2.6 in Chapter 1, and in Fig. A4.1) and the higher ordered modes (Fig. A4.1) with the following argument. At resonance, the induced dipole for the fundamental dipolar mode is along the diameter of the ring, parallel to the light polarization. Due to the structural geometry, this dipole could be treated as two mirror dipoles (Fig. A4.3(a)), with the mirror plane parallel to the light polarization. Each dipole has an effective length of $l_{eff} = C/2$, with C the perimeter of the structure [143]. Even for elliptical ring with the uniform cross section, the induced dipoles will still have an effective length l_{eff} around $C/2$, therefore no obvious in-plane optical anisotropy could be observed [142,143]. Due to the possible near-field electrostatic interaction between the two mirror dipoles [140,158] and between the high order harmonic dipoles, the corresponding actual resonance wavelength could deviate from the one predicted by

Eq. A4.2 [142,143].
For elliptical ring with nonuniform ring section (Fig. A4.1(g) and Fig. A4.3(b)), l_{eff} are different for light polarizations along the long and short axes of the structure, therefore in-plane optical anisotropy is induced by this shape anisotropy [142].

A4.2 Summary of LSP Nanoring Applications and Fabrication Methods

For completeness of the topic and convenience of the readers, here we summarize some of the references of the LSP nanoring applications and fabrication methods.
Due to the unique structural characteristic, at low energy (LE) resonance mode the symmetric charge distribution on the surface of the nanoring provides a uniform and sizable electric field in the central "cavity" (or hole), and as an additional advantage, the cavity provides the room to allow a significant volume of analyte to enter, therefore the nanoring structure is particularly attractive for bio- [34] and chemical [148-152] sensing applications, as well as for the surface-enhanced Raman scattering (SERS) [153,154].
Furthermore, the nanoring has been exploited as the plasmonic waveguides [155], nanoantennas to enhance the photoluminescence [95], bio-imaging platform [156], as well as for directly confining and manipulating light in small volumes [157].
Considering the fabrication methods, different techniques have been applied for the nanoring generation, such as colloidal lithography [153,158-160], electron beam (E-beam) lithography [150,152,154,157,161,162], phase-shifting photolithography (PSP) [157], combined double patterning and (E-beam) lithography [163], nanoimprinting [151], self-assembling [164], etc.

A5 Kerr Rotation and Ellipticity of Nanodisk to Nanoring Structures

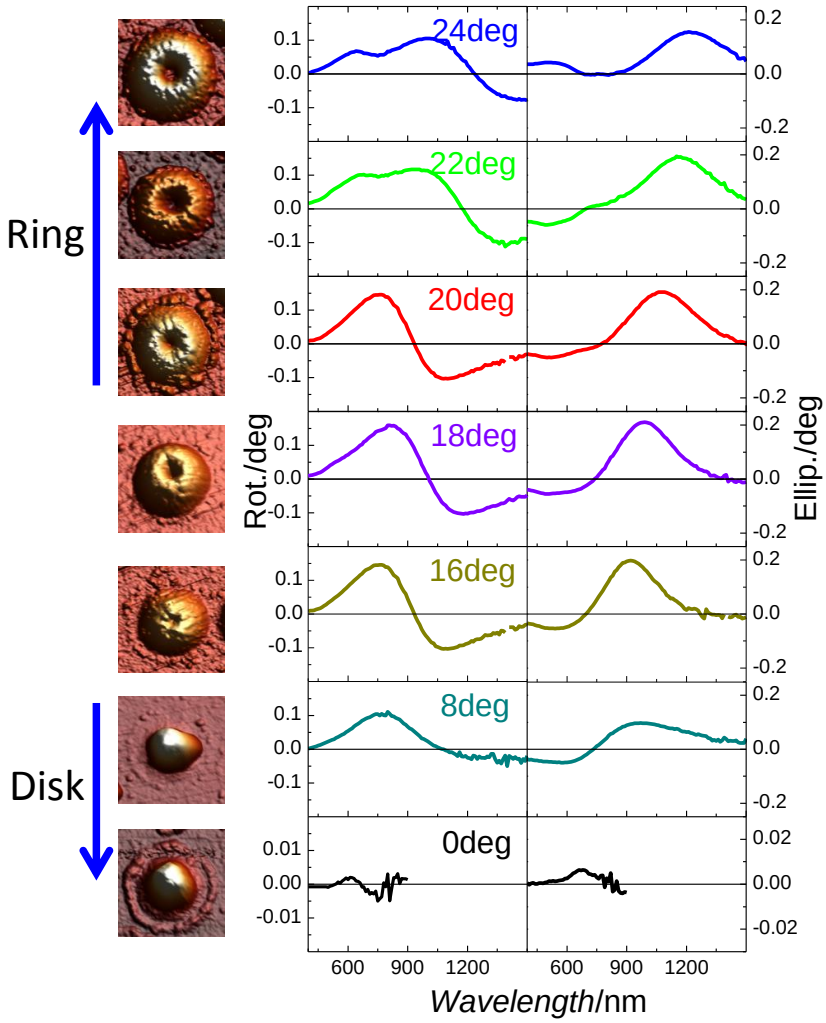

Fig. A5.1 Left: AFM images of the nanoentities. Right: Spectra of Kerr Rotation and Ellipticity for the corresponding nanostructures at polar MO Kerr configuration and saturated magnetization. (For nanodisks deposited at 0°, the data scale is different.)

Conclusiones

A lo largo de esta tesis, se ha realizado un estudio sistemático de la respuesta óptica y magneto-óptica (MO) en el rango de visible e infrarrojo cercano de estructuras tipo nanoanillo con componentes plasmónicos y magnéticos. Por otra parte, se han propuesto e implementado una serie de métodos con el fin de controlar e incluso mejorar dichas respuestas ópticas y MO de las estructuras fabricadas.

En primer lugar, se ha optimizado e implementado un protocolo completo basado en el método de litografía coloidal con agujeros (HCL) para adaptarse a la fabricación de estructuras tipo nanoanillo. La fabricación de la máscara HCL se ha optimizado centrándose en varios aspectos. Se ha controlado la densidad de esferas de PS, lo que a su vez determinará la densidad de nanoanillos obtenidos. El espesor de la máscara de Au en la plantilla, crítico para la formación de los nanoanillos, también ha sido optimizado. Además, se ha explorado un control adicional de la forma y el diámetro del orificio variando el ángulo de deposición para la máscara de Au y girando el sustrato, incluso mediante una deposición adicional de Au después de completar la plantilla.

El proceso de deposición de las nanoestructuras con la plantilla HCL se ha analizado geométricamente. Básicamente, la morfología de la nanoestructura se controla mediante el ángulo de deposición y la rotación de la máscara. Con un ángulo de incidencia adecuado y una rotación continua es posible definir nanoanillos a voluntad. Al alternar la fuente de material, es posible obtener nanoanillos con componentes múltiples (como Au /Co/Au). También se pueden insertar estructuras de tipo nanodisco y nanosector de Co en anillos complejos de Au.

Con este protocolo de fabricación, se han completado y estudiado una serie de estructuras de tricapas Au/Co/Au que evolucionan en complejidad desde el nanodisco hasta el nanoanillo, por ejemplo mediante control del ángulo de deposición. En paralelo, el comportamiento de resonancia plasmónica unimodal del nanodisco

evoluciona al comportamiento de resonancia bimodal del nanoanillo.

Se ha observado que la relación de aspecto (diámetro exterior / altura) de la nanoestructura es un factor relevante en la determinación de la posición espectral de la resonancia plasmónica en el rango espectral de baja energía (LE) así como en el correspondiente pico de MO. Para la estructura de nanoanillo la posición espectral del pico de alta energía (HE) está controlada principalmente por la sección transversal del brazo del nanoanillo. El comportamiento de las respuestas ópticas y MO de los nanoanillos se explica correctamente con el modelo de hibridación de plasmones. Mediante el aumento del ángulo de deposición, la sección transversal de la estructura de nanoanillo puede controlarse continuamente, trasladándose a un control fino de la relación de aspecto de la nanoestructura, y por tanto de las posiciones espectrales de las resonancias plasmónicas y los picos de actividad MO.

Por otra parte, se ha conseguido incorporar en posiciones específicas de anillos de Au componentes de Co en forma de disco o sector. Las diferentes constantes ópticas de Co de Au modifican la distribución del campo electromagnético en el plano de las nanoestructuras en resonancia, induciendo una clara anisotropía óptica en el plano. Las respuestas MO de estas estructuras, por otro lado, siguen siendo proporcionales a la cantidad de Co.

Por último, se propone un método de prueba de concepto para potenciar aún más el efecto MO en tales anillos magnetoplasmónicos a través de la maximización del campo electromagnético (EM) en regiones específicas donde se deposita el elemento MO-activo. Esto se consigue mediante la generación de una brecha en la parte superior del nanodisco Co incrustado en el nanoanillo de Au. Con esto se consigue una localización adicional de campo EM en el área de hueco en la resonancia plasmónica de baja energía, dando como resultado un aumento del efecto MO. Este aumento se optimiza realizando un estudio en función de la apertura de esta brecha, alcanzando un factor de mejora en la actividad MO de 3 con respecto al anillo magnetoplasmónico equivalente sin brecha de apertura. Esta localización del campo EM en el área de la brecha se confirma además tanto teóricamente con mapas de distribución de campo electromagnético, y experimentalmente con imágenes de cartografía de señal EEL.

List of Publications

Publications related to this thesis

- *Magnetoplasmonic Nanorings as Novel Architectures with Tunable Magneto-optical Activity in Wide Wavelength Ranges*
  Hua Yu Feng, Feng Luo, Renata Kekesi, Daniel Granados, David Meneses-Rodr ǵuez, Jorge M. Garc á, Antonio Garc á-Mart ń, Gaspar Armelles, and Alfonso Cebollada,
  Advanced Optical Material, vol. 2, p. 612 (2014)
- *From Disk to Ring: Aspect Ratio Control of the Magnetoplasmonic Response in Au/Co/Au Nanostructures Fabricated by Hole-mask Colloidal Lithography*
  Hua Yu Feng, Feng Luo, David Meneses-Rodr ǵuez, Gaspar Armelles, and Alfonso Cebollada
  Applied Physics Letters, vol. 106, p. 083105 (2015)
- *Active Magnetoplasmonic Split-ring/Ring Nanoantennas*
  Hua Yu Feng, Feng Luo, Raul Arenal, Luc Henrard, Fernando Garc á, Gaspar Armelles, and Alfonso Cebollada
  Nanoscale, vol. 9, p. 37 (2017)

Other publications

- *Interaction Effects between Magnetic and Chiral Building Blocks: A New Route for Tunable Magneto-chiral Plasmonic Structures*
  Gaspar Armelles, Alfonso Cebollada, **Hua Yu Feng**, Antonio Garc á-Mart ń, David Meneses-Rodr ǵuez, Jun Zhao, and Harald Giessen
  ACS Photonics, vol. 2, p. 1272 (2015)

Nomenclature

AFM	Atomic force microscope
AR	Aspect ratio
DDA	Discrete dipoles approximation
EELS	Electron energy loss spectroscopy
EMA	Effective medium approximations
EM	Electromagnetic
E-beam	Electron-beam
FND	First neighbor distance
FIB	Focused ion beam
HE	High-energy
HCL	Hole-mask colloidal lithography
LE	Low energy
LSP	Localized Surface Plasmons
MO	Magneto-optical
MOA	Magneto-optical activity
MOKE	MO Kerr effects
	p-MOKE polar MOKE
	l-MOKE longitudinal MOKE
	t-MOKE transverse MOKE
MSE	Mean square error
MOSPR	MO surface plasmon resonance
MO SLR	MO surface lattice resonances
MBE	Molecular beam epitaxy
NIR	Near-infrared
PDDA	Poly-diallyldimethyl-ammonium
PMMA	Poly(methyl methacrylate

PS	Polystyrene
RIE	Reactive ion etching
SE	Spectroscopic ellipsometry
SPP	Surface plasmon polaritons
SPR	Surface plasmon resonance
SPs	Surface plasmons
UHV	Ultra-high vacuum

Bibliography

1. E. Hecht, *Optics* (Addison Wesley, 2002).
2. E. Ozbay, "Plasmonics: merging photonics and electronics at nanoscale dimensions," Science **311**, 189-193 (2006).
3. D. Gramotnev and S. Bozhevolnyi, "Plasmonics beyond the diffraction limit," Nat. Photonics **4**, 83-91 (2010).
4. W. Barnes, A. Dereux, and T. Ebbesen, "Surface plasmon subwavelength optics," Nature **424**, 824-830 (2003).
5. S. A. Maier, *Plasmonics: Fundamentals and Applications* (Springer, 2007).
6. F. J. Rodríguez-Fortuño, A. Espinosa-Soria, and A. Martínez, "Exploiting metamaterials, plasmonics and nanoantennas concepts in silicon photonics," J. Opt. **18**, 123001 (2016).
7. M. Stockman, "Nanoplasmonics: the physics behind the applications," Phys. Today **64**, 39 (2011).
8. J. Anker, P. Hall, O. Lyandres, N. Shah, J. Zhao, and R. Duyne, "Biosensing with plasmonic nanosensors," Nat. Mater. **7**, 442-453 (2008).
9. C. Haynes, A. McFarland, and R. Duyne, "Surface-enhanced Raman spectroscopy," Anal. Chem. **77**, 338A-346A (2005).
10. M. Osawa, "Surface-enhanced infrared absorption," Topics Appl. Phys. **81**, 163-187 (2001).
11. D. Lehr, J. Reinhold, I. Thiele, H. Hartung, K. Dietrich, C. Menzel, T. Pertsch, E.-B. Kley, and A. Tünnermann, "Enhancing second harmonic generation in gold nanoring resonators filled with lithium niobate," Nano Lett. **15**, 10251030 (2015).
12. A. Zvezdin and V. Kotov, *Modern Magnetooptics and Magnetooptical Materials* (Taylor & Francis Group, 1997).
13. G. Armelles, A. Cebollada, A. García-Martín, and M. U. González, "Magnetoplasmonics: combining magnetic and plasmonic functionalities," Adv.

Opt. Mater. **1**, 10-35 (2013).

14. A. V. Kimel, A. Kirilyuk, P. A. Usachev, R. V. Pisarev, A. M. Balbashov, and Th. Rasing, "Ultrafast non-thermal control of magnetization by instantaneous photomagnetic pulses", Nature **435**, 655-657 (2005).
15. V. Temnov, G. Armelles, U. Woggon, D. Guzatov, A. Cebollada, A. Garcia-Martin, J.-M. Garcia-Martin, T. Thomay, A. Leitenstorfer, and R. Bratschitsch, "Active magneto-plasmonics in hybrid metal–ferromagnet structures," Nat. Photonics **4**, 107-111 (2010).
16. M. Faraday, "Experimental Researches in Electricity," Phil. Trans. R. Soc. Lond. **136**, 1-20 (1846).
17. J. Kerr, "XLIII. On rotation of the plane of polarization by reflection from the pole of a magnet," Philos. Mag. **3**, 321-343 (1877).
18. J. González-Díaz, A. García-Martín, G. Armelles, J. García-Martín, C. Clavero, A. Cebollada, R. Lukaszew, J. Skuza, D. Kumah, and R. Clarke, "Surface-magnetoplasmon nonreciprocity effects in noble-metal/ferromagnetic heterostructures," Phys. Rev. B **76**, 153402 (2007).
19. B. Sepúlveda, A. Calle, L. M. Lechuga, and G. Armelles, "Highly sensitive detection of biomolecules with the magneto-optic surface-plasmon-resonance sensor," Opt. Lett. **31**, 1085-1087 (2006).
20. D. Regatos, D. Fariña, A. Calle, A. Cebollada, B. Sepúlveda, G. Armelles, and L. M. Lechuga, "Au/Fe/Au multilayer transducers for magneto-optic surface plasmon resonance sensing," J. Appl. Phys. **108**, 054502 (2010).
21. D. Regatos, B. Sepúlveda, D. Fariña, L. G. Carrascosa, and L. M. Lechuga, "Suitable combination of noble/ferromagnetic metal multilayers for enhanced magneto-plasmonic biosensing," Opt. Express **19**, 8336-8346 (2011).
22. V. Bonanni, S. Bonetti, T. Pakizeh, Z. Pirzadeh, J. Chen, J. Nogués, P. Vavassori, R. Hillenbrand, J. Åkerman, and A. Dmitriev, "Designer magnetoplasmonics with nickel nanoferromagnets," Nano Lett. **11**, 5333-5338 (2011).
23. N. Maccaferri, K. Gregorczyk, T. Oliveira, M. Kataja, S. Dijken, Z. Pirzadeh, A. Dmitriev, J. Åkerman, M. Knez, and P. Vavassori, "Ultrasensitive and label-free molecular-level detection enabled by light phase control in magnetoplasmonic nanoantennas," Nat. Commun. **6**, 6150 (2015).
24. M. G. Manera, G. Montagna, E. Ferreiro-Vila, L. González-García, J. R. Sánchez-Valencia, A. R. González-Elipe, A. Cebollada, J. M. García-Martín, A.

Garcá-Martín, G. Armelles, and R. Rella, "Enhanced gas sensing performance of TiO2 functionalized magneto-optical SPR sensors," J. Mater. Chem. **21**, 16049-16056 (2011).

25. V. Safarov, V. Kosobukin, C. Hermann, G. Lampel, J. Peretti, and C. Marlière, "Magneto-optical effects enhanced by surface plasmons in metallic multilayer films," Phys. Rev. Lett. **73**, 3584-3587 (1994).
26. C. Hermann, V. Kosobukin, G. Lampel, J. Peretti, V. Safarov, and P. Bertrand, "Surface-enhanced magneto-optics in metallic multilayer films," Phys. Rev. B **64**, 235422 (2001).
27. J. González-Díaz, A. Garcá-Martín, J. Garcá-Martín, A. Cebollada, G. Armelles, B. Sepúlveda, Y. Alaverdyan, and M. Käll, "Plasmonic Au/Co/Au nanosandwiches with enhanced magneto-optical activity," Small **4**, 202-205 (2008).
28. J. B. González-Díaz, A. Garcá-Martín, G. Armelles, D. Navas, M. Vázquez, K. Nielsch, R. B. Wehrspohn, and U. Gösele, "Enhanced magneto-optics and size effects in ferromagnetic nanowire arrays," Adv. Mater. **19**, 2643-2647 (2007).
29. H. Shimizu and Y. Nakano, "First demonstration of TE mode nonreciprocal propagation in an InGaAsP/InP active waveguide for an integratable optical isolator," Jpn. J. Appl. Phys. **43**, L1561-L1563 (2004).
30. W. Parys, B. Moeyersoon, D. Thourhout, R. Baets, M. Vanwolleghem, B. Dagens, J. Decobert, O. Gouezigou, D. Make, R. Vanheertum, and L. Lagae, "Transverse magnetic mode nonreciprocal propagation in an amplifying AlGaInAs/InP optical waveguide isolator," Appl. Phys. Lett. **88**, 071115 (2006).
31. D. Floess, J. Chin, A. Kawatani, D. Dregely, H.-U. Habermeier, T. Weiss, and H. Giessen, "Tunable and switchable polarization rotation with non-reciprocal plasmonic thin films at designated wavelengths," Light Sci. Appl. **4**, e284 (2015).
32. P. Nordlander, "The ring: a leitmotif in plasmonics," Acs Nano **3**, 488 (2009).
33. P. Yu, S. Chen, J. Li, H. Cheng, Z. Li, and J. Tian, "Co-enhancing and -confining the electric and magnetic fields of the broken-nanoring and the composite nanoring by azimuthally polarized excitation," Opt. Express **21**, 20611 (2013).
34. E. M. Larsson, J. Alegret, M. Käll, D. S. Sutherland, "Sensing characteristics of NIR localized surface plasmon resonances in gold nanorings for application as ultrasensitive biosensors," Nano Lett. **7**, 12561263 (2007).

35. H. Fredriksson, Y. Alaverdyan, A. Dmitriev, C. Langhammer, D. S. Sutherland, M. Zäch, and B. Kasemo, "Hole–mask colloidal lithography," Adv. Mater. **19**, 4297-4302 (2007).
36. J. C. Maxwell-Garnett, "Colors in metal glasses and in metallic films", Philos. Trans. R. Soc. London **203**, 385 (1904).
37. G. Mie, "Beiträge zur Optik trüber Medien, Speziell Kolloidale Mettall osungen", Ann. Phys. **25**, 377 (1908).
38. A. Sommerfeld, "Ueber die Fortpflanzung elektrodynamischer Wellen lang eines Drahtes," Ann. Der Phys. und Chemie **303**, 233-290 (1899).
39. R. W. Wood, "On a remarkable case of uneven distribution of light in a diffraction grating spectrum," Rroc. Phys. Soc. London **18**, 269 (1902).
40. R. H. Ritchie, "Plasma losses by fast electrons in thin films," Phys. Rev. **106**, 874-881 (1957).
41. L. Kelly, E. Coronado, L. Zhao, and G. Schatz, "The optical properties of metal nanoparticles: the influence of size, shape, and dielectric environment," J. Phys. Chem. B **107**, 668-677 (2003).
42. C. F. Bohren and D. R. Huffman, *Absorption and Scattering of Light by Small Particles* (John Wiley & Sons, 1998)
43. P. Hanarp, M. Käll, and D. Sutherland, "Optical properties of short range ordered arrays of nanometer gold disks prepared by colloidal lithography," J. Phys. Chem. B **107**, 5768-5772 (2003).
44. F. Wang and Y. Shen, "General properties of local plasmons in metal nanostructures," Phys. Rev. Lett. **97**, 206806 (2006).
45. E. Prodan, C. Radloff, N. J. Halas, and P. Nordlander, "A hybridization model for the plasmon response of complex nanostructures," Science **302**, 419-422 (2003).
46. E. Prodan, and P. Nordlander, "Plasmon hybridization in spherical nanoparticles," J. Chem. Phys. **120**, 5444 (2004).
47. H. Wang, Y. Wu, B. Lassiter, C. Nehl, J. H. Hafner, P. Nordlander and N. J. Halas, "Symmetry breaking in individual plasmonic nanoparticles," Proc. Natl. Acad. Sci. **103**, 10856 (2006).
48. C. Radloff and N. J. Halas, "Plasmonic properties of concentric nanoshells," Nano Lett. **4**, 1323 (2004).
49. H. Wang, D. W. Brandl, F. Le, P. Nordlander and N. J. Halas, "Nanorice: a

hybrid plasmonic nanostructure," Nano Lett. **6**, 827 (2006).

50. P. Nordlander, C. Oubre, E. Prodan, K. Li and M. I. Stockman, "Plasmon hybridization in nanoparticle dimers," Nano Lett. **4**, 899 (2004).
51. D. W. Brandl, N. A. Mirin and P. Nordlander, "Plasmon modes of nanosphere trimers and quadrumers," J. Phys. Chem. B **110**, 12302 (2006).
52. F. Le, N. Z. Lwin, J. M. Steele, M. Käll, N. J. Halas and P. Nordlander, "Plasmons in the metallic nanoparticle-film system as a tunable impurity problem," Nano Lett. **5**, 2009-2013 (2005).
53. A. M. Funston, C. Novo, T. J. Davis and P. Mulvaney "Plasmon coupling of gold nanorods at short distances and in different geometries," Nano Lett. **9**, 1651-1658 (2009).
54. A. Dmitriev, T. Pakizeh, M. Käll, and D. S. Sutherland, "Gold-silica-gold nanosandwiches: tunable bimodal plasmonic resonators," Small **3**, 294–299 (2007).
55. P. Jain, W. Huang, and M. El-Sayed, "On the universal scaling behavior of the distance decay of plasmon coupling in metal nanoparticle pairs: a plasmon ruler equation," Nano Lett. **7**, 2080-2088 (2007).
56. A. Sheridan, A. Clark, A. Glidle, J. Cooper, and D. Cumming, "Multiple plasmon resonances from gold nanostructures," Appl. Phys. Lett. **90**, 143105 (2007).
57. S. Sugano, and N. Kojima, *Magneto-Optics* (Springer, 2000).
58. C. Dehesa-Martínez, L. Blanco-Gutierrez, M. Vélez, J. Díaz, L. M. Alvarez-Prado, and J. M. Alameda, "Magneto-optical transverse Kerr effect in multilayers," Phys. Rev. B **64**, 024417 (2001).
59. B. Sepúlveda, J. B. González-Díaz, A. García-Martín, L. M. Lechuga, and G. Armelles, "Plasmon-induced magneto-optical activity in nanosized gold disks," Phys. Rev. Lett. **104**, 147401 (2010).
60. N. de Sousa, L. S. Froufe-Pérez, G. Armelles, A. Cebollada, M. U. González, F. García, D. Meneses-Rodríguez, and A. García-Martín, "Interaction effects on the magneto-optical response of magnetoplasmonic dimers," Phys. Rev. B **89**, 205419 (2014).
61. N. Maccaferri, A. Berger, S. Bonetti, V. Bonanni, M. Kataja, Q. Qin, S. Dijken, Z. Pirzadeh, A. Dmitriev, J. Nogués, J. Åkerman, and P. Vavassori, "Tuning the magneto-optical response of nanosize ferromagnetic Ni disks using the phase of

localized plasmons," Phys. Rev. Lett. **111**, 167401 (2013).

62. N. Maccaferri, J. González-Díaz, S. Bonetti, A. Berger, M. Kataja, S. Dijken, J. Nogués, V. Bonanni, Z. Pirzadeh, A. Dmitriev, J. Åkerman, and P. Vavassori, "Polarizability and magnetoplasmonic properties of magnetic general nanoellipsoids," Opt. Express **21**, 9875 (2013).
63. N. Maccaferri, M. Kataja, V. Bonanni, S. Bonetti, Z. Pirzadeh, A. Dmitriev, S. Dijken, J. Åkerman, and P. Vavassori, "Effects of a non-absorbing substrate on the magneto-optical Kerr response of plasmonic ferromagnetic nanodisks," Phys. Status Solidi. **211**, 1067–1075 (2014).
64. K. Lodewijks, N. Maccaferri, T. Pakizeh, R. Dumas, I. Zubritskaya, J. Åkerman, P. Vavassori, and A. Dmitriev, "Magnetoplasmonic design rules for active magneto-optics," Nano Lett. **14**, 7207-7214 (2014).
65. S. Albaladejo, R. Gómez-Medina, L. S. Froufe-Pérez, H. Marinchio, R. Carminati, J. F. Torrado, G. Armelles, A. García-Martín, and J. J. Sáenz, "Radiative corrections to the polarizability tensor of an electrically small anisotropic dielectric particle," Opt. Express **18**, 3556-3567 (2010).
66. G. Armelles, A. Cebollada, A. García-Martín, J. García-Martín, M. González, J. González-Díaz, E. Ferreiro-Vila, and J. Torrado, "Magnetoplasmonic nanostructures: systems supporting both plasmonic and magnetic properties," J. Opt. Pure Appl. Opt. **11**, 114023 (2009).
67. G. Armelles, A. Cebollada, A. García-Martín, M. U. González, F. García, D. Meneses-Rodríguez, N. de Sousa, and L. S. Froufe-Pérez, "Mimicking electromagnetically induced transparency in the magneto-optical activity of magnetoplasmonic nanoresonators.," Opt. Express **21**, 27356–70 (2013).
68. J. B. González-Díaz, B. Sepúlveda, A. García-Martín, and G. Armelles, "Cobalt dependence of the magneto-optical response in magnetoplasmonic nanodisks," Appl. Phys. Lett. **97**, 043114 (2010).
69. G. Ctistis, E. Papaioannou, P. Patoka, J. Gutek, P. Fumagalli, and M. Giersig, "Optical and magnetic properties of hexagonal arrays of subwavelength holes in optically thin cobalt films," Nano Lett. **9**, 1–6 (2009).
70. I. Zubritskaya, K. Lodewijks, N. Maccaferri, A. Mekonnen, R. Dumas, J. Åkerman, P. Vavassori, and A. Dmitriev, "Active magnetoplasmonic ruler," Nano Lett. **15**, 3204-3211 (2015).
71. W. B. Xia, J. L. Gao, S. Y. Zhang, X. J. Luo, L. Y. Chen, L. Q. Xu, S. L. Tang,

and Y. W. Du, "Optical and magneto-optical anisotropies in large-area two-dimensional Co antidots film," Opt. Express **22**, 1359 (2014).

72. E. Papaioannou, V. Kapaklis, E. Melander, B. Hjörvarsson, S. Pappas, P. Patoka, M. Giersig, P. Fumagalli, A. García-Martín, and G. Ctistis, "Surface plasmons and magneto-optic activity in hexagonal Ni anti-dot arrays," Opt. Express **19**, 23867-77 (2011).
73. E. Th. Papaioannou, V. Kapaklis, P. Patoka, M. Giersig, P. Fumagalli, A. García-Martín, E. Ferreiro-Vila, and G. Ctistis, "Magneto-optic enhancement and magnetic properties in Fe antidot films with hexagonal symmetry," Phys. Rev. B **81**, 054424 (2010).
74. N. Maccaferri, X. Inchausti, A. García-Martín, J. Cuevas, D. Tripathy, A. Adeyeye, and P. Vavassori, "Resonant enhancement of magneto-optical activity induced by surface plasmon polariton modes coupling in 2D magnetoplasmonic crystals," ACS Photonics **2**, 1769–1779 (2015).
75. J. Banthí, D. Meneses-Rodríguez, F. García, M. González, A. García-Martín, A. Cebollada, and G. Armelles, "High magneto-optical activity and low optical losses in metal-dielectric Au/Co/Au-SiO_2 magnetoplasmonic nanodisks," Adv. Mater. **24**, OP36–OP41 (2012).
76. G. X. Du, T. Mori, M. Suzuki, S. Saito, H. Fukuda, and M. Takahashi, "Evidence of localized surface plasmon enhanced magneto-optical effect in nanodisk array," Appl. Phys. Lett. **96**, 081915 (2010).
77. G. X. Du, T. Mori, M. Suzuki, S. Saito, H. Fukuda, and M. Takahashi, "Magneto-optical effects in nanosandwich array with plasmonic structure of Au/$[Co/Pt]_n$/Au," J. Appl. Phys. **107**, 09A928 (2010).
78. G. X. Du, T. Mori, S. Saito, and M. Takahashi, "Shape-enhanced magneto-optical activity: Degree of freedom for active plasmonics," Phys. Rev. B **82**, 161403(R) (2010).
79. G. X. Du, S. Saito, and M. Takahashi, "Spectroscopic characterization of magnetoplasmonic nanodisk array: size, shape and lattice constant," arXiv:1306.1451 (2013).
80. L. Wang, C. Clavero, Z. Huba, K. Carroll, E. Carpenter, D. Gu, and R. Lukaszew, "Plasmonics and enhanced magneto-optics in core-shell Co-Ag nanoparticles," Nano Lett. **11**, 1237–40 (2011).
81. L. Wang, K. Yang, C. Clavero, A. J. Nelson, K. J. Carroll, E. E. Carpenter, and R.

A. Lukaszew, "Localized surface plasmon resonance enhanced magneto-optical activity in core-shell Fe-Ag nanoparticles," J. Appl. Phys. **107**, 09B303 (2010).

82. P. Jain, Y. Xiao, R. Walsworth, and A. Cohen, "Surface plasmon resonance enhanced magneto-optics (SuPREMO): Faraday rotation enhancement in gold-coated iron oxide nanocrystals," Nano Lett. **9**, 1644–1650 (2009).
83. R. Dani, H. Wang, S. Bossmann, G. Wysin, and V. Chikan, "Faraday rotation enhancement of gold coated Fe_2O_3 nanoparticles: Comparison of experiment and theory," J. Chem. Phys. **135**, 224502 (2011).
84. G. Armelles, A. Cebollada, A. García-Martín, J. M. Montero-Moreno, M. Waleczek, and K. Nielsch, "Magneto-optical properties of core-shell magneto-plasmonic Au–$Co_xFe_{3-x}O_4$ nanowires," Langmuir **28**, 9127–9130 (2012).
85. Y. Li, Q. Zhang, A. V. Nurmikko, and S. Sun, "Enhanced magnetooptical response in dumbbell-like Ag-$CoFe_2O_4$ nanoparticle pairs," Nano Lett. **5**, 1689–92 (2005).
86. D. Meneses-Rodríguez, E. Ferreiro-Vila, P. Prieto, J. Anguita, M. González, J. García-Martín, A. Cebollada, A. García-Martín, and G. Armelles, "Probing the electromagnetic field distribution within a metallic nanodisk," Small **7**, 3317–3323 (2011).
87. M. Kataja, T. K. Hakala, A. Julku, M. J. Huttunen, S. van Dijken, and P. Törmä, "Surface lattice resonances and magneto-optical response in magnetic nanoparticle arrays," Nat. Commun. **6**, 7072 (2015).
88. M. Kataja, S. Pourjamal, N. Maccaferri, P. Vavassori, T. Hakala, M. Huttunen, P. Törmä, and S. Dijken, "Hybrid plasmonic lattices with tunable magneto-optical activity," Opt. Express **24**, 3652–3662 (2016).
89. E Hutter and J. H. Fendler, "Exploitation of localized surface plasmon resonance," Adv. Mater. **16**, 1685-1706 (2004).
90. J. Zhao, B. Frank, F. Neubrech, C. Zhang, P. Braun, and H. Giessen, "Hole-mask colloidal nanolithography combined with tilted-angle-rotation evaporation: A versatile method for fabrication of low-cost and large-area complex plasmonic nanostructures and metamaterials," Beilstein J. Nanotechnol. **5**, 577–86 (2014).
91. M. A. McCord, and M. J. Rooks, *Handbook of Microlithography, Micromachining, and Microfabrication* (SPIE, 1997), Chap. 2.
92. S. T. Davies, and B. Khamsehpour, "Focused ion beam machining and

deposition for nanofabrication," Vacuum, **47**, 455 (1996).

93. G. M. Wallraff, and W.D. Hinsberg, "Lithographic imaging techniques for the formation of nanoscopic features," Chem. Rev. **99**, 1801 (1999).
94. C. Haynes and R. Duyne, "Nanosphere lithography: a versatile nanofabrication tool for studies of size-dependent nanoparticle optics," J. Phys. Chem. B **105**, 5599–5611 (2001).
95. H. Gong, L. Zhou, X. Su, S. Xiao, S. Liu, and Q. Wang, "Illuminating dark plasmons of silver nanoantenna rings to enhance exciton-plasmon interactions," Adv. Funct. Mater. **19**, 298-303 (2009).
96. J. Zhao, C. Zhang, P. Braun, and H. Giessen, "Large-area low-cost plasmonic nanostructures in the NIR for Fano resonant sensing," Adv. Mater. **24**, OP247–OP252 (2012).
97. S. Cataldo, J. Zhao, F. Neubrech, B. Frank, C. Zhang, P. Braun, and H. Giessen, "Hole-mask colloidal nanolithography for large-area low-cost metamaterials and antenna-assisted surface-enhanced infrared absorption substrates.," ACS Nano **6**, 979-85 (2011).
98. J. Zhao, S. Jaber, P. Mulvaney, P. Braun, and H. Giessen, "Repetitive hole-mask colloidal lithography for the fabrication of large-area low-cost plasmonic multishape single-layer metasurfaces," Adv. Opt. Mater. **3**, 680-686 (2015).
99. B. Frank, X. Yin, M. Schäferling, J. Zhao, S. Hein, P. Braun, and H. Giessen, "Large-area 3D chiral plasmonic structures," ACS Nano **7**, 6321–9 (2013).
100. K. Seshan, *Handbook of Thin-film Deposition Processes and Techniques: Principles, Methods, Equipment and Applications* (Noyes Publications/William Andrew Publishing, 1995), Chap. 8.
101. D. A. Glocker and S. I. Shah, *Handbook of Thin film Process Technology* (Taylor & Francis Group, 1995).
102. G. Binnig, C. F. Quate and Ch. Gerber, "Atomic force microscope," Phys. Rev. Lett. **56**, 930 (1986).
103. *Manual for the Olympus BX51*, OLYMPUS CORPORATION.
104. *Shamrock 303i product list*, ANDORTM.
105. H. Fujiwara, *Spectroscopic Ellipsometry: Principles and Applications* (John Wiley & Sons, 2007).
106. *Guide to Using WVASE32*, J.A. Woollam Co., Inc.
107. *CompleteEASE™ Data Analysis Manual*, J. A. Woollam Co., Inc.

108. M. Schubert, “Polarization-dependent optical parameters of arbitrarily anisotropic homogeneous layered systems,” Phys. Rev. B **53**, 4265 (1996).
109. D. A. G. Bruggeman, “Calculation of Various physics constants in heterogenous substances I Dielectricity constants and conductivity of mixed bodies from isotropic substances,” Ann. Phys. **24**, 636 (1935)
110. W. S. Kim, M. Aderholz, and W. Kleemann, “Calibration of polar Kerr rotation and ellipticity measurements,” Meas. Sci. Technol. **4**, 1275 (1993).
111. J. B. González Díaz, *MagnetoPlasmonics. MagnetoOptics in Plasmonics Systems* (PhD thesis, Universidad Autónoma de Madrid, 2010)
112. S. Chen, M. Svedendahl, R. Duyne, and M. Käll, “Plasmon-enhanced colorimetric ELISA with single molecule sensitivity,” Nano Lett. **11**, 1826–1830 (2011).
113. S. Sani, J. Persson, A. Dmitriev, M. Käll, and J. Åkerman, “Hole mask colloidal lithography on magnetic multilayers for spin torque applications,” J. Phys. Conf. Ser. **200**, 072078 (2010).
114. S. Kristensen, G. Pedersen, R. Ogaki, V. Bochenkov, L. Nejsum, and D. Sutherland, “Complex protein nanopatterns over large areas via colloidal lithography,” Acta Biomater. **9**, 6158–6168 (2013).
115. S. Dubas and J. Schlenoff, “Factors Controlling the growth of polyelectrolyte multilayers,” Macromolecules **32**, 8153–8160 (1999).
116. S. Syrenova, C. Wadell, and C. Langhammer, “Shrinking-hole colloidal lithography: self-aligned nanofabrication of complex plasmonic nanoantennas,” Nano Lett. **14**, 2655–2663 (2014).
117. P. Hanarp, D. Sutherland, J. Gold, and B. Kasemo, “Control of nanoparticle film structure for colloidal lithography,” Colloids Surfaces A: Physicochem. Eng. Aspects **214**, 23–36 (2003).
118. J. I. Martin, J. Nogués, K. Liu, J. L. Vicent, and I. K. Schuller, “Ordered magnetic nanostructures: fabrication and properties,” J. Magn. Magn. Mater. **256**, 449, (2003).
119. E. Ferreiro Vila, *Intertwined magnetoopitcal and plasmonic properties in metal and metal/dielectric magnetoplasmonic multilayers* (PhD thesis, Universidad de Santiago de Compostela, 2012)
120. C. Ross, S. Haratani, F. J. Castaño, Y. Hao, M. Hwang, M. Shima, J. Y. Cheng, B. Vögeli, M. Farhoud, M. Walsh, H. Smith, “Magnetic behavior of

lithographically patterned particle arrays (invited)," J. Appl. Phys. **91**, 6848 (2002).

121. M. Demand, M. Hehn, K. Ounadjela, R. Stamps, E. Cambril, A. Cornette, and F. Rousseaux, "Magnetic domain structures in arrays of submicron Co dots studied with magnetic force microscopy," J. Appl. Phys. **87**, 5111 (2000).
122. C. Miramond, C. Fermon, F. Rousseaux, D. Decanini, and F. Carcenac, "Permalloy cylindrical submicron size dot arrays," J. Magn. Magn. Mater. **165**, 500–503 (1997).
123. R. P. Cowburn, D. K. Koltsov, A. O. Adeyeye, M .E. Welland and D. M. Tricker, "Single-domain circular nanomagnets," Phys. Rev. Lett. **83**, 1042 (1999).
124. O. Kazakova, M. Hanson, P. Blomquist, and R. Wäppling, "Arrays of epitaxial Co submicron particles: Critical size for single-domain formation and multidomain structures," J. Appl. Phys. **90**, 2440 (2001).
125. Y. G. Yoo, M. Kläui, C. A. F. Vaz, L. J. Heyderman, and J. A. C. Bland, "Switching field phase diagram of Co nanoring magnets," Appl. Phys. Lett. **82**, 2470 (2003).
126. J. Rothman, M. Kläui, L. Lopez-Diaz, C. A. F. Vaz, A. Bleloch, J. A. C. Bland, Z. Cui, and R. Speaks, "Observation of a bi-domain state and nucleation free switching in mesoscopic ring magnets," Phys. Rev. Lett. **86**, 1098–101 (2001).
127. M. Kläui, C. A. F. Vaz, J. A. C. Bland, T. L. Monchesky, J. Unguris, E. Bauer, S. Cherifi, S. Heun, A. Locatelli, L. J. Heyderman, and Z. Cui, "Direct observation of spin configurations and classification of switching processes in mesoscopic ferromagnetic rings," Phys. Rev. B **68**, 134426 (2003).
128. M. Kläui, C. A. F. Vaz, L. Lopez-Diaz and J. A. C. Bland, "Vortex formation in narrow ferromagnetic rings," J. Phys.- Condens. Matter **15**, R985 (2003).
129. C. Clavero, K. Yang, J. Skuza, and R. Lukaszew, "Magnetic field modulation of intense surface plasmon polaritons," Opt. Express **18**, 7743–7752 (2010).
130. K. Kämpf, S. Kübler, F. Herberg, A. Ehresmann, "Magneto-optic surface plasmon resonance optimum layers: Simulations for biological relevant refractive index changes," J. Appl. Phys. **112**, 034505 (2012).
131. S. Kübler, N. Müglich, A. Ehresmann, "Magneto-optic surface plasmon resonance of Au/IrMn/Co/Au exchange biased layer systems," J. Appl. Phys. **116**, 064502 (2014).
132. S. Matsuda, Y. Yasuda, and S. Ando, "Fabrication of polyimide-blend thin films

containing uniformly oriented silver nanorods and their use as flexible, linear polarizers," Adv. Mater. **17**, 2221–2224 (2005).

133. M. Kociak, O. Stéphan, "Mapping plasmons at the nanometer scale in an electron microscope," Chem. Soc. Rev. **43**, 3865 (2014).
134. R. Arenal, L. Henrard, L. Roiban, O. Ersen, J. Burgin and M. Treguer, "Local plasmonic studies on individual core-shell gold-silver and pure gold nano-bipyramids," J. Phys. Chem. C **118**, 25643 (2014).
135. F. J. Garcia de Abajo, "Optical excitations in electron microscopy," Rev. Mod. Phys. **82**, 209 (2010).
136. J. Reece Roth, *Industrial Plasma Engineering* (CRC Press, 1995).
137. S. M. Sze, and M.-K. Lee, *Semiconductor Devices: Physics and Technology* (John Wiley & Sons, 2012)
138. J. Aizpurua, L. Blanco, P. Hanarp, D. S. Sutherland, M. Käll, G. W. Bryant, and F. J. G. de Abajo, "Light scattering in gold nanorings," J. of Quant. Spectrosc. Radiat. Transfer **89**, 1116 (2004).
139. A. Mary, A. Dereux, and T. Ferrell, "Localized surface plasmons on a torus in the nonretarded approximation," Phys. Rev. B **72**, 155426 (2005).
140. C. Dutta, T. Ali, D. Brandl, T.-H. Park, and P. Nordlander, "Plasmonic properties of a metallic torus," J. Chem. Phys. **129**, 084706 (2008).
141. S. Zou, "Light-driven circular plasmon current in a silver nanoring," Opt. Lett. **33**, 2113 (2008).
142. Y. Cai, Y. Li, P. Nordlander, and P. S. Cremer, "Fabrication of elliptical nanorings with highly tunable and multiple plasmonic resonances," Nano Lett. **12**, 4881 (2012).
143. Q. Xu, J. Bao, R. Rioux, R. Perez-Castillejos, F. Capasso, and G. Whitesides, "Fabrication of large-area patterned nanostructures for optical applications by nanoskiving," Nano Lett. **7**, 2800 (2007).
144. L. Novotny, "Effective wavelength scaling for optical antennas," Phys. Rev. Lett. **98**, 266802 (2007).
145. C.-Y. Chen, S.-C. Wu, and T.-J. Yen, "Experimental verification of standing-wave plasmonic resonances in split-ring resonators," Appl. Phys. Lett. **93**, 034110 (2008).
146. F. Neubrech, T. Kolb, R. Lovrincic, G. Fahsold, A. Pucci, J. Aizpurua, T. Cornelius, M. Toimil-Molares, R. Neumann, and S. Karim, "Resonances of

individual metal nanowires in the infrared," Appl. Phys. Lett. **89**, 253104 (2006).

147. G. Laurent, N. Félidj, J. Aubard, G. Lévi, J. Krenn, A. Hohenau, G. Schider, A. Leitner, and F. Aussenegg, "Evidence of multipolar excitations in surface enhanced Raman scattering," Phys. Rev. B **71**, 045430 (2005).
148. C.-Y. Tsai, S.-P. Lu, J.-W. Lin, and P.-T. Lee, "High sensitivity plasmonic index sensor using slablike gold nanoring arrays," Appl. Phys. Lett. **98**, 153108 (2011).
149. H. Jiang, and J. Sabarinathan, "Effects of coherent interactions on the sensing characteristics of near-infrared gold nanorings," J. Phys. Chem. C **114**, 15243-15250 (2010).
150. A. Mary, D. Koller, A. Hohenau, J. Krenn, A. Bouhelier, and A. Dereux, "Optical absorption of torus-shaped metal nanoparticles in the visible range," Phys. Rev. B **76**, 245422 (2007).
151. S. Kim, J.-M. Jung, D.-G. Choi, H.-T. Jung, and S.-M. Yang, "Patterned arrays of Au rings for localized surface plasmon resonance," Langmuir **22**, 7109 (2006).
152. S. Teo, V. Lin, R. Marty, N. Large, E. Llado, A. Arbouet, C. Girard, J. Aizpurua, S. Tripathy, and A. Mlayah, "Gold nanoring trimers: a versatile structure for infrared sensing," Opt. Express **18**, 22271 (2010).
153. M. Green, and F. Liu, "SERS substrates fabricated by island lithography: the silver/pyridine system," J. Phys. Chem. B **107**, 13015 (2003).
154. M. Banaee, and K. Crozier, "Gold nanorings as substrates for surface-enhanced Raman scattering," Opt. Lett. **35**, 760 (2010).
155. K.-Y. Jung, F. L. Teixeira, and R. M. Reano, "Au/SiO_2 nanoring plasmon waveguides at optical communication band," J. Lightwave Technol. **25**, 2757 (2007).
156. C.-K. Lee, H.-Y. Tseng, C.-Y. Lee, S.-Y. Wu, T.-T. Chi, K.-M. Yang, H.-Y. Chou, M.-T. Tsai, J.-Y. Wang, Y.-W. Kiang, C.-P. Chiang, and C. C. Yang, "Characterizing the localized surface plasmon resonance behaviors of Au nanorings and tracking their diffusion in bio-tissue with optical coherence tomography," Biomed. Opt. Express **1**, 1060 (2010).
157. Y. Babayan, J. M. McMahon, S. Li, S. K. Gray, G. C. Schatz, and T. W. Odom, "Confining standing waves in optical corrals," ACS Nano **3**, 615 (2009).
158. J. Aizpurua, P. Hanarp, D. S. Sutherland, M. Käll, G. W. Bryant, and F. J. García de Abajo, "Optical properties of gold nanorings," Phys. Rev. Lett. **90**, 057401

(2003).

159. F. Hao, E. Larsson, T. Ali, D. Sutherland, and P. Nordlander, "Shedding light on dark plasmons in gold nanorings," Chem. Phys. Lett. **458**, 262 (2008).
160. J. Ye, P. Dorpe, L. Lagae, G. Maes, and G. Borghs, "Observation of plasmonic dipolar anti-bonding mode in silver nanoring structures," Nanotechnology **20**, 465203 (2009).
161. C.-Y. Tsai, C.-Y. Wu, K.-H. Chang, and P.-T. Lee, "Slab thickness dependence of localized surface plasmon resonance behavior in gold nanorings," Plasmonics **8**, 1011 (2013).
162. F. Hao, P. Nordlander, M. Burnett, and S. Maier, "Enhanced tunability and linewidth sharpening of plasmon resonances in hybridized metallic ring/disk nanocavities," Phys. Rev. B **76**, 245417 (2007).
163. D. Lehr, K. Dietrich, C. Helgert, T. Käsebier, H.-J. Fuchs, A. Tünnermann, and E.-B. Kley, "Plasmonic properties of aluminum nanorings generated by double patterning," Opt. Lett. **37**, 157 (2012).
164. W.-S. Chang, L. Slaughter, B. Khanal, P. Manna, E. Zubarev, and S. Link, "One-dimensional coupling of gold nanoparticle plasmons in self-assembled ring superstructures," Nano Lett. **9**, 1152 (2009).